IGCAR ANNUAL REPORT 2006

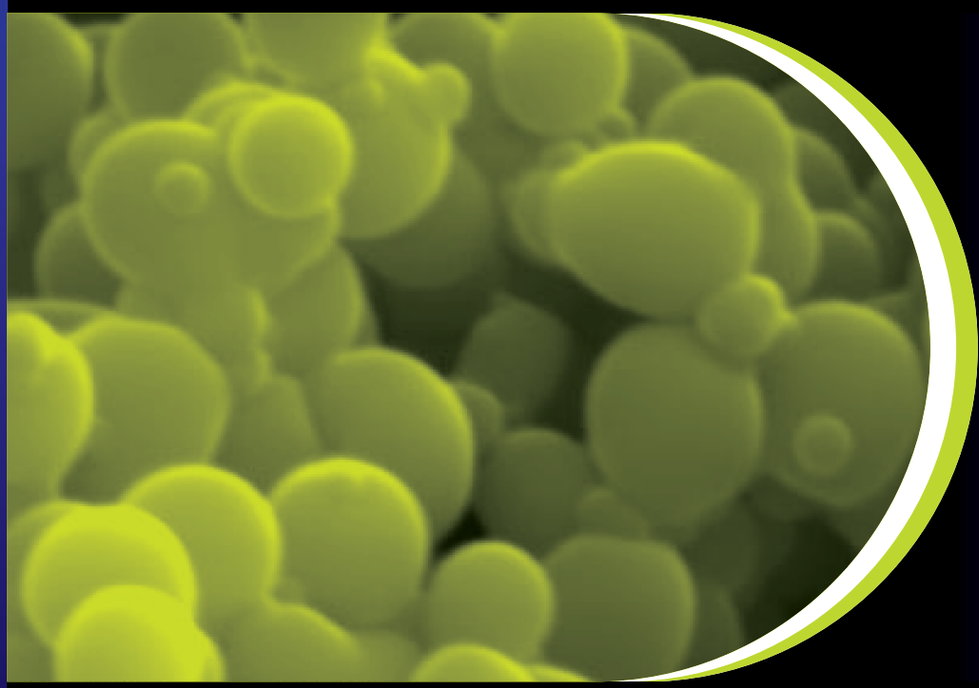

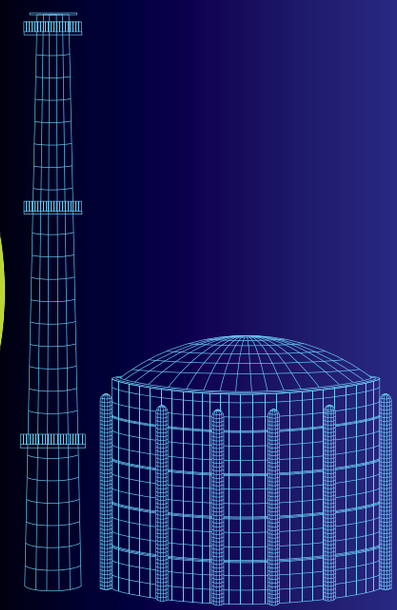

IGCAR

ANNUAL REPORT 2006

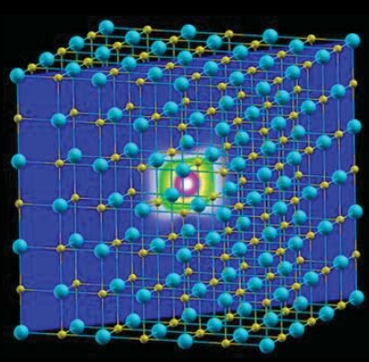

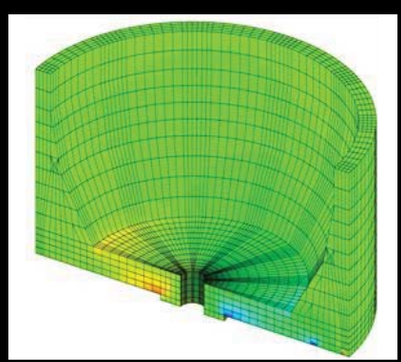

GOVERNMENT OF INDIA
DEPARTMENT OF ATOMIC ENERGY
INDIRA GANDHI CENTRE FOR ATOMIC RESEARCH
KALPAKKAM - 603 102

सत्यमेव जयते

IGC

Annual Report 2006

Government of India
Department of Atomic Energy
Indira Gandhi Centre for Atomic Research
Kalpakkam - 603 102.

Editorial Committee

Address for Correspondence

Dr. P.R. Vasudeva Rao

Chairman, Editorial Committee,

Director, Chemistry, Metallurgy and Materials Groups

Indira Gandhi Centre for Atomic Research,

Kalpakkam - 603 102

Phone: +91-44-27480229

Fax: +91-44-27480065

Email: vasu@igcar.gov.in

Published by:

Scientific Information & Resources Division (SIRD),

Indira Gandhi Centre for Atomic Research,

Kalpakkam - 603 102

Website: www.igcar.gov.in

February 2007

"Actions today mould our tomorrows"

Indira Gandhi

"… There is a need for a constant interplay between basic sciences, technology and industrial practice if economic progress is to result from the activity undertaken…"

- Vikram Sarabhai

CONTENTS

Cover Page

TOP

Scanning Electron Microscopic image of boron produced indigenously.

LEFT

Intricate piping in Compact Reprocessing facility for Advanced Fuels in Lead cells (CORAL).

CENTRE

Visualization of positron trapping at TiC particle in Steel matrix.

RIGHT

Structural Integrity Assessment of Reactor Vault - Stress distribution at the bottom of Inner Wall.

EDITORIAL

The editorial committee takes great pleasure in presenting the annual report of IGCAR for the year 2006. The Centre is going through a golden period of achievements in fast reactor technology. The completion of twenty years of successful operation of FBTR with excellent performance of its various sub-systems and the fuel reaching the high burn-up of 155 GWd/t without any fuel pin failure in the core. This international bench mark called for a celebration, which was well attended and well appreciated. Now, the FBTR team is poised to take up a series of experimental irradiations and also life extension through safety evaluation. With plans to introduce test fuels such as the mixed oxide fabricated through the sol-gel route and the U-Pu-Zr metallic alloys, we can expect FBTR to continue to achieve many more significant milestones.

Backed by sound expertise in experimentation as well as modeling and design, the entire gamut of programmes related to the development of fast breeder reactor as well as fuel cycle have progressed impressively, as can be judged from a reading of the report. Clear targets have been set for innovations towards reaching higher burn-ups and for making the reactor more economical and safe. Research programmes in fuel cycle are aimed at improved operations, reduced waste and increased life of the plants. In all areas addressed by the centre, including physics, chemistry, safety, materials, electronics and instrumentation, sodium technology, etc., we have a diverse and vibrant R & D programme, making it a difficult task for the editors to choose the areas to report on! The scientific achievements apart, the progress of the national and international collaborations as well as the commencement of the Training school at IGCAR facilitate immense value addition to human resource development and place our Centre in a firm position to advance towards attaining global leadership in fast reactor technology and associated fuel cycle development.

We are grateful to Dr Baldev Raj, Director, IGCAR for being a constant source of inspiration. As a person who believes that there is no limit to excelling one's own performance, he has been the driving force behind the continuous improvements in this publication. We have immensely benefited from his guidance and support.

This report comes with a new layout which we believe, is more aesthetic and easy on the reader. We compliment all the authors for the scientific and technical achievements as well as for cooperating with us to realize the publication on time. I thank Shri M. Somasekharan, Head, SIRD and Shri M. Ganapathy for their co-ordination efforts at the final stages of publication. As the Chairman of the committee, it is my pleasure to acknowledge the untiring efforts of the editorial committee, and especially Dr. G. Amarendra and Shri R. V. Subba Rao, whose committed involvement has added flavor and substance to the report besides expediting the publication.

We had received many valuable comments regarding the annual report of 2005 from the readers, and many suggestions for improvement. We have tried our best to incorporate these suggestions. We would greatly appreciate receiving any suggestions from our eminent readers regarding the current issue as well, which would help us to improve the publication further.

(P.R.Vasudeva Rao)
Chairman, Editorial Committee
Director, Chemistry, Metallurgy & Materials Groups

FOREWORD

The Centre visualizes world leadership in Fast Reactor and associated Closed Fuel Cycle through robust and safe technologies based on breakthroughs provided by basic science and engineering disciplines. I am a firm believer in seamless science and technology. I quote Bill Wulff *"There is only one nature - the division into science and engineering is a human imposition, not a natural one. Indeed, the division is a human failure; it reflects our limited capacity to comprehend the whole"*. We thus have to visualize the totality of the picture and evolve towards the common goal of the Centre, with our complementary and corroborative contributions relating to our specializations. I take pride in sharing a few achievements of the Centre with you.

The Fast Breeder Test Reactor (FBTR), the pride of the Centre, has continued to scale new international heights by successfully operating and making the mixed carbide fuel reach a burn-up of 155 GWd/t, without any fuel failure. FBTR is also acting as a test-bed for the PFBR MOX fuel, which has already undergone 60 GWd/t of burn-up as against target burn-up of 100 GWd/t. This will provide very valuable data on the irradiation behavior of the oxide fuel. We have received regulatory clearances for doing some state-of-art and relevant experiments to enhance safety of future Sodium Cooled Fast Reactors. Analytical and experimental investigations are being pursued towards life management of FBTR to ensure that FBTR is available to us for next twenty years.

The Prototype Fast Breeder Reactor (PFBR) construction has progressed as scheduled, and we are sparing no efforts to ensure that it will be commissioned by September 2010. The Centre continues to provide robust design and R & D support to PFBR. A few important components like Safety Vessel, Main Vessel and Inner Vessel have arrived at site. Many of the reactor components are in advanced stage of fabrication. It is a matter of great satisfaction for us that we have achieved quality levels better than specified and also many international benchmarks.

Closing the fuel cycle is very important and critical aspect of Fast Reactor technology and thus reprocessing of the spent fuel is very crucial for this. We are taking all necessary and urgent steps towards robust fuel cycle technologies. Integrated Fast Reactor Fuel Cycle Facility (FRFCF) co-located with Prototype Fast Breeder Reactor (500 MWe) is making good progress. Work on plant design engineering consultancy has been completed, including the geo-technical work, which is important aspect of the plant safety. Activities connected with the Head End Facility are in progress to integrate with Demonstration Fuel Reprocessing Plant (DFRP) to be commissioned in 2009. DFRP is designed for reprocessing irradiated FBTR fuel on regular basis and demonstrating 'process and plant' for reprocessing of irradiated mixed oxide fuel of PFBR.

The full power operation of the Steam Water System of

the Steam Generator Test Facility is an event that we are keenly looking forward to. The operation of the SGTF would provide valuable insights into the design and operation of the steam generators, which are vital for FBRs. Similarly, the testing of various components in sodium and the setting up of the full scale simulator for PFBR are in exciting periods of progress.

While we note with pride our Centre's progress so far, we realize the need to embark on an intense and focused long term R&D programme to introduce innovations in reactor design, construction and operation as well as the fuel cycle so that the reactors and the fuel cycle facilities not only provide power at an economical tariff but also operate safely with high availability factors. Our Centre has already arrived at a framework of R&D programme, which has to be pursued in order to meet these objectives. The R&D programmes encompass many areas of science and technology including physics, chemistry, structural mechanics, electronics, safety etc. Thus it is obvious that the entire Centre must focus on these R&D programmes in order to elevate the fast reactor programme to higher domain. It is very important that we involve all the young minds of the Centre to ponder over the issues related to economics and safety of the reactors and fuel cycle and take up R&D programmes with commitment and focus.

We have a unique opportunity to play a leading role in the global development of fast reactors and fuel cycle. It is not an exaggeration to state that our success in the PFBR project and associated closed fuel cycle will be an important ingredient, in subsequent decisions about the development of fast reactors and their enhanced contribution to nuclear energy production not only in our country, but also other countries. The world nuclear community is watching with keen interest and admiration our progress in fast reactor technology. We must make every effort to achieve total success in these programmes and also keep up the momentum of R&D to reach higher levels of maturity in this technology.

We have always believed that quantum jumps in technology can only take place through scientific breakthroughs. It is for this reason that we have a strong and focused programme of basic research in our Centre, covering a wide spectrum of activities such as ab-initio computations, nano coatings, etc. To further strengthen our human resources and the vitality of our Centre and continuity of knowledge, we have started a Training school at IGCAR in core engineering disciplines starting from this year. While, presently it caters to chemical engineering, electronics and instrumentation and mechanical engineering, we hope to add more disciplines in the years to come. With IGCAR becoming a constituent institution (CI) under Homi Bhabha National Institute (HBNI), having a university status under University Grants Commission, we can hope to further strengthen our human resources by inducting more young students in various research programmes, besides fulfilling the academic aspirations of our colleagues. This definitely provides a rich academic atmosphere to our mission-mode research programmes.

Fast Reactor Science & Technology is an important area, where continuous quest for knowledge, understanding and innovations is necessary to enable a quantum leap in our endeavor to be a world leader. We should evolve and mature from the questions of *"What ? Why? How ?"* to aiming for bigger things and be confident to ask *"Why not?"*. Let me quote Albert Einstein, *"The mere formulation of a problem is far more essential than its solution, which may be merely a matter of mathematical or experimental skills. To raise new questions, new possibilities, to regard old problems from a new angle require creative imagination and marks real advances in science."* Let us all march together to attain such a state of collective scientific maturity and wisdom.

I am pleased to note that IGC Annual Report depicting various frontline research and development that were carried out at our Centre during the year 2006 is being released within a couple of months of 2007. I would like to compliment Dr. P. R. Vasudeva Rao, Chairman, Editorial Committee and the members of the committee for putting up their best and sincere efforts in recoding our achievements with high standards of technical as well as aesthetic quality.

With my best wishes and warm regards,

(Baldev Raj)
Director
IGCAR

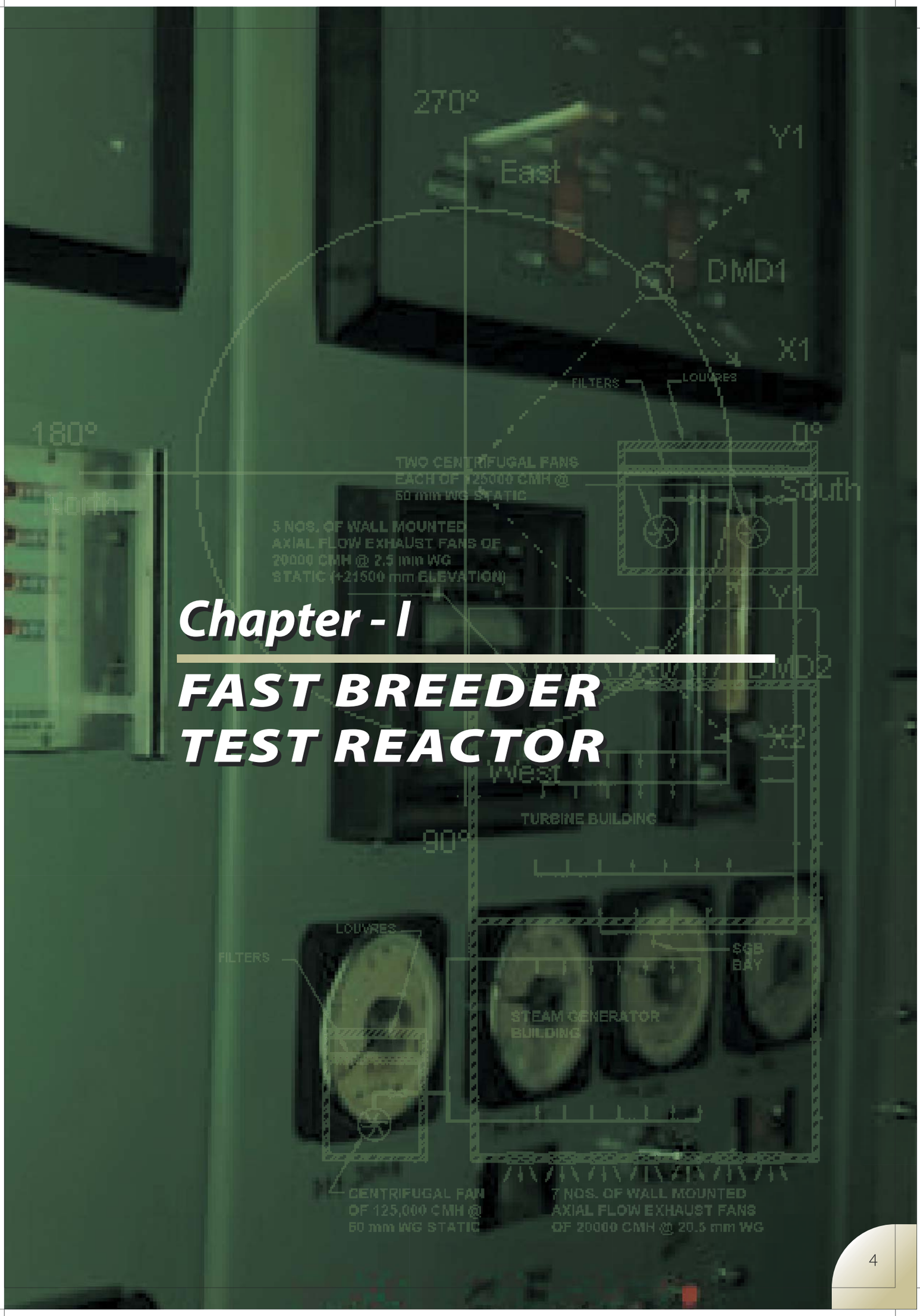

Chapter - I

FAST BREEDER TEST REACTOR

1.1 Twenty Years of Successful Operation of FBTR

Fast Breeder Test Reactor completed twenty years of operation in October 2005. The operation of the reactor has been successful and has provided the confidence to take up the construction of the 500 MWe Prototype Fast Breeder Reactor (PFBR). The operating experience of FBTR has been factored into the design of the PFBR. Besides, FBTR has also been a good base for development of human resources which is vital for the construction and operation of PFBR and future reactors.

The unique Pu-rich U,Pu mixed carbide fuel of FBTR has performed excellently. Four MK-I subassemblies have reached a peak burn-up of 155 GWd/t without any failure- a landmark in the history of carbide fuels. One subassembly has been discharged for Post-Irradiation Examination (PIE), and the other three loaded outside the core, awaiting results of PIE . At this burn-up level, the porosities in the fuel are expected to have been exhausted, and the fuel will be examined to find out how it has behaved in the post-porosity exhaustion phase. It is also to be noted that over the years, we have taken SS 316 to very high dpa levels (80-85 dpa), probably the highest in published literature for this material. The present PIE will address the swelling and residual ductility of the clad and the wrapper. The force required to discharge the SA was periodically measured at the end of each campaign. The results showed an increasing trend with burn-up, but the peak load has always been below the high tension trip settings of the gripper hoist

Pioneers In the Construction, Commissioning and Operation of FBTR, Gathered on The Occasion of the Commemorate Function On 18th July 2006 to Celebrate 20 Years of Successful Operation of FBTR.

mechanism of the discharging flask. It would hence be interesting to know whether the clad and wrapper will allow further extension of burn-up with sufficient confidence. If so, the three high burn-up subassemblies loaded in the periphery could be moved back to the first ring.

Safety clearance has been obtained for the hybrid core of 27 MK-I & 57 MOX subassemblies. Safety report for the hybrid core has been submitted to the safety authorities. The first lot of eight MOX subassemblies have been loaded inside the reactor, and the 14th irradiation campaign will be with a core of 49 fuel subassemblies (27 MK-I, 13 MK-II, eight MOX and one PFBR test fuel).

Having completed twenty years, FBTR is due for periodic Safety Review by AERB. The aspects to be covered in periodic safety review are: actual physical condition of the nuclear power plant, safety analysis, equipment qualification, management of ageing, safety performance, use of experience from other nuclear power plants and of research findings, procedures, organization and administration, human factors, emergency planning and environmental impact. The document on periodic safety review of FBTR was submitted to AERB. Based on the initial review, the chapters on equipment qualification and ageing management are being revised. For equipment qualification, a list of more than 2500 components has been identified, and their operational history is being compiled.

Ageing management requires quantitative assessment of the damage accumulated by the passive and non-replaceable components so far and the available residual life. This exercise is now in progress. Due to operation below the creep range, with thermal fatigue cycles of lower temperature range than taken in design, there is no concern for the residual life of the plant as far as the creep-fatigue damage mechanism is concerned. The plant life seems to be governed by the neutron induced degradation of the grid plate. The present indication is that for an allowable residual ductility of 10%, the grid plate will have a residual life of 11.5 effective full power years, (where full power refers to the reactor power corresponding to the driver fuel operation at LHR of 400 W/cm). Since the assessment is based on computed fluxes and literature on the neutronic embrittlement of stainless steel, it is planned to measure the actual flux at the grid plate location in the 14th campaign. Based on the measured flux, it is also planned to irradiate test specimens to fluence levels simulating end of life dose levels.

Another important aspect of the review is the seismic re-evaluation of the plant to the present norms. This has been taken up as a joint research project of IGCAR and SRI. The first portion of the project comprises the seismic qualification of at least one safety chain related to shutdown, decay heat removal and containment of radioactivity. The second part of the research project comprises seismic margin assessment of the plant, conceived more as an academic exercise rather than mandatory requirement. The criteria document has been prepared by the task force and is submitted to AERB for review. The list of structures, systems and equipment is being compiled by constructing event trees and fault trees following a seismic event. This will be followed by a preliminary screening plant walkdown. It is targeted to complete the minimum requirement for plant re-licensing before the end of 2007, unless the analysis and plant walk-down indicate the need for major strengthening.

To commemorate and highlight the completion of 20 years of excellent operation of FBTR, a simple function was held in March 2006. The invitees were the delegates of the two IAEA technical meetings held at IGCAR and DAC members. A video film titled `A journey through FBTR' prepared for this occasion was shown to the audience. The foreign delegates were quite impressed with the achievements of FBTR, with practically no external guidance. The French team presented a plaque from Phenix, complementing FBTR.

A more detailed and formal function was held on 18th July. The commemorative function on 18th July also practically coincided with the end of the 13th irradiation campaign with 29 MK-I, 13 MK-II & one PFBR test fuel subassemblies. Hon'ble Defence Minister Shri Pranab Mukherjee, Hon'ble Minister of state Shri Prithiviraj Chavan and Dr. Georges Vendryes, Hon. Executive Vice President of French Atomic Energy Commission participated in the function. About forty retired senior officers of the centre, who had contributed to FBTR, also participated in the function. All the dignitaries and invitees visited FBTR. The Defence Minister expressed his appreciation for the successful operation of FBTR for 20 years. He said that FBRs are destined to play a major role in the energy security of India in the coming years, and the successful operation of FBTR was a stepping stone for the next phase of our nuclear programme. Dr. Vendryes was briefed about the operating history of FBTR and was so impressed with resilience of the team in the several challenges faced over the years that he made a crisp comment `you truly deserve to celebrate twenty years of FBTR operation'.

I.2 Augmentation of Ventilation System for Steam Generator and Turbine Buildings

The Turbine Building (TB) of FBTR, having 45 m length, 27 m width and 25 m height along with Steam Generator building (SGB) having 45 m length, 18 m width and 25 m height are ventilated by means of three tube axial fans each of 85000 m3/h capacity. During high power operations, the maximum ambient temperature in these buildings at certain locations were found to be >45°C. This has affected the smooth operation of the lubrication circuit of secondary sodium pump in SGB as well as hydraulic circuits of bypass control valves of steam turbine in TB. Systematic measurement of air flow through various ventilation grills at high power operation revealed that only 60% of the total airflow requirements for SGB as well as TB were met by the three supply fans. It was hence decided to suitably augment the ventilation system for these buildings.

Various augmentation schemes were discussed and finally the best of these schemes comprising two additional supply fans each of 1,25,000 m^3/h capacity and 5 exhaust fans each of 20,000 m^3/h capacity for TB and one additional supply fan of 1,25,000 m^3/h capacity and 7 exhaust fans each of 20,000 m^3/h capacity was selected. Additional duct work of 3000 m^2, louvers and filters were also envisaged. For housing the supply fans, two fan rooms were constructed surrounding the SGB and TB.

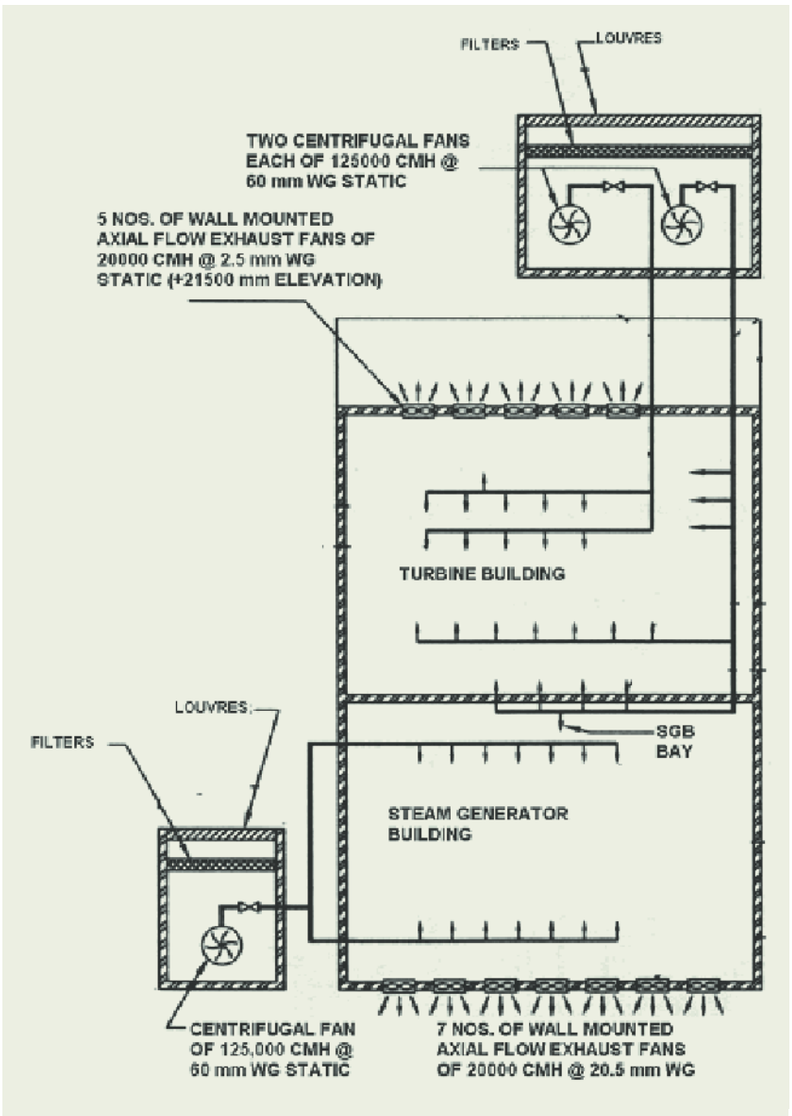

Fig.1
Simplified Schematic of Augmentation of Ventilation for Steam Generator and Turbine Buildings

Augmentation work (Fig.1) was taken up in 2004 and completed by Aug 2006. Construction of two fan rooms was quite involved since retrofitting has to take care of site interferences such as under ground fire water lines, earthling routing, raw water supply lines etc. Further, ductwork involved intricate routing to avoid site interferences with the existing systems. During commissioning, flow rates through the additional ventilation grills were measured and were found to meet the additional demand. Ambient temperatures measurements at critical areas with the augmented ventilation with sodium temperatures corresponding to high power operation revealed that there is a reduction of about 5°C in ambient temperature, which meets the design basis for the augmentation.

I.3 Commissioning of Real-time Computer System

The central data processing system (CDPS) of FBTR carries out safety critical functions namely supervision of outlet temperature of all fuel sub-assemblies to safeguard against events namely coolant flow blockage, fuel-clad hot spot and undesirable power excursions and initiation of LOR on control rod level discordance and water leak in steam generator and fine impulse testing of safety logic circuits. It performs many safety related functions namely discordance supervision of triplicated channels, checking conditions for authorization of reactor and fuel handling start-up, initiation of auto-flooding of reactor vessel with sodium during leak of sodium from main and double envelope pipe of reactor vessel and detection of plugging of siphon break-line . It also performs the non-safety functions, namely, logging of certain plant parameters

CDPS consisted of PDP-11/84 as sub-system–I (SS-I) and Unipower-30 supplied by ECIL as sub-system-II (SS-II). After a few years of operation, these systems developed a number of problems viz., failures of components due to ageing, non-availability of spares due to component obsolescence and failure of moving parts like hard-disc due to wear and tear. Hence, it was decided to replace these systems one-by-one with state-of-the-art, disc-less, embedded, real-time systems with the features of high-reliability and availability, ease of program development and maintenance, ease of hardware maintenance and insurance against component obsolescence. For meeting these requirements, the VME bus architecture with proven reliability was chosen. The Motorola 68020-based CPU card and analog and digital I/O cards were all developed in-house by the Electronics & Instrumentation Division conforming to VME bus standards. The salient features of this system named as ED-20 are

- Advanced diagnostic features like single-bit memory error correction and double bit error detection.
- No hard disk, for program or data storage and no operating system. Hardware is directly accessed making the program highly efficient.
- Smart Analog Input Card with built-in calibration facility.
- Optically-isolated Digital Input Card with online testability and status display features.
- Mono-shot configurable Relay Output Card with status display incorporating fail safe design.

It was decided to first replace the Unipower-30 based SS-II, which is normally a stand-by system. The architecture of ED-20 system (Fig.1) employs three independent systems to perform safety critical, safety related and non-safety functions to improve the reliability and availability of the system. All the analog inputs from the plant were galvanically isolated from the sensitive electronic circuits by providing 3-port isolating amplifiers and the digital inputs through opto-isolators. It was also decided that the software development will adhere to the AERB DG-25 guideline. Hence documents namely system requirement specification (SyRS), system architecture design (SAD), software requirement specification (SRS) and software design document (SDD) were prepared prior to taking up the system development. The design documents including the code were checked by an internal verification & validation (V&V) team from E&I Division. After incorporating the internal V&V team's comments, V&V of the software was carried out by SARCOP sub-committee for computers and Instrumentation (SCCI).

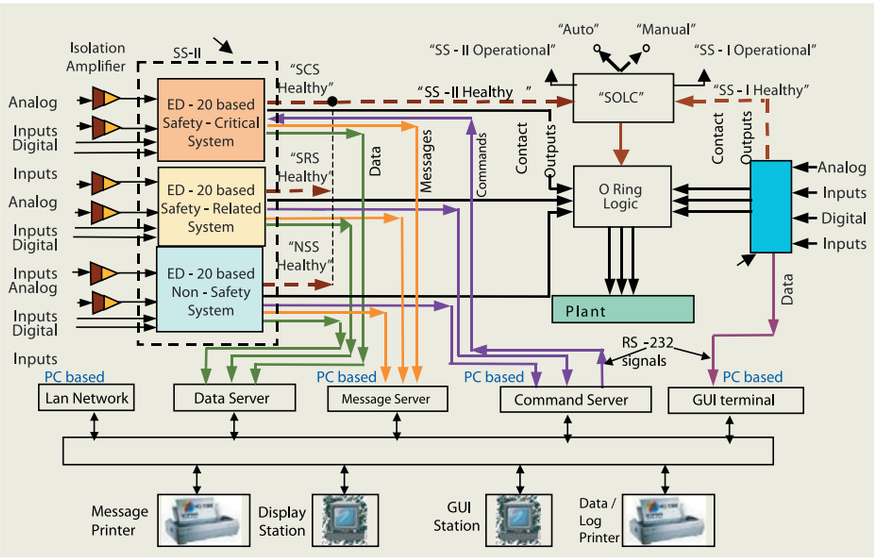

Fig.1
Architecture Of CDPS

In tune with the proven model used in the PDP-11 system, waterfall model was adopted in application software development. The software was developed in house using 'C' language satisfying MISRA-C guidelines. The developed software is downloaded, into the EPROM (Erasable Programmable Read-Only Memory) on the CPU board. The modifiable parameters, which include various threshold values for alarms, LORs and SCRAMs, are stored in an EEPROM (Electrically Erasable Programmable Read-Only Memory). The application programs run on the VME-based systems and the outputs like alarms, LORs and SCRAMs are initiated through relay output cards. The ED-20 system periodically sends the scanned data to a Industrial computer based data server for storage. The stored information is available to the graphical user interface (GUI) for data display, logging and mimics display. The three VME based systems also send coded messages generated by the supervision programs to another Industrial computer based message server which decode the messages appropriately and sends them to the display station and the on-line network printer. The messages are further stored in database tables for storage and archiving. The installation of the ED-20 system was started in November, 2004 and commissioned by October, 2005. The performance of the system was assessed in off-line mode with all the plant inputs connected, all the programs operational but outputs of the system to plant disconnected during October-November, 2005 and was satisfactory. Then the system performance was evaluated in on-line mode (with its output connected to the plant) during April-August, 2006 and was satisfactory. The clearance from SARCOP was obtained in Sept, 2006 to commence 14th irradiation campaign with ED-20 system on-line and PDP-11 as manual standby. After assessing the performance of ED-20 system on-power for about 3 months, the replacement of PDP-11/84 with identical system will be taken up.

As this replacement was a retro-fitting work, it was quite challenging. It involved carrying out installation and commissioning of the new system in the midst of operating plant, retaining the existing control panels and field cables without disturbing the operating PDP-11 system. The system to be employed to PFBR is similar to ED-20 system and hence the performance of ED-20 system will give vital feedbacks in the design of the system for PFBR.

I.4 Triplication of Steam Generator Leak Detection System

The secondary sodium systems have two Steam Generator (SG) modules connected in parallel in each loop. The SG module is a once-through type heat exchanger in which sodium flows in the shell side at a low pressure (2 to 3 bars) and water/ steam flows in the tube side at a high pressure (~125 bars). In case of breach in tube integrity, water/steam will leak into sodium resulting in undesirable violent reaction between sodium and water. The reaction products which are corrosive in nature produce high pressure surges in the shell side of SG and lead to undesirable consequences. A Steam Generator Leak Detection System (SGLDS) has been incorporated in FBTR to detect water/steam leak into sodium at the incipient stage itself by on-line measurement of hydrogen in sodium and to isolate the defective SGs before the leak escalates. Also, this system serves to gauge the magnitude of the leak.

The leak is detected by monitoring the increase in hydrogen concentration in sodium due to the dissolution of hydrogen produced during the reaction of sodium and water / steam ($2Na+2H_2O \rightarrow 2NaOH+H_2\uparrow$). The sample sodium drawn from the outlet of each SG module is passed through a nickel diffuser. Around the diffuser, a vacuum chamber is provided with an ultra high vacuum maintained by a sputter-ion pump. In case of a leak, due to higher influx of hydrogen into vacuum chamber, there will be an increase in the equilibrium pressure that is detected by the increase in the sputter-ion pump current. With the calibrated system, apart from detecting the leak, its magnitude also can be computed.

Though the SGLDS of FBTR was commissioned in 1992,

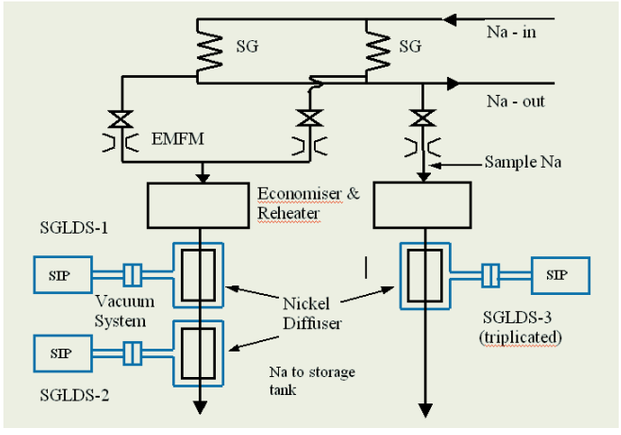

Fig.1
Triplication of SGLDS

many modifications were required to improve its performance over the years. However, there was no provision to confirm the genuineness of a leak signal and the availability of the system was very much dependent on single channel in each secondary sodium loop. To have redundancy in SGLDS, to improve availability of the plant and to avoid spurious actuation of leak signal, the system was duplicated in the first phase by adding one more nickel diffuser-vacuum system in each secondary system in series with the existing Ni diffuser (Fig.1) in July 2004. However, the safety action on reactor continued to be from single channel with the duplicated channel serving as standby.

In the second phase, the third channel of the SGLDS was added for initiating safety action on 2/3 logic. The sodium sampling line was tapped off from the common outlet header of both SG modules (Fig. 1). Sodium pipelines with EM flow meter, re-heater, nickel diffuser, associated valves, line heaters, sodium leak detectors and surface thermocouples were installed (Fig.1) and commissioned. An ultra high vacuum chamber consisting of sputter ion pump and sorption pump were connected and associated instrumentation and control logic were incorporated and commissioned. The safety logic on SG leak was modified to incorporate 2/3 coincidence SGLDS leak signals to initiate safety actions on the reactor. The retrofitting and commissioning was completed for the east secondary sodium system in September, 2005. Incorporation of third channel in west secondary system was completed in February, 2006. Calibration of the systems was carried out by injection of H_2 in sodium in both the secondary sodium systems and response of all the channels in both systems was found to be satisfactory.

Retrofitting a new channel in the existing plant, in-situ welding of stainless steel pipe lines in sodium loop and quality assurance in realising an ultra high vacuum environment were technically quire challenging. With the addition of the third channel and wiring of 2/3 logic for safety actions, the reactor operation can be continued with two healthy channels with the third one taken for maintenance. The triplication of this system yielded a robust SGLDS ensuring a high degree of reliability and availability of the reactor.

I.5 Intelligent Displacement Measuring Device

FBTR is a sodium-cooled loop-type reactor, where the reactor vessel is suspended from the top. The vessel is subject to a lot of mechanical, thermal and irradiation stresses, as a result of which, it may tilt to one side. Since this is a safety hazard, any such tilt must be detected in time and corrective actions taken. So the displacement of the reactor vessel in all the three directions (X, Y and Z) has to be monitored periodically. For this purpose a displacement measuring device (DMD) assembly exists at FBTR. The displacements are measured at two locations in FBTR, at 45° and 315° from the sodium inlet axis, as shown in Fig. 1.

The DMD assembly is shown in Fig. 2. Plumb wires are suspended from the reactor vessel at the two points where displacement is to be measured. A rectangular metallic frame is positioned such that the plumb wire passes through it. This frame is moved along the X or Y axis by an AC synchronous motor until it touches the plumb wire. The frame is connected to a potentiometer slider whose body is fixed to a mechanically rigid platform. The potentiometer is provided with a fixed DC excitation, and the ratio of the variable resistance to the total resistance is measured by the DMD controller. The distance traveled by the frame with respect to the initial position to establish contact with the plumb wire, is the measure of the reactor vessel's displacement in that axis. While commissioning the DMD assembly in FBTR, initial readings were taken and kept as reference for further calculation. Hence difference in current reading and the initial reading gives the displacement of vessel. Thermocouples present at the grid plate of the reactor provide temperature signals to the system for correction for vessel expansion due to change in temperature. The displacement in Z-direction is measured using a spring-loaded potentiometer whose slider follows the movement of reactor vessel in that axis.

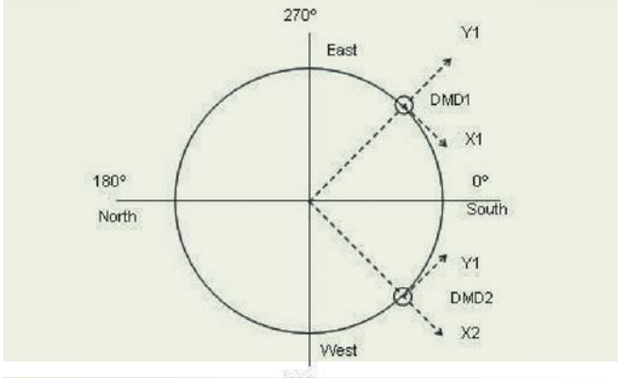

Fig.1
DMD Locations In FBTR

A Programmable Logic Controller (PLC) based DMD Controller has been designed and commissioned as part of the DMD assembly described above. The block diagram of the PLC-based system and photograph of the system in operation in FBTR are shown in Figs. 3 and 4.

The system reads in the potentiometer input signals, temperature signals and operator commands and provides displays on the front panel. For measuring displacement, the controller must drive the four motors, (X1, Y1, X2 and Y2) in forward as well as reverse directions. When the frame touches the plumb wire, the motor must be stopped and the reading must be taken. The plumb wire - frame touch signals for the four axes are also sensed for this purpose. The location for displacement measurement, the axis and direction are selected through switches on the front panel.

The system has two modes of operation: Manual and Auto. In the manual mode, the operator specifically selects the location, axis and direction for which he wishes to take a reading. In the auto mode, the operator simply presses a button, and the system takes care of all the measurements.

The PLC-based DMD controller device is operator-friendly and its features like the Auto mode help in automating the entire displacement measurement process.

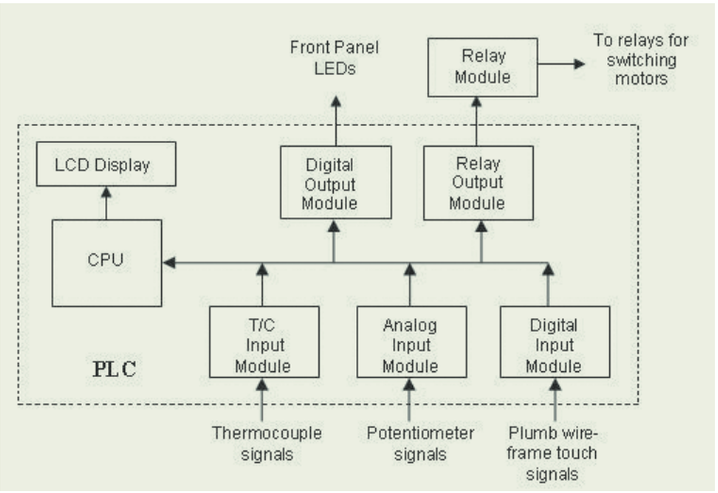

Fig.3
DMD Controller Block Diagram

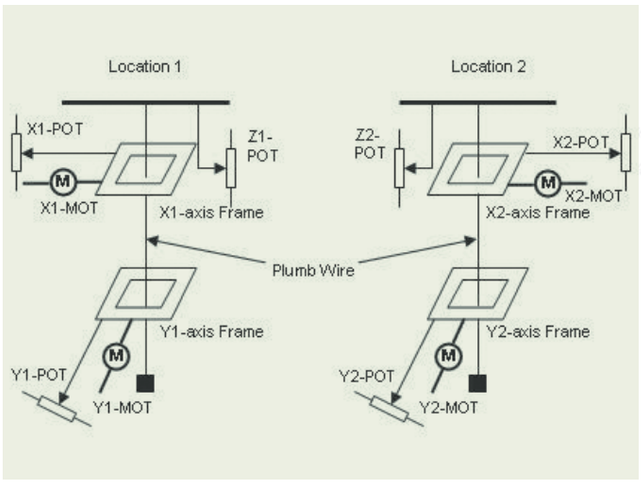

Fig.2
DMD Assembly

Fig.4
DMD Controller Photograph

I.6 Pulsating Sensor Based Conductivity Monitoring Device

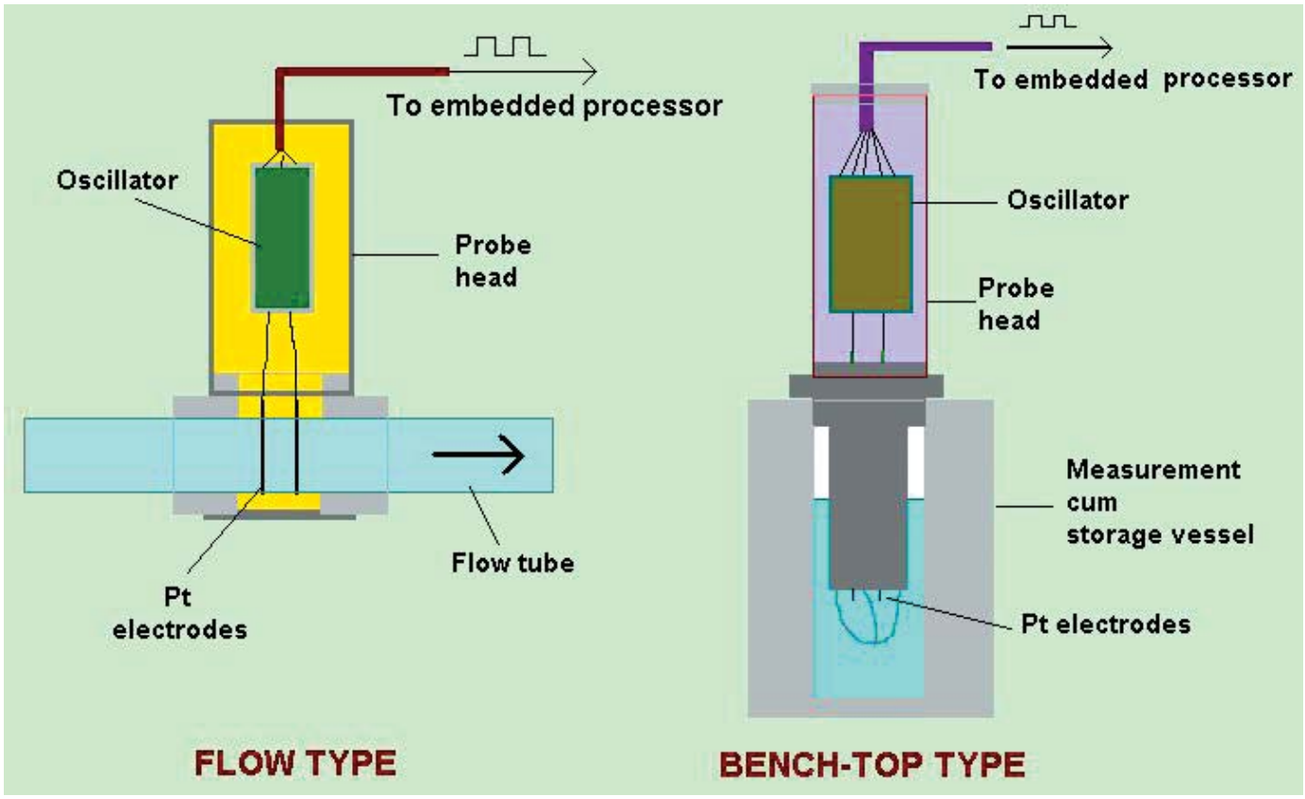

Fig.1
Schematic Representation of Flow and Bench-top Type Conductivity Probes.

On-line and off-line conductivity monitoring devices have been developed and deployed for routine characterisation of water of varying purity used in different water circuits of FBTR. Probes housing the pulsating sensors of unique design were fabricated for mounting on the flow paths for real time monitoring. Appropriate probes were also fabricated as portable devices for off-line measurements.

All aspects of the instrumentation, starting from sensors, associated signal generation and processing to final data presentation, have been designed and developed in-house at the Innovative Instrumentation Section. The working principle of the sensors is based on the approach of direct conversion of ionic conductance of liquid, as sensed by a pair of inert electrodes, to digital pulse frequency. The output oscillates between logic states '0' and '1', providing, consequently, a train of rectangular pulses as primary signal. These pulsating sensors are designed to operate on 5 V DC with very low power consumption. The pulse freque from a given sensor carries information on the prevailing conductivity of the liquid being sensed by a pair of tiny platinum electrodes as the probe. Schematic diagrams of typical flow and bench-top type sensors are shown in Fig. 1.

Signal is handled with the help of laboratory developed embedded pulse processors that have built-in features such as pulse counting, frequency determination, conversion of pulse frequency to specific conductance in $\mu s.cm^{-1}$ through evaluation of pre-established polynomial equations representing the calibration relationships, and display of prevailing conductivity at desired intervals.

A pulsating type thermal sensor has also been made and incorporated for monitoring temperature of flowing warm water whose conductivity has to be sensed. The pulsed signal from the temperature sensor is processed simultaneously by the embedded processor in a separate channel to facilitate an optional feature of accurate conversion of measured conductivity at the prevailing temperature to that at the reporting temperature of 25°C for display.

Dedicated probes were fabricated for low, medium and high levels of conductivity monitoring for convenience and

also to avoid cross contamination in industrial environment for the bench-top models. Pulse frequency to conductivity relationship for a high sensitive probe in low range is shown in Fig. 2. Photographs of representative conductivity probes, both bench-top and flow types, together with the 3-channel embedded processors are given in Fig. 3.

These pulsating sensor based on-line and off-line conductivity monitors are operational in FBTR. The probes are highly sensitive, compact and inexpensive. Features such as handling of digital signal throughout starting from primary signal generation in pulse mode, low power consuming simple electronics and easy signal transmission are added advantages for remote monitoring and reliable performance.

Fig.2
Pulse Frequency to Specific Conductance Relationship for a Typical Sensitive Flow Type Conductivity Probe

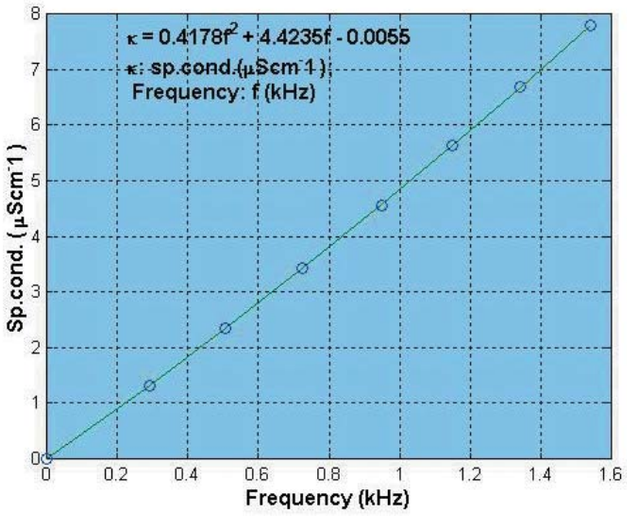

Fig.3
Typical Probes and Embedded Processors for Round-the-clock On-line Conductivity Monitoring and for Bench-top Off-line Conductivity measurements.

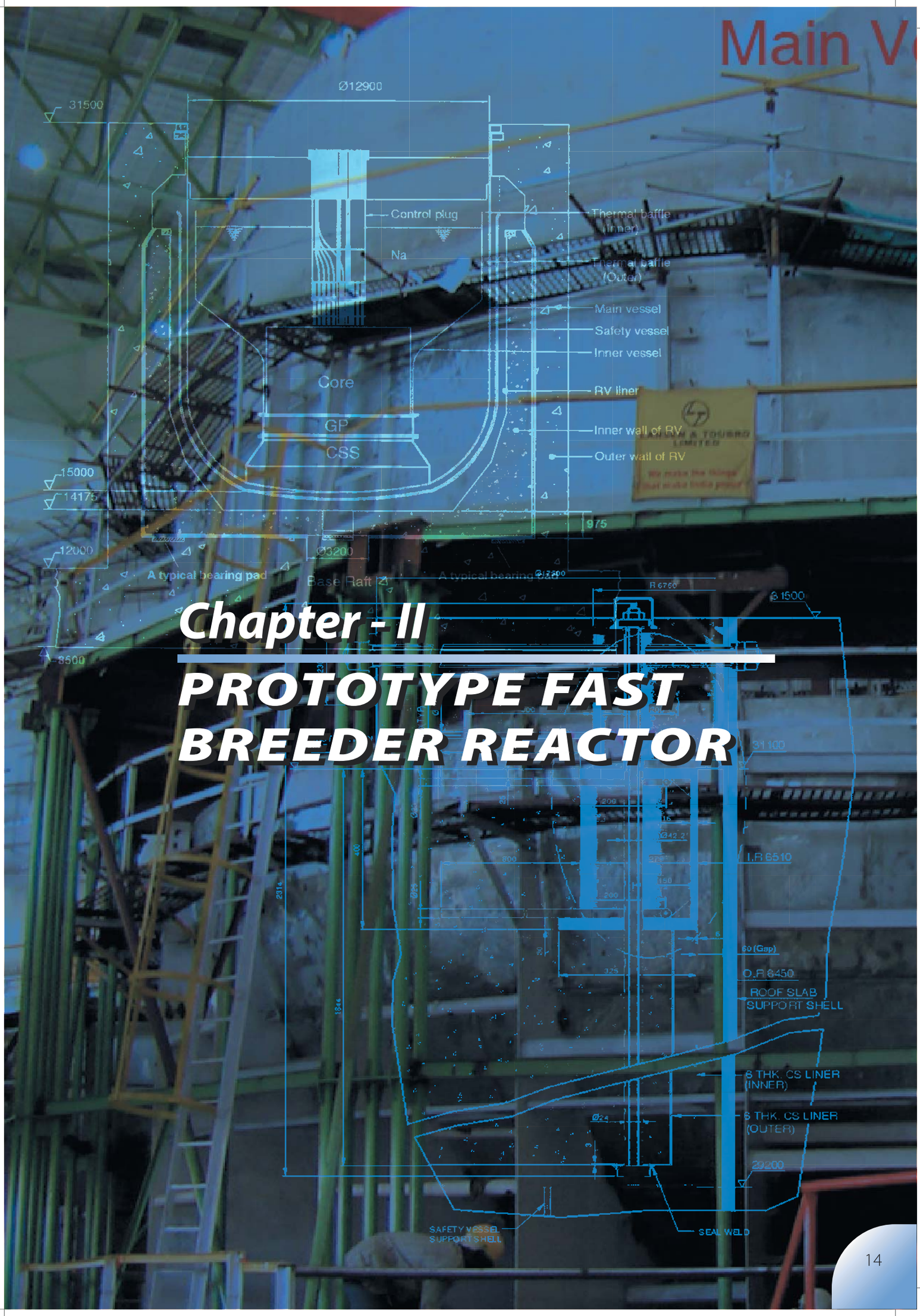

Chapter - II

PROTOTYPE FAST BREEDER REACTOR

II.1 Construction Status of PFBR

The Government of India had accorded administrative approval and financial sanction for construction of the 500 MWe Prototype Fast Breeder Reactor (PFBR) at Kalpakkam in September 2003. Bharatiya Nabhikiya Vidyut Nigam Limited a public sector company under DAE, is responsible for construction and operation of PFBR. IGCAR is responsible for design, associated R&D and manufacturing technology, and getting consent from regulatory bodies for construction of reactor.

The construction of PFBR has progressed very well. Presently, the construction of the 8 numbers of Nuclear Island connected Buildings (NICB) is in progress at various elevations. Construction of electrical building 1&2, control building, and rad waste building has reached up to operating floor level. The excavation of Power Island has been completed. The construction of reactor vault has commenced and the lower lateral liner fabrication and erection has been completed. Manufacturing of long delivery mechanical components of Nuclear Steam Supply System (NSSS), viz core support structure, IHX, sodium pumps, grid plate, shutdown mechanisms, steam generators, sodium tanks and sodium pumps are in different stages of progress in Indian industries. Manufacturing of core catcher has been completed and the component has been received at site. Manufacturing of safety vessel, main vessel, inner vessel and main sodium tanks are in an advanced stage at site assembly shops.

Purchase orders have been placed for sodium valves. Tender evaluation is in advanced stage for major packages for turbine generator and associated water-steam cycle equipment, switchyard, diesel generators, switchyard, sodium metal and Balance of Plant civil package. Overall, the project is on schedule and the reactor is expected to be commissioned by September 2010.

Fig.1
Overall View of NICB

Fig.2
Main Vessel Fabrication at SAS

II.2 Erection Methodology for Major Reactor Assembly Components

The reactor vault which supports the reactor assembly of PFBR consists of inner and outer walls made of reinforced N45 concrete. While the inner wall supports the safety vessel, the outer wall supports the main vessel, its internals and top shield. The inner portions of wall that receive direct heat flux from the reactor assembly are cooled by water circulated in biological shield cooling system. The two walls are separated by 50 mm expanded polystyrene (EPS) insulation. The overall height of inner is 13.7 m (from 13.2 m elevation to 26.9 m elevation) and 19.5 m (from 12 m

elevation to 31.5 m elevation) for the outer wall. Both main and safety vessels are suspended from the top most elevations of walls. Rigid carbon steel box type structures are embedded in the walls on which the vessels are erected. Fig.1 shows the schematic sketch of reactor vault along with vessels mounted on it.

The article deals with the erection of safety vessel, main vessel along with internals and top shield, respecting various erection tolerances giving due considerations to time and economy.

Requirement of Tolerances

Both the vessels should be coaxial within the specified tolerance on the nominal annular gap of 300 mm, so that a robot designed with overall dimension of 570 x 900 x 270 mm can travel freely during the periodic in-service inspection of the vessels planned during the reactor shutdown. For arriving at the tolerance, the minimum gap available for the robot is ensured after accounting for the various conditions and mechanisms that lead to reduction of gap. It is to be noted that the vessels have been manufactured with the radial deviations less than ± ½ wall thickness. The grid plate which supports the entire core should be erected with the horizontality within the specified value which decides the verticality of the core, important from the control rod insertability consideration. This also ensures the horizontality of thermal baffles that have been welded with the main vessel to close tolerance on the parallelism with the grid plate surface, to achieve the uniform weir flow to maintain uniform main vessel cooling over the circumference. In order to respect these requirements, the horizontality after erection of main vessel has been specified after accounting for the horizontality achieved in the manufacturing of vessels and internals. In summary, there are tight tolerance requirements on the horizontality, verticality, concentricity and relative elevations at the respective locations on the vaults.

Recommended Erection Sequences

A robust erection methodology for the reactor assembly components to respect the specified tolerances has been developed jointly with BHAVINI by introducing many innovative features, giving due considerations to the views expressed by the experts from NPCIL, BARC and AERB. The overall erection sequence is depicted pictorially (Fig.2-5). The methodology documents prepared based on this sequence have been approved by a specialist group constituted by AERB.

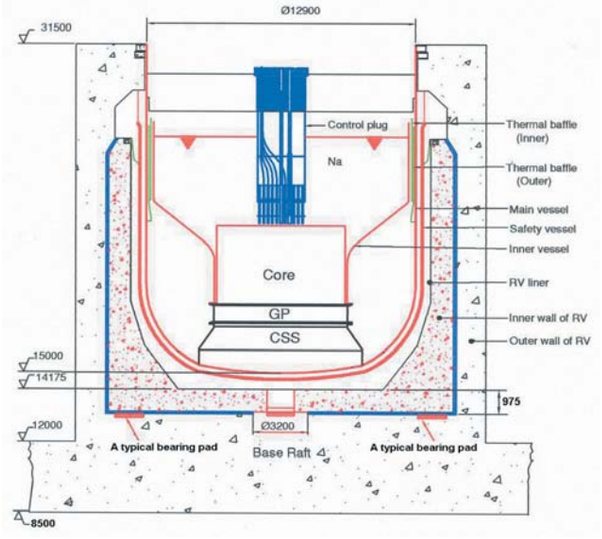

Fig.1
Schematic of PFBR Reactor Assembly Components

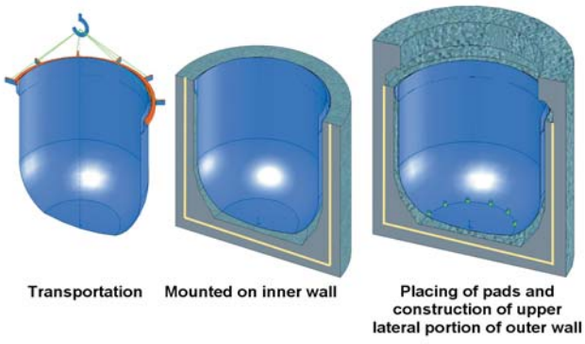

Fig.2
Safety Vessel Erection

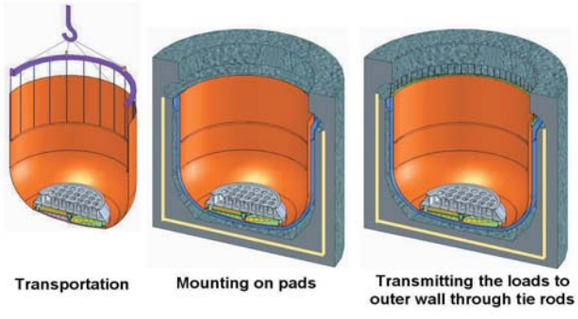

Fig.3
Erection of Main Vessel Along with Core Catcher and Core Support Structure

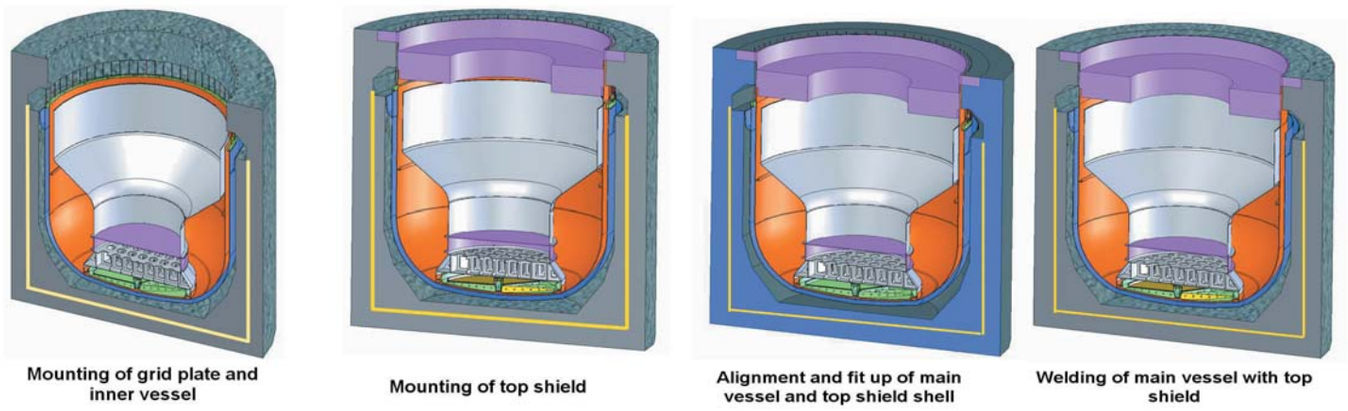

Fig.4
Erection of Grid Plate, Inner Vessel and Top shield

Fig.5
Welding of Main Vessel with Top Shield

II.3 Structural Design of Reactor Vault for the Support Main Vessel

The reactor assembly houses the entire primary sodium circuit. It consists of main vessel & its internals including core, top shield & the components mounted on it and liquid sodium. The main vessel along with its internals and top shield is suspended from the reactor vault, the schematic sketch of which is shown in Fig.1.

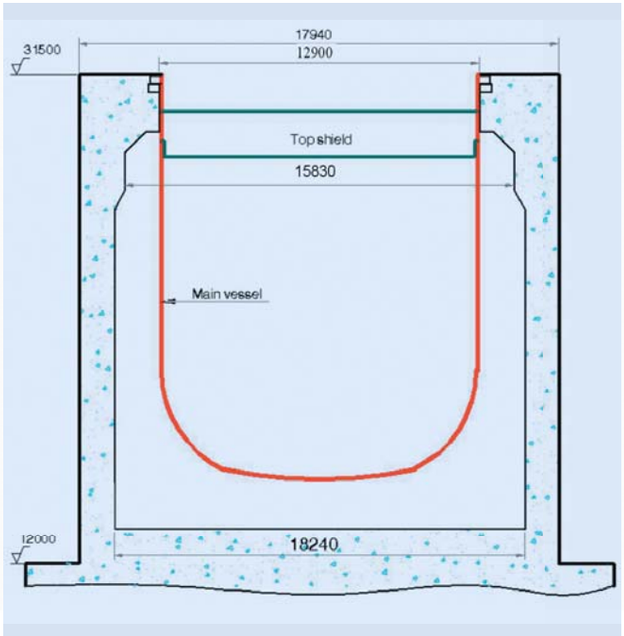

Fig.1
Reactor Vault Outer Wall Supporting the Main Vessel

The dead load of reactor assembly (~ 3700 t) is transmitted to the upper lateral portion of the reactor vault under normal operating conditions. This apart, high dynamic forces in the form of axial, shear and bending moments are developed during seismic events. Typical forces under safe shutdown earth quake are: 1800 t additional downward load apart from dead load, 1400 t shear force and 15200 t-m bending moment. In addition, core disruptive accident (CDA) develops a net upward thrust of ~ 1600 t on the support. The design of robust support structures, which distributes these forces developed at the junction of reactor support shell in the form of line loads to the top portion of the reactor vault, is the most challenging activity completed by reactor engineering group. The novel features of design and associated analysis completed towards finalizing the design are dealt in this article.

The thickness of outer wall is 1 m with the increased thickness of ~ 2 m in the upper portion (upper lateral) for the smooth distribution of loads to the concrete. The top edge of the reactor assembly shell is welded to a rigid box type structure having height of 400 mm, made of top & bottom plate flanges connected by 288 vertical radial stiffeners. This structure is supported on another similar box type structure with matching stiffeners embedded in the upper lateral region. The embedded structures are provided

with 144 vertical tie rods to absorb the mechanical energy released under CDA and 144 horizontal tie rods are incorporated to offer resistance to the shear forces developed under seismic loads. Upper lateral region of reactor vault is provided with double liner arrangement (a) to have additional barrier between vault and main vessel to take care of the eventuality of possible leak in the biological shield cooling system, (b) for providing leak tightness required for nitrogen in the inter-space between main vessel and safety vessel and (c) for accommodating the relative seismic and thermal movement between inner and outer walls of reactor vault. Vertical tie rods penetrate the inner liner at their bottom, where the circular head of tie rod butts against the horizontal bottom surface of inner liner and are welded to the inner liner. Top ends of tie rods are fastened with washers and nuts and are closed with end caps and seal welded for providing leak tightness for nitrogen in the inter-space between main vessel and safety vessel. The geometrical features are presented in the schematic sketch shown in Fig.2.

The material of the support structure is carbon steel of special grade (A48P2). The adequacy of strength of steel structures, tie rods, concrete thickness and reinforcements are ensured by detailed static and dynamic stress analysis. The stress distribution on the top and bottom flanges and a typical radial stiffener are shown in Fig.3. The stress distribution in the upper lateral region of concrete is shown in Fig.4 The structural design meets both RCC-MR (edition 2002) and AERB safety guide lines.

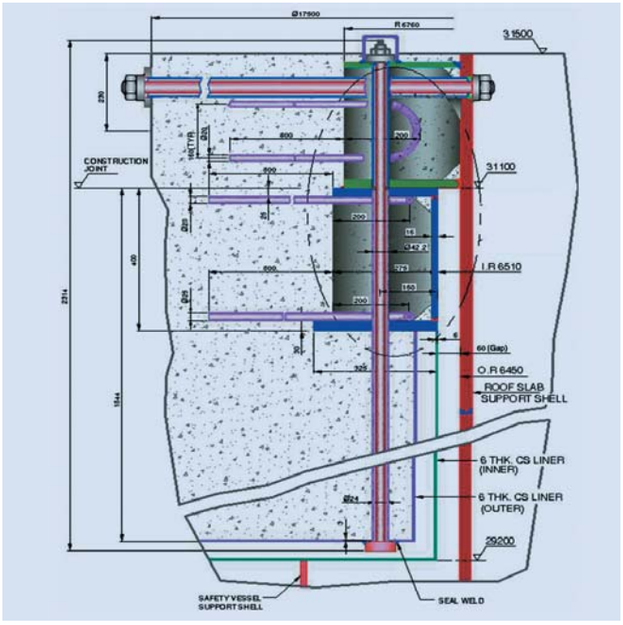

Fig.2
Geometrical Features of Upper Lateral Region of Reactor Vault

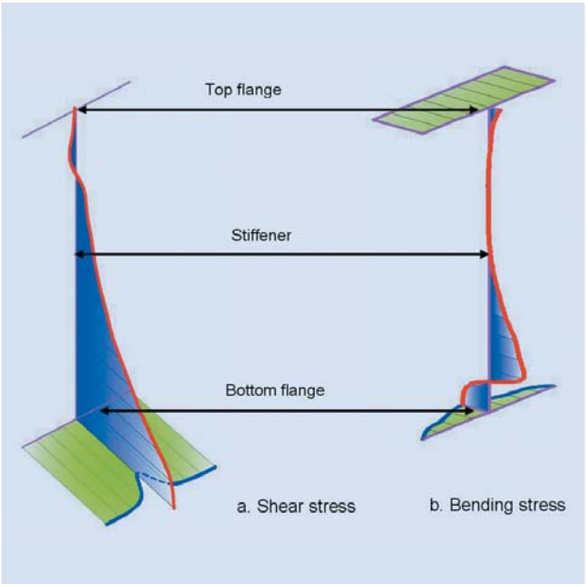

Fig.3
Stress Distributions in Reactor Assembly Support Structure

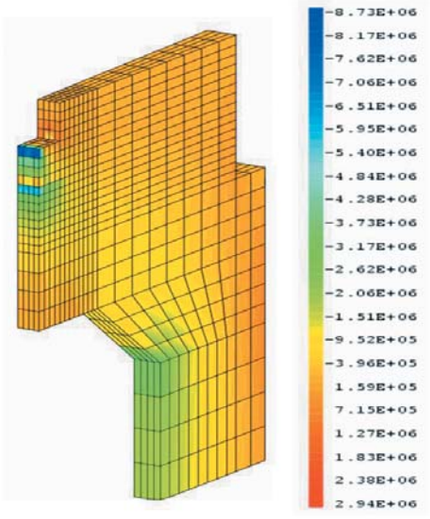

Fig.4
Axial Stress In the Upper Lateral Region Under Net Load

II.4 Fabrication of Dummy Fuel Sub-assemblies

Dummy Fuel (110 Nos.) sub-assemblies (DFSAs) were fabricated for core mechanics experiments to validate PFBR core restraint system design and to check the mechanical interlock along with grid plate sleeve. DFSAs will be instrumented to measure the displacement and interaction loads between the sub- assemblies. DFSAs will be inserted / assembled vertically in Grid plate model of diameter 2.5m, which simulates the grid plate (miniature size with 115 sleeves) of PFBR. Fabrication of DFSAs at Central Workshop Division (CWD) was aimed to evolve cost effective robust manufacturing methodology. Each DFSA consists of five precise components namely Discriminator, Coolant Entry tube, Support Block, Hexagonal sheath and Handling Head, made of SS 304L material. Overall size of the assembly is 4.5 m long with Hexagonal sheath of A/F 131.6 mm. Two numbers of DFSAs were fabricated to standardize and optimize the machining / fabrication parameters and process sequences. A procedure was evolved based on the experience gained in fabrication of DFSA. Due to the constraints in supply of D9 pilgered hexagonal sheaths by the vendors, it was decided to fabricate hexagonal sheaths by forming and welding technique.

Hexagonal Sheath Fabrication by Forming and Welding Using Manual GTAW process:

The hexagonal sheath of size 131.6 A/F and 3572 mm long was made from 3.2 mm thick SS 304L material. Considering the available machine capacities at CWD and the raw material, hexagonal sheaths were fabricated by forming and welding with two longitudinal seams and one circular seam weld joint. Half-hexagonal geometry was formed using press brake. A fixture was designed to assemble half-hexagonal sheaths, then two half-hexagonal sheaths of length 2000 mm and 1572mm were joined to get full length of 3572 mm. Extreme care was taken during welding, GTAW process (manual), single 'V' groove butt joint, weld arc gap 2mm, heat input 900 J/mm, a special fixture with copper back plate (heat sink) was used to control distortion in welding and achieved Straightness within 3mm.

Fig.1
Fabricated Dummy Fuel Sub-assemblies

Hexagonal Sheath Fabrication by Forming and Automatic GTAW Process with Activated Flux (ATIG)

In order to meet the targeted schedule and mass production of DFSAs, a need was felt to develop an automatic GTAW technique to accelerate the productivity in fabrication of hexagonal sheaths. An automatic GTAW system was designed and activated flux developed by the MMG was used, square butt joint, arc gap 1 to 1.5 mm, heat input 500 J/mm and manual argon back purging was adopted to weld 3.2mm thick hexagonal sheath. Mock-up using this technique was carried out and the results were satisfactory. To standardize the technique and meet the code requirement, Welding Procedure Specification (WPS), Procedure Qualification Record (PQR), Welder's Performance Qualification (WPQ), non-destructive tests LPI / UT, destructive tests, tensile test, root and face bend tests were carried out as per ASME SEC. IX. Development of this technique has reduced total work content and increased the productivity.

One hundred and ten DFSA were manufactured meeting the stringent specifications and were completed 4 months ahead of targeted schedule. Fig.1. shows the fabricated DFSAs.

II.5 Experimental Flow Blockage Studies in Fuel Sub-assembly

Fuel sub-assembly blockage is one of the important safety issues in the operation of the fast reactors as it may lead to enhanced heating in subassemblies with a potential to cause fuel melt down. Steel chips or particles resulting from the machining process in the construction stage or accumulation of non-fuel debris arising from corrosion and erosion or other reaction products of primary sodium with organic materials may be transported and settled in the fuel sub-assembly causing flow blockage. Hence understanding of the blockage phenomenon is very important.

An experimental water test loop with 37-pin fast reactor test sub-assembly was set up at Safety Engineering Division to investigate the implications of blockage due to such external debris. The schematic diagram of experimental loop and cross-section of the test sub-assembly are given in the Fig.1 and Fig.2 respectively. Stainless steel piping of 50 mm nominal bore size is used in the loop. The geometrical features of the pin bundle are the same as that for PFBR, except that the length of the test section is 800 mm (four helical pitches). A venturi meter with a range of 17- 30 m^3/hr was used for flow measurement. ΔP measurement system with a range of 0 to 1500 kPa was used for the pressure drop measurement along the test section. The water temperature is maintained at 50±2°C by an automated cooling water system during the experiments. ADAM data acquisition system was used for recording the real time data of flow rate, pressure drop and temperature.

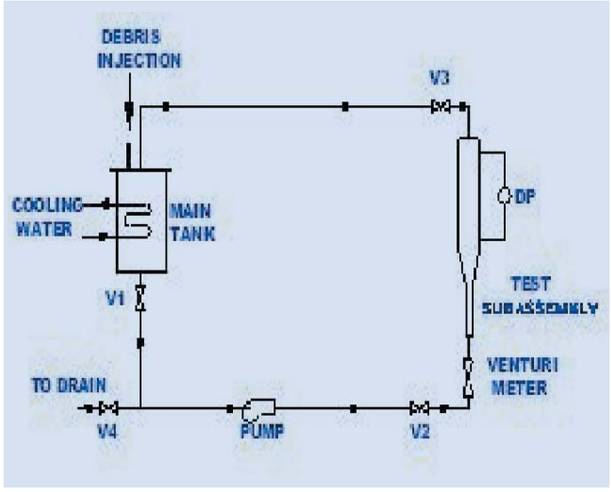

Fig.1
Schematic Layout of Experimental Loop

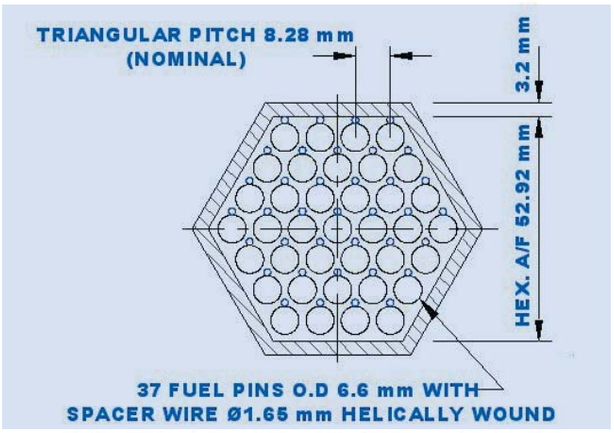

Fig.2
Cross-section of 37- pin Sub-assembly

Experiments were carried out with stainless steel cylindrical debris (with diameter to height ratio of 1) of size 1.6 mm and 1.2 mm at different concentrations ranging from 3 ppm to 20 ppm for varying flow values. The concentration is based on the volume of water in the loop, which is around 0.55 m^3. 1 ppm of debris occupies 0.06 % of sub-assembly flow volume.

The percentage distribution of debris along the pin length were obtained for different size debris at 5 ppm concentration and shown in Fig.3. The 2 mm size debris is observed to penetrate up to one pitch length (i.e., 200 mm) of the subassembly. All the debris of 1.6 mm size were trapped within four pitches of test sub-assembly and around 80 % of these debris settled in the first two pitches. Debris of size 1.2 mm showed almost uniform settlement throughout the length of the test sub-assembly and 90 to 95 % of the debris was found to be trapped in the sub-assembly. The 0.8mm size debris.

settled in the sub-assembly was around 25% only.

The particle settlement can be explained based on the maximum Sub-channel Passage Diameter (SPD). SPD for the test sub-assembly is 2 mm (shown in Fig.4). Hence 2 mm particles are arrested within the first pitch of the pin bundle from inlet where as particles of size less than 2 mm are able to pass and settle along the total length of the subassembly. The particle settlement pattern shows that the particles of sizes 1.6 mm and above will not be able to penetrate to the active core region (which starts 5 pitches after inlet) of PFBR fuel subassembly. The particles of size less than 1.6 mm will penetrate and settle at the active core region causing local hot spots.

In each run, after addition of the required concentration of debris and collection of all the particles in the test section, the flow rate was varied gradually from 30 m^3/h to 22 m^3/h in steps of 1m^3/h and the pressure drop measured. The variation of pressure drop (ΔP) can be expressed as $\Delta P = K\rho V^2/2$ where 'K' is the pressure loss coefficient. The pressure drop without debris is 180 kPa at 30 m^3/h flow rate and the corresponding pressure loss coefficient 'K' is 6.8. The pressure loss coefficient thus obtained can be used for estimating the flow reduction due to debris addition. The variation of pressure loss coefficient with Reynolds number for 1.6mm and 1.2mm debris is shown in Figs.5 and 6, respectively.

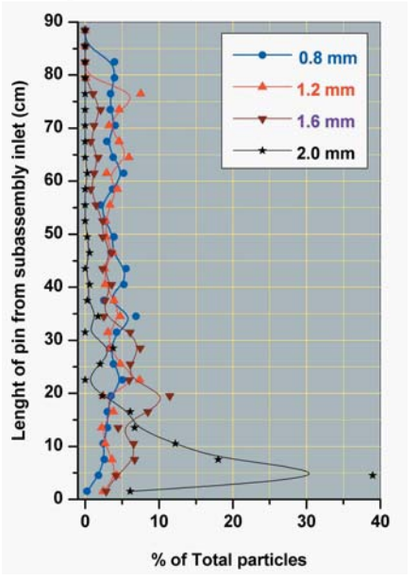

Fig.3
Debris Distribution In 5ppm Concentration Runs

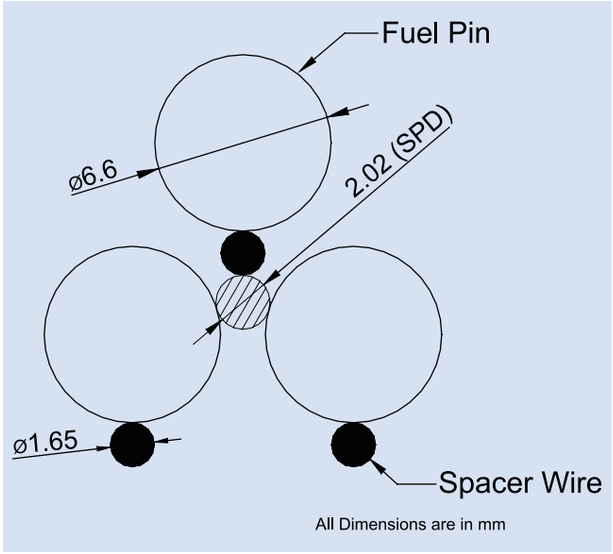

Fig.4
SPD: Sub-channel Passage Diameter

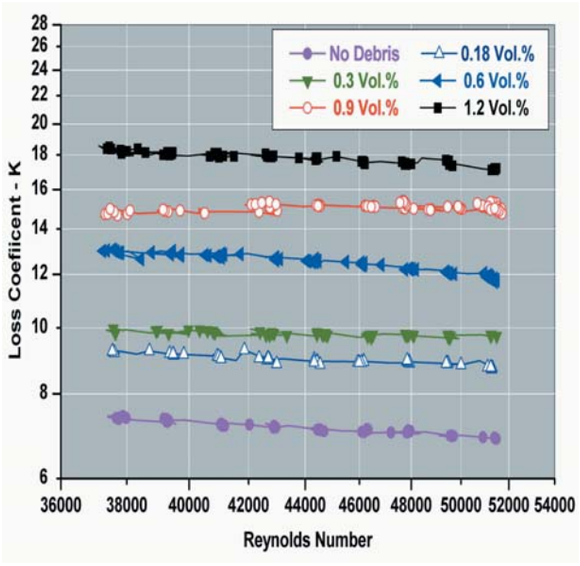

Fig.5
Variation of Pressure Loss Coefficient with Reynolds Number (for 1.6mm)

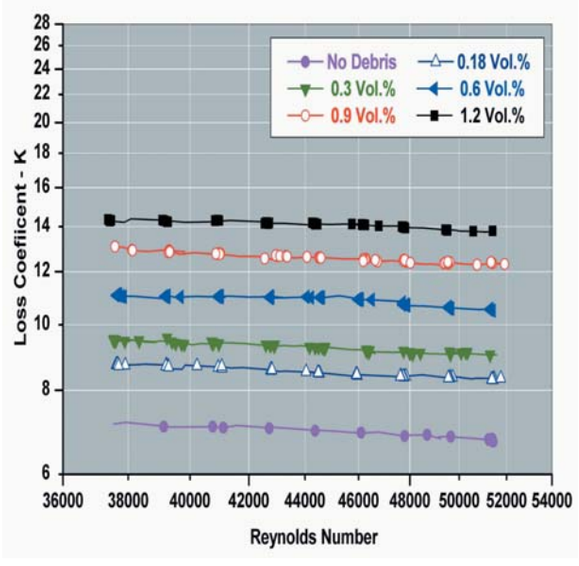

Fig.6
Variation of Pressure Loss Coefficient with Reynolds Number (for 1.2mm)

II.6 Investigation on Buckling of PFBR Vessels under Seismic Loadings with Fluid Structure Interactions

Figure.1 shows the schematic of reactor assembly of PFBR along with the vessels addressed in the paper. The main vessel houses the entire radioactive primary sodium circuit which include core, grid plate (GP), core support structure (CSS), apart from liquid sodium. GP supports inner vessel which separates hot and cold sodium pools. To protect the main vessel from heat flux radiating from the hot pool, a set of two thermal baffles, viz. inner and outer baffles are attached with the main vessel. The main vessel is closed at the top by a top shield which is basically box type steel structure filled with concrete. The top shield supports primary sodium pumps, intermediate heat exchangers (IHX), control plug and component handling systems. The main vessel along with its internals and top shield is called reactor assembly. The reactor assembly is supported at the top of reactor vault, which is an annular reinforced concrete structure resting on the common base raft.

The large diameter shell structures in the reactor assembly are main vessel, inner vessel and thermal baffles. For these vessels, possible lower wall thickness is selected due to: (1) low design pressure at the operating temperatures (sodium can remain in liquid state up to about 950°C in the reactor), (2) requirement of adequate flexibility under various operating conditions (550°C for hot pool & 400°C for cold pool under steady state, isothermal temperature of 220°C during shutdown and thermal transient of about 15 K/s during reactor scram) and (3) economic considerations (capital cost is a strong function of steel consumption). Typically, the diameter to thickness ratios for the main vessel (12900mm diameter & 25mm thickness), inner vessel (12000mm diameter & 15mm thickness), inner baffle (12400mm diameter & 20mm thickness) and outer baffle (12600mm diameter & 20mm thickness) fall in the range 500 - 800 to consider that they are thin walled shell structures, which are prone to buckle.

The main vessel carries a total mass of about 2500 t contributed mainly by sodium (1150 t), core (550 t) and self weight of main vessel and its internals. The weight of top shield along with the components supported by it is about 1200 t. Thus the reactor assembly weighs about 3700 t which is hanging from the top support. Further, there exists relatively thin annulus of liquid between: (1) inner vessel to inner baffle, (2) inner baffle to outer baffle and (3) outer baffle to main vessel. The annulus gap to diameter ratio is w/D ~ 1/100, which contributes significant added masses to the adjacent shells. The existence of large free fluid surfaces is the source of sloshing phenomena during normal operation as well as seismic events.

Due to these features, the reactor assembly components have their fundamental natural frequencies less than 10 Hz, over which seismic floor responses spectra show maximum dynamic amplifications. Hence, seismic events impose high dynamic forces, even though mechanical loadings (self weight and hydrostatic pressure heads) are low under normal operating conditions.

From the above said structural and loading characteristics, it is clear that buckling of thin walled shell structures should be investigated critically under seismic induced forces. The investigation calls for sophisticated analysis methodologies to determine realistic dynamic pressure distributions on vessel wall surfaces giving due consideration for the possible randomness of support excitations and 3 D buckling analysis considering the effects of plasticity and initial geometrical imperfections introduced during manufacturing stage itself.

An integrated analysis for determining realistic forces and critical buckling loads at any instant during the seismic event has been carried out for the reactor assembly vessels. The dynamic forces including pressure distributions generated on the vessel surfaces are determined by seismic analysis of reactor assembly with time history approach. Elastoplastic analysis followed by buckling analysis is carried out on 3 D shell geometries. In order to save significant computational time, analysis is carried out only at a few critical time steps which are identified based on strain energies that are associated with the shear and compressive

stresses developed at the portions of the vessels prone to buckle. The shear buckling of main vessel straight portion and buckling of toroidal portion of inner vessel and thermal baffles are found to be important. The possible randomness of support excitation time histories is accounted by compressing as well as expanding the nominal time histories by 10 %. Buckling strength reduction factors due to the initial geometrical imperfections are adopted from the literature. Fig.2 shows the details of finite element mesh, an important mode shape, pressure distribution along vessels and buckling mode shapes at a critical instant during seismic event.

Analysis indicates that the inner vessel is the most critical component from point of view of buckling under seismic loadings, which has the minimum buckling load factor of 1.54 under SSE, higher than the minimum factor of 1.3 specified by RCC-MR corresponding to level D loadings. There exists very comfortable margins for the main vessel and thermal baffles.

The integrated approach followed in this investigation provides realistic results with higher confidence in the buckling design of critical vessels of PFBR.

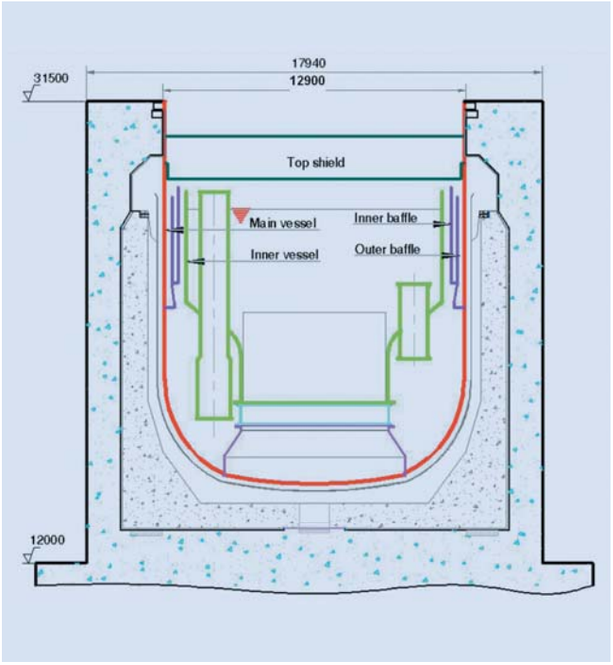

Fig.1
Schematic Sketch of Reactor Assembly Vessels

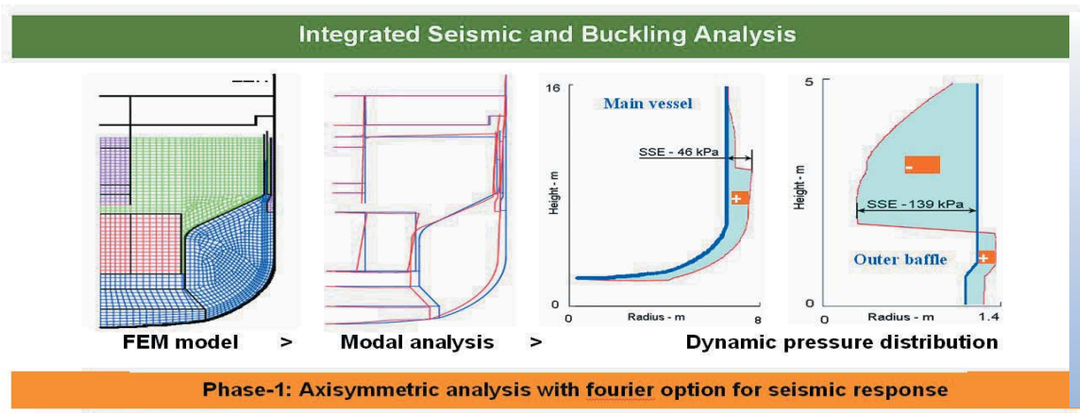

Fig. 2 (a)
Integrated Seismic Buckling Analysis.

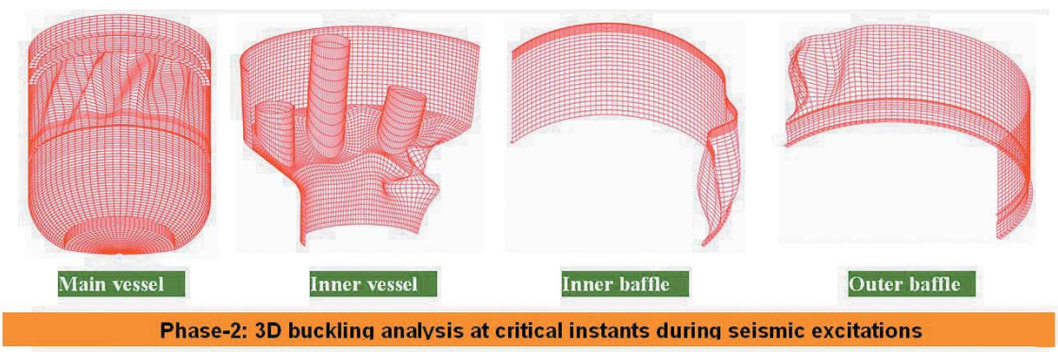

Fig. 2 (b)
Showing the Details of Finite Element Mesh

II.7 Structural Integrity Assessment of Reactor Vault under Seismic Loading During MainVessel Leaked Condition

The main vessel is most important component which houses the entire radioactive primary sodium circuit and hence, the vessel is designed with high reliability starting from the choice of ductile material (austeinitic stainless steel SS 316 LN), detailed analysis, adopting high quality manufacturing and inspection standards and in-service inspection to monitor the cracks. Further, the main vessel is surrounded with another coaxial vessel called safety vessel. The purpose of safety vessel is to maintain the sodium level in the main vessel to facilitate the sodium flow through heat exchangers (safety grade decay heat exchangers and intermediate heat exchangers), towards ensuring decay heat removal, even in case of main vessel leakage. The safety vessel is supported on the inner wall of reactor vault and a schematic sketch is shown in Fig.1.

Under normal operating conditions with the absence of sodium in the inter-vessel space between main vessel and safety vessel, the load transmitted to the inner wall is insignificant (the dead load of ~ 250t only acts in the vertical direction). The major load acts on it during a seismic event under main vessel leaked condition. The sodium levels are indicated in Fig.2 during normal as well as main vessel leaked conditions.

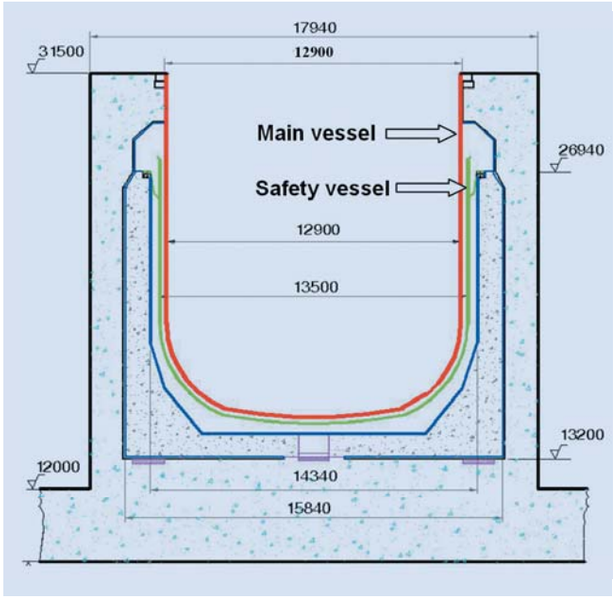

Fig.1
Schematic Sketch of Reactor Vault with Vessels

The dynamic pressure developed in the sodium confined in the inter vessel space is the root cause of generating high dynamic forces under seismic loading condition. The inner wall has been investigated for this loading to demonstrate that the vault is integral even during safe shutdown earthquake (SSE) under main vessel leaked condition.

Towards demonstrating the structural integrity of reactor vault under such extreme loading condition, detailed finite element analysis has been carried out using CAST3M issued by M/s.CEA, France. The first step in the analysis is finite element discretisation of various geometries such as reactor assembly including reactor internals and sodium, sodium free levels and fluid-structure interactions, safety vessel and reactor vault. The finite element mesh thus generated is shown in Fig.3.

The second step is the determination of natural frequencies and modeshapes up to 50 Hz wherein the seismic excitations have significant energies. The analysis indicates two important additional modes of natural vibration viz.in-plane and out-of-plane vinration of main vessel and safety vessel coupled by liquid sodium confined in the intervessel space. These modes are responsible for generating high inertia forces on the inner wall during SSE. The natural frequecies (4.4 Hz in-plane and 7.8 Hz out-of-plane) and associated mode shapes are shown in Fig.4. The in-plane mode contributes signicantly for the vault loadings, rather than out-of-plane mode.

The third step is the seismic response analysis by which seismic forces on the vaults are quantified. The vertical force on the inner wall experiences peak dynamic force of 270t in the vertical direction which has to be added with the about 250t dead load acting at the support location. Further, additional shear forces and bending moments are also generated during seismic events. The peak shear force and bending moment values acting on the inner wall are insignificant when there is no leak in the main vessel (20t and 500t-m), which however increase significantly (250t and 6300t-m respectively) under SSE with main vessel leaked

condition. For these forces, the structural integrity of inner wall is ensured as per AERB safety guide. This analysis calls for detailed 3 D modeling of the inner wall with central pedestal specially provided to resist the shear forces and 12 bearing pads provided to take care of axial forces along with bending moment. The boundary conditions to simulate the support condition (inner wall is simply resting on the bearing pads) call for non-linear contact mechanics analysis methodology specially incorporated in CAST3M. The deformed shape of the wall and stress distributions on the bottom part of the inner wall (IW) which is the integral part of central pedestal, are depicted in Fig.5 and Fig.6 respectively. The outcome of the investigation forms an important part of the in-depth safety assessment methodologies adopted for the reactor vault.

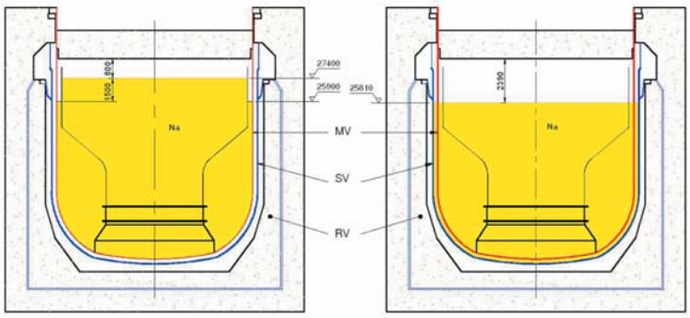

Fig.2
Sodium Levels under Normal and Main Vessel Leaked Conditions

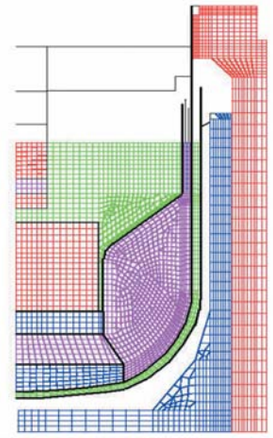

Fig.3
Finite Element Model

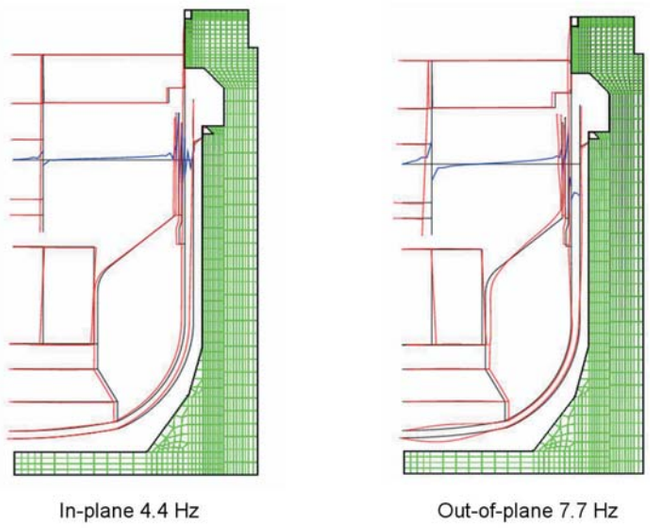

Fig.4
Important Natural Vibration Mode Shapes and Frequencies

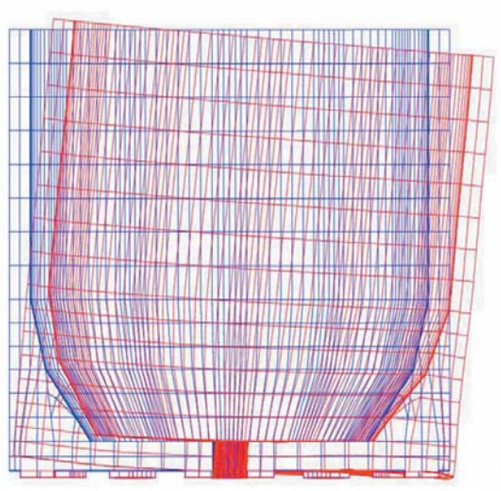

Fig.5
Deformed Shape of Inner Wall

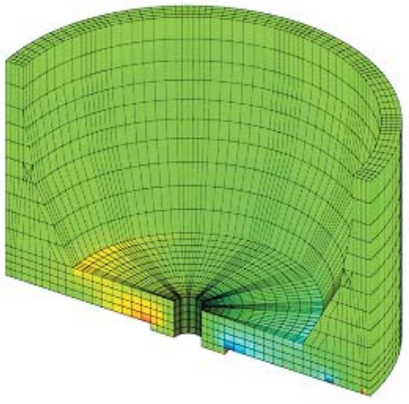

Fig.6
Stress Distribution in IW Bottom

II.8 Heat Transfer Experiments in Multiple Plate Reflective Insulation Panel for Safety Vessel

In PFBR, the Safety Vessel (SV) is at 673K (400°C) under normal reactor operation and transfers heat to Reactor Vault (RV). The Reactor Vault concrete temperature is to be limited below 339 K (66°C). To reduce heat transfer to Reactor Vault, thermal insulation panel which has 34 numbers of stainless steel reflective insulation plates is provided on sides and bottom of the safety vessel.

To test the effectiveness of the design and to ensure that the heat flux to reactor vault is within limits, an experiment was carried out with one panel as shown in Fig.1. The insulation panel comprised of 34 reflective plates of size ~ 0.93 x 0.43 m each, fixed on a plate simulating SV. Heaters are fixed on outside of the plate simulating the heat coming from safety vessel. The other end of the box, which simulates RV is provided with air-cooling system. The gaps between the insulation panel and the rectangular box are filled with mineral wool insulation. Nitrogen is filled in the gap between insulation panel and the box to maintain the emissivity of reflective plates. Stainless steel sheathed thermocouples are fixed on the reflective plates to get the temperature distribution.

First the insulation panel was kept vertical and the temperature of the SV plate was brought to nearly 673 K (400°C). At steady state, temperatures of SS plates, air inlet and outlet temperatures and airflow rate were collected and heat transfer rate was determined as 220 W/Sq.m. Then the insulation panel was kept horizontal with heater at top and reflective plates insulation at bottom to simulate heat transfer in the bottom portion of SV. When the insulation was kept horizontally, convection heat transfer was minimum and the heat transfer was mainly by radiation. The heat transfer from the Safety Vessel to reactor vault was found to be 85 W/sq.m. The temperature distribution in the multiple plate reflective insulation panel remained almost same in both vertical and horizontal positions. Fig.2 shows the experimental results in terms of temperature as a function of thickness from safety vessel. This experiment confirmed the predictions and justified the design.

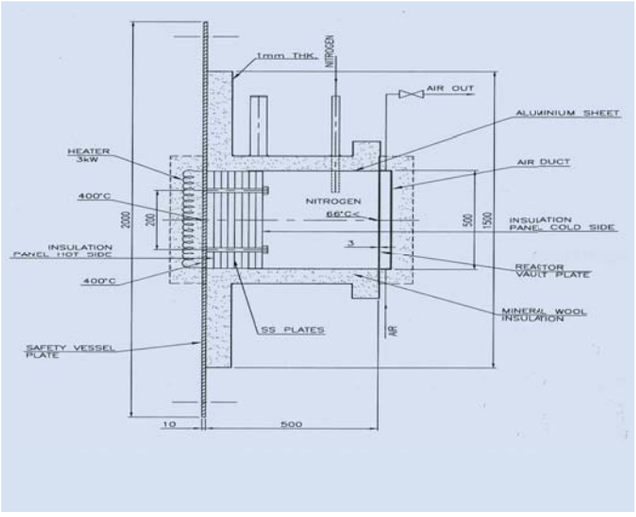

Fig.1
Modified Experimental Setup for Multiple Plate Insulation (Vertical)

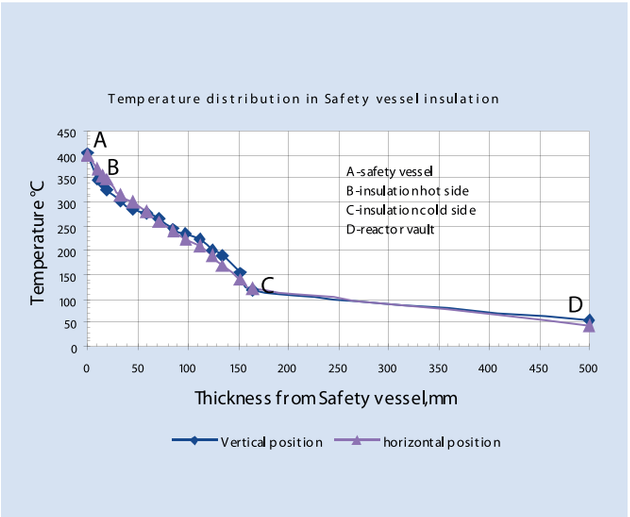

Fig.2
Temperature Distribution in Safety Vessel Insulation

II.9 Computational Prediction and Experimental Validation of Pressure Drop in the Spherical Header of Primary Sodium Pump

In PFBR, primary sodium from cold pool is sucked by two primary sodium pumps operating in parallel, delivering 7000 kg/s at a head of 75 mlc. Sodium from each of these pumps enters a spherical header, where it branches into two streams to two primary pipes before entering the grid plate. Grid plate is a high pressure plenum which distributes sodium to various subassemblies where nuclear heat is generated. It is essential to minimize the pressure loss in the "header-primary pipe" assembly. Towards this, baffles coupled with a central cone are provided inside the header. No standard pressure loss relations are reported in literature for these types of special geometries. Hence, pressure loss in this system needs to be evaluated from first principles. The shape of the internal baffles has been optimized by a computational fluid dynamics (CFD) study, to minimize the pressure loss. The integrated CFD model extends from heat exchanger outlet windows in the cold pool to grid plate inlet, comprising 2 heat exchangers and 1 primary sodium pump (Fig.1). Along with the cold pool, the pump suction casing, pump impeller, pump diffuser, pump discharge pipe, spherical header with the flow distribution baffles and the primary pipes have been modelled in detail with over 30 lakhs mesh points in the CFD code CFX (Figs. 2 & 3).

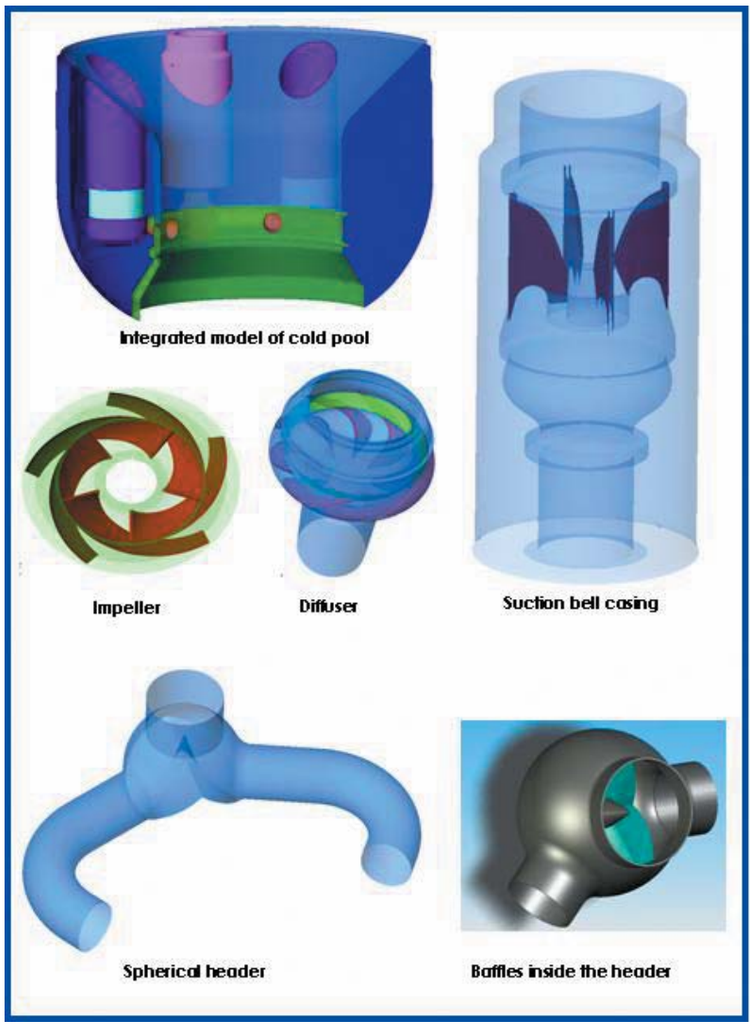

Fig.1
Integrated CFD Model of Cold Pool

The numerically predicted pressure loss was also validated by performing experiments in a 1:3 scaled down air model (Fig.4). In the air model studies, geometric similarity is respected, maintaining Reynolds number in the turbulent regime. Experiments have been conducted on two header models, viz. the basic header and the header with internal baffles, optimised though CFD studies.

The entire work has been carried out as collaborative projects between three institutes. While the computational studies have been carried out at Anna Univeristy, Chennai, the experimental studies have been carried out at Fluid Control Research Institute, Palghat.

Based on these studies, it was found that pressure loss coefficient for the basic header assembly (without internal baffles) is 7.2. Provision of internal baffles reduces the loss coefficient by a factor of over 5. With the present design of the internal baffles with cone, the loss coefficient is 1.2. The corresponding values measured in the experiments are 6.0 and 1.25, validating the computational studies for the complicated flow distribution.

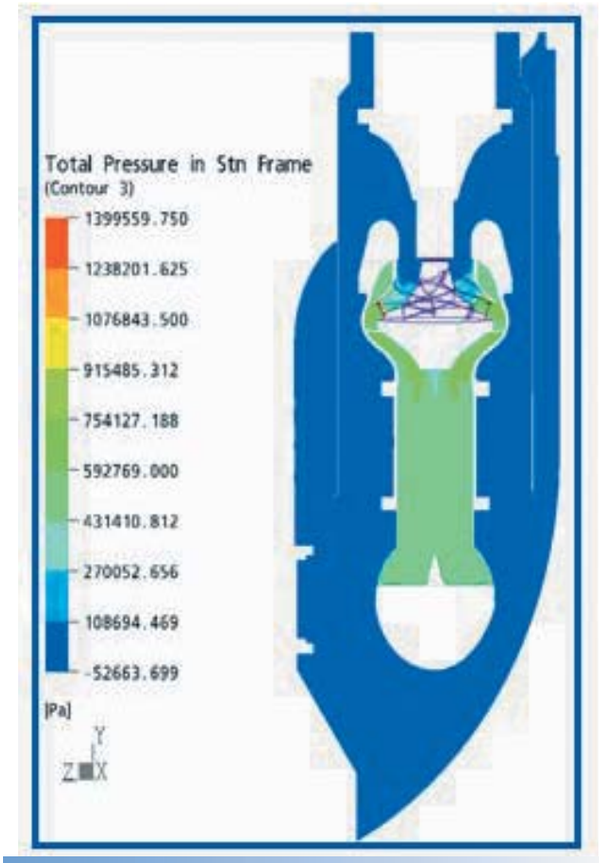

Fig.2
Pressure distribution in a Section through the Pump

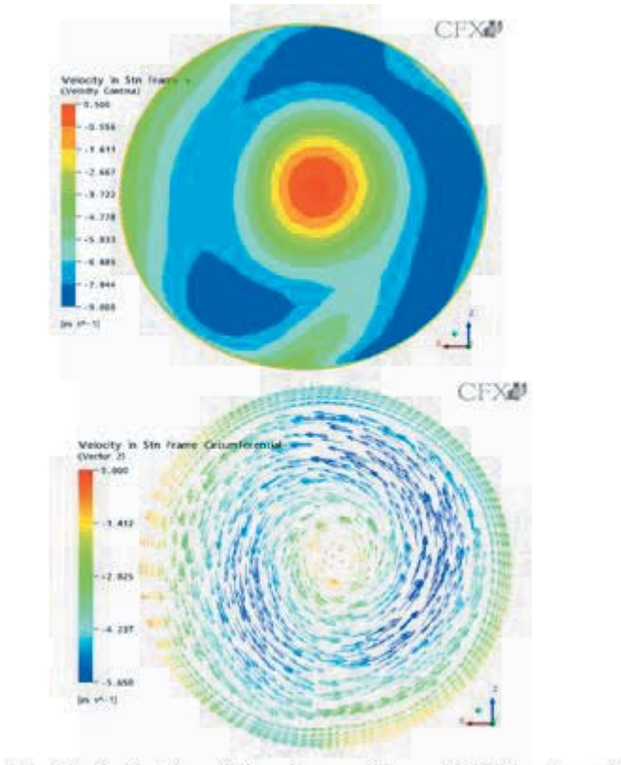

Fig.3
Axial (top) & Circumferential (Bottom) Velocity Distribution at the Inlet of Header

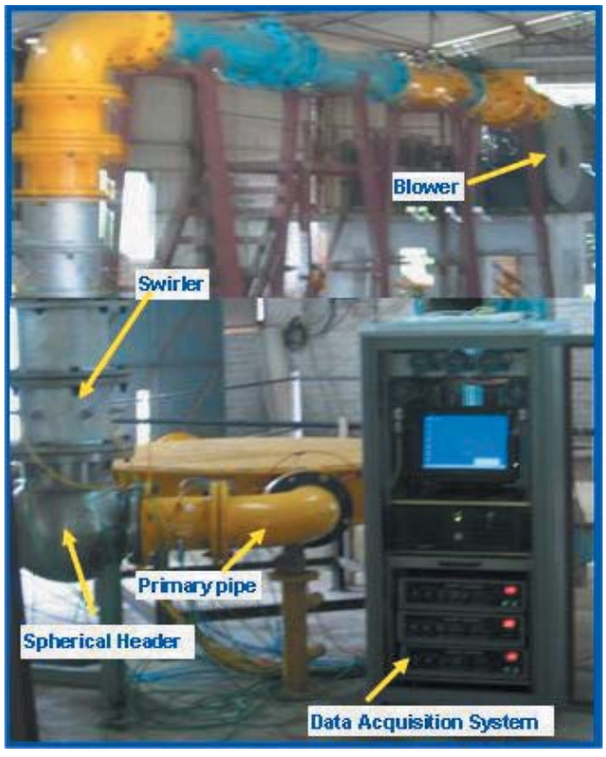

Fig.4
Experimental Test Facility for Hydraulic Testing of Spherical Header established at FCRI, Palghat

II.10 Pressure Drop Devices for Blanket Zones

Reactor core consists of different subassemblies (SA) like fuel, Blanket, Control rod etc. In order to get the maximum mean outlet temperature. Flow to the different SA should be proportional to the power generated in these SA. Flow is achieved by use of proper pressure drop devices at the SA inlet. For the Blanket SA's, labyrinth type devices were tested earlier and were found not suitable from cavitation considerations. A single hole single plate sharp edged orifice appears to be attractive for achieving the desired pressure drop by varying the opening ratio. However such an effort results in excessively high velocities leading to cavitation. Multi-hole orifice plates in series were then tried. For multi-hole assemblies the main advantage is that the spacing required between the plates is less. Hence the machined orifice plate of multi-hole multiplate configuration was designed for all the three zones. In order to achieve higher loss coefficient the devices were mis-aligned by 30 degrees. A typical 6 holed orifice as well as assembly consisting of 4 plates are depicted in the Fig.1.

Hydraulic testing was carried out to find out the pressure drop as well as the cavitation performance. The results obtained from the studies are summarized in table 1. Fig.2 shows the variation in pressure drop and flow rate against their respective design values. All the devices are free from cavitation performance at the required flow rate.

Table 1. Results of hydraulic tests

Zone No.	Descritption	Flow rate (Kg/s)	Pressure drop in bare AS (mNa)	Pressure drop required in the Device (mNa)	Pressure drop achieved in the Device (mNa)
8	Blanket	6.03	5.12	51.84	50.76
9	Blanket	5.69	4.59	52.36	49.88
10	Blanket	4.3	2.74	54.21	50.03

Fig.1 a
Typical 4-plate Orifice Plate (zone-10)

Fig. 1 b
Typical 4-plate Orifice Assembly

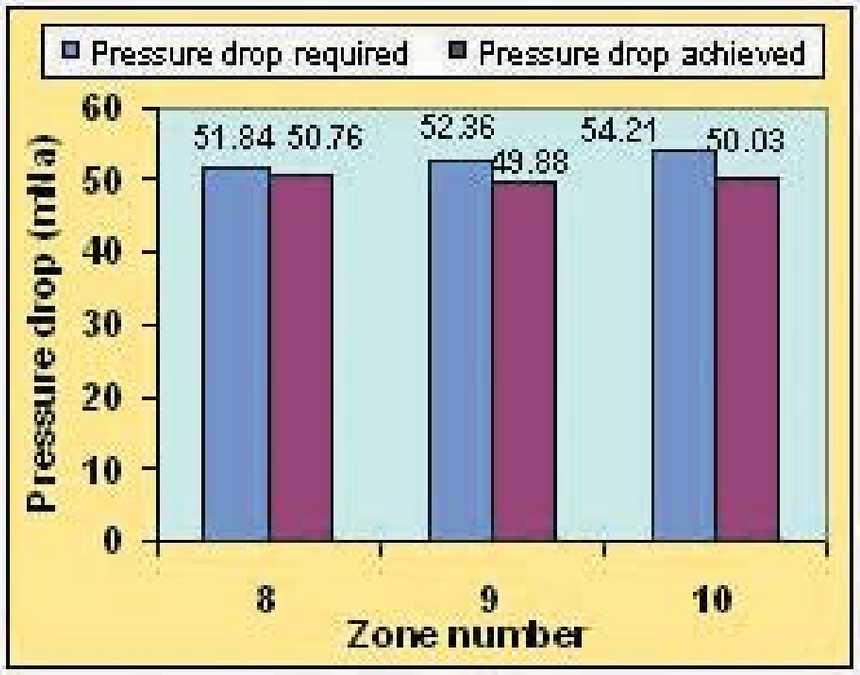

Fig.2 a
Comparison of Required and Achieved Pressure Drop at Rated Flow Condition.

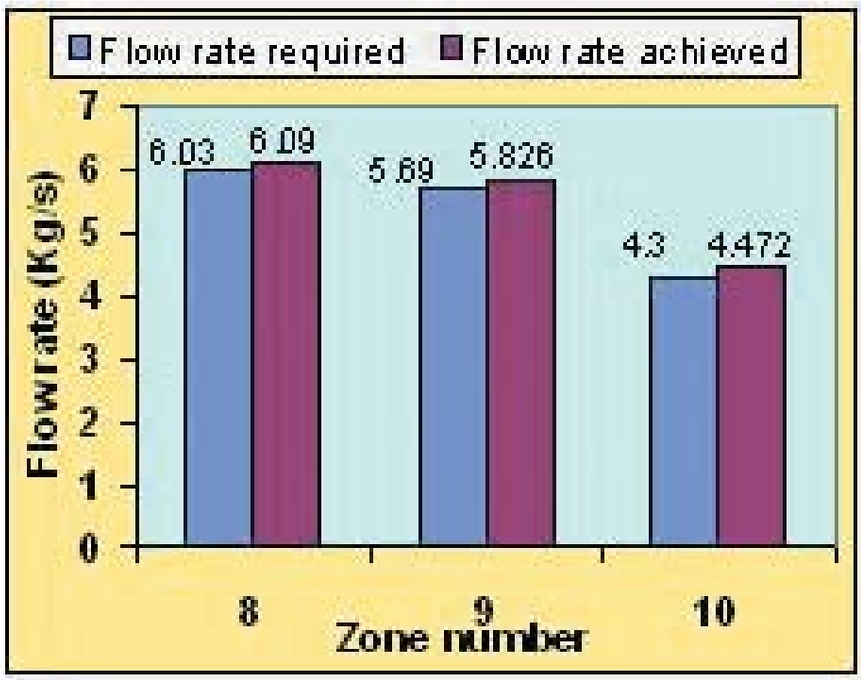

Fig.2 b
Comparison of Required and Achieved Flow at Rated Pressure Drop.

II.11 Monte-Carlo Estimation of Secondary Sodium Activity and Dose Rate in Steam Generator Building

The Intermediate Heat Exchanger (IHX) in PFBR is located inside the reactor vessel through penetrations in the roof slab. It is a vertical shell and tube counter-flow unit, with primary sodium on shell side and secondary sodium on tube side. Its main function is to transfer heat from primary to secondary sodium. The secondary sodium, while circulating through the IHX, gets activated by the capture of the leaking neutron from the core. The design criterion is to restrict the secondary sodium activity in IHX below 92 Bq/cc and hence the dose rate in steam generator building below 25 µSv/h. Now the in-vessel radial and axial shield configurations of PFBR are optimized in such a way to get low secondary sodium activity in IHX and sufficient detector counts at the control plug location. For the optimised in-vessel shield, the dose rate in steam generator building is found to exceed the design limit if no local shield is provided for IHX. Hence, IHX is provided with a local shield of stainless steel containing natural boron. To decide the local shield required to meet the design limit, refined calculations have been done using neutron transport theory methods.

First, discrete ordinate transport calculations were performed with DORT code in R-Z geometry in 100 to 175 neutron energy groups. This gives the neutron distribution in space and energy surrounding the core in the in vessel shields and sodium. The results of this computations were coupled ingeniously midway in the sodium with Monte-Carlo simulations. The Monte-Carlo (MCNP) surface source calculation was carried out by simulating the neutron transport in one-fourth sector of the reactor assembly around the IHX using MCNP. The spatial and angular distribution of the incident source for MCNP simulation of IHX were generated from the angular flux distribution derived from P_3S_8 calculation using DORT at a radius of 300 cm. A special source sub-routine need to be developed and attached to MCNP to achieve the specification of surface source. The continuous energy cross sections generated from ENDF/B-VI were used in MCNP.

The local shield is made up of borated steel. As shown in Fig.1, the local shield covers the bottom dished head and only the front portion of the region of shell and tube ranging from 196.5 cm to 654.5 cm from IHX bottom. Sets of calculation were done to estimate the IHX local shield requirement, either by varying the thickness of the local shield or by varying weight percentage of natural boron in the shield. It is seen that to meet the design requirement, the local shield is to be made up of 1.2 % borated steel of 28 mm thickness in shell and tube region plus 12mm shield for bottom dished head. For the recommended configuration of IHX, the estimated that upper limit of dose rate in steam generator building is 23.5 µSv/h (1m from sodium pipes) after allowing for uncertainty in calculation

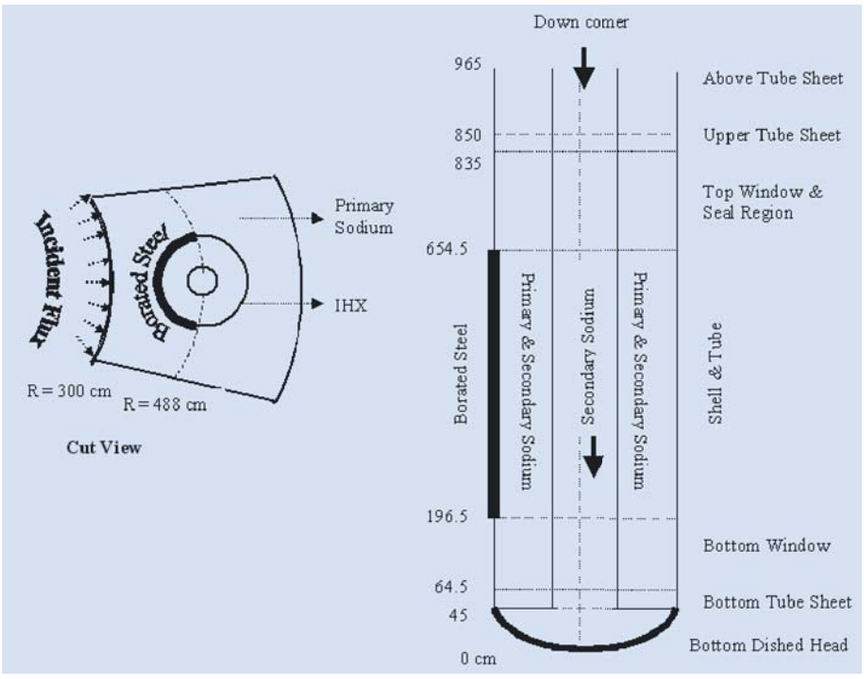

Fig.1
IHX with Local Shield

II.12 Frequency Response Studies on Mutual Inductance Type Level Probe

The Continuous level probe working on the principle of variation of mutual inductance between two windings when they are immersed in an electrically conducting fluid such as sodium is used in Fast Reactor systems. It comprises of a bobbin on which coils are wound and placed in a pocket. The gap between the ID of pocket and OD of bobbin needs to be kept to a minimum to achieve maximum sensitivity. Studies were conducted using bobbins of different dia. (28, 30, 32 mm dia) alongwith standard pocket size (1in. Sch 40) of 1000mm active length (AL) in sodium at temperatures ranging from 150 to 550 deg. C. The discrete type level probe with 5 discrete levels is used as a reference probe.

It can be seen from Table.1 that 32mm bobbin gives higher sensitivity compared with 28 and 30mm bobbins. Considering the adequacy of sensitivity and ease of insertion and withdrawal, 28mm bobbin has been selected for PFBR.

The temperature corrections for the sensor become difficult due to different temperature coefficient for the uncovered and fully covered portion of the sensor. The mutual inductance in both states increase with increasing temperature but at different rates. The values of these individual temperature coefficients also depend on the operating frequency of the sensor. Fig.1 shows sensitivity (%) Vs frequency graph indicating that sensitivity reduces as the frequency increases. Fig.2 shows a graph in larger scale from 2 kHz to 3 kHz. The graph clearly indicates that the variation in % sensitivity due to temperature is minimum at 2.5 kHz.

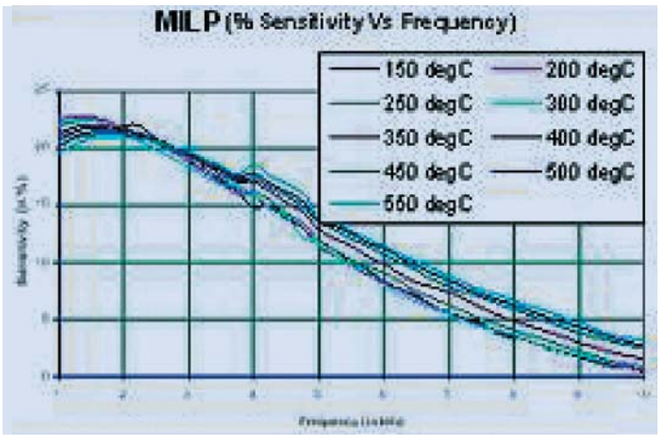

Fig.1
Sensitivity Vs Frequency

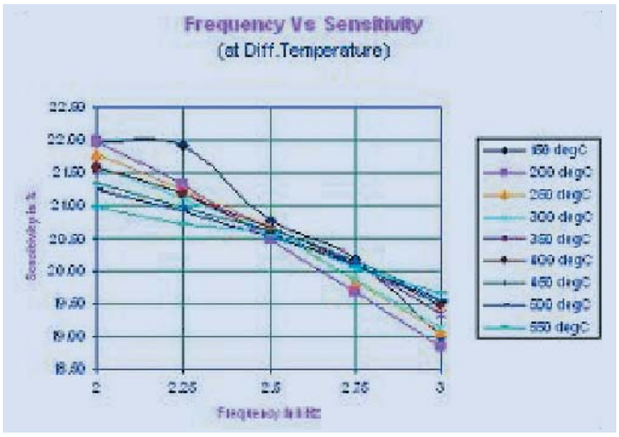

Fig.2
Sensitivity Vs Frequency (2-3 Khz)

Table 1. Sensitivity & Temperature effect at 2.75 kHz

Bobbin diain mm	Sensitivity %	Tempe. Coff in % level		Analog indicatin error (%)
		Zero level	Full level	
28	19.84	21.19	13.56	0.8 to -8.4
30	22.08	14.97	11.40	21 to -7.4
32	26.84	20.33	12.63	24 to - 4

II.13 Flow Distribution and Lift Force Measurement in DSRSA Using Water as Simulant Fluid

To achieve the desired safety level, the reliability of shut down system must be very high. With this objective, two reliable, independent, automatic, fast acting shut down system operating on diverse principle are provided in PFBR. The Control and Safety Rod (CSR) system comprises of nine absorber rods while the Diverse Safety Rod (DSR) system has three rods. Hydraulic performance study of DSR was carried out in a full scale model using water as simulant. Some of the studies are discussed in the following paragraphs.

Flow Distribution in DSRSA

The coolant flow rate required through DSRSA is 3 kg/s to remove the heat generated in each absorber rod during shut down of the reactor. This flow is distributed between the absorber rod and the annular space between DSR and the hexagonal sheath. The flow distribution depends on the relative flow path resistance. Therefore, the flow distribution was estimated by determining relative flow path resistance from experiment. For this purpose flow path in DSR was blocked by an adapter and pressure drop studies were carried out. Fig.1 shows the transposed results in reactor condition at shut down. It is estimated that 15.7% to 17% of total DSRSA flow will bypass the absorber rod at shut down condition of reactor, which meets the required safety criteria.

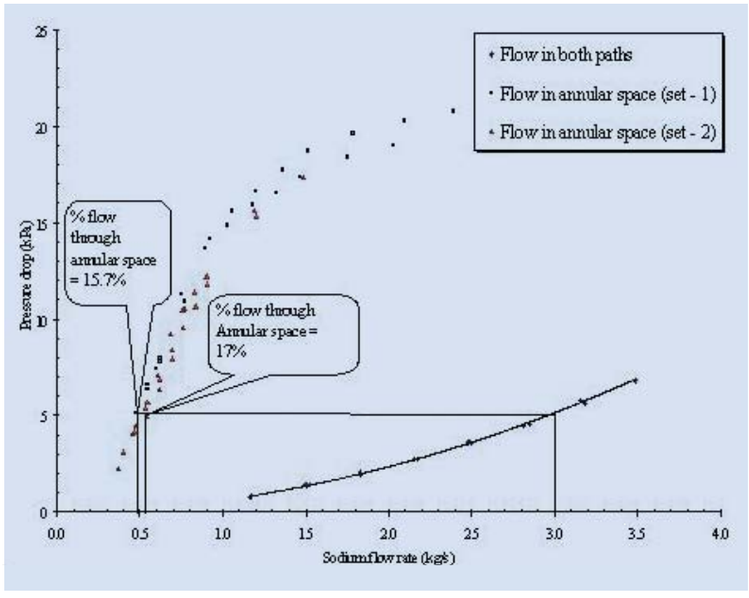

Fig.1
Flow Distribution at Shut down

Fig.2 shows the result during normal operation of the reactor when the rod is lifted to the topmost position. It is estimated from the experiment that 84% to 88% of total DSRSA flow will bypass the absorber rod at this operating condition.

Measurement of Lift Force Acting on DSR at Shut down Condition of the Reactor

Another important safety criterion is that, the absorber rod should not be lifted by the coolant thrust force at shut down condition of the reactor. An experiment was carried out to measure the upward thrust force acting on DSR by the flow at shut down condition using a load cell. The net upward force acting on the DSR is the sum of buoyancy force and the drag force due to the coolant flow. This force is expressed as the percentage of body weight and plotted against the percentage of the nominal flow rate as shown in Fig.3. It can be seen from this figure that the net upward force acting on DSR when it is deposited in the dashpot is around 27% of its body weight at nominal flow rate. This force is within the prescribed safety limit.

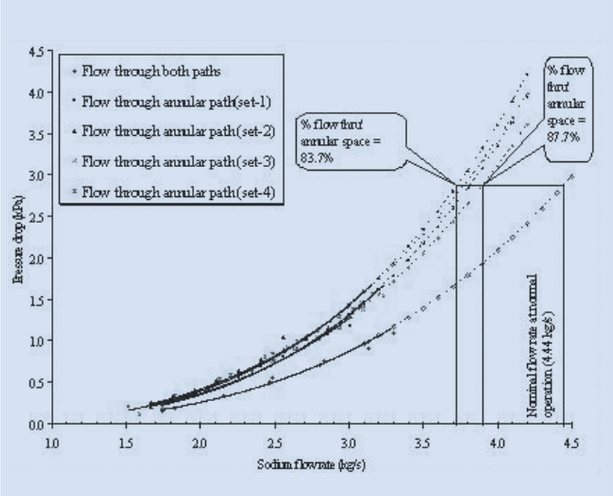

Fig.2
Flow Distribution During Normal Operation

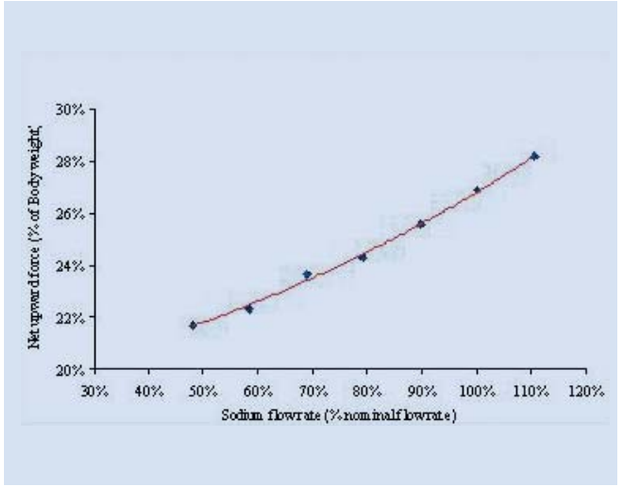

Fig.3
Upward Force Acting on DSR at Shut down Condition of the Reactor

II.14 Geo Grids for Engineered Backfill

Tunnels and trenches carry important services such as pipe lines and cable trays, for all the buildings of PFBR. Total length of the tunnels and trenches is approximately four kilo metres. Founding tunnels and trenches on the backfill has advantages from layout, construction, economy and safety. As these tunnels and trenches carry important services, they fall in nuclear safety related structures category. Structural design of these involves dynamic effects due to seismic excitations in transverse, vertical and longitudinal directions. Besides tunnels and trenches, retaining walls separating different grade levels are also supported on backfill. Dynamic Stability of backfill under seismic excitation is checked by numerical methods. Geogrids (grid-like materials, hence the name, with relatively large open spaces called apertures between polymer ribs used primarily as reinforcement of unstable soil and waste masses.) are proposed underneath the retaining walls, tunnels and trenches. Geo grids are also used underneath the roads in the nuclear island of PFBR to avoid deformation of the sub base, which in turn rests on backfill.

Three layers of geogrids at a spacing of 0.5m are laid beneath tunnels, trenches, retaining walls and roads.

Table 1. Factor of safety (FS) for various structures for two levels of earthquake

Sl. No.	Alternatives	Structures	FS for liquefaction	
			SSE	OBE
1	Without geogrids at the base	Retaining	2.13	2.04
2	With geogrids at the base	Walls	2.47	2.23
3	Without geogrids at the base	Tunnels	4.2	3.8
4	Without geogrids at the base		5.45	4.31
5	Without geogrids at the base		5.78	4.65
6	Without geogrids at the base	Trenches	6.21	5.13

Typical details for retaining walls are shown in fig.1. Detailed analysis was carried, to evaluate the increase in engineering properties of backfill with the introduction of geogrids.

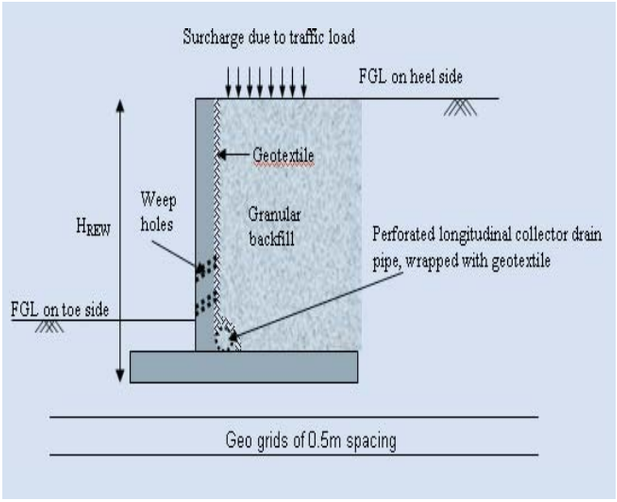

Fig.1.
Typical Cross Section of Retaining Wall

Results of the analysis were summarised in Table 1. It is observed that geogrids improves engineering properties of backfill during earthquake excitation. Geogrids at the base act as a damping layer and reduce the effect of vertically propagating shear waves on the structure. Geogrids make failure mechanism complex as they interact with potential failure surfaces.

Geogrids having reference strength of 20 kN/m with a quality control strength of 6.12 kN/m are (equivalent to Tensar biaxial geogrids of type SS20) used below tunnels, trenches, retaining walls and roads. Lengths of geogrids for reinforced soil beds below the tunnels and trenches is 2 times the width of the tunnel at the base. The lengths of geogrids recommended for reinforced soil beds below the pavements for roads is 1.2 times the width of the road (distributing equally from the center line of the road). Use of geogrids significantly reduced the complexity of foundations for tunnels, trenches, retaining walls and roads for PFBR.

II.15 Studies on Bio-fouling and Its Control for PFBR Cooling Water System

Power plants located near coast generally use seawater for extraction of heat from condenser and other auxiliary system. Thus, components of these two systems are prone to the settlement of organisms present in seawater. This process is called bio-fouling (Fig.1 a cleaned panel and Fig. 2 a fouled panel). Bio-fouling adversely affects the efficiency of cooling water system (reduction of heat transfer in condenser, partial to full blockage of condenser tubes, siltation in pump chamber, blockage of various screens, etc.). Thus bio-fouling control is an integral part of any cooling water treatment programme. To evolve an effective bio-fouling control strategy, it is essential to know the type of organism (macrofoulants whether soft bodied or hard bodied and microfoulants) present in seawater. With this in mind, studies on bio-fouling on teakwood panel exposed to Kalpakkam coastal water is being carried out to assess its monthly, seasonal, & annual variations. The results showed a wide variation in intensity of fouling ranging from 21 to 71 numbers per sq cm in weekly panel wherein the % of coverage varied between 25 to 75% and the biomass varied between 3 to 6 g/100 sq cm. Barnacle (52 to 89 %) and mussel (0 to 5 %) were found to be two dominant species. A steep increase in biomass was observed in 30 d (77g/100 sq cm) and 60 d (97 g/100 sq cm) old panels as compared to 7 d old panels. Species diversity was found to be higher for 30 d old panel than that of 7 d. The unique feature of this study is that for the first time photographs of each series and the fouling pattern at an interval of 7 d are available in digital form. A striking feature observed was that the fouling pattern was significantly different between weeks (e.g. Fig.3 & 4). Possibly this startling result could be used to optimize bio-fouling control regime for PFBR.

The process seawater cooling system of PFBR is to have Ti Plate Heat Exchanger (PHE). Titanium is known to be prone to bio-fouling and the small gap between plates (3-4 mm) could prove to be more troublesome by fouling organisms. Considering this pitfall, a test facility (Fig.5) with 3 PHEs having ten plates each has been set up at MAPS pump house to study the bio growth rate under different flow

rates (0.5, 1.0, & 2.0 m/s). Tests have been carried out at a flow rate of 0.5 m/s. Barnacle settlement was observed (Fig. 6) on the plate in spite of chlorination. Silt deposition (Fig.7) at a rate of 1.5 g/day and a gradual decrease in its content from the inlet to the middle and subsequent increase from middle to the outlet was observed.

Fig.1
A Cleaned Teak Wood Panel

Fig.2
A Teak Wood Panel Fouled by Green Mussel

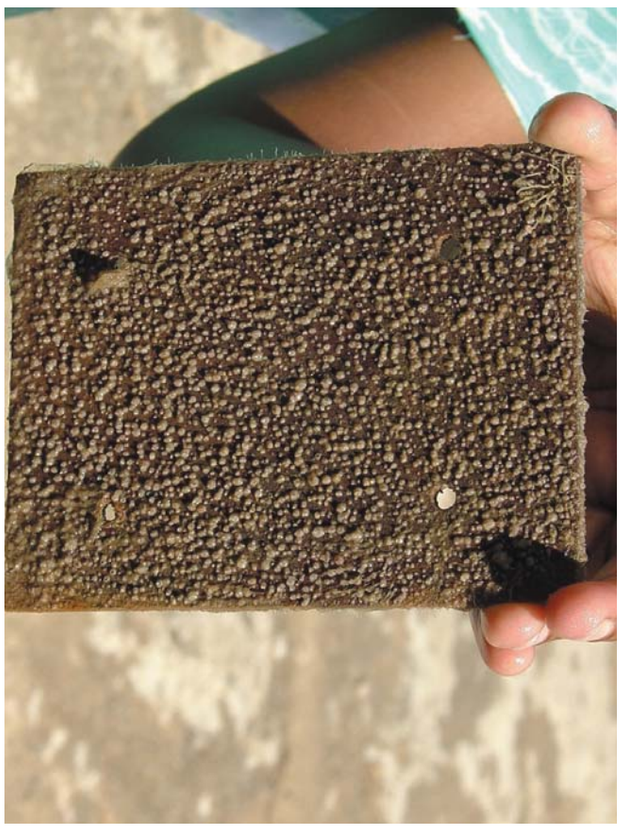

Fig.3
Fouling on a Week old Panel Exposed During May (18.05.06-25.05.06)

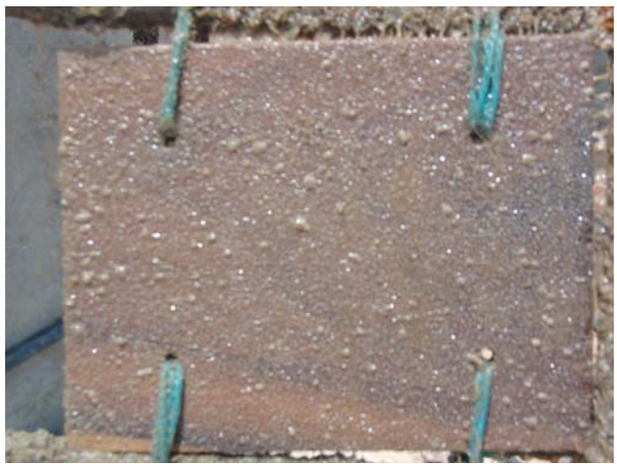

Fig.4
Fouling on a Week old Panel Exposed During June (01.06.06 - 08.06.06)

Fig.5
A View of the Plate Heat Exchanger (PHE)
Bio-fouling Test Facility

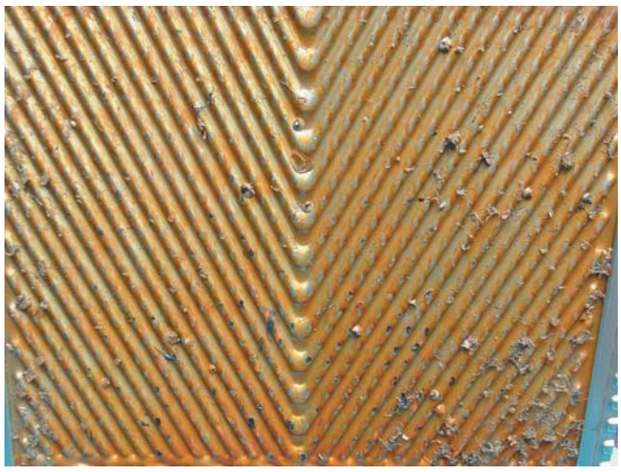

Fig.7
A View of Silt Deposition on PHE

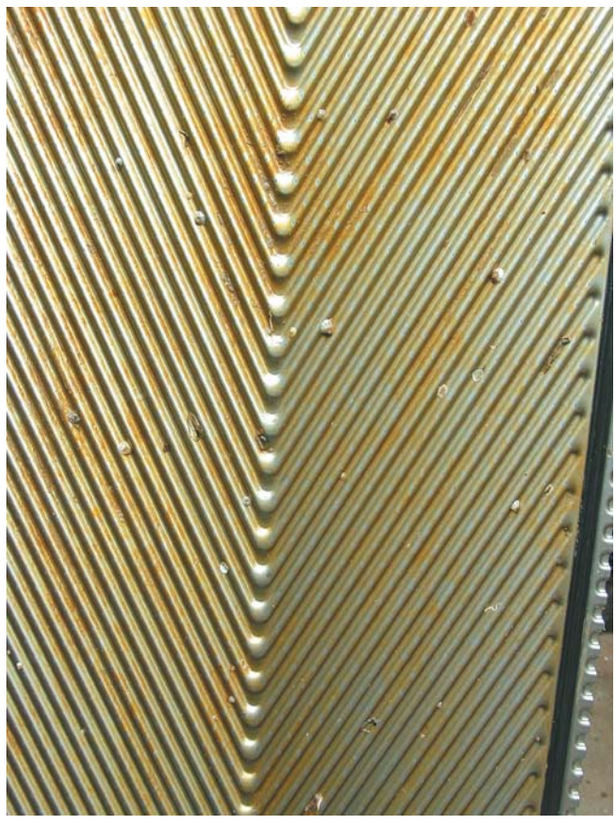

Fig.6
A View of Barnacle Settlement on PHE

Chapter - III

R&D FOR FBRs

MODELLING AND SIMULATION EXPERIMENTS FOR REACTOR CORE & OTHER COMPONENTS

III.1 Studies on Physics Parameters of Metal Fuelled FBR

For faster growth of nuclear power in India, it is essential to shift to use of metal fuel in FBR, which gives a higher breeding ratio (BR) and lower doubling time (DT). As a part of the centre's programme to develop the technology for metallic fuelled rectors, a study of physics parameters of various metal-fuelled cores using XSET-98 cross-section set has been done as a function of the reactor power, fuel smear density, zirconium content in the fuel and number of radial blankets. More emphasis was given on the BR, DT estimation and methods to reduce sodium void reactivity effect, as it is an important safety parameter.

The physics parameters of a 500 MWe fast breeder reactor (FBR) with different metal fuels were analysed and the main results are given in Table.1. The number of fuel assemblies, pin diameter and heat rating are same as that of PFBR. The BR, DT and sodium void reactivity effect of a 500 MWe oxide core are 1.05, 65 yrs and 1.7 $ respectively with 2 rows of radial blanket. With metallic U-Pu-Zr10% fuel, the BR, DT and sodium void reactivity effect become 1.25, 14.2 yrs and 4.4 $ respectively. While one $ (delayed neutron fraction) reactivity is about 350 pcm (1pcm = 0.001 %) in oxide core, it is about 400 pcm in metal core due to higher U-238 fissions. The fuel Doppler reactivity feed back is also more negative with metal fuel. If the number of rows of radial blanket becomes 3, it is possible to attain higher BR, with no further increase in sodium void reactivity effect. With U-Pu fuel, the BR becomes 1.488 and DT becomes 8.1 yrs. The sodium void reactivity effect increases slightly. By increasing the number of rows of radial blanket in to 3, it is possible to increase the BR from 1.488 to 1.520.

These studies show that for 500 MWe core it is possible to achieve a reactor fuel doubling time of about 8 years in metal U-Pu fueled FBR with sodium void reactivity effect of nearly 5$, which is acceptable to regulatory bodies.

For 1000 MWe core, fuel pin diameter, heat rating and number of core and blanket sub-assemblies were optimized. A three-fuel zone core with 3 rows of blanket was designed (Fig.1) with a pin diameter of 0.8 cm and fuel assembly size of 16.8 cm. When it is fuelled with U-Pu-Zr10%, it is found that the breeding ratio obtained is 1.38 and the DT is 9.7 yrs, with a sodium void reactivity effect of 8 $. With the U-Pu fuel, the BR attainable is 1.607 with a DT of 6.6 years, with the same sodium void reactivity effect. The higher BR, which results in a low burn-up reactivity loss, can be gainfully utilized for high fuel burn-up and longer cycle lengths. It was noticed that the sodium void reactivity effect was high for 1000 MWe core.

Table 1: The Physics Parameters of Metal Fueled FBR

No	Parameter	500 MWe with 2 Rows of radial blanket			1000 MWe with 3 rows of radial blanket	
		Oxide	Metal Zr=10%	Metal Zr=0%	Metal Zr=10%	Metal Zr=0%
1	Breeding Ratio	1.051	1.253	1.488	1.376	1.607
2	Reactivity swing (pcm)	3500	2000	1000	1000	0
3	Reactor fuel doubling time (years)	65	14.2	8.1	9.7	6.6
4	Sodium void reactivity	+584	+1730	+2094	+3279	+3473
	effect (pcm and $)	(1.7 $)	(4.4 $)	(5.0$)	(8.1$)	(8.02$)

Two ways of reducing sodium void reactivity effect were considered (Table.2). The first method is the introduction of a sodium plenum in the upper axial blanket region and the second method is by using a fuel with reduced smear density. The first method is applied to a 1000 MWe, U-Pu-Zr10% fuelled core. The sodium void reactivity effect reduces from 8.1 $ to 4.6 $ with the modification, even though it leads to slight decrease in BR. In the case of a 1000 MWe U-Pu fuelled core, with a decrease of smear density from 0.75 to 0.62 reduces the sodium void reactivity effect from 8 $ to 7.4 $, the corresponding fall in BR is from 1.6 to 1.5. In addition, both the modification can lead to a more negative Doppler constant, which is favourable in safety point of view. Thus, the most effective way of reducing sodium void reactivity effect is found to be introduction of sodium plenum.

Table 2: Modifications in the 1000 MWe Metal Core to Reduce the Sodium Void Reactivity effect

Parameters	U-Pu-Zr10%		U-Pu	
	Reference core	Modified core with Na-plenum	Reference core smear density=0.75	With smear density =0.62
Breeding Ratio	1.376	1.310	1.607	1.503
Reactor fuel doubling time (years)	9.68	11.76	6.6	7.3
Doppler constant (pcm)	-527	-608	-479	-500
Sodium void reactivity effect (pcm)	3279 (8.1$)	1861(4.6$)	+3473 (8.02$)	+3123 (7.4$)

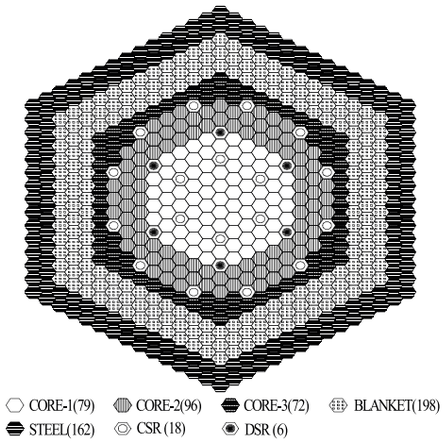

Fig.1
A 1000 MWe Metal Fuelled FBR Core

III.2 Numerical and Experimental Studies on Velocity Pattern in the Hot Pool of SAMRAT Model

A steady state hydraulic analysis of SAMRAT model (1/4 scale model of PFBR primary circuit) was carried out using PHOENICS, a commercial Computational Fluid Dynamics (CFD) package. Though the model is symmetric in 1800 sector, analysis could call for large number of grids involving large computation time and difficulty in achieving convergence. Therefore a 90° sector model of hot pool in cylindrical coordinate system with one IHX and half pump as shown in Fig.1 was considered for analysis.

The computational domain was subdivided with a grid structure of 45X54X68 to achieve fairly accurate results independent of grid.. The core was modeled as solid cylinder. Fixed mass flow rate was provided as the inlet boundary condition at Fuel, Blanket, Storage and Cavity zone as shown in Fig.1. The skirt was modeled as porous plate. Flow through control plug (CP) was modeled by specifying mass sink at the bottom of the CP and flow was considered to enter the hot pool uniformly at different levels of the CP. All the structural components in hot pool were modeled by blocking the cells at corresponding locations. The conical portion of the inner vessel as shown in Fig. 1 was modeled as steps. The IHX was modeled as a hollow cylinder.

The numerical results were compared with experiment and a fair agreement was found. The flow pattern in a vertical plane (r-z plane) passing through the middle of IHX is presented in Fig. 2.

The resultant cross velocity as found from numerical analysis around IHX inlet window (Fig.3) was also compared with the measured value in four equispaced vertical planes and good matching was found.

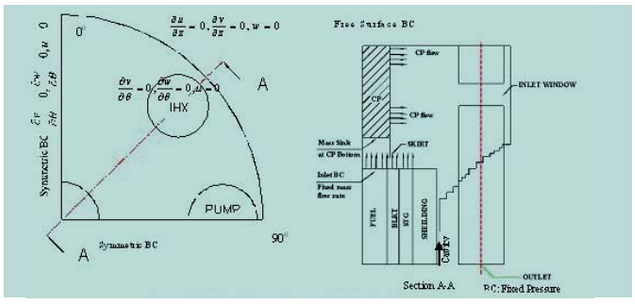

Fig.1
CFD Model and Boundary Condition

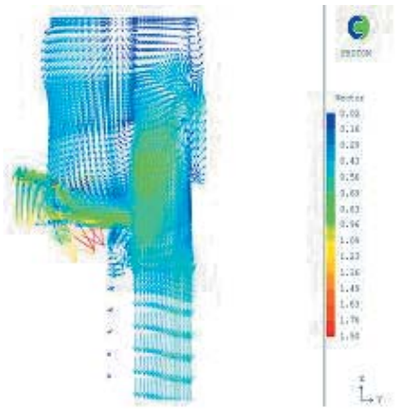

Fig.2
Velocity Pattern in a Vertical Plane

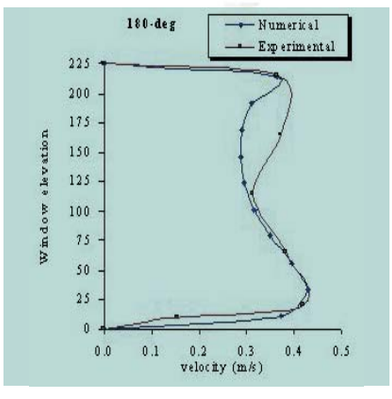

Fig.3
Velocity Distribution Around IHX Inlet Window

III.3 Multidimensional CFD Analysis of Air Heat Exchanger of Safety Grade Decay Heat Removal System

Heat continues to be generated in the nuclear reactor even after shut down due to the radioactive decay of fission products. This heat is termed as decay heat. The normal heat removal circuit is designed to remove this heat also. When this circuit is unavailable, then the decay heat removal function is achieved through an alternate circuit. In order to have high reliability, the alternate circuit selected is nearly passive in nature working under natural convection mode. This circuit is known as Safety Grade Decay Heat Removal System (SGDHRS). SGDHRS circuit consists of sodium to sodium heat exchanger (DHX) and a sodium to air heat exchanger (AHX) linked by an intermediate sodium circuit. DHX is a simple shell and tube heat exchanger dipped in hot pool and AHX is a finned tube sodium to air heat exchanger. Heat generated in the core is transferred to intermediate circuit through hot pool and DHX. AHX transfers heat from the intermediate circuit to air. The thermal center difference between DHX and AHX aids the natural circulation flow in the intermediate circuit. A 30 m tall stack at the top of AHX provides sufficient buoyancy head for the air to flow through the AHX.

One of the challenges involved in the design of AHX is the management of flow by-pass which seriously affects the heat exchange capacity and the other is uncertainty in the reported heat transfer correlations. When an AHX is used in a natural circulation loop, the complexity gets added due to the dependence of the estimated natural convection flow on pressure drop correlations. Therefore, designing the heat exchanger with minimum flow bypass and careful use of heat transfer and pressure drop coefficients with suitable margin are very essential. Achieving this objective is becoming increasingly simpler due to the advancement in the Computational Fluid Dynamics (CFD). In this context, CFD tools have been employed to study and manage the above aspects and thereby arrive at a sound thermal hydraulic design of AHX.

Flow distributions in the inlet header on the sodium side and 90° bend inlet duct on the air side have been investigated to study their influence on the AHX heat removal. Velocity and temperature distributions of air flow over finned tubes, predicted for a typical condition is shown in Fig.1. With the knowledge of velocity distribution of sodium and air at the inlet header and inlet duct respectively, a porous medium analysis of AHX with suitable numerical models for heat exchange between sodium and air (based on the numerically derived correlations) have been carried out further to estimate AHX heat removal capacity. Suitable baffles to arrest air flow by-pass (Fig.2) have been arrived at based on the analysis, to improve the heat exchange capacity of AHX from 5.4 MW to 8.27 MW.

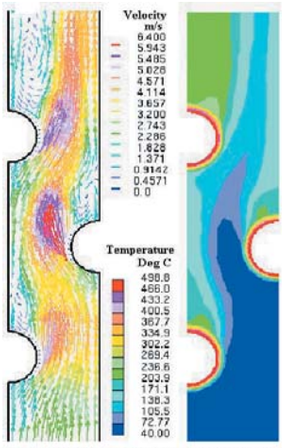

Fig.1.
Velocity and Temperature Distributions of Air in between Finned Tubes

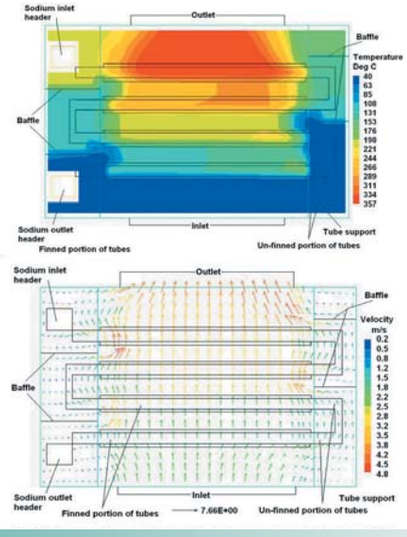

Fig.2.
Velocity and Temperature Profiles in the Recommended Design of AHX

III.4 Experimental Investigation on Hydrodynamic and Thermal Fragmentation During Melt - Coolant Interaction

In the event of core meltdown scenarios in FBR, during melt–coolant interaction the main safety issues are avoiding coolability and recriticality of the debris. Both these issues are dependent on the type of molten fuel coolant interaction and relocation of the debris inside the reactor. Experimental investigations have been carried out in SED to address this issue. Experiments were carried out with a few kilograms of Sn, Bi, Pb, Zn and Woods Metal with water as coolant. These metals are considered as appropriate for such studies, as the density ratio of metal to water is similar to that of UO2 - Na system. The surface tension and kinematic viscosity of woods metal are also nearly equal to that of liquid UO2 debris size characterization, pressure generation, melt spread area on a collector plate and central lump height during such interaction have been measured. Pool and long water column geometry were used for the study with various melt superheat and water temperature combinations.

Molten material spreading on a collection plate, for a typical 1 kg trial of all the four melts (Sn, Bi, Pb and Zn) in pool geometry, is shown in Fig-1. A central lump height of 84 mm, 57 mm, 88 mm and 30 mm and base spread area of 105 cm^2, 45 cm^2, 65 cm^2 and 235 cm^2 were obtained for Sn, Bi, Pb and Zn respectively for 2 kg trials, the mass median diameters [MMD] for Sn, Bi, Pb and Zn for melt superheat of 100 °C and water at 30 °C are 1.9 mm, 0.7 mm, 3.2 mm and 4.2 mm respectively. With 1 kg Sn and water at 30 °C the first pressure peak of 68 kPa with 140 ms rise time was obtained.

Kelvin Helmholtz Instability and Rayleigh Taylor Instability are the hydrodynamic phenomena, which govern the molten jet break up leading to fragmentation and generation of particulate debris. The most probable particle diameter is reported by Kelvin Helmholtz Instability theory as $d = 2\Pi\sigma (\rho_j + \rho_w) / (U^2 \rho_j \rho_w)$, where U is the velocity of molten jet, σ is the surface tension of molten jet, ρ_j and ρ_w are the densities of molten jet and water respectively. From the present experiments it was found that the Kelvin Helmholtz Instability is more predominant in the jet break up. Fig.2 gives the comparison of the experimental Mass Median Diameter (MMD) and calculated values for all the melts. For a fixed Sn melt superheat, increase in initial water temperature resulted in shallow bed formation. With Sn under pool geometry, the detached debris generation is vigorous for melt superheat to water sub-cooling ratio more than ~ 6.0. Of all the four melts Sn, Bi, Pb and Zn interaction in long water columns, Bi shows better fluidization property leading to fine particulate debris, owing to higher Weber no and higher flow conductance. In case of Zn fine debris are not generated due to large melt surface tension and low flow conductance.

With Woods metal-water system experiments were carried out for different boiling regimes of water. Debris sizes were assessed for different water heights and temperatures, melt mass and temperature. Contribution due to coolant boiling resulted in more particulate debris generation in the size less than 4 mm. Fig-3 gives the debris size range less than 4

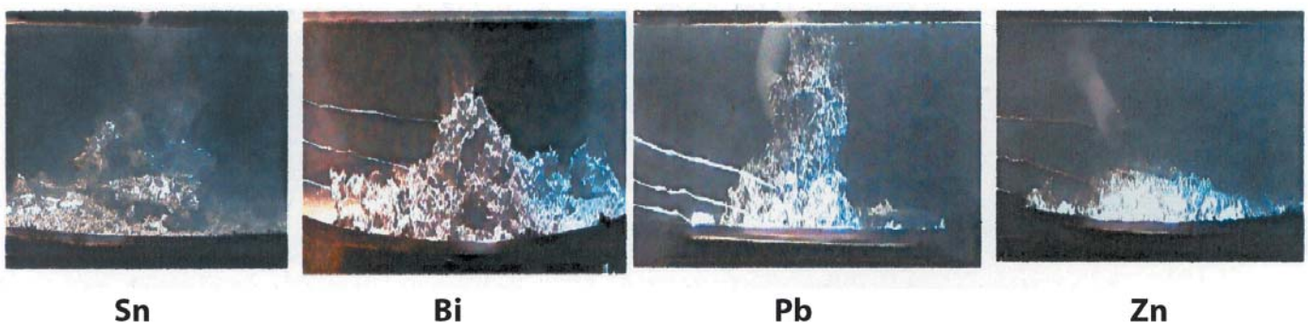

Fig.1
Melt profiles for 1 kg Sn, Bi, Pb & Zn Runs in Pool Geometry
(Melt Super Heat 100°C, Water Temp 30°C, Water Column Height 80 mm)

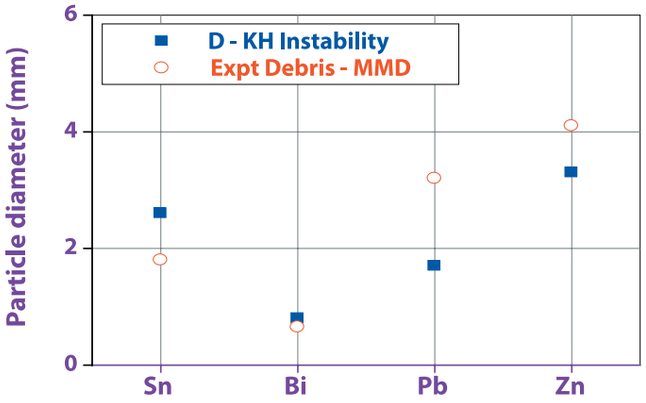

Fig.2
Comparison of MMD of the Debris with Most Probable Diameter of Kelvin Helmholtz Instability

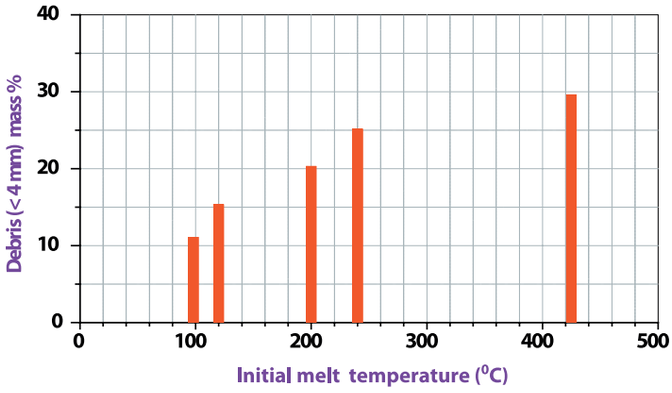

Fig.3
Effect of Melt Temperature (Woods Metal) (Melt Inventory 750g. Water Column Ht 1100mm, Water Temp 30°C)

mm for melt temperatures of 98°C, 120°C, 200°C, 240°C and 425 °C which covers convective, nucleate, transition and film boiling regimes of water. Thermal fragmentation dominated the fuel coolant interaction process when first contact temperature is more than spontaneous nucleation temperature (T_{SN}) leading to more fines generation (< 1 mm). Higher inventory resulted in the formation of very large globules, due to agglomeration of unsolidified droplets on the target plate.

III.5 Vibration Analysis of Steam Generator Tube

The steam generator (SG) module is a straight shell and tube type with 19 tubes once through steam generator rated for 5.5 MWt. The tube bundle consists of 19 tubes of 17.2mm OD/2.3mmWT and is 23m long, arranged in a triangular lattice pattern (Fig.1). SG tubes are subjected to cross flow of the liquid sodium at the inlet and exit sections, making it susceptible to Flow Induced Vibrations (FIV) due to different excitation mechanisms. Considering turbulence buffeting as the cause of vibrations, an analysis has been done to estimate the response of the tube to random excitation forces.

When turbulent flow comes into contact with a surface some of the momentum is converted into fluctuating pressures. Since this is a random phenomenon, the excitation forces can only be described on a statistical basis. For structural analysis, information on fluctuating pressures is best expressed by the power spectral density of the pressure field. By doing this we can find out the pressures that have a frequency component closer to the natural frequency of the structure. The knowledge of the random forces enables the prediction of the response of the structure.

The root mean square response at various points along the span of the tube was calculated using the ASME guide lines. The discretization of such a big structure using 3D elements results in huge amount of calculation and the time taken is considerably high. So, 2D beam elements with 6 degrees of freedom are chosen. The added mass effect of sodium on the dynamic characteristics is taken into account and a code was developed in MATLAB. The tube is simply supported at 19 positions and also supported at the center of the expansion bend. Fig.2 shows the first two mode shapes of the SG tube.

Using the estimated modal frequencies, mode shapes and the flow velocity distribution at the inlet window, the response of the tube at each nodal point was calculated assuming a joint acceptance (J) integral of 1 (ASME Section-III, Appendix N). Fig.3 shows the displacement values at various nodal points along the length of tube. It can be seen that the root mean square response is not

exceeding 1mm for a joint acceptance of 1. The correlation length used in calculating the joint acceptance will not exceed 3 times the external diameter of the tube and hence the joint acceptance integral will be around 0.1, and the response will be of the order of 0.1mm. This value is less than the permissible limit of tube vibration of 0.35 mm (rms) for this tube. This analysis indicates that PFBR tube design is safe against turbulent buffeting.

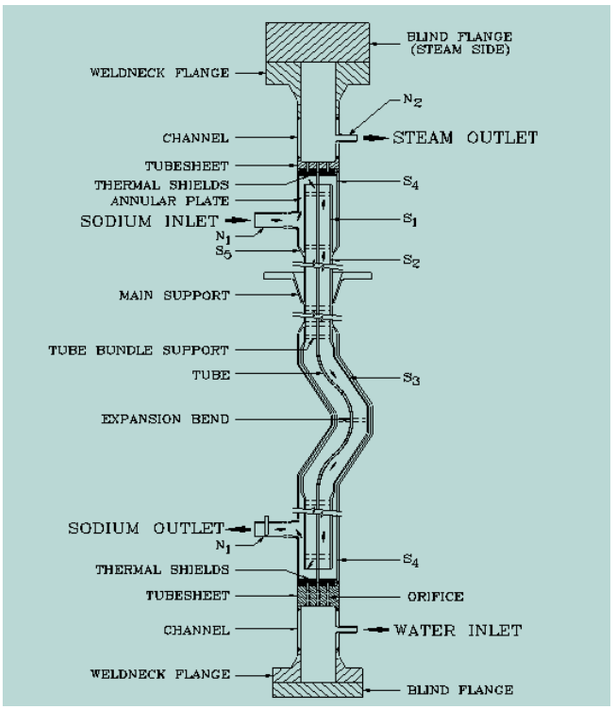

Fig.1
SGTF Steam Generator

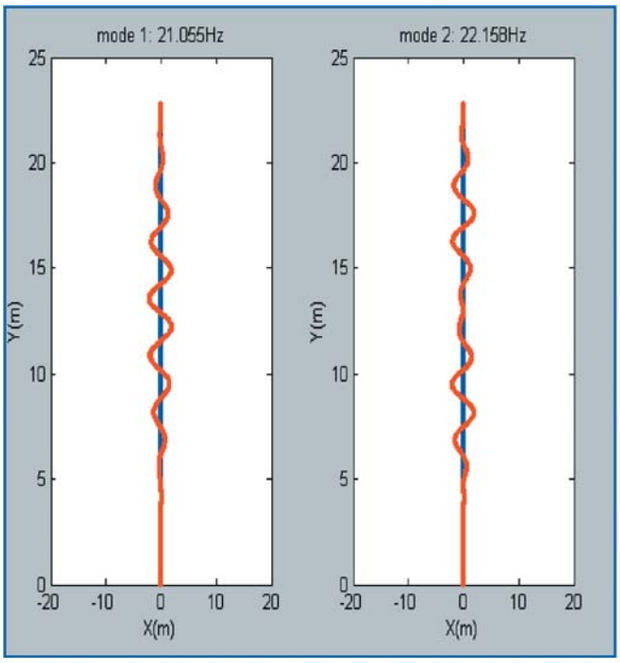

Fig.2
First two Mode Shapes of SG Tube

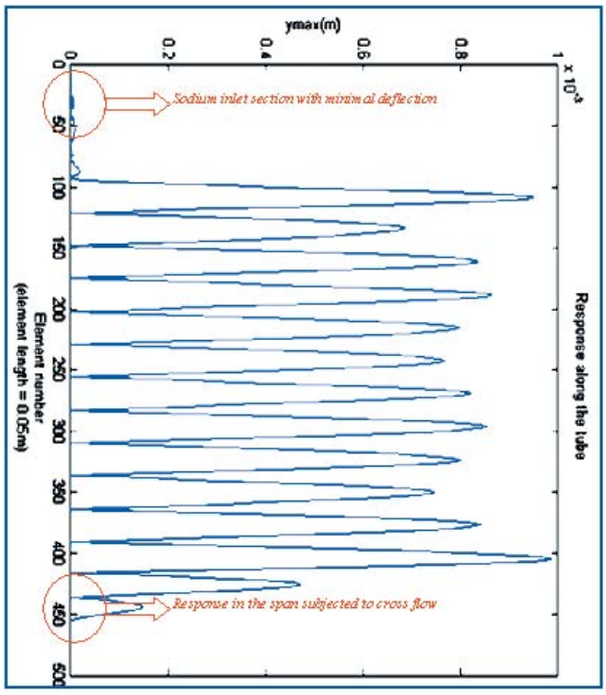

Fig.3
Maximum Response at Each Span

III.6 Experiments in the 5/8 Scale Model of the Surge Tank

Surge tank is one of the components in the secondary circuit of PFBR, provided to take care of pressure surges in case of a sodium water reaction in Steam Generators (SG). The blanket of argon cover gas at the top of the tank acts as a cushion for the surges. The argon gas above the free surface of sodium in the tank is also a source of entrainment into the sodium which is undesirable from the consideration of effective heat transfer in Intermediate Heat Exchanger (IHX) and SG, cavitation in pumps and operational problems. The prediction of gas entrainment phenomenon using computational tools is difficult and the mechanisms of gas entrainment are best investigated using experimental models. To investigate the phenomenon of gas entrainment in surge tank, hydraulic experiments are being conducted in water using 5/8 scaled model respecting Froude and Weber similitude simultaneously while flow is kept in turbulent region. This research work is being carried out in association with FCRI, Palghat.

The model shown in Fig.1 is a fully cylindrical shell model with dished end bottom. Two inlets are provided in the dished end. Four outlets are provided in the cylindrical portion of the Surge tank. The model is fabricated with Stainless steel material except for a small area which is provided with perspex shell for visualizing the gas entrainment phenomenon. A perforated plate of 10% porosity is fixed above the inlet of the surge tank.

The aim of the study was to visually check for the presence of gas entrainment in the model at the minimum level and if present, find ways to avoid it. Experiments were conducted by varying the flow with different devices as given below:

1) Studies without any internal devices.
2) Studies with Dummy plate (0% porosity) located at 1D of inlet nozzle
3) Studies with plate porosity of 10, 20 & 30%.
4) Studies with combination of porous plates and stiffener ring plates of 30°, 45° & 90° located at 1.5 D of inlet nozzle, with various air pressures above the water level (atmospheric pr., 0.3 bar and 0.7 bar)
5) Addition of Circular rings above the stiffener ring.

The studies have confirmed the need to introduce devices to mitigate gas entrainment. From the various configurations of the devices tested, the best possible combination which required a lower height of water column without any gas entrainment was the 20% porous plate with 30° stiffener ring. Fig.2 shows the minimum height to avoid gas entrainment for various configurations.

Fig.1
5/8 Scale Model Surge Tank

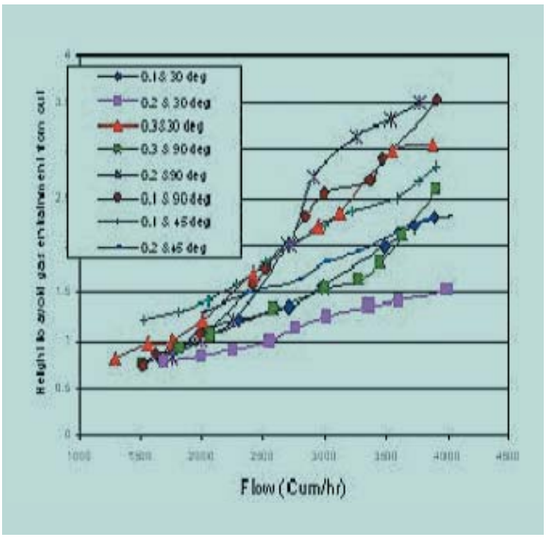

Fig.2
Minimum Height Required to Avoid Gas Entrainment at Various Flow Rates

III.7 Cold Trap Mass Transfer Modelling

Cold traps are used to maintain the desired sodium purity during normal plant operation. The main function of the cold trap is to decrease the oxygen and hydrogen contents in sodium. The principle of sodium purification is based on the property of reduction of solubility of impurities such as sodium oxide and sodium hydride in sodium with decrease in temperature. A computer code for calculation of impurity removal in a cold trap was developed and trapping efficiency and capacity of a model cold trap calculated.

The model cold trap used for calculation is shown in Fig.1. This consists of a cooling zone at the top and an isothermal zone at the bottom. In cooling zone, wire mesh trays are provided with sufficient flow area for sodium. In isothermal zone, concentric graded wire mesh arrangements are provided around the central tube and sodium flow is radial towards the center.

The temperature of sodium controls solubility of hydrogen impurities. The mass of sodium hydride trapped changes the porosity of wire mesh. The calculation is repeated until pressure loss through the trap reaches the limiting value.

The results of cold trap modeling are shown in Fig.2 to Fig.4. From Fig.3 the amount of sodium hydride removed in model cold trap is 0.016 kg / mm circumference of wire mesh. Total sodium hydroxide removed is 7.41 kg. The efficiency decreases from 98% to 24% with deposition of impurity in the wire meshes. The capacity of the cold trap is equal to 53.3 %. The model cold trap is being tested in SOWART sodium facility to validate the numerical calculation.

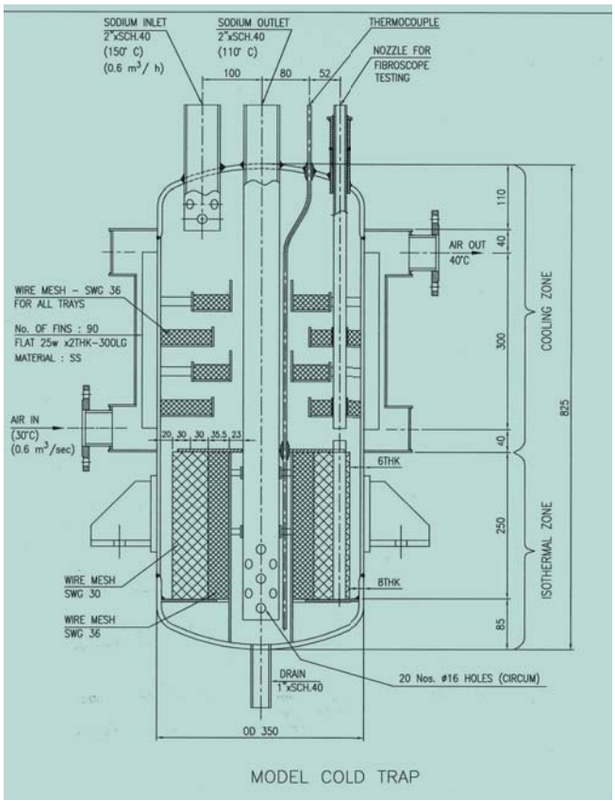

Fig.1
Cold Trap Model

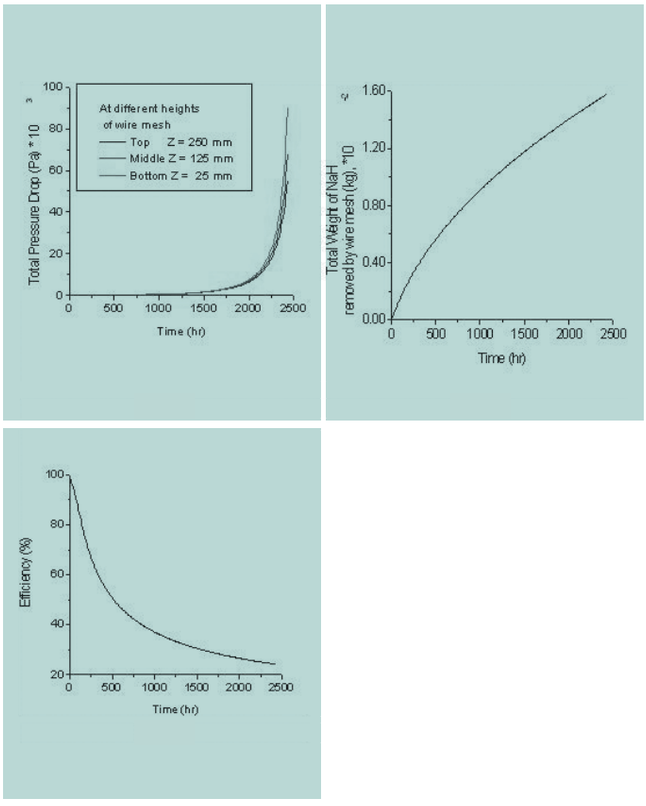

Fig. 2, 3 & 4
Results of Cold Trap Modelling

III.8 Experiments with Ring Baffle to Mitigate Gas Entrainment at Free Surface of Hot Pool

Pool hydraulics studies form an important element of design of the reactor. One of the issues to be resolved is the entrainment of argon cover gas into liquid sodium in the hot pool of PFBR due to high free surface sodium velocities. This phenomenon has undesirable effects on the smooth operation of the reactor. The present study was aimed to choose an appropriate device to mitigate gas entrainment by reducing the free surface velocities. Studies were carried out numerically to achieve the optimum dimension of a ring baffle plate and its location inside the hot pool. Three configuration of baffle plate with radial width of 37.5 mm, 70 mm and 125 mm were investigated. Typical velocity profile is shown in Fig.1. It is found from the numerical study that the choice of a baffle plate with radial size of 125mm and located above the intermediate heat exchanger inlet window is most suitable for reducing the free surface velocity to 0.25 m/s in model, which is equivalent to 0.5 m/s in PFBR.

Based on the above numerical study, the selected configuration of baffle plate was fabricated and installed in ¼ scale SAMRAT model of PFBR. For each experimental run, velocity was measured at the free surface to find out the maximum magnitude of radial velocity. Visual observation of the free surface was carried out to find out occurrence of vortices. The pump suction side region was observed from the perspex window provided at the main vessel of cold pool side to find out gas entrainment. The free surface textures with and without baffle plate are shown in Fig.2. Both the numerical results and experimental findings are summarized in Table – 1 for quick assessment of the effectiveness of baffle plate and are found to be in good agreement.

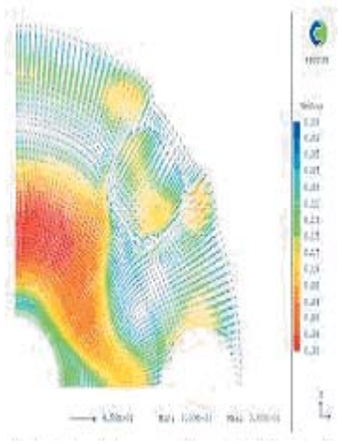

Fig.1
Velocity Profile at Free Surface for Various Configuration of Baffle Plate

Tabel 1. Summary of numerical and experimental results

Sl. No.	Radial width of Baffle Plate	Position below free surface (mm)	Maximum free surface velocity (m/s) (Numerical)	Maximum free surface velocity (m/s) (Experimental)	Visual observation during experiment
1	No Baffle (Reference design)	-	0.5	0.56	Free surface is highly turbulent formation observed at the free surface.
2	37.5 mm	315	0.44	-	-
		360	0.41	-	-
3	70 mm	315	0.37	-	-
		360	0.36	-	-
4	125 mm	240	0.33	0.30	Free surface is still turbulent
		315	0.30	0.25	Free surface is almost calm and no vortex was seen at free surface.
		360	0.27	0.24	Vortex was observed in the free surface near Pump

Flow pattern at free surface without any baffle plate

Flow pattern at free surface (Baffle place Fixed below 315mm from free surface)

Fig.2
Flow Pattern at Free Surface for Various Experimental Runs

SODIUM TECHNOLOGY

III.9 Experimental Prediction of Grid Plate Leakage Flow

Grid plate is one of the important and critical components of reactor assembly of PFBR. It is designed to support all the 1758 core subassemblies and is about 6.8 m in diameter and 1 m in height. Apart from serving as a high pressure plenum for distributing the coolant to the core subassemblies, precise location of subassemblies and maintaining their verticality are some of the few important functional pre-requisites.

Owing to the large size of the component, finer requirements on dimensional tolerances, precise locations of corresponding holes in top and bottom plates, ease of manufacture and assembly, the chosen design for grid plate incorporates bolted joints between Shell – Top / Bottom plate and Sleeve – Top / Bottom plate interfaces. Briefly, the grid plate is a box structure consists of top and bottom plates (6.8 m diameter and 55mm thick) fastened at the periphery to a circular shell. The plates are interconnected and fastened by 1758 sleeves that receive the core subassemblies. 4 inlet nozzles, 2 each connected to a primary sodium pump through a spherical header are welded to the shell at its periphery at predetermined angular locations. As the pressure inside the grid plate is high (0.62 MPa-g), the leakage of coolant at bolted joints is a matter of concern. Therefore experiment was conducted on grid plate for technology development. The design of grid plate for technology development had all representative design features of full-scale grid plate with a large diameter bottom plate, smaller shell and top plate (diameter 2.52 m). The flange widths, diameter of sleeves penetrations and gap tolerances were kept the same as in prototype. The component has about 115 sleeve penetrations. Out of this, the hydraulic experiment was planned with 19 sleeves located at the central region as it is representative of the core geometry and also the number of sleeves is large enough to permit meaningful extrapolation to the prototype.

The experimental test setup is shown in Fig.1. Necessary arrangements were made for collection and quantification of the leak from different interfaces of grid plate.

Leakage Through Flanges

When the grid plate is filled with DM water and pressurized, water started leaking from both top and bottom flanges. The leaked water from the top and bottom flanges was measured separately by a collection passage built it around the flanges, made of polythene sheets. Test has been carried out at various pressures from 0.2 MPa-g to 0.8 MPa-g. Based on the measured water leak rate in the model, the sodium leak for the reactor was extrapolated. The extrapolated value of sodium leak for the top flange is depicted in Fig.2. Fig. 2 gives leakage through top flange joint. In this case also the leak rate increases more or less linearly with pressure except for low tightening torque of 250 N-m. The dependence of leak rate on tighting torque becomes absent beyond 350 N-m.

The estimated sodium leak rates though the top and bottom flange joint even at 0.8 MPa-g is only 0.04% of core flow whereas the acceptable value is 0.5%. This validates the tolerances and flatness specified for the flange joints.

Leakage Through Top and Bottom Sleeve Nuts

Out of 115 sleeves test has been carried out in the central 19 sleeves. The leakage from the individual sleeves is collected separately using perspex cylinders. The level rise in the

Fig.1
Experimental Setup of Grid Plate Leakage Measurement for Technology Development

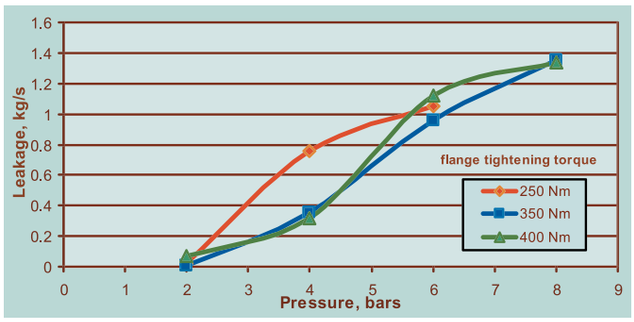

Fig.2
Leakage Through the Top Flanges, Bottom Flange Torque = 350 Nm

cylinder is measured by using sophisticated laser level measurement system (Fig.3). Sodium leakage extrapolated and measurement is plotted in Fig. 4. As the pressure increases the leak rate increases for both top and bottom sleeve joints, with the expected trend of $\Delta P \sim KQ^2$. For the same tightening torque of 350 N-m the leakage through bottom sleeve nut is slightly more compare to that of the top, which seems because of manufacturing tolerances. When the tightening torque is reduced for top sleeves from 350 N-m to 175 N-m the leakage increases, showing the same trend with respect to pressure.

The estimated top and bottom sleeve joint leakage for 0.6 MPa-g is only 0.04% of the core flow while the acceptable value is 0.5%. This confirms the tolerances and flatness specified for the joints.

Fig.3
Laser level probes arrangement for leakage though top sleeves nuts

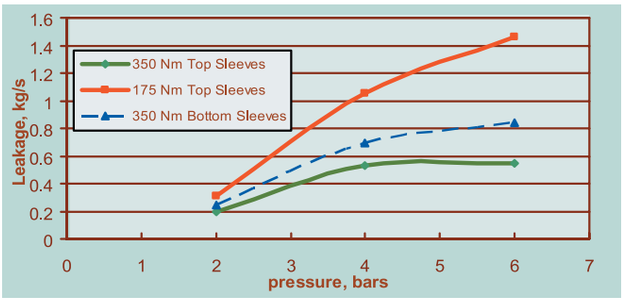

Fig.4
Total leakage though sleeves nut

III.10 Detection of Sodium in Fired Heater Pipelines of SGTF

After filling of sodium in the purification circuit of Steam Generator Test Facility (SGTF), the sodium storage tank level was continuously dropping. This indicated that in addition to purification loop, sodium was entering into some other part of the loop. While checking fired heater mimics, it was found that two skin thermocouple readings (Radiant section outlet – North) and (Radiant section outlet –South) were showing higher temperature of the order of 85°C confirming presence of sodium in the fired heater coils. This occurred due to the passing of sodium through fill line valve.

To confirm the presence of sodium and also to find the level of the coils, up to which sodium entered, a few NDT techniques such as Eddy current testing and Ultrasonic testing were applied.

MI Type Sensor for Detection of Sodium in Pipeline

A sensor working on the principle of variation in mutual inductance between two windings when they are surrounded by electrically conducting fluid such as sodium is used to detect the sodium in pipe line. Since this sensor is a non-contact type, it can be located outside the pipe line. This in-house developed sensor was used to find the presence of sodium heater pipe lines in SGTF.

The sensor consists of primary and secondary coils wound using 1mm dia. mineral insulated cable (MI) on an SS circular plate of 100mm dia with thickness of 3mm. as shown in Fig.1. The primary and secondary coils are wound alternatively one after the other in a circular fashion. Coils are held in position by spot welding a shim across the MI cable. An A.C source with constant current and frequency is used to excite the primary coil. The secondary voltage is measured using a digital multimeter.

The primary winding is excited by a current source of 1 kHz, which was found suitable for this material and wall thickness (7mm). When the sensor detects sodium, eddy currents are induced in sodium and there is a reduction in the main flux linking the secondary winding which causes the reduction in the secondary voltage.

Measurements were taken at 6 places in each row in the

north and south banks at the bottom, middle and top locations. The reduction in output was nearly 1mv (12% output reduction) which indicated the presence of sodium as shown in Table below.

Sensor position	Full sodium	Partially filled	No sodium
Top	7.36 mv	8.08 mv	8.07 mv
Bottom	7.26mv	7.36 mv	8.01 mv
90 Deg.	7.32 mv	7.74 mv	8.11 mv

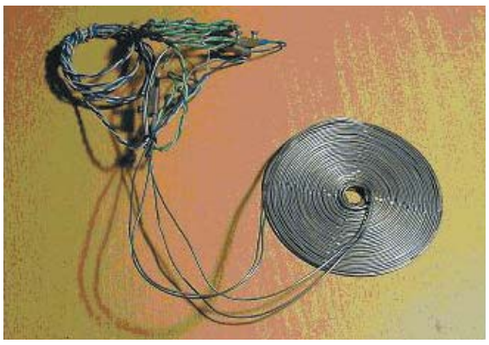

Fig.1.
Mutual Inductance Sensor

Ultrasonic pulse echo method (normal beam, 10 MHz) was employed. As adherence of sodium to ID of pipe is expected to lower the back wall echo amplitude due to transmission of ultrasound sound into sodium, attenuation of back wall echo from the ID/sodium interface was analysed to find out the presence of sodium.

Testing was carried out on eastern and western locations on each of the 4 bottom pipes, on North as well as South side pipes of the heater. At each location, testing was carried out on three clock positions i.e. 12'o Clock (Top of pipe), 9'o Clock (inspector side) and 6'o Clock (Bottom of pipe) to know the extent of filling. The results of eddy current and ultrasonic techniques confirmed that sodium had entered up to the second coil in both north and south passes of fired heater.

It was thus concluded that both the mutual inductance measurements and ultrasonic methods can be used for assessing the presence of sodium in bare pipes.

III.11 Innovative Design of Supports for Large Size Hot Sodium Tanks

Design of support for sodium tanks need attention from thermal and seismic loading considerations. The types of supports used are lug / bracket type or skirt type depending upon the application. Flexible supports are favoured to reduce discontinuity stresses at the hot junction but rigid support attachments are necessary from the point of view of seismic loading. The sodium tanks are hot due to the operating temperature and hence peak thermal stress at the junction is of concern from creep-fatigue damage considerations. Apart from the requirement of comparable flexibility of support with main shell, it is essential to minimize the thermal gradient near the shell to support junction. This is achieved by selectively removing the insulation near the support. It is also needed to have the temperature of bolts as low as possible (below 150 deg C). Each of the tanks like SGDHR expansion tank, secondary sodium surge tank and primary sodium purification tank are analysed with above considerations. The design and analysis of priming tank of primary sodium purification circuit which carries radioactive sodium is presented in this article.

This tank is categorized as safety class –1. It contains radioactive primary sodium. The total weight of priming tank, including the sodium in it is 1.6 t. It is provided with double envelope to avoid release of radioactive sodium in reactor control building in case of leak in tank. Nitrogen is filled in annular space to provide an inert atmosphere. The material of the priming tank and the double envelope is SS 304 LN. The normal operating temperature of the priming tank is 400° C. During SGDHR the temperature rises to 540° C and reduces to 200° C during fuel handling condition. The tank is insulated to reduce the heat loss to surroundings.

The supporting arrangement for the tank is designed (Fig.1) to meet various conflicting requirements. The basic requirement is that the weight shall be transformed to support directly from main shell and the main shell shall be covered fully by double envelope. The design code requirements are the stresses / strains under thermo mechanical and seismic loadings as well as crep fatique damage at the junction shall be within the allowable limit. Further the temperature at bolt location (end of the flange) shall be limited (say less than 100°C) and easy manufacturing shall be ensured.

To meet the above features, a conical support shell has been designed to support the priming tank. The conical support shell has been attached to the priming tank through a ring. The double envelope is also attached to the ring (Fig. 1). Inside diameter and shell thickness of the tank main shell are

750 mm and 8mm respectively. Outer diameter and thickness of the double envelope are 870 mm and 3mm respectively. Ring between the two concentric shells is 15 mm thick, the conical shell is 8 mm thick and flange is 20 mm thick.

This supporting arrangement was analysed for dead load and thermal loads during normal operation, fuel handling condition and SGDHR condition. Two governing events namely loss of steam water system occurring 47 times in design life (8.5 h for decay heat removal each time) and the offsite power failure occurring 160 times in design life (6.75 h for decay heat removal each time) were considered for the analysis. The operating time for the tank at 540° C during SGDHR is ~1480 h. Since this exceeds the creep cross over curve limit of RCC-MR (the curve which define the significance of creep), the junction was analysed for creep damage.

Finite Element analysis of the priming tank along with the double envelope and support shell and flange was carried out using CAST 3M. At first axi-symmetric thin shell element was used to arrive at the height of the cone and insulation so as to meet the stress limits of RCC-MR. The junction 'A' between ring and cone (Fig. 1) was found to be critical location, at which the maximum membrane and bending stresses are occuring for thermal loading under SGDHR condition. No variation in the primary stresses is expected, as the weight loading is not changing. However, the absolute value of primary membrane plus bending stress intensity (14 MPa) itself is small. The range of primary plus secondary stresses intensity is limited to 3.0 Sm (design code limit). Accordingly the height of the cone and height of insulated portion of cone from the junction were arrived at as 600 mm and 300 mm respectively.

After finalizing the height of the cone and insulation height the structure was modeled with 8 noded axi-symmetric solid elements to get the peak stresses at the junctions needed for creep-fatigue damage evaluation. The FEM model is shown in Fig. 2.

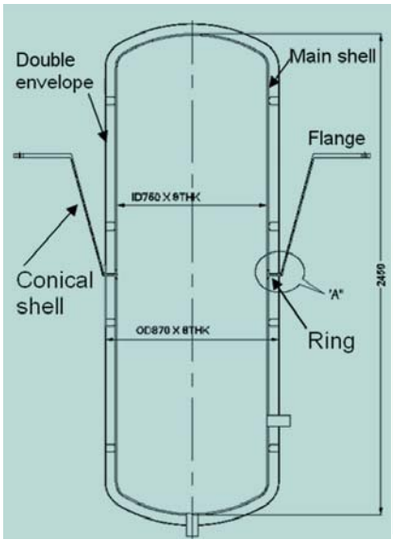

Fig.1
Priming Tank with Conical Support

The deflection pattern under thermal loading (SGDHR condition) is shown in Fig. 3. The peak surface stress intensity at the junction 'A' is found to be 148 MPa during SGDHR condition. The Von Mises stress distribution during SGDHR condition is shown in Fig. 4. The corresponding values during normal operation and fuel handling are 107 MPa and 48 MPa respectively. Considering 207 cycles between SGDHR and fuel handling the stress range (Δσ) is 100 MPa (148 -48). The elastic plus plastic strain range is evaluated based on the elastic analysis results as 0.11% as per RCC-MR procedure. The creep-fatigue damage was assessed at the junctions. For the design life of 40 years, the fatigue damage was found to be negligible and the creep damage at the junction of conical support shell to ring attached to main tank was found to be 0.074, which is acceptable. The structural integrity of proposed configuration was thus confirmed by analyses.

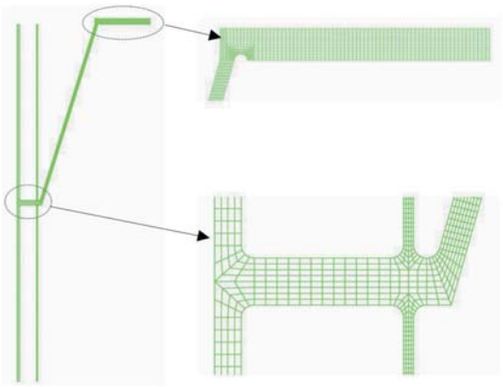

Fig.2
FE model using 8 noded Axisymmetric Solid Element (QUA8 element)

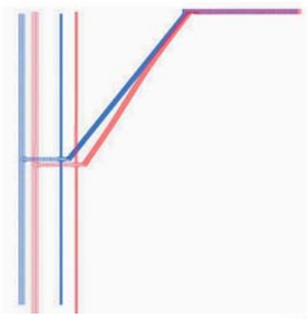

Fig. 3
Deflected Pattern under Thermal Loading

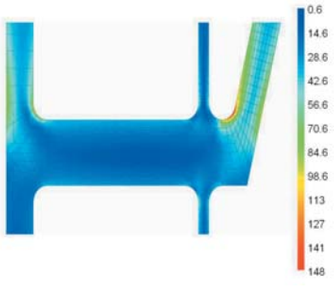

Fig. 4
Von Mises Stress Distribution (MPa) during SGDHR

III.12 Sodium Aerosol Dispersion Studies

PFBR design is such that design basis sodium leak events are possible only in the Steam Generator Building (SGB). During such leak events, sodium comes in contact with air and reacts immediately to form sodium oxides, which react with moisture present in the air to form sodium hydroxide almost instantaneously. Sodium hydroxide particles (generally referred to as sodium aerosols) react with CO_2 in air to form sodium carbonate particles. As sodium hydroxide can cause damage to human health, an assessment was made to find the concentration of sodium aerosol (in the form of NaOH) at the site boundary and within the plant due to sodium leak. Available literature supports the fact that concentration less than 2 mg/m^3 does not pose any health problem for repeated exposure for 8 h everyday for 40 y.

Sustained sodium burning inside SGB is possible only due to pool fire mode of sodium combustion. Spray fire mode of sodium combustion will be rare and its effect will be pronounced only for a short duration in the beginning and hence is not considered in the analysis. Rate of release of sodium aerosols from SGB depends on the burning rate of sodium (40 kg/h/m^2) in a pool fire, area of pool fire formed (1.2 m^2 for Category 2 and 3 leaks and SGB floor area for Category 4 leak), extent of aerosols formed (30% of combustion) and extent of aerosols deposited within the SGB (80 % of aerosols formed). With these values, rate of release of sodium aerosol is 1.4 g/s for Category 2 and 3 leaks and for Category 4 leak the same is 552 g/s. Many experimental studies prove that nearly 90 % of sodium hydroxide is converted to harmless sodium carbonate after 260 s at relative humidity greater than 50 %. In our study conversion to carbonate is considered as a first order reaction with a rate constant of 0.2 min^{-1}.

Gaussian Dispersion Model is used for estimating the aerosol concentration for plain, uninterrupted terrains, which are a few hundreds of meters away from the source (Fig.1).

With the additional term at the end for the carbonate conversion by first order reaction, the standard equation for the Gaussian Plume Dispersion becomes,

$$C(x,y,z)=\frac{Q}{2\pi\sigma_y\sigma_z u}\left\{\exp\left[\frac{-(z-h)^2}{2\sigma_z^2}\right]+\exp\left[\frac{-(z+h)^2}{2\sigma_z^2}\right]\right\}\left\{\exp\left[\frac{-(y)^2}{2\sigma_y^2}\right]\right\}\{\exp(-x/u\tau)\}$$

where τ is the time constant for the first order reaction of sodium hydroxide conversion to sodium carbonate in seconds.

It is observed from Fig. 2 that the aerosols get dilluted to 10^{-4} -10^{-5} mg/m^3 even for a category 4 leak at 1.6 km (site boundary). For Category 2 and 3 leaks, these values are even lesser in the range of 10^{-6} to 10^{-9} mg/m^3. Therefore, concentration of sodium hydroxide at the site boundary due to any sodium leak in SGB does not pose any safety concern.

The dispersion of sodium aerosols within the plant boundary depends to a large extent on the wind field, weather conditions and on the presence of intervening buildings and structures, especially for areas close to the point of release. Within the plant, the intervening buildings and structures alter the velocity field to a large extent. Therefore, a combination of Eularian Box Model for the 3-D velocity field and Monte-Carlo Particle Random Walk Model for the aerosols dispersion has been used for the estimation of the aerosol concentration field within the plant boundary.

The entire PFBR site and major buildings are brought into the models with a grid resolution of 60 by 60 by 20 with a mesh size of 10mx10mx5m. The 600mx600m area thus comprises of the site buildings plus an extra free space at the boundaries so that boundary conditions assumed for wind field are not significantly altered. For all calculations, a uniform wind speed of 1 m/s is considered.

The dispersion studies have been carried out for the release of sodium aerosols at 5 m, 10 m, 20 m and 30 m elevations from the ground and for five different wind directions – East to West, South to North, West to East, North to South and South-east to North-west. The last case has been studied because this is the case that gives maximum concentration around the Administrative Building, where the plant personnel are expected to assemble during any plant - emergency condition. Computations have been carried out for stable and unstable (turbulent) weather conditions also. A typical plume behavior for the west to east stable wind is shown in Fig. 3.

A summary result of the concentrations of sodium aerosols at various parts of the plant is given in Table 1.

Table 1. Concentrations of sodium aerosols at different locations due to Category 4 sodium leak in SGB

Point of Release	Wind Direction	Max. Concentration at Ground Level (mg/m3)				
		Security Gate 1	Security Gate 2	Canteen	Office	Admn. Building
5 m	East to West	232.6	1711	5.0	No impact	138
	South-East to North-West	0.08	8.86	235.2	No impact	1980
10 m	East to West	59.4	10.2	0.22	No impact	0.4
	South-East to North-West	No impact	0.06	13.4	No impact	40.8
20 m	East to West	1.2	0.002	0.01	No impact	0.0002
	South-East to North-West	No impact	No impact	0.0018	No impact	0.004

The ground level concentrations within the plant in several areas are much higher than the limiting values when the aerosols are released from the vents at 5m and 10m elevations. It is also observed that when the release point is at 20 m elevation or above, the maximum concentration in almost all the areas is well below the tolerable limits.

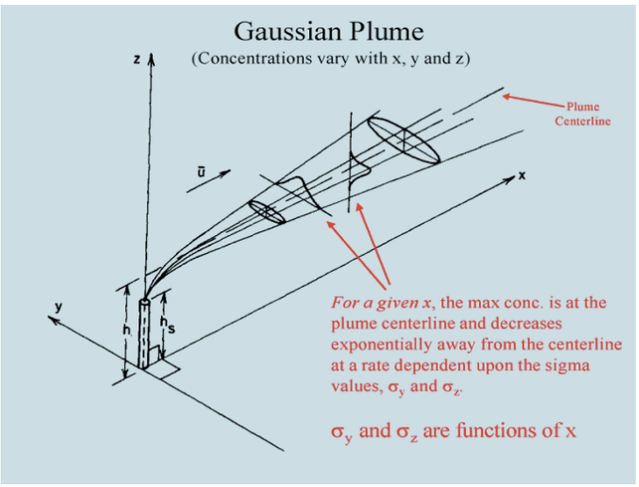

Fig.1
Gaussian Plume Behavior

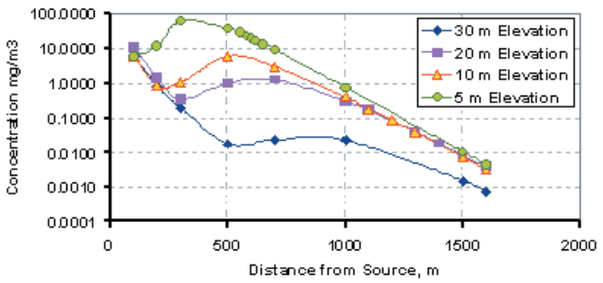

Fig. 2
Aerosol Dispersion in Open Terrain for 1 m/s Stable Wind

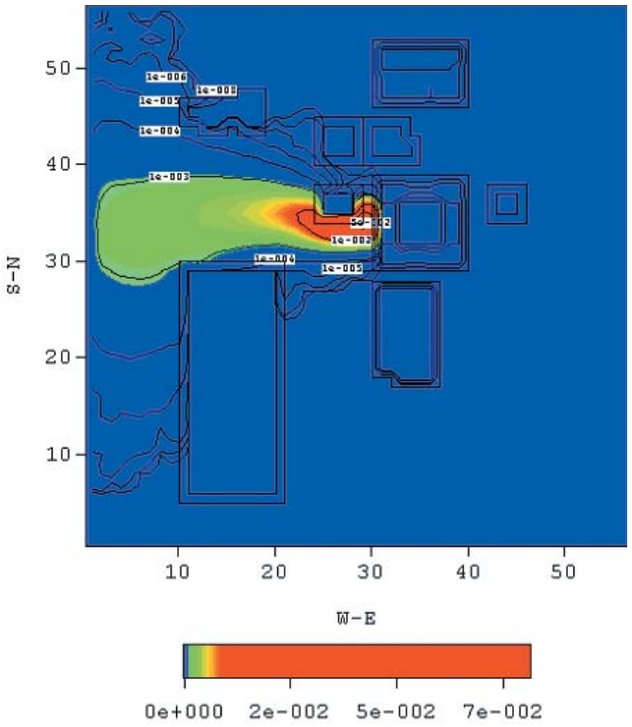

Fig. 3
Plume Dispersion and Contours for 1 m/s Wind Impinging on the Western Face of the PRBR Complex.

III.13 Evaluation of Wear, Friction and Self-welding Susceptibility of Mating Surfaces of Reactor Components in Flowing Sodium

In PFBR, there are many components with mating surfaces which are in static contact with each other for long duration or in relative motion in flowing sodium environment. Wear and friction data for some of these material combinations in flowing sodium were generated using indigenously developed reciprocating type tribometer installed in one of the sodium loops. The materials combinations so far tested include 316LN against 316LN, 316LN against NiCr-B hardfaced deposit, NiCr-B against NiCr-B, NiCr-B against Cr plating and aged alloy D9 against itself. Mating surfaces of these material combinations are encountered in various reactor components like grid plate, DSRDM, CSRDM, PSP, fuel subassemblies etc. The testing parameters were chosen to simulate the reactor operating conditions for these components. Table 1 gives the static friction coefficients for different material combinations. In general, friction coefficient is high for austenitic stainless against itself without any hard coating. The static friction coefficient is typically in the range of 0.2-0.7 and it is found to increase with increase in applied stress. In contrast, the material combinations in which at least one of the mating surfaces is hardfaced have much lower coefficient of friction, with μs typically below 0.1. Wear loss or damage observed in these material combinations were minimal. The results show that even the material combination in which only one of mating surfaces is hardfaced has very low friction coefficient compared to mating surfaces involving only austenitic stainless steels.

For evaluating susceptibility for self-welding, a separate set up was employed in which the mating surfaces were kept in contact under stress in flowing sodium. These tests were conducted for a duration of 3 and 6 months each and the stress level is chosen in such a way that tests of 3 month duration simulate the reactor operating condition and if no self-welding is observed at the end of this test, it can be concluded that the components with this pair of mating surfaces in contact in reactor environment is unlikely to self-weld. Studies conducted on annealed D9 and 20% cold worked D9 alloys (structural material for wrappers) showed that no self-welding occurs in the simulated reactor operating condition for these alloys. However, in the tests conducted for 6 months duration, one pair of 20% cold worked D9 alloy specimens exhibited self-welding as shown in Fig.1. The force required for separation of this pair was measured to be 196N in shear mode. Self-welding susceptibility of Cr plated 2.25 Cr-1 Mo Steel and Ni Cr-3 (Inconel 82) weld metal (material combination encountered in DSR and DSRDM), Specimens have also been evaluated and this material pair did not exhibit any self-welding in simulated reactor operating conditions.

Table 1: Friction coefficients in flowing sodium for different mating surfaces encountered in reactor

Material combination	Stress level (MPa)	Friction Coefficient (μ_s)
316LN vs. 316LN	10	0.18
316LN vs. 316LN	40	0.7
NiCr- B vs. NiCr -B	10	< 0.1
NiCr-B vs. NiCr -B	11	< 0.05
NiCr- B vs. Cr-plating	6	0.12
Aged D9 vs. Aged D9 alloy	3.5	0.65

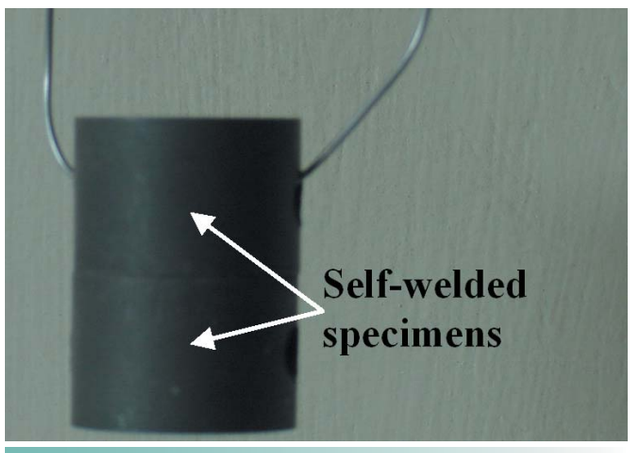

Fig.1
Cold Worked Alloy D9 Specimens in Self-welded Condition

III.14 Database of Events in Various Sodium Rigs towards Knowledge Management

During the past twenty five years various sodium loops have been in operation in the Fast Reactor Technology group. During this period many events have taken place in these loops. The causes for most of the events may be attributed to failure of certain components, which form part of the respective systems like instrumentation or electronics parts, electrical systems, or mechanical components. Some of the incidents had also occurred due to other operation related causes. Of the above events sodium leak events are important from safety point of view. It was observed that most of the sodium leak events were due to bellows failure in bellows sealed valves.

Taking into consideration the importance of the events and to make available the data for operation of sodium loops in an effective and efficient manner, a database of events was prepared. As a head start to the campaign in preparing the database, reports on individual events were prepared. Subsequently the data were classified under various headings, such as Sodium leak events, Instrumentation events, Electrical events and Mechanical events.

A web page with the above events has been designed. The home page of the events database consists of names of different loops placed in links. On navigating further through these links another page consisting of buttons named with different types of events is displayed. Next page displays a list of events. On navigating further details about the individual events are displayed. A search engine has been made ready for accessing the above database. A box diagram showing the details of the event database is given in Fig.1.

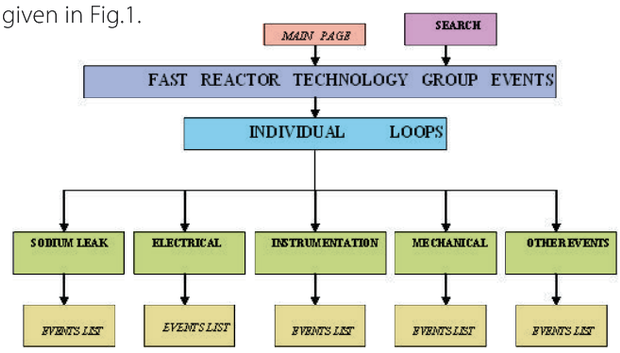

Fig.1.
Database of Events

III.15 Thermal Decomposition and Kinetic Analysis of Sodium Alkoxides

Components exposed to liquid sodium in coolant circuits of Fast Reactors get wetted with sodium. As a consequence, they need to be cleaned free of sodium when removed from coolant circuits for periodic maintenance or replacement. As sodium reacts aggressively with moisture and oxygen present in air, careful handling and safe cleaning procedures are required to avoid any possible damage to men and material. Generally, water vapour-nitrogen (WVN) process and water vapour-carbon dioxide process are preferred for cleaning large components like pumps, IHX, storage tanks etc. Alcohols like methanol, ethanol, propanol etc. are widely used as cleaning agents for small components such as bellow sealed valves, gripper tools, sampling devices and impurity monitoring devices etc., while long chain alcohols such as butyl cellosolve (2-butoxy ethanol) and ethyl carbitol (2, 2' ethoxy ethoxy ethanol) were used in certain cases in countries like France and Germany for disposing residual quantities of sodium in tanks. The run-away reaction leading to accident reported in literature when ethyl carbitol was used for sodium cleaning purpose was postulated to be due to the thermal instability of the reaction product of sodium and ethyl carbitol. As low

molecular weight alcohols are employed for sodium cleaning of small components at IGCAR, the thermal stability of sodium alkoxides namely sodium methoxide, sodium ethoxide, sodium n-propoxide and sodium iso-propoxide were studied.

Sodium alkoxides were prepared by reacting sodium metal with excess alcohol and subsequent separation of pure sodium alkoxide by distilling off the excess alcohol. The formation and purity of the sodium alkoxides prepared were confirmed by IR spectroscopy and X-ray powder diffraction studies while the chemical assay was determined by atomic emission spectroscopy and elemental analysis. Typical IR spectrum and XRD pattern of sodium ethoxide are shown in Figs.1 and 2. Absence of spectral features around 3500 and 1600 cm^{-1} region clearly shows that the sodium ethoxide prepared is free of alcohol and moisture. The XRD patterns of these compounds matched well with those reported in the literature thereby confirming the formation as well as the purity of sodium methoxide and ethoxide used in the present study.

Thermal decomposition of these sodium alkoxides was studied using a thermogravimetric analyzer coupled with quadrupole mass spectrometer under non-isothermal and isothermal conditions. Typical decomposition of sodium ethoxide at a heating rate of 5 K min^{-1}, giving rise to various gaseous products is shown in Fig. 3.

Kinetic parameters, namely, activation energy and pre-exponential factor were deduced from the dynamic TGA and MS data. The activation energies were derived from isothermal runs for sodium methoxide, sodium ethoxide, sodium n-propoxide and sodium iso-propoxide and these values were found to be in close agreement with the values derived from the non-isothermal runs. On decomposition, sodium alkoxides form gaseous products of saturated and unsaturated hydrocarbons leaving behind residue consisting of sodium carbonate, sodium hydroxide and free carbon.

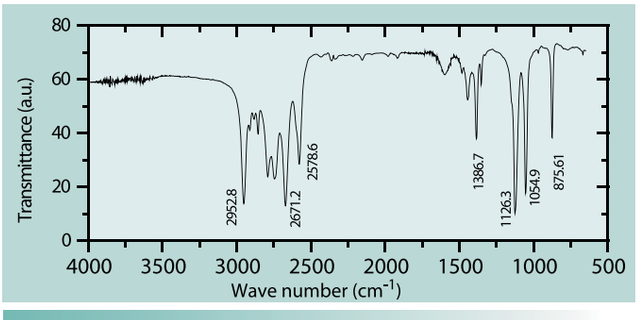

Fig.1
IR Spectra of Sodium Ethoxide

From all these observations the possible decomposition reaction for the sodium alkoxide involving low molecular weight alcohols can be written as follows.

$RONa \rightarrow m\ Na_2CO_3 + x\ C + 2m\ NaOH + y\ C_nH_{2n+2} + z\ C_nH_{2n}$

where m, x, y, and z are the number of moles of the species involved; n is the number of carbon atoms present in the hydrocarbon; x = 1.5, 2, 4 and 5 for the decomposition of the methoxide, ethoxide, n-propoxide and iso-propoxide of sodium respectively. R represents methyl, ethyl, normal and iso-propyl group.

Thermal decomposition of sodium methoxide, ethoxide, n-propoxide and iso-propoxide starts above 573 K. The decomposition temperature is well above the boiling point of alcohols and melting point of sodium (normally sodium cleaning carried out below the melting point of sodium). Hence, this study demonstrates that low molecular weight alcohols can be safely used for sodium cleaning purposes. Any unexpected temperature raise up to 550 K during sodium cleaning process, due to exothermic reactions caused by accidental conditions would not lead to thermal decomposition of the reaction products and consequent run-away conditions.

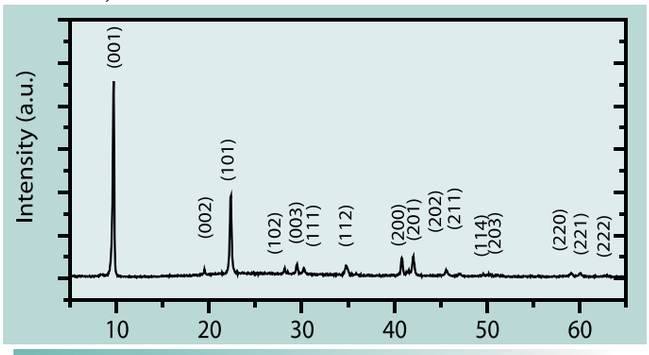

Fig.2
X-Ray Diffraction Pattern of Sodium Ethoxide

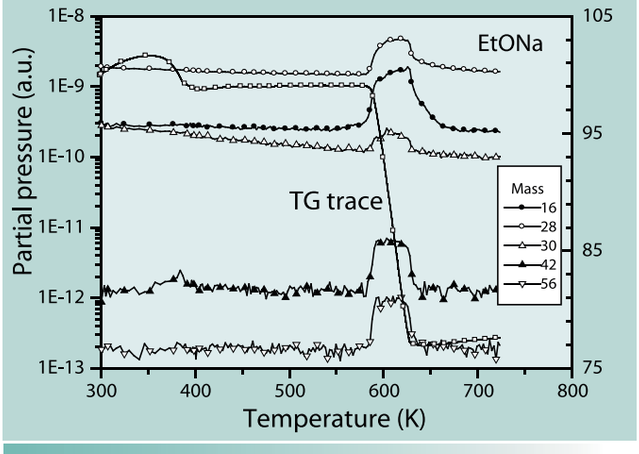

Fig.3
Typical TGA-MS Curve for Decomposition of Sodium Ethoxide at a Heating Rate of 5 K min^{-1}

CORE AND STRUCTURAL MATERIALS

III.16 Fracture Toughness Evaluation of an Indigenous SS 316(N) Weld

Consumables for welding the SS 316L(N) components of PFBR have been developed indigenously at IGCAR. In view of the embrittlement of the weld metal on extended thermal ageing, a detailed study has been undertaken to characterize the quasistatic *J*-R curves for the indigenously developed SS 316(N) weld material at both ambient and service temperatures and also to assess its degradation after simulated service exposure. The results for the test temperature 643 K after prior "advanced" ageing condition according to the RCC-MR design code , i.e, > 4000 h at 923 K are presented.

Quasistatic fracture tests were conducted using 10 mm thick CT specimens of SMA welded SS 316(N) thermally aged for 4200 h at 923 K The *P*-LLD plots (Fig.1) showed clear evidence of pop-in crack extensions. However, these were not significant as per ASTM E 1820-01 standards and could be ignored for multiple specimen (MS) data analysis. The J_{nom}-Δa curve obtained using MS method of data analysis is given in Fig.2. For the initial crack blunting line, $J/(\sigma_f \Delta a) = 2$ has been used in this study. The data fit to a power law $J_{nom} = C.\Delta a^n$ with C = 308 ± 6 and n = 0.47 ± 0.02. Even though the number and disposition of the data generated do not conform to the requirements of the ASTM multiple specimen method, the constants C and n are well-determined. The value of $J_{0.2}$ obtained from this plot is 243 ± 8 kJ.mm^{-2}.

The single specimen normalization method (SSN) is attractive in that a single test is adequate and on-line crack length measurements are not necessary, which considerably reduce the test burden in terms of number of specimens or complexity of testing, and yet reliable J-resistance curves can be established. Therefore, SSN was explored for estimating $J_{0.2}$, using the results from multiple specimen analyses as objective assessment criteria. However, since the ASTM E1820-01 prescription for SSN method does not deal with the issue of pop-in crack extension. Therefore, one of the two alternative methods developed in-house for such cases was used. This assumes a vanishingly "small" pop-in crack extension, in the context of development of crack tip plastic zone during loading immediately following a pop-in event. In this case pre- and post-pop-in crack tip plastic zones must match, and the J-resistance curve should be continuous, with possible local disturbances for pop-ins. The MS analysis too, implies continuity of J - Δa plots, which corresponds to this small pop-in crack growth assumption. Figure 3 (a) shows typical plots of P_N - v_p / W obtained using the above procedure; the discontinuity in these plots is a measure of the deviation from the "vanishingly small" assumption. The P_N - v_p / W data, excluding the segment clearly identifiable with transient following pop-in crack extension, is used for obtaining the *J* - Δa curves, Fig. 3 (b). It may be noted that the specimen-to-specimen scatter in Fig. 3(a) are not reflected in Fig. 3(b). The *J* values for different extents of crack growth from each of these four single specimen *J* - Δa curves are given in Table 1. Generally, for fixed Δa levels, the data fall within a scatter band of ± 5%. These are also similar to the corresponding J_{nom} values determined using the multiple specimen method up to 1.5 mm crack growth. These results confirm the viability of the method developed here for *J* estimation procedure for the case of data showing "small" pop-in crack extension behaviour.

The *J* values obtained in this study are much higher than those indicated in RCC-MR design documents; in this document, for this class of welds in the advance aged condition, the *J* values at 643 K are given as 40 and 105 kJ.m^{-2} for 0.2 and 1.0 mm crack growth respectively. However, it may be noted that RCC-MR uses $J/(\sigma f.\Delta a) = 4$ for the crack tip blunting. Even if this value were to be used, $J_{0.2}$ would have been obtained as ≈ 180 kJ.m^{-2}, significantly higher than the RCC-MR value. The excellent fracture toughness of the weld even after advanced ageing is attributed to the high cleanliness of the indigenous weld.

Table 1: *J* values from SSN and J_{nom} from MS analyses.

	J values (kJ.m^{-2}) for crack growth in mm				
Sl. No.	**0.2**	**0.5**	**1.0**	**1.5**	**2.0**
1	245	312	365	413	435
2	250	339	386	-	-
3	253	290	-	-	-
4	252	339	401	427	-
J_{nom}	243	310.5	390	452	504

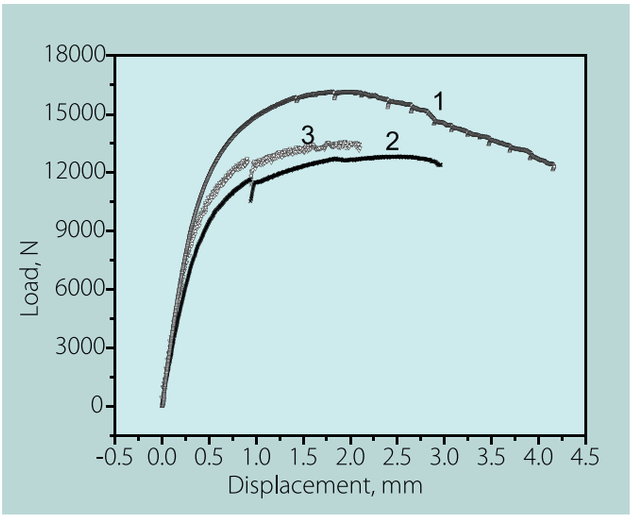

Fig.1
Plots of Load (P) versus Load Line Displacement (LLD) for the Ramp tests. (In all cases, sudden load drops corresponding to pop-in crack extensions are observed.)

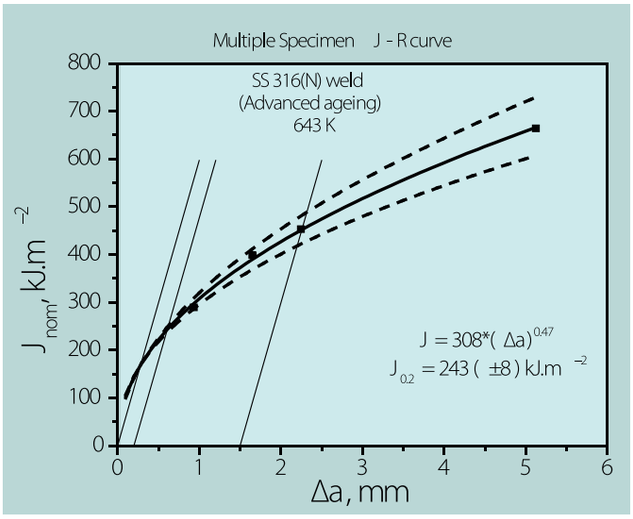

Fig.2
The J_{nom}-Δa curve from Multiple Specimen Data Analysis. The blunting lines are also shown. The solid line represents the fitted curve indicated in the graph and the dotted lines, the 95% confidenceinterval for the fit.

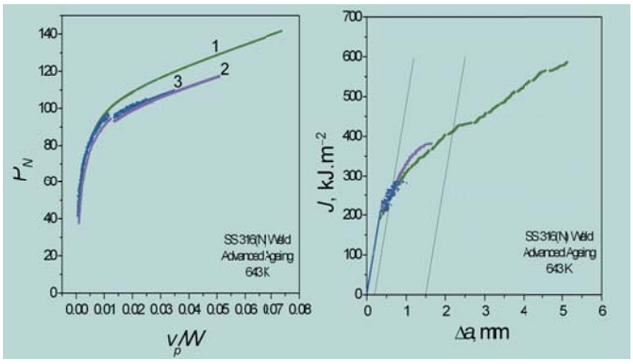

Fig.3
(a) Plots of v_p-P_N Corrected for Crack Extension from Normalization Method Modified with Small Pop-in Assumption. (b) Single specimen J-R curves obtained using normalization method with "small" pop-in assumption for all the four tests.

III.17 Dynamic Fracture Toughness Based Reference Temperature Evaluation of Indigenously Developed Modified 9cr-1Mo Steel

Mod.9Cr-1Mo steel is one of the candidate wrapper materials for achieving high burn up (>2,00,000 MWd/t) owing to its excellent resistance to irradiation induced long term void swelling, dimensional stability and high thermal conductivity. However, the transition does not depend on temperature of fracture mode and irradiation induced rise of the transition temperature is a matter of concern, especially under dynamic/accidental loading scenario during spent fuel handling operation. Thus it is important to characterize the material's fracture behaviour in the transition temperature regime under dynamic loading conditions. It is also appreciated that the material undergoes cold working during fabrication processes and its influence needs to be assessed to fix the maximum limit of allowable cold work in terms of shift in ductile-brittle transition temperature.

In this study, the ductile-brittle transition temperature of an indigenously developed modified 9Cr-1Mo steel in 0%, 5%

and 10% cold worked conditions (CW) has been characterized in terms of ASTM E-1921 based reference temperature (T_0) approach. T_0 is defined as the temperature at which the median fracture toughness (cumulative probability of failure = 0.5) of 100 MPa.m$^{0.5}$ is obtained for specimens of one inch thickness equivalence. T0 however is defined for quasi-static loading conditions. In this study the concept has been extended to high loading rate scenario by obtaining dynamic fracture toughness data from instrumented pre-cracked Charpy testing. The corresponding reference temperature thus determined, designated as T_0^{dy}, was evaluated to be 14 °C at a loading rate of 5.12 m/s. This is much higher than the corresponding T_0^{dy} of plain 9Cr1Mo steel, evaluated as -52 °C. Figure 1a and 1b show the differences in crack initiation mechanism for modified 9Cr-1Mo steel and plain 9Cr-1Mo steel. Where an embrittlement induced grain boundary decohesion is observed for the modified steel (Fig.1a), the matrix-carbide decohesion mechanism has been identified for the plain 9Cr-1Mo steel (Fig.1b). The result is attributed to the higher embrittlement susceptibility of the present modified 9Cr-1Mo steel owing to high P concentration. P segregation at the prior austenitic grain boundaries has been confirmed SIMS study, the result of which is described in Fig.2. Experimental results also show that the cold working for this modified 9Cr-1Mo steel does not affect the T0dy to a significant extent

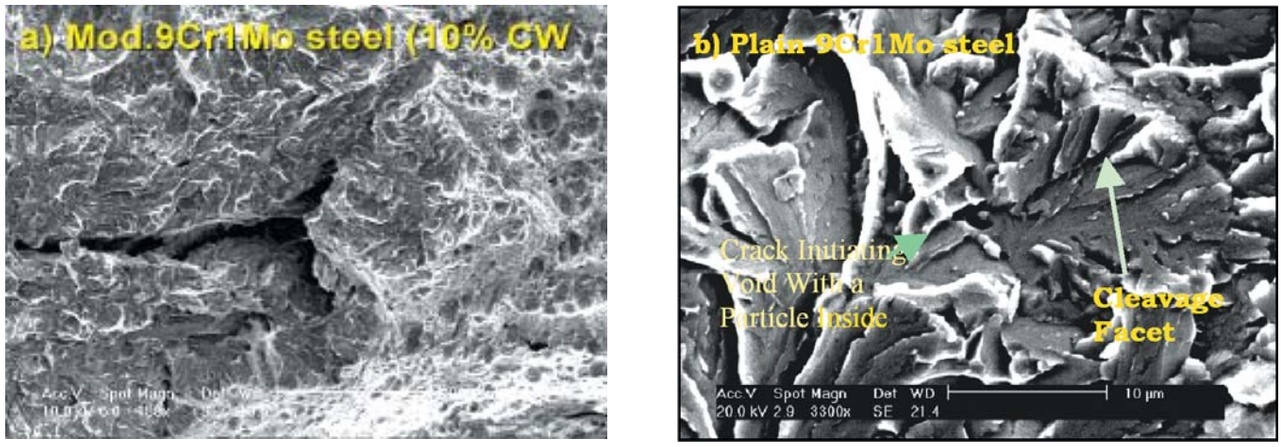

Fig.1
a) Crack Initiation at Modified 9Cr-1Mo Steel by Grain Boundary Decohesion.
b) Crack initiation at plain 9Cr-1Mo steel by carbide-matrix decohesion.

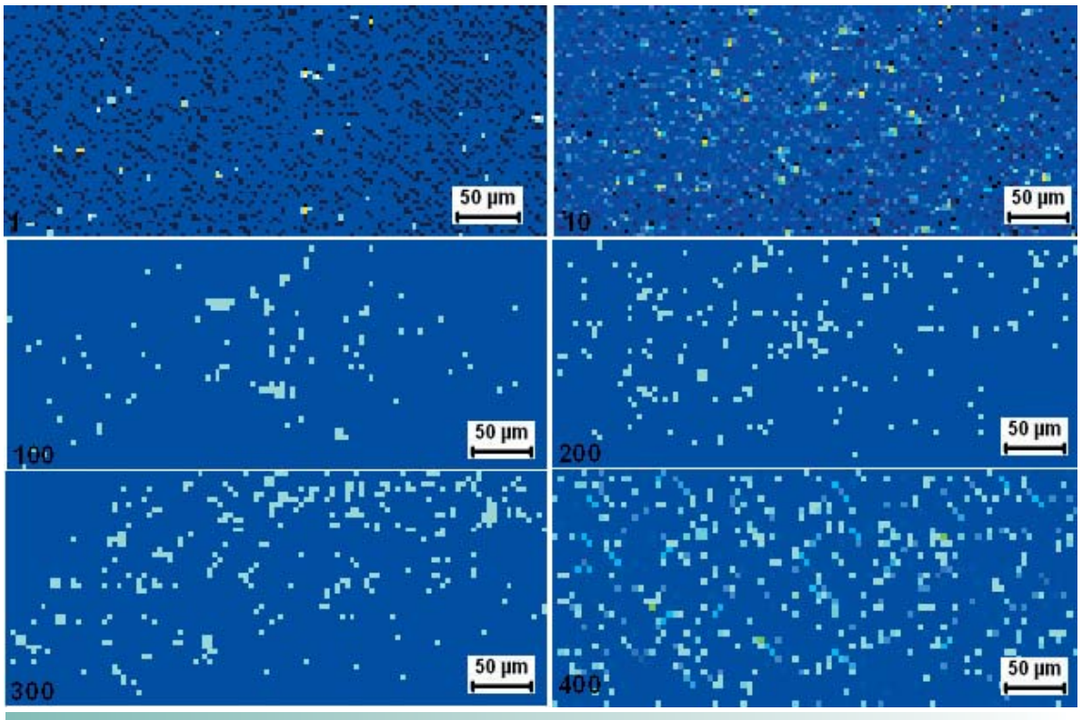

Fig.2
SIMS Results Showing P-segregation at Prior Austenitic Grain Boundaries of 0% CW Mod.9Cr-1Mo Steel

III.18 Creep Properties of Advanced Stainless Steel

The core structural materials chosen for fuel clad and wrapper of PFBR is 20% cold worked alloy D9 stainless steel for the initial core. Creep tests were conducted on alloy D9 clad tubes produced by Nuclear Fuel complex at Hyderabad, (NFC tubes) at 923 K and 973 K and in the stress range 100-250 MPa and the results are compared with those of clad tubes imported from M/s.Valinox, France. Valinox tubes crept at a lower rate than NFC tubes at all these test conditions. The creep rates were nearly one order of magnitude lower than those obtained for NFC tubes. A power law relation $\varepsilon_s = A\sigma^n$, where is ε_s the steady state creep rate, σ is the applied stress, n is the stress exponent, and A is an empirical constant) was found to be obeyed between applied stress and minimum creep rate by both the materials. The power law creep equations are given below.

For NFC tubes

$\dot{\varepsilon} = 1.05 \times 10^{-31} \sigma^{9.8}$ at 923 K

$\dot{\varepsilon} = 5.65 \times 10^{-22} \sigma^{6.3}$ at 973 K

For Valinox tubes

$\dot{\varepsilon} = 2.63 \times 10^{-34} \sigma^{10.6}$ at 923 K

$\dot{\varepsilon} = 6.1 \times 10^{-30} \sigma^{9.2}$ at 973 K

Rupture life of Valinox clad tubes is better than that of NFC tubes by a factor of about ten at stress levels below 200 MPa and by a factor of about six at stress levels above 200 MPa A power law relationship was found to be obeyed between applied stress and rupture life. (Figs 1(a) and 1(b). In general, ductility was very low (<15%). Rupture ductility of NFC clad tubes was generally higher than Valinox tubes.

Metallographic investigations were carried out on Valinox clad tubes and NFC tubes to estimate the grain size (in the longitudinal and transverse directions). The grains were not equiaxed since the tubes were finished in 20% cold worked condition. The aspect ratio of the grain size (ratio of the longitudinal length to transverse length) was 1.21 and 1.36 for NFC and Valinox tubes respectively. A lower value of the aspect ratio is generally indicative of lower degree of cold work. Hence the lower life exhibited by NFC clad tubes can be attributed to the lower amount of cold work. Inclusion content was estimated for NFC and Valinox tubes. Only globular oxide type (D) inclusions were present in both the tubes. The corresponding Estimation of ASTM number for these inclusions are <1 for Valinox tubes and 1.5 for NFC tubes.

For future cores of PFBR, a modified composition of alloy D9 (with phosphorus, titanium and silicon additions) known as D9I, is considered in the light of international experience. Alloy D9I composition is derived keeping the basic composition of alloy D9 with additions of phosphorus (0.025 and 0.04) and silicon (0.75 and 0.95) and titanium (0.16, 0.2, 0.24 and 0.3). Fifteen heats of this material were produced by Midhani, Hyderabad. The creep properties are being evaluated at 973 K in the stress range 175-250 MPa on these heats. Creep tests have been completed at 973 K /250 MPa in the on the heats with P 0.025, Si 0.75 and Ti 0.16, 0.20, 0.24, and 0.30. The heat with higher titanium content of 0.3, exhibited higher creep rates and lower rupture lives than the other heats with lower titanium contents. (Figs. 2 (a) and 2(b). Based on the mechanical properties evaluated, the composition of D9I in terms of P, Si and Ti will be optimized.

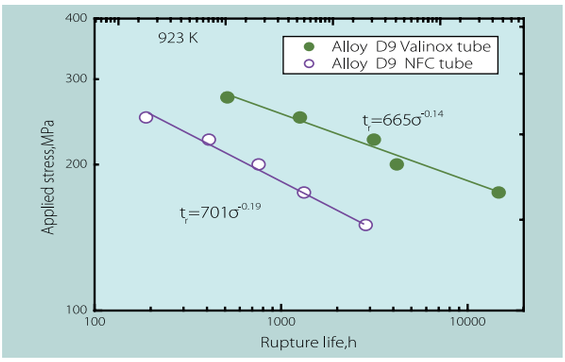

Fig.1 (a)
Relationship Between Applied Stress and Rupture Life of Valinox and NFC Tubes at 923 K.

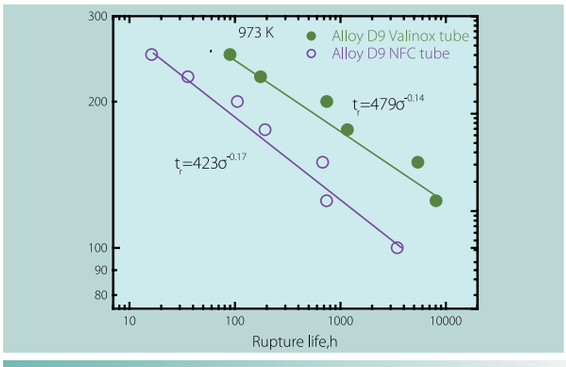

Fig.1 (b)
Relationship between Applied Stress and Rupture Life of Valinox and NFC Tubes at 973 K.

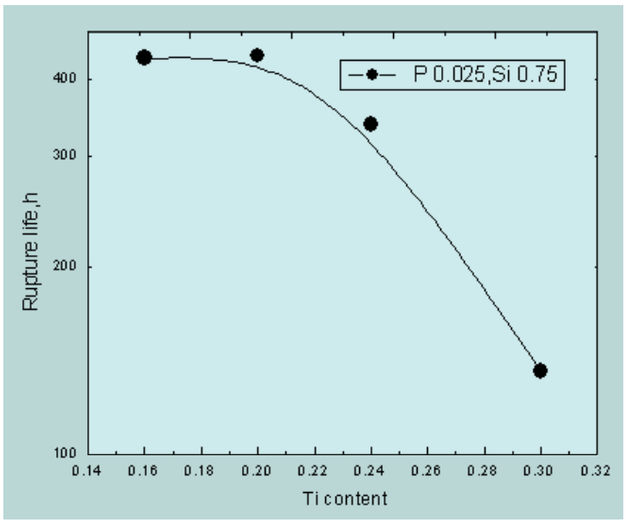

Fig.2 (a)
Increase in Minimum Creep Rate with Titanium Content.

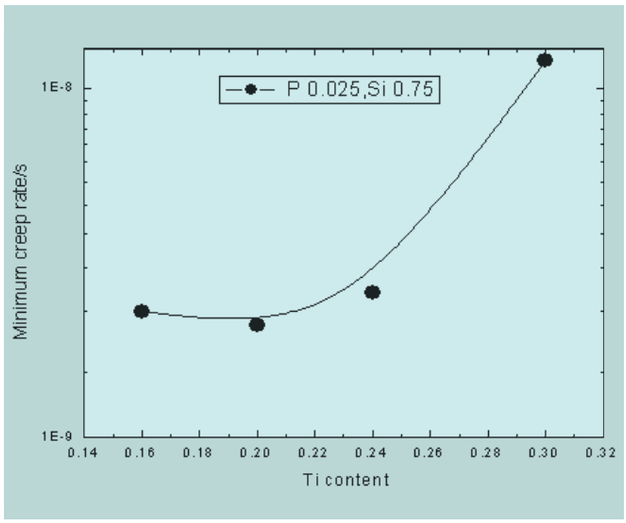

Fig.2 (b)
Decrease in Rupture Life with Titanium Content.

III.19 Low Cycle Fatigue and Creep-Fatigue Interaction Behavior of Indigenous Modified 9Cr-1Mo Ferritic Steel and its Weldment

Modified 9 Cr-1 Mo steel, a modified version of plain 9 Cr-1Mo ferritic steel with the alloy addition of niobium and vanadium is used extensively as structural material for steam generator components of FBRs and fossil fired power plants. It is observed that even though the base material has superior creep rupture property compared to other low alloy steels, many in-service problems are associated with weld joints due to the mismatch in the creep behavior of the parent material, the weld metal and the heat affected zone (HAZ). The HAZ is made up of a number of relatively narrow sub-regions, which have different creep strengths. This leads to complex stress distribution and complex states of stress is set up locally which has a great influence on the accumulation of creep damage and on the subsequent failure of the weldment. This mode of failure is known as type IV cracking and is associated with relatively large strains taking place within a very localised region of the HAZ known as the intercritical region. Apart from the strain localization in the fine grained HAZ, microstructural degradation such as coarsening of the carbide precipitates and sub-structural changes such as formation of cells/subgrains from the martensitic laths also occur.

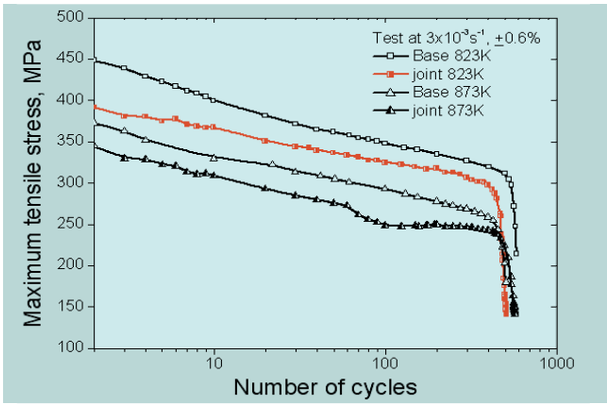

Fig.1
Comparison of Cyclic Stress Response of Base and Weld Joint

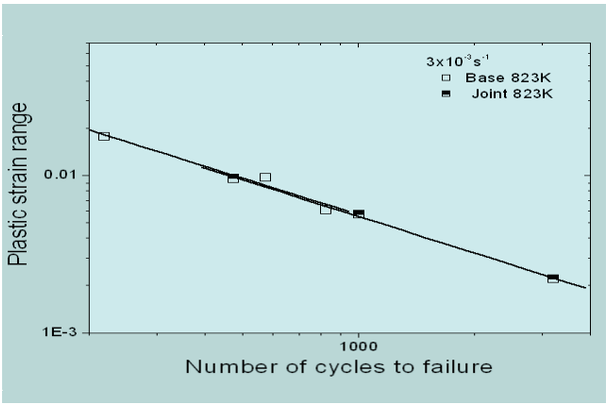

Fig.2
Strain-life Plot Showing Comparison Between Base and Weld Joint

Studies on the evaluation of low cycle fatigue and creep-fatigue interaction behavior of modified 9 Cr 1Mo ferritic steel weldments are relatively scanty compared to the vast data available on the creep behavior of this alloy. In view of this, an attempt has been made to further the current understanding on the low cycle fatigue and creep fatigue interaction behavior of weld joints and base material of modified 9 Cr-1 Mo ferritic steel. Low cycle fatigue tests were carried out on both base material and welded joints of the P91 material at 773, 823 and 873 K at strain rate 3 x 10^{-3} s^{-1}, employing various strain amplitudes. Post-weld heat treatment was done on the weld joint at 1033 K for 3h followed by air cooling.

Fig.1 shows continuous cyclic softening from first cycle onwards during all the tests in both weld joints and the base material. The overall stress response decreased with increase in temperature at all strain amplitudes employed during the test for both base and joint.

Fig.2 shows the comparison of base and joint data on a strain-life plot and Fig. 3 for the weld joint at three temperatures 773K, 823K and 873K. The creep-fatigue interaction data are also plotted in Fig. 3 for comparison with the continuous cycling condition. At 823 K there was not much difference in fatigue life between base metal and weld joint. Application of hold in either tension or compression side led to a life reduction. Almost all the specimens of the weld joints tested under continuous cycling or under the application of hold fractured in the weld heat affected zone. Compression hold was found to be more damaging than the tension hold condition at both 823K and 873K. The lower life under compression hold has been attributed to the deleterious effect of oxidation.

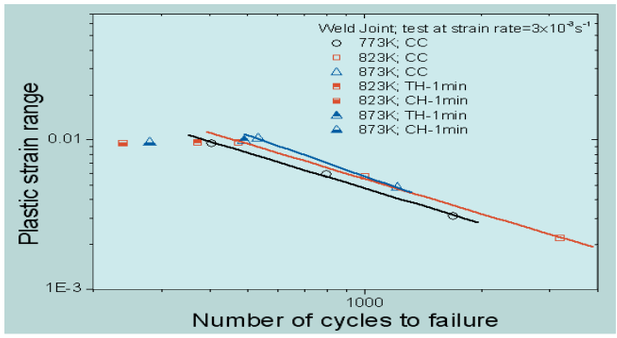

Fig.3
Coffin - Manson Plot showing Strain-Life Relation at Three Temperatures.

III.20 Prediction of Formation and Prevention of Hard Zone in Dissimilar Weldments of Ferritics

Exposure of dissimilar weldments of ferritic steels to elevated temperature results in the formation of undesirable "hard" brittle zone at their interface. Diffusion of carbon from low Cr steel to high Cr steel aided by the chemical potential gradient is responsible for the above process. The 'hard' brittle zone on the high Cr side and 'soft' precipitate free zone on the low Cr side of the weldment are susceptible to failure under cyclic loading conditions. Hence, methods have to be identified to predict their formation and prevention.

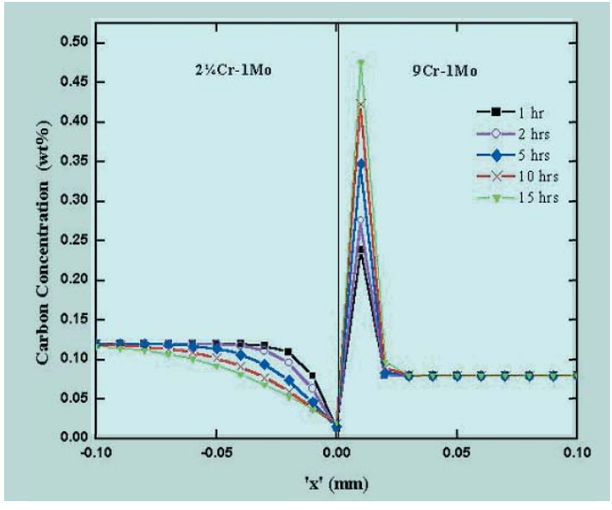

Fig.1
Simulated Carbon Concentration Profiles For PWHT at 1023 For 1 to 15h ('X' – Distance)

In the present work a theoretical model based on the finite difference technique was developed to simulate the diffusion profiles of all elements at high temperatures and identify various elements which if introduced, can prevent the formation of hard zone and also to evaluate the effectiveness of one such barrier, Ni between joints of 9Cr-1Mo and 2¼Cr-1Mo ferritic steel. The calculations were further extended to optimize the thickness of the chosen diffusion barrier, i.e., Ni to prevent the formation of deleterious zones, which was experimentally confirmed.

To determine the flux of the diffusing element one

dimentional diffusion equations were set up using Fick's second law. Using Schmit's method, these differential equations were transformed to finite differential equations using a one dimentional grid of mesh points in space 'x' and time't'. The mesh points were assumed to be separated by a space increment of Δx and time increment Δt. A computer program was written to solve the numerical equations. Fig.1 shows the simulated carbon concentration profiles assuming post weld heat treatment of the dissimilar weldment at 1023 K for 1 to 15h. It is shown clearly that there is a carbon enriched zone on the high Cr side (9Cr-1Mo) and a carbon depleted zone on the low Cr side (2¼Cr-1Mo) of the weldment. The profile agrees very well with the experimental observation that maximum carbon content in the hard zone is ~0.47wt%.

The calculation was also extended to predict possible alternate elements other than Ni which could act as diffusion barriers for carbon. It was found that a 40 μm thick Cu interlayer (ξc^{Cu}= +3.5) or 60mm thick Co interlayer (ξc^{Cu}= +2) is sufficient to prevent the formation of hard zone in dissimilar weldments of ferritic steels.

The calculation of diffusion profiles was extended to evaluate if the introduction of a Ni based Inconel interlayer of various thicknesses could prevent diffusion of carbon across the fusion boundary. Ni has a positive interaction coefficient with carbon (ξc^{N}= +2) which means there is a repulsive interaction between the Ni and C. In the presence of a Ni interlayer the driving force for the diffusion of carbon is reduced as a large activation energy barrier exists at the interface. This in turn prevents the formation of soft and hard zones on exposure of the weldments to high temperature. Calculations were performed for various thickness of the Ni interlayer and Fig.2 shows the variation of maximum carbon content in the hardzone with the thickness of the interlayer. From the plot the optimum thickness of the Ni interlayer to be introduced between the ferritic steels to avoid the formation of hardzone was found to be 80 μm.

To validate the predictions of the computational studies transition joints were fabricated in the form of bead on plate welds with different thickness of Inconel 182 (66% Ni) interlayer and then subjected to heat treatment at 1023K for 1 to 15h. Experimental observations (Fig.3) also confirmed that formation of hard and soft zones is effectively prevented in dissimilar weldments of ferritic steels if a Ni based interlayer is used.

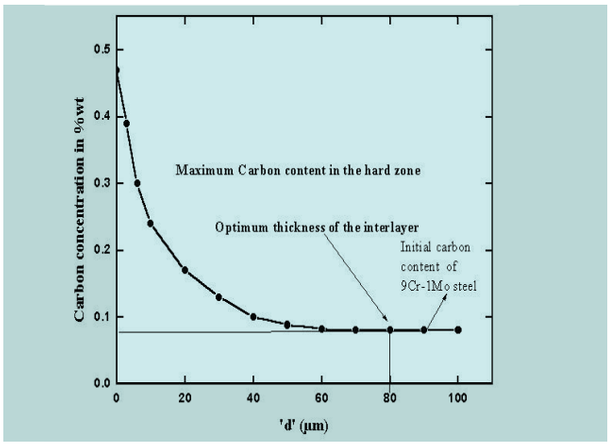

Fig.2
Variation of Maximum Carbon Content in the Hard Zone with Increase in the Thickness 'd' of the Interlayer.

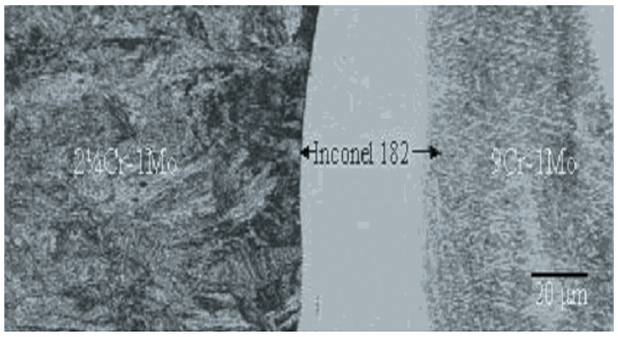

Fig.3
Optical Micrograph Showing the Absence of Hard and Soft Zones in Dissimilar Weldments of Ferritic Steels with Inconel Interlayer After PWHT at 1023 K for 1h.

III.21 High Temperature Low Cycle Fatigue Properties of Indigenous 316(N) Weld Metal and 316L(N) / 316(N) Weld Joints

316L (N) austenitic stainless steel is the material chosen for the primary components in FBRs due to its excellent high temperature mechanical properties and compatibility with liquid sodium. The high temperature components of PFBR are subjected to temperature gradient induced thermal stresses, which are cyclic in nature as a result of start-ups, shutdowns and transients. Further, steady state loading at elevated temperatures in combination with cyclic loading leads to Creep Fatigue Interaction damage. Low Cycle Fatigue behavior of indigenous 316L(N) \ 316(N) weld joints and 316(N) weld metal are studied in the temperature range 773 K - 873 K. Fully reversed total axial strain-controlled LCF tests were conducted on weld metal and weld joint specimens, using a servo hydraulic machine, equipped with a radiant heating furnace. Tests were conducted at strain amplitudes of + 0.4 %, + 0.6 % and + 1.0 %, at a constant strain rate of 3 x 10^{-3} s^{-1}. The typical cyclic stress response behaviour of the base, weld and weldment is shown in Fig.1. Weld metals displayed a gradual softening regime for the major portion of the life after a brief period of hardening. The gradual softening has been attributed to break down of dislocation tangles and subsequent annihilation of dislocations of opposite sign in to and fro motion during cycling. Weld joints exhibited initial hardening followed by a continuous and gradual softening regime, except at low strain amplitudes. Initial hardening is similar to that observed in 316L(N) base metal, though the degree of hardening is less. This seems to be justifiable since major part of the gauge length is made up of base metal. At all the testing conditions, weld joints showed lower fatigue lives compared with weld metal, (Fig.2). This can be ascribed to the microstructural influence on the fatigue crack initiation and crack propagation. Crack initiation and propagation was found to be transgranular at all testing conditions, in both weld metal and weld joints. Crack initiation in weld joint occurred in coarse-grained HAZ. Though the observed crack initiation in both weld metal and weld joint was transgranular, there exists significant differences in crack propagation that display profound influence on their fatigue life. In austenitic stainless steel welds, the delta ferrite intentionally introduced to reduce their tendency to hot cracking and microfissuring gets transformed to a hard and brittle sigma phase when these materials are exposed to elevated temperatures, 773 to 1173 K, for extended periods of time. The fine duplex austenite-ferrite micro-structure of weld metal, with its many transformed phase boundaries during testing, offers greater resistance to the extension of fatigue cracks by causing deflection of the crack path, resulting in reduced stress intensity at the crack tip and an associated reduction in the crack propagation rate. In the weld joints, the resistance to transgranular crack propagation in HAZ is less due to its coarse-grain size, i.e. the larger the grain size the less is the number of crack-arrest events that causes the crack front to be held back and necessitates the crack initiation phase to occur in the adjacent grain. It has been well established that larger grain size leads to a faster crack propagation rate under LCF deformation. Comparison of the fatigue life of the weld metal and weld joints generated at IGCAR, with the fatigue curve in RCC-MR code indicate that these lives fall within the scatter band. Hence it is concluded that RCC-MR design curves can be safely used for design purposes.

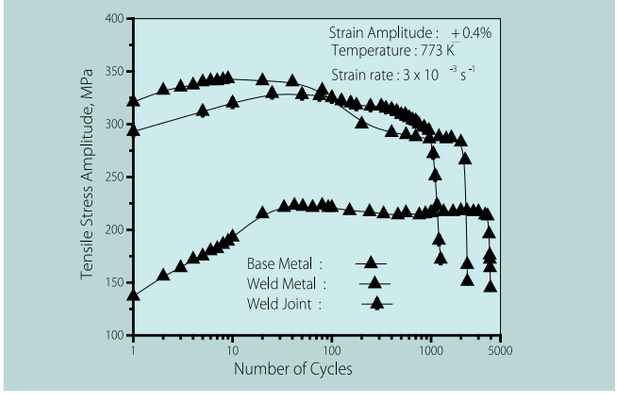

Fig.1
Cyclic Stress Responses of Base Metal, Weld Metal and Weld Joint at 773 K.

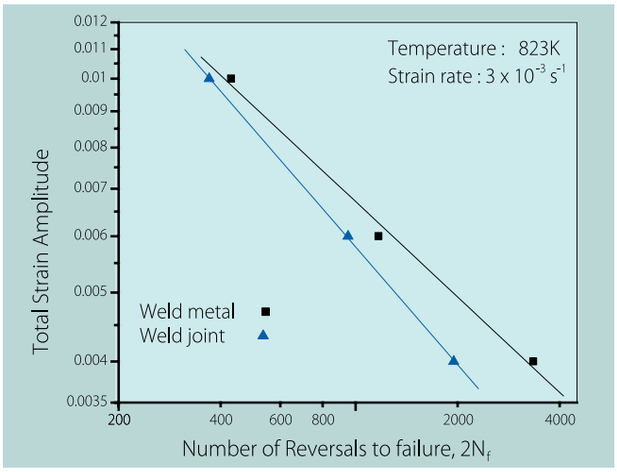

Fig.2
Comparison of Low Cycle Fatigue Resistance of Weld Metal and Weld Joint at 823 K.

III.22 Constitutive Flow Behavior of Austenitic Stainless Steels under Hot Deformation:Artificial Neural Network Modelling

Hot working operations such as rolling, forging and extrusion are necessary not only to break the cast structure into a wrought product but also to achieve the required shape and size. Determination of the load required to carry out these operations is of paramount importance. The load depends on flow stress of the materials, besides the geometry of deformation and the friction at tool-work-piece interface. Therefore, understanding of the constitutive flow behavior linking process variables such as strain, strain rate and temperature to the flow stress of the deforming materials is necessary. Towards this end, a robust Artificial Neural Network (ANN) model has been developed to predict the constitutive flow behavior of a wide variety of austenitic stainless steels as a function of process variables and chemical compositions. Besides, the relative importance of individual alloying elements to the flow stress in austenitic stainless steels has been quantified and sensitive parameters to the flow stress have been identified. An attempt has also been made to understand and evaluate the correlation between individual alloying elements and high temperature flow behavior.

The present model is based on three layers feed forward ANN with back propagation (BP) learning algorithm. The input parameters of the neural network are alloy compositions and process variables. The compositions include: C, Ni, Cr, Mo, Ti and N. The process variables include three most important hot deformation parameters namely strain, strain rate and temperature. The output is flow stress. A variety of austenitic stainless steels that are used for applications as various components in fast breeder reactors are investigated in the present study. The flow stress data for all these steels are evaluated based on isothermal hot compression testing in the temperature range 1123-1523 K and strain rate range 10^{-3} to 10^{2} s^{2}. The performance of the developed model has been evaluated using a wide variety of statistical performance indices rather than relying on a few global error statistics. A good agreement between experimental and predicted data has been obtained. The effect of alloying additions on flow stress has also been simulated using the developed model. The effect of Ni and Ti on flow stress has been shown in Fig.1 and Fig.2 respectively. Since this model can simulate the effect of individual alloying elements on flow stress, it can also be used as a guideline for designing new and advanced austenitic stainless steels.

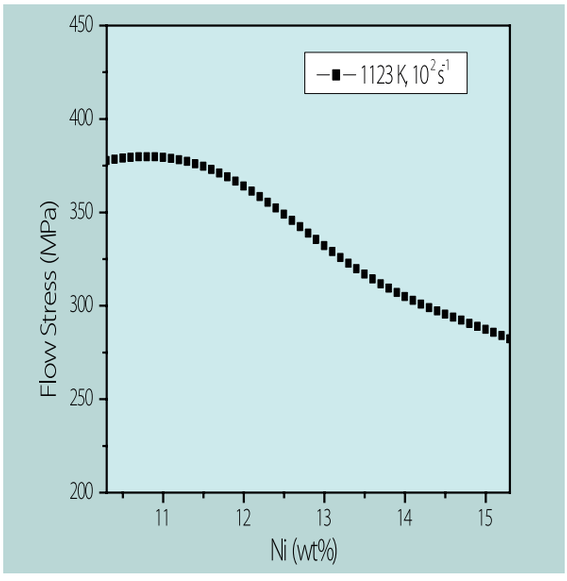

Fig.1
Neural Network Predictions for the Influence of Ni on Flow Stress of AISI Type 304 Steel at 0.5 Strain Level

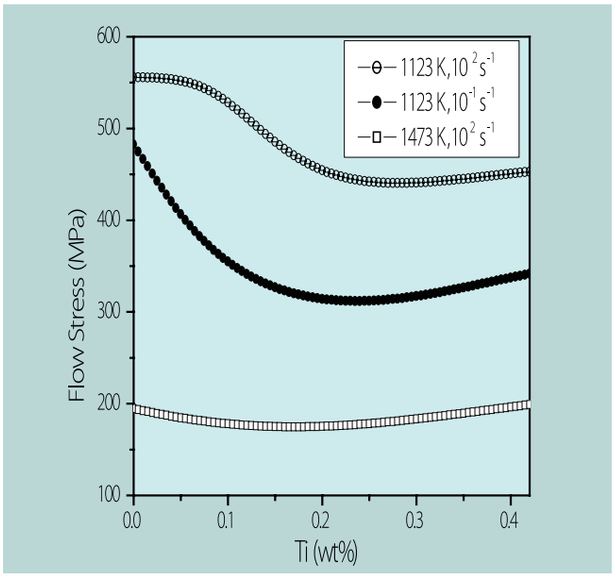

Fig.2
Neural Network Predictions for the Influence of Ti on Flow Stress of D9 at 0.5 Strain Level

III.23 Determination of Diffusion Coefficient of ^{54}Mn in D9 Alloy

During the operation of FBR, the activated corrosion products from the structural materials and fission products from fuel pins, in the event of fuel failure, enter liquid sodium in the primary circuit. Release, transport and deposition of radionuclides with fairly long half-lives such as ^{54}Mn, ^{60}Co and ^{137}Cs in fast reactors cause operation and maintenance problems due to build up of radioactivity in the primary system. Among the activated corrosion products, ^{54}Mn is the major contributor to the deposited radioactivity. One of the important input parameters for modelling the above process is the diffusion coefficient of ^{54}Mn in structural materials. Upon prolonged operation, this nuclide gets deposited in various regions of the coolant circuit and penetrates into the structural material by diffusion thereby rendering simple decontamination procedures difficult and inadequate. Knowledge of diffusion coefficient of manganese in structural and clad materials becomes very important. Hence, the determination of diffusion coefficient of ^{54}Mn in D9 alloy which is the candidate - clad material for PFBR was taken up.

The diffusion of radioactive manganese in D9 alloy sheets was studied by tracer technique. Experiments were carried out with both vacuum annealed (VA) and 20% cold worked (CW) sheet specimens in which the specimens were diffusion annealed in sodium containing a known activity of ^{54}Mn at various temperatures ranging from 773 to 873 K for specified lengths of time from 500 to 3000 h. At the end of diffusion annealing, the specimens were cleaned free of sodium, dried, weighed and the residual activity of 54Mn was measured using a well-type NaI (Tl) detector after micro-sectioning of the layers electrochemically. A mixture of 65% phosphoric acid, 20% sulphuric acid and 15% water by volume was used as electrolyte with a current density of 0.2 A cm^{-2}. 54Mn tracer penetration profiles were analysed using the thin film solution to Fick's II law assuming diffusion in semi-infinite medium. Concentration profiles of ^{54}Mn were obtained by plotting the residual radioactivity on the specimens measured after each electropolishing step as a function of square of distance from the initial specimen surface. Fig. 1 shows a typical penetration plot of alloy D9 diffusion annealed at 873 K for 1000 h, which has three linear regions with different slopes.

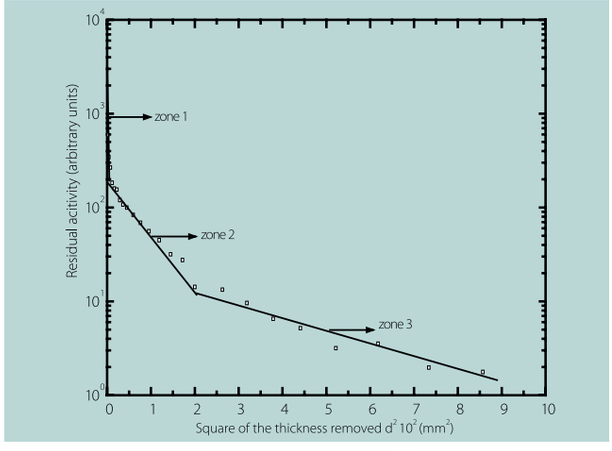

Fig.1
Typical Penetration Plot of VA Alloy D9 Specimen Diffusion Annealed at 873 K for 1000 h

The three zones indicate that the diffusion of the deposited radioisotope in the structural material takes place by three distinct processes. The outermost zone (zone 1) corresponds to the manganese radioactivity in the depleted layer formed by preferential dissolution of Ni and Cr from the specimen into sodium. The thickness of the depleted layer varies according to the time and temperature of exposure to sodium and in the present study is of the order of 3-5 µm. From the slope of the intermediate zone (zone 2), which is the zone of interest, the bulk diffusion in the material is calculated. The thickness of the diffusion zone in the present study is found to be in the range of 12 to 15 µm. Following the intermediate zone is the diffusion in the tail zone (zone 3). The radioactivity in the tail zone indicates slight contribution from grain boundary diffusion and approaches background values. Figs. 2 and 3 show the penetration plots in vacuum annealed and cold worked specimens. The diffusion coefficient values in the present study range from 1.99 x 10^{-18} to 5.79 x 10^{-18} m^2 S^{-1} for vacuum annealed alloy D9 specimens in the temperature range of 773 to 873 K and 1.53 x 10^{-18} to 2.12 x 10^{-18} m^2 S^{-1} for cold worked alloy D9 specimens in the temperature range of 823 to 873 K. Fig.4 shows the dependence of D with 1/T. The activation energies for diffusion in vacuum

annealed and cold worked specimens are calculated to be 60.76±17.40 and 38.88±12.01 kJ mol^{-1} respectively and the respective frequency factors are

$$\left\{ 2.24 \begin{matrix} +26.45 \\ -2.07 \end{matrix} \right\} \times 10^{-14} \text{ and } \left\{ 4.62 \begin{matrix} +20.77 \\ -3.77 \end{matrix} \right\} \times 10^{-16} \ m^2 \ s^{-1}$$

The results of the present study show that under the operational conditions of fast reactor, penetration of 54Mn into the stainless steel matrix depends on the thermo-mechanical treatment and operation history of the material. These diffusivity data were employed in estimating the extent of material removal in decontamination studies. It is well known that longer exposure of the matrix to sodium containing ^{54}Mn at higher temperature results in higher diffusion length. Hence it is required to remove several mm thick layers of the material for effective decontamination, while at lower temperatures it is required to remove only a few µm thickness of the material.

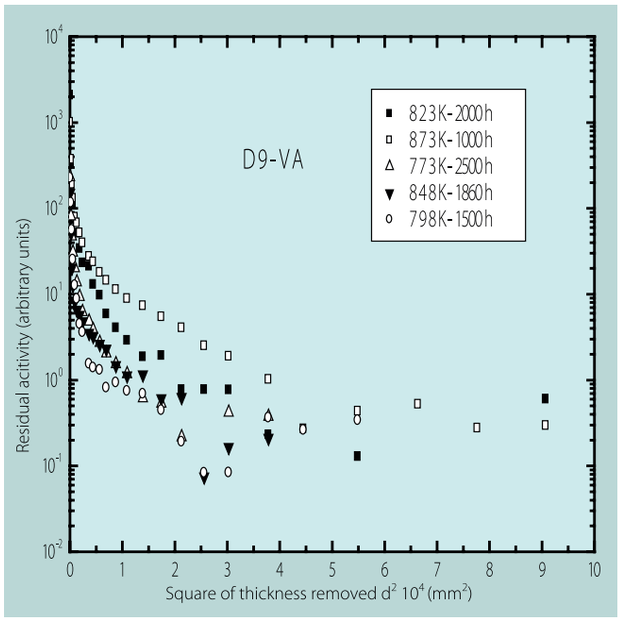

Fig.2
Residual Activity of ^{54}Mn as a Function of d^2 in VA Specimens

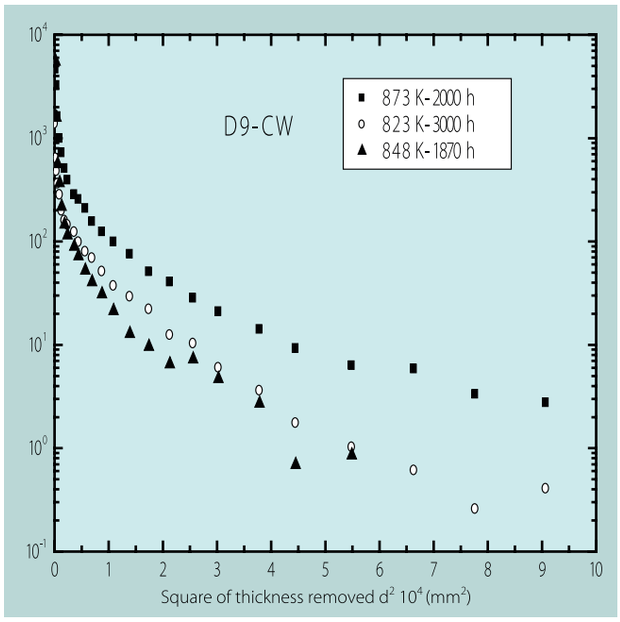

Fig.3
Residual Activity of ^{54}Mn as a Function of d^2 in CW Specimens

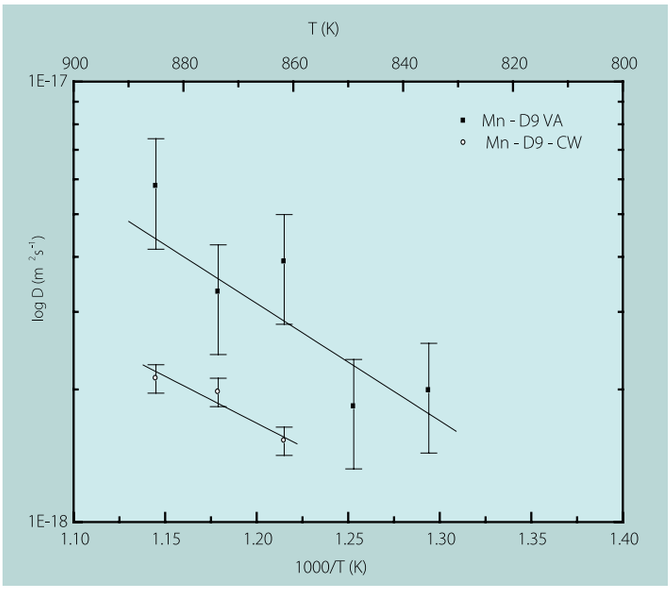

Fig.4
Bulk Diffusion of ^{54} Mn in Alloy D9 in Annealed and Cold Worked Conditions

III.24 Surface Modification of Titanium to Control Microbial Fouling

Titanium is a highly reactive metal. However, when the fresh metal surface is exposed to air and/or moisture, it forms spontaneously and instantly a very stable, continuous, highly adherent and protective oxide film on its surface making it passive. Titanium and its alloys find extensive application under severe corrosive conditions because of the excellent corrosion resistance imparted by this passive film. Some of the common applications are as heat exchanger surfaces in seawater-cooled equipment and as orthopaedic implants. But the inert nature of these materials also creates problems of different nature; titanium surface becomes a host to a variety of microorganisms present in natural environment. In the case of heat exchangers, the bio-films formed by these microorganisms reduce flow of cooling water and decrease heat transfer characteristics of the material thus, affecting the efficiency of the equipment. Colonization of titanium body implants by harmful bacteria causes severe infection, often forcing replacement of the medical devices.

Taking cue from the vast literature on the photocatalytic activity of semi conducting oxides especially the anatase form of titanium oxide, studies were carried out to see whether microbial attachment on Titanium and Ti6Al4V alloy surfaces can be reduced by photocatalytic killing of the cells. Anatase form of TiO_2 was produced on Ti and Ti6Al4V surfaces by anodizing in dilute phosphoric acid solution at 30V for 48 h. The anodizing parameters were optimized to produce the best anatase film as confirmed by glancing incidence X-ray diffraction (GIXRD) and photocatalytic degradation of methylene blue dye. The anodized surfaces were then exposed to dilute cultures of fresh water bacterial strains of Pseudomonas spp. and Micrococcus spp. as well as marine bacterial strains of Bacillus spp. and Pseudomons spp., as these were the major colonizers of fresh water and marine biofilms. It was found that there was significant reduction in the total viable counts of all these bacteria on the anodized surface under near-UV illumination (350-380nm) using black light blue (BLB) fluorescent lamps. The results are illustrated by the total viable counts (TVC) on different surfaces given in Fig.1 and the epifluorescent micrographs of Fig.2. It was also found that anodized Ti6Al4V alloy shows better photocatalytic cell killing than anodized Ti. The GIXRD and AFM results showed that the oxide formed on anodized alloy has higher crystallinity and is composed of particles, which are smaller in size; both these attributes are reported to enhance photocatalytic activity. It was also observed that anodized Ti6Al4V surface showed bactericidal effect even in visible light, probably due to the presence of vanadium in the titanium oxide lattice that is reported to shift the photo response of the anatase to visible range. Heat treatment of the anodized Ti surfaces at 500°C for 3h was found to improve the bactericidal property of the surface by an order of magnitude. Structural characterization of the oxide by GIXRD showed that there was partial conversion of anatase to rutile on heat treatment and it has been demonstrated by earlier workers that a mixture of anatase and rutile is a better photocatalyst than anatase alone.

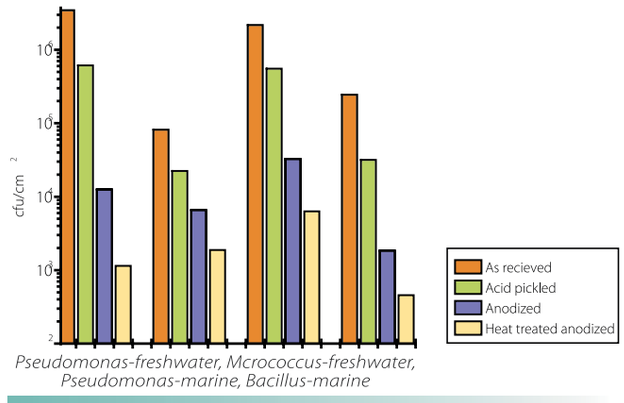

Fig.1
Total Viable Counts of Bacteria on Titanium Surface Under Different Conditions Exposed to Bacterial Cultures Under Near - UV Light Illumination

The total viable counts (TVC) of bacterial cells on anodized Ti surfaces enumerated by the pour plate method were significantly less than the acridine orange counts suggesting that photocatalytic cell killing was due to damage to the cell membrane which inhibits growth on the agar plate. In order to further confirm the damage to the cells, the growth kinetics of photocatalytically deactivated bacterial cells were compared with that of normal cells in liquid

culture medium. The photocatalytically deactivated cells showed a delay in reaching the exponential or dividing phase of growth, suggesting that cell damage has taken place. Thus, our extensive studies on Ti and Ti6A14V alloy has shown that anodization is an effective method to reduce bacterial attachment on these surfaces.

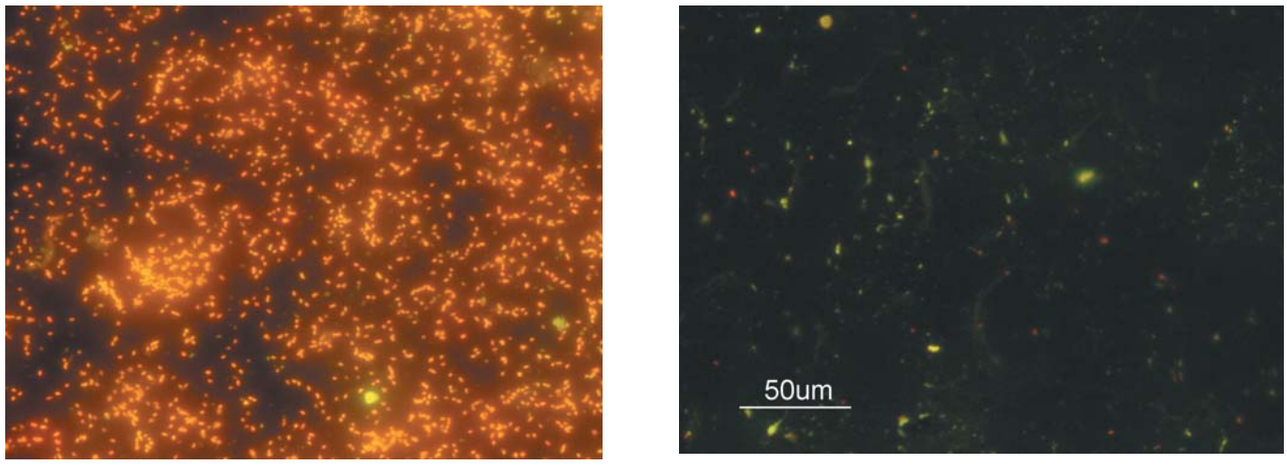

Fig.2
Epifluorescence Micrographs of Bacterial Cells on Acid Pickled, and Anodized and Heat Treated (30V/48h) Titanium Surfaces

CONTROL ROD MATERIALS

III.25 Characterization of Electro-deposited Elemental Boron

Boron carbide containing boron enriched in 10_B isotope will be used in the control rods of the PFBR. The boron carbide will be fabricated by reacting elemental boron with carbon. Elemental boron, in turn, is prepared by converting boric acid to potassium tetrafluoroborate (KBF_4) followed by molten salt electrolysis. A diagram of the electrowinning set-up is given in Fig. 1. In a typical electrowinning experiment, elemental boron is recovered from a near-saturated solution of KBF_4 in a molten mixture of KCl and KF held at 1073 K in a graphite crucible, by the application of a DC potential (1.5 to 4.5 V). During this electrolysis boron is electrodeposited on a mild steel cathode ("raw boron"), while chlorine evolves at the graphite crucible, which serves as the anode. The elemental boron obtained using the above process is purified further, in order to remove the major impurities viz., Cl^-, F^-, Fe and Ni. The characteristics of boron produced by electrowinning were studied in detail to optimize the process parameters.

The specifications of the elemental boron powder to be used for the production of boron carbide pellets for reactor applications and the typical chemical assay of the elemental boron produced through electrowinning process are given in Table 1. The major impurity present in the "raw boron" powder is iron. Contamination of the electrodeposited boron with the corrosion products of the mild steel cathode and the nickel shaft on which it is mounted results in a deposit containing iron and nickel impurities. The carbon particles, which are eroded from the surface of the anode crucible, contaminate the deposit with significant quantities of carbon. The amount of carbon residue present in the "processed boron" samples varied over a wide range viz., 0.3 to 1 wt %. Surface oxidation of boron could occur when the hot electrodeposited boron is quenched in water as well as during subsequent processing of the powder. It is reasonable to expect that the surface oxide film and the moisture adsorbed on to the surface of these fine boron particles would lead to a product with significant oxygen impurity. A comparison of the assay presented in Table 1 with the specifications, reveals that the process conditions established in-house are capable of producing an elemental boron

powder that conforms to the target specifications.

The scanning electron micrographs of the "raw boron" as well as "processed boron" samples are shown in Fig.2 (a) and (b) respectively. The average size of an individual spheroidal aggregate is about 1µm. Subsequent processing of the electrodeposited boron (grinding, leaching with boiling water and HCl) does not alter the size and morphology of these particles significantly.

Specifications for the elemental boron and chemical assay of produced boron powder

S.No.	Element	Specification (Wt %)	Raw boron	Processed boron
1.	Boron	95 min.	95.9	97
2.	Boron + Carbon	98 min.	96.7	98
3.	Calcium	0.3 max.	<0.1	<0.1
4.	Iron	1.0 max.	2.8	0.98
5.	Aluminum	0.3 max	<0.2	<0.2
6.	Magnesium	0.15 max	0.06	0.12
7.	Silicon	0.15 max	0.14	0.13
8.	Oxygen	---	0.35	0.284
9.	Nitrogen	---	0.03	0.029
10.	Fluoride	---	0.22	0.006
11.	Chloride	---	0.04	0.002

The bulk density of the boron powder varies from 0.45 to 0.60 Mgm^{-3} and increases with the fraction of the bigger particles. The surface area of these powders is inversely correlated with their size. The oxygen content in the boron powders increase with the fraction of grains due to the increase in the area available for surface oxidation. Therefore it is necessary that enough care be exercised in handling the boron powder during processing in order to minimize the oxygen pick up. The chemical state of the matrix as well as the impurity phases present in them were established using X-ray photoelectron spectroscopy (XPS).

The raw and leached boron samples were examined for their surface composition using X-ray photoelectron spectroscopy (XPS). In the raw boron, peaks pertaining to O (1s), B (1s), K ($2p_{3/2}$), F (1s), Fe ($2p_{3/2}$), Ni ($2p_{3/2}$) and chlorine Cl (2p) were observed. It is observed that the raw boron probably contains NiF_2 and $NiCl_2$, a nickel boride, $FeCl_2$, $FeCl_3$, FeF_2, FeF_3 and the borides of iron. In the processed boron sample O (1s), B (1s), F (1s) and Ni ($2p_{3/2}$) peaks were observed. B (1s) peak was broad but not as broad as in the raw B sample and could be de-convoluted into three peaks. All peak positions are similar to raw B sample but the peak pertaining to Fe_xB is absent. All other peaks except B (1s) peak were feeble which show that the reagent and the method used for leaching is effective in removing the impurities present in the boron powder. A thermodynamic analysis was carried out to interpret and understand the XPS results. The various corrosion products that would be formed in the head space above the melt were predicted using a simple computation employing the software HSC Chemistry (version 5.0). These predictions are in agreement with the phases identified in the raw-boron and processed boron samples using XPS.

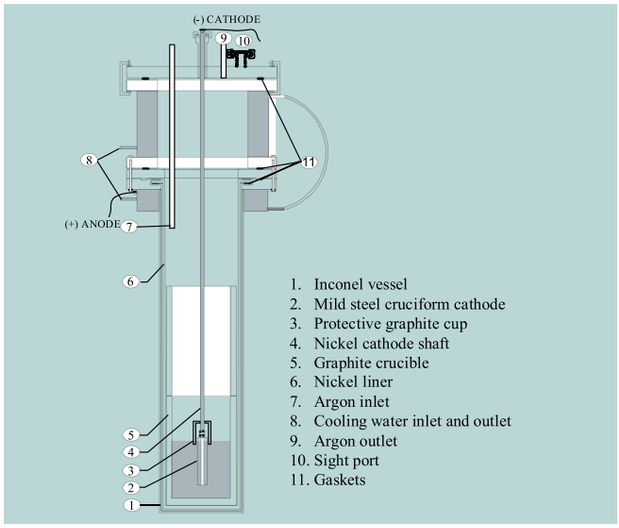

Fig.1
Schematic of Electrowinning Setup

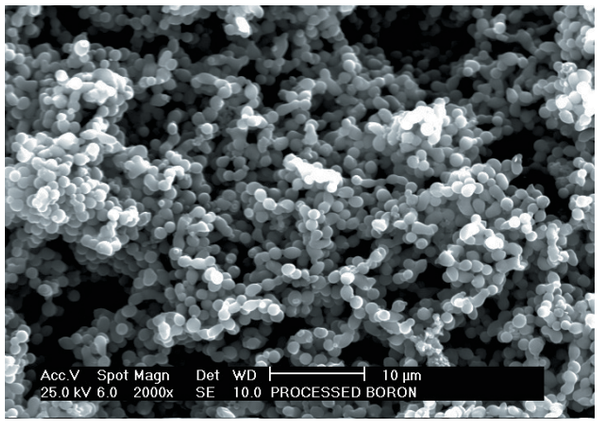

Fig.2 (a)
SEM Image of Raw Boron

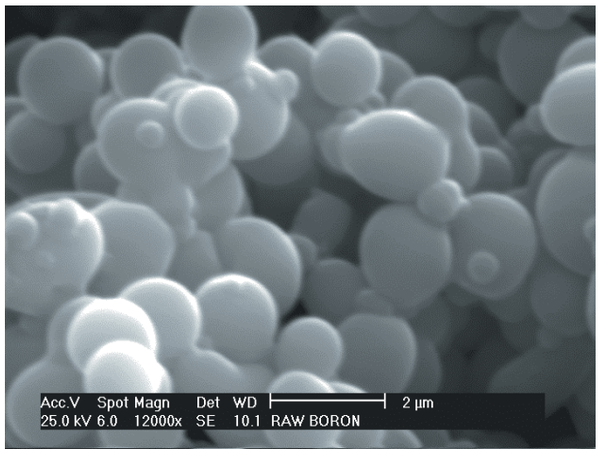

Fig.2 (b)
SEM Image of Processed Boron

INSTRUMENTATION

III.26 A Novel Technique for Sub-assembly Imaging for Bow Measurements

The ultrasonic under sodium scanner for PFBR will be used for two purposes; a) to detect the protruding sub-assembly (SA), if any, using 4nos. of side viewing transducers and b) to position the scanner at 10mm above the top of the SAs using 4nos. downward viewing transducers before starting the side scanning. A Multi Transducer approach using eleven trasducers for imaging the top of a single SA was reprted earlier. This method has a limitation that scanning has to be carried out for each SA. Alternatively a novel technique has been developed to image the top of SAs and to measure the displacement due to bowing using four transducers and also a single scan is adequate for imaging of six SAs. It also does not involve any change in design of the above scanner mechanism, rotation of plugs and altering the sequence of operation for position sensing.

The four downward viewing transducers (DVT) mounted on the scanning head are located at particular distances (57,120,160 and 187mm) from the scanner vertical axis, so as to cover SAs in all the 3 rings. The SA top surface has an inner radius of 55mm and outer radius of 58mm. To cover the center SA top, the first transducer is located at 57mm from the scanner vertical axis. The other two transducers are located at 120mm and 160mm to cover the 6 SAs in the next ring and also to accommodate maximum expected bow of 30mm. The 187mm transducer covers the top surface of alternate six SAs in the next outer ring.

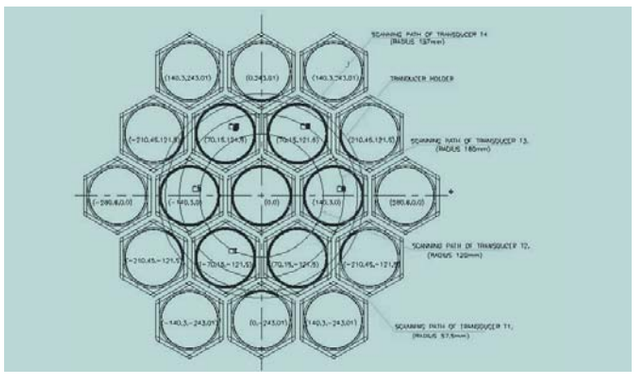

Fig.1
Scanning Path of 4 DVT

The 'Bow' measurement method is explained as follows: When the scanning head is rotated once about the spinning tube axis, each of the four DVTs make one circular scanning path over the SA head top surfaces, as shown in Fig.1. A PC interfaced with the ultrasonic equipment detects the echo output and plots a pixel on the monitor at the co-ordinates (x, y) corresponding to the DVTs position. Thus whenever each DVT passes over the circular surface of the top of SAs, a group of pixels are plotted on the screen. The four scanned circular arcs on a SA in the middle ring are imaged as shown in Fig.2 and the center of the SA top surface is computed from the coordinates of the circular arcs. The difference between the above and the initial location of the center of the SA gives the bow.

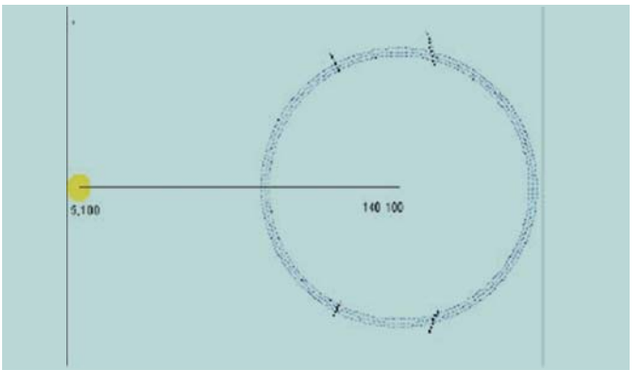

Fig.2.
Images of Sub-assembly Top

In order to validate the concept of 'bow' measurement by the technique described above, a PC-controlled mock-up scanner was designed and developed. The schematic of the set-up is as shown in Fig.3. The mock-up scanner has two transducers mounted at 120 and 160 mm from the spinner axis.

A PC is used to control the whole sequence of scanning, to acquire ultrasonic data such as amplitude, transit time, the transducer position etc. and imaging operations. A self correcting algorithm was implemented to limit the maximum cumulative error to 0.1° over 360°.

Experiments were conducted in water with two transducers and SA heads positioned at 135mm (say zero offset), 145mm (10mm offset), 155mm (20mm Offset) and 165mm(30 mm offset), thus simulating the SA top at different bowing conditions. Scanning was carried out over 360°

to cover the SA head. The scanned images of the four arcs and center of SA top are shown in Fig.2. Using the coordinates of any three arcs corresponding to the largest peak amplitude of the echos as the vertices of a triangle, the radius of the circumcircle and circumcentre of the triangle were computed. The circumcentre represents the centre of the SA top surface. The centre thus obtained has an error less than 3mm. This exercise has given confidence to the estimation of bowing using imaging techniques.

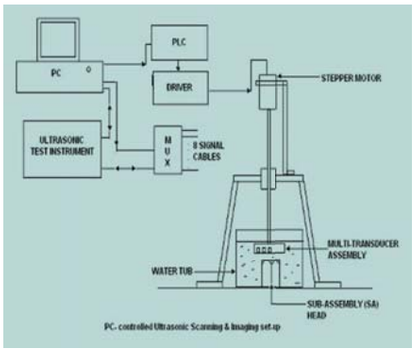

Fig.3
PC-Controlled Ultrasonic Scanning and Imaging Set-up

III.27 Development of Remotely Operable Optical Micrometer Based System for Precise Measurement of Diameter of D9 Pressurised Capsules

Pressurised capsules of D9 alloy would be irradiated in FBTR under desired conditions of temperature and stress to determine the irradiation creep rate. Increase in diameter of D9 pressurised capsules due to irradiation swelling and creep is expected to be of the order of a few micrometers. To measure the diameter of pressurised capsules before and after irradiation, a highly accurate and precise measuring system is required. A measuring system based on commercially available high-speed, high accuracy optical micrometer has been developed for this purpose. This optical micrometer has two parts viz. a measuring head and a controller. To hold the pressurised capsules appropriately and move it in the central region of the measuring head for measuring the diameter and to rotate / move in the desired direction, a fixture has been developed that can be operated remotely. Since the dimensions of the pressurised capsule are to be measured in the hot cell after irradiation, modification of the equipment for remote operation of the fixture is necessary.

The system (Fig. 1) consists of a base plate made of stainless steel. On the base plate an EZ Limo is fixed for linear motion. EZ limo is an integrated linear motion product containing motor, ball screw and feed back system housed in a compact body providing sophisticated motion control. Over the movable part of EZ limo, a pneumatic chuck is fixed. It can hold a tube of diameter in the range of 5 to 25 mm. The pneumatic chuck can be operated at an air pressure of about 0.7 MPa. A servomotor is connected to the chuck to rotate it in a controlled manner. The measuring head of the optical micrometer is fixed on the base plate in such a way that the object being measured is located in its central region. A panel board houses the drives of EZ limo, servomotor and programmable logical controller and software for the operation of the devices is installed in a host PC. The system is designed to hold the cylindrical pressurised capsule using the pneumatic chuck and rotate it incrementally about the axis of the capsule at intervals of 45° to measure the diameter of the pressurised capsule at each position. After the measurement, it can move the pressurised capsule along the axial direction by a distance of 5 mm using the EZ limo and again rotate the pressurized capsule at 45° intervals to measure the diameter at this new axial location. The fixture can repeat this process for measurement of diameter of pressurised capsule at five locations along the length of the pressurised capsule. The repeatability for this system is ± 0.05 µm in the measuring range of 5 to 25mm.

Fig.1
Remotely Operable Optical Micrometer System

III.28 Development of a Reflectron Time-of-flight Mass Spectrometer for Non-destructive Analysis of Isotope Ratios in Irradiated B_4C Pellets-Test Measurements on an Unirradiated FBTR Control Rod Pellet

A stack of ten B_4C pellets (40 mm dia and 40 mm length), 90% enriched in ^{10}B contained in stainless steel clad is used as control rod in FBTR. ^{10}B present in these B_4C pellets is burned out only to a lesser extent, as the rod is kept out of active core level for considerable part of its life in a reactor (life of control rod is determined by the SS clad) and the maximum burn-up of ^{10}B occurs only in the lower part of the rod. To decide if the pellets from such an irradiated stack can be reused or relocated, one needs to know the $^{10}B/^{11}B$ ratio present in such irradiated pellets. The accuracy needed for such isotope measurements is about ± 1%. Though neutron irradiated B_4C is not expected to be radioactive, the common trace impurities such as Eu present in the B_4C pellet can lead to considerable levels of radioactivity. Hence, the method used for the $^{10}B/^{11}B$ ratio measurements on irradiated B_4C pellets needs to be amenable for remote operation. Further more, B_4C is one of the hardest materials known, next to diamond and cubic boron nitride. Any destructive method to analyze isotope ratio of B in B_4C is cumbersome. Hence, a non-destructive method is preferred not only to avoid the difficult dissolution or powdering process, but also because the pellet taken for analysis can be reused, as it is, after the measurement. One such method is laser vaporization mass spectrometry (LMS). In LMS, the laser vaporization removes only a few picograms of the material from the laser-irradiated spot of the surface, without any physical damage to the pellet. For a nanosecond laser pulse, the transiently heated part of surface is typically 0.5 mm in diameter and a few tens or hundreds of Å depth. A laser mass spectrometric facility has been developed using a home-built reflectron time-of-flight mass spectrometer (RTOFMS) to analyze the isotopic ratio of $^{10}B/^{11}B$ present in B_4C pellets. The schematic of the facility is shown in Fig.1 and typical mass spectrum obtained for an unirradiated FBTR pellet and a pellet of natural composition used as shielding material in PFBR are shown in fig. 2. This facility can analyze the isotopic ratio with a spatial resolution of 400 µm. A typical ratio measurement on a 40mm diameter pellet is shown in Fig.3. The typical values obtained for % of ^{10}B present in FBTR and PFBR pellets are: 90.3 ± 0.4 & 20.7 ±0.5; the corresponding thermal ionization mass spectrometric values obtained using the powdered B_4C samples are: 90.65 ± 0.07 & 19.90 ±0.07, respectively. Efforts are underway to improve the accuracy and precision obtained using LMS and to make the system ready to handle irradiated pellets inside a glove box.

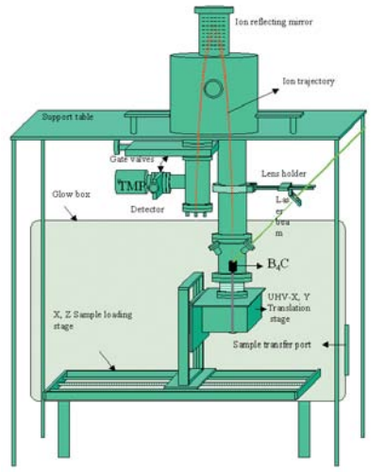

Fig.1
Home-built Reflectron Time-of-Flight Mass Spectrometer for the Analysis of $^{10}B/^{11}B$ Ratio in FBTR Control Rod B_4C Pellet

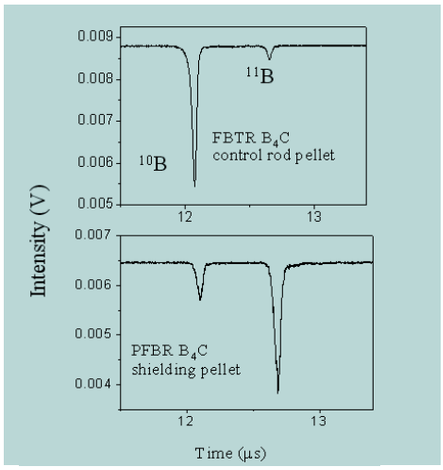

Fig.2
Typical Mass Spectrum of Isotope of B Obtained for B_4C Pellets.

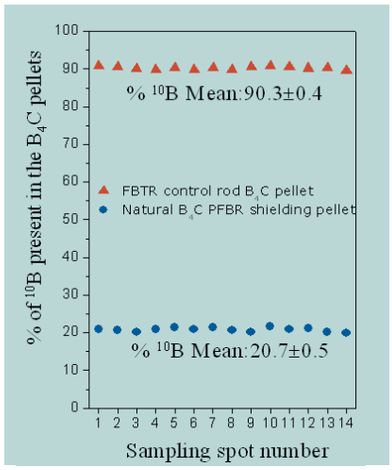

Fig.3
% of ^{10}B Measured over 40mm dia B_4C pellet along a Straight Line: Laser spot dia: ≈ 400µm

III.29 High Temperature Vacuum Brazing of Mineral Insulated Cable for Neutron Detectors for PFBR

Mineral Insulated (MI) tri-axial cables are chosen as a signal transmission cable for neutron detectors in the fission chambers of PFBR. MI cable is selected in view of the performance specifications. The cable assembly involves joints between Inconel 600 (IN600) sleeve to cable sheath of 316L stainless steel (316L SS); One of the main concerns is the integrity of the ceramic to metal seal between the concentric electrodes and of the tri-axial cables that should withstand a temperature of 873K. The other concern is that of joining the conductor to Inconel sleeve and Inconel ferrules to the middle sheath of tri-axial cable, with the sheath being made of copper coated with 0.3 mm thick 316L SS.

The optimum conductors for vacuum (10^{-5} torr) brazing with BNi2 foil have been found to be 15 minutes at 1323K, after conducting a few trials of brazing. The brazed joints (Fig.1) were subjected to thermal cycling between 473 and 923K over 50 thermal cycles, simulating PFBR operating conditions, and it was found to have tensile strength similar to those in the as-brazed condition with tensile failure occurring in the cable sheath. Metallographic investigations confirmed that the brazed joints were free of voids, and that the brazing procedure adopted had excellent reproducibility. Leak tightness of less than 10^{-8} std. CC/s of the thermal cycled brazed joints before and after tensile test was also found to be satisfactory.

Fig.1
Photograph of as-brazed Joint of IN600 Sleeve to SS Sheath of MI Cable

III.30 Participation in ICARB Campaign of ISRO and PRWONAM Experiment for Regional Scale Real Time Weather Prediction

An Integrated Campaign for Aerosol Radiation Budget (ICARB) was organised by ISRO Bio-sphere Geosphere Programme (IGBP). This national programme with multi-institutional participation is aimed at developing a quantitative understanding about the aerosol and trace gas environment, their transport over Indian and adjoining oceanic regions and to characterize the meteorological process responsible for this transport. Obviously, extensive measurement of meteorological parameters formed an important component of the campaign.

The atmospheric study group of IGCAR participated in the planning and carrying out of surface level cruise measurement over ocean along with VSSC team as a part of the campaign. State-of-art equipments like GPS based radiosondes, Phased array Sodar and Automatic Weather Stations were used for the first time on board the Department of Ocean Development (DOD)'s Ocean Research Vessel ORV SAGARKANYA (Fig.1). The structure of the coastal boundary layer at a coastal site becomes increasingly complex in the vicinity of ocean fronts, land-sea breeze circulation and changes in stability allow the development

of internal boundary layer that affect the turbulence diffusion of pollutants. While there have been intensive measurements available over land, no data has so far been collected over ocean to validate the numerical models. Participation in ICARB enabled for the first time an insight into the meteorological condition over the sea on the Arabian sea, Indian Ocean and Bay of Bengal in general and near Kalpakkam coast in particular. The sea surface temperature (SST) was high in Indian Ocean region compared to the Bay of Bengal and the mean sea air temperature difference was about 1.25 deg C. The heat flux varied between -18-20 W/m^2, and -18-30 W/m^2 respectively in Bay of Bengal and Indian Ocean regions. Over the land the value would be usually about 250W/m^2. The aerodynamic roughness over ocean is about 0.005 to 0006 m whereas in the inland sites its variation is between 0.2 -0.8 m. An important component of the meteorological observation was the measurement made by the Phased array Sodar (Fig.2). An observed wind profile by Sodar profile near Cochin port is shown in Fig.3. Interesting observation in this vertical profile data is that there is a convectively induced circulation, the land-sea breeze, at Cochin similar to that at Kalpakkam and the direction reversal takes place at a height of 200m. Air borne effluents released from a 100m stack would get entrained in the circulation and likely to come back to the source location during sea breeze. Detailed analysis would be carried out along with other participating institutes. A comprehensive data set would be assimilated for use in model validation study.

Prediction of Regional Weather with Observational Meso-Network and Atmospheric modeling (PRWONAM) is another national programme launched by ISRO with four nodal agencies, namely, SHAR Sriharikotta, IGCAR Kalpakkam, ISRO Bangalore and IMD Chennai, in the study region. The objective is to develop the skill of the regional weather model to provide precise short range (1-3 days) weather forecasts. This requires accurate representation of initial conditions and physical processes in models. The task is two-fold; the first involves an improvement in the initial conditions, well resolved in space from a dense network of observations, and the second needs development and evaluation of physics of various atmospheric processes especially for the atmospheric boundary layer turbulent diffusion. Atmospheric circulations on different scales viz., synoptic, regional and meso-scale influence the weather and the pattern of atmospheric dispersion in the Kalpakkam region in the south-east coast. Disturbances from Bay of Bengal, wave disturbances from the north, low pressures from the equator, thermally induced local land-sea breezes, convective thunderstorms and the monsoon trough etc are a variety of phenomena that influence the weather in this region. The existing observational network needs to be extended with careful measurements to capture the dynamical phenomena for better initial conditions in the real-time model.

Radiological Safety Division (RSD) has implemented an On-line Decision-Support System for nuclear/radiological emergency response with inputs from real-time weather and dispersion models, real-time meteorological / dose observations and Web-GIS based query tools. A multi-scale regional weather model MM5 is executed on a parallel computer to forecast the wind field and other meteorologi-

Fig.1
The ORV Sagar Kanya and the IGCAR Meteorological Mast

cal parameters needed for the prediction of the radioactive plume movement and dispersion of air-borne effluent releases in the Kalpakkam coastal environment. Realistic calculation of atmospheric dispersion and dose estimation depends on accurate prediction of meteorological fields i.e., winds, mixing height, turbulence parameters and their spatio-temporal heterogeneity.

The meso-network of observations (Fig.4) implemented under PRWONAM provides improved initial conditions in the weather model of the DSS. The network includes distribution of Automatic Weather Stations (AWS), multi-level meteorological towers at IGCAR, existing surface and upper air observations from IMD, ISRO, Airforce, Navy etc. In the initial phase about 40 AWS are installed in the southern region including 4 AWS being installed at IGCAR, Kalpakkam. The AWS provides continuous data on temperature, atmospheric pressure, wind speed and direction, rainfall, relative humidity, solar radiation etc which is communicated to the data bank at Space Applications Centre through satellites. IGCAR receives this data through ftp mode for assimilation in the real-time model. A series of field experiments are planned to study the physical processes, impact of initial conditions in the model using GPS sondes, MST radar profiles, and the existing surface and upper air measurements. The data collected during the first Pilot field campaign held during May-July 2006 were used in model assimilation at IGCAR for real-time dispersion forecasting and for weather advisory for special events of interest by ISRO. The prediction of surface wind speed with and without data assimilation for a case on 9-12 July 2006 is shown in Fig.5. Advanced data assimilation techniques are being developed for use in real-time dispersion prediction system.

Fig.2
Dr. P.S.Goel, Secretary, Ministry of Earth Sciences and other Scientists being Shown the mini-Sodar system Installed on-board Sagar Kanya.

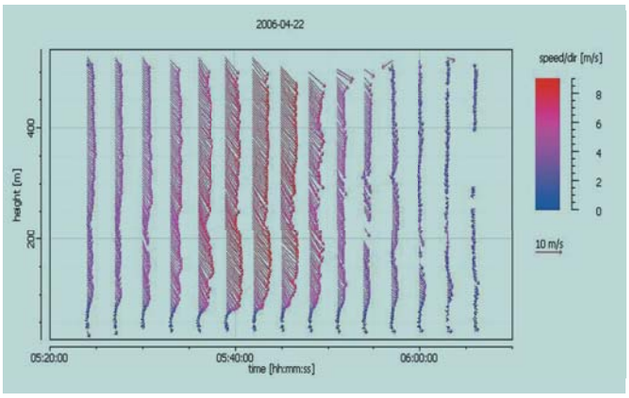

Fig.3
The Wind Velocity Profile over the Sea from Sodar as a Function of Height and Time

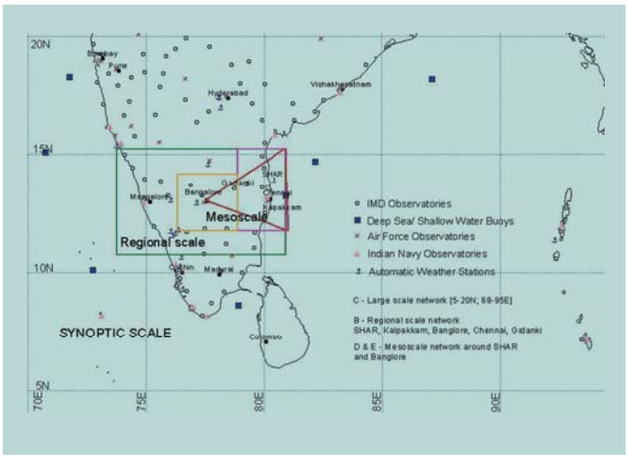

Fig.4
The Meso-network of Meteorological Stations in the PRWONAM Region

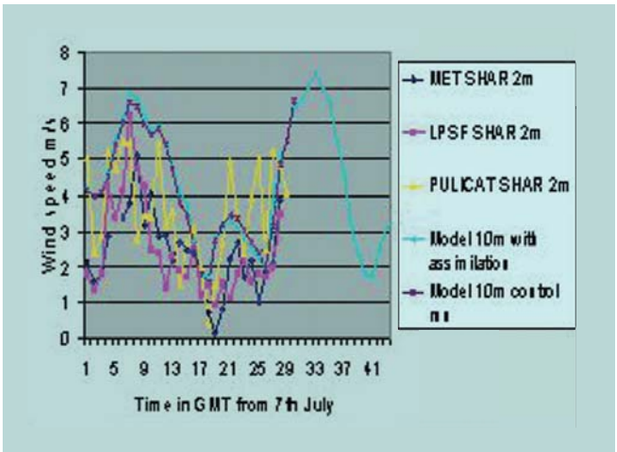

Fig.5
Forecast Results of Wind Speed with and without the Realtime Data Assimilation

III.31 On-line Nuclear Emergency Response System (ONERS) and GIS Mapping of the Environmental Radiation for Source Term Assessment

One of the important issue in managing a nuclear emergency is the ability to promptly determine and take action to protect the public. The radiological assessment also should take into account of all critical information available at anytime and must be interactive, dynamic, process aimed at reviewing the response as more detailed and complete information becomes available. With this goal, a web enabled Geographic Information System based Decision Support System (GIS-DSS) is developed for carrying out the geo-spatial analysis of radioactivity spread in the event of an inadvertent air borne release at Kalpakkam (Fig.1). The indigenous GIS and query modules are developed by the expert group in Regional Remote Sensing Service Centre (RRSSC), ISRO, Nagpur In contrast to the readily available DSS software for nuclear emergency like RODOS, ARAC etc. which are too detailed and tuned to the European and American conditions respectively, the DSS developed at Kalpakkam provides integrated decision support based on AERB guidelines as well as the database structured in the lines of the national disaster management system.

The radiological scenario is assessed using a dispersion forecast model based on Monte Carlo method to describe the diffusion and transport. The meteorological parameters are obtained form the state of art mesoscale weather forecast model MM5, where the later is executed in a parallel computing system (Linux Cluster). The forecast model covers an area of 100km around the site. For a very accurate assessment in a local scale of about 10km radius, local meteorological data are directly used in a now-casting dispersion model which is run for every 10min. interval.

Further, the terrain, land-use and soil texture data used as input to the weather forecast model MM5 and the query module of the DSS are the realistic data base prepared by resource organizations like RRSSC, National Bureau of Soil Survey NBSS-LUC, IARI, Nagpur and Survey of India. The most difficult part in the GIS-DSS is the seamless merging of all the data accurately. This required conversion of the data into an uniform projection parameter, made for Kalpakkam as the central geographical position so that the positional accuracy of different layers are achieved with in the limit of the data source. The left-side column of Fig.2 shows various types of data base in the form of geographical layers used in ONERS. The icons displayed on the top row correspond to various functions that can be done by all clients on the LAN. For example, by clicking icon 'i', the information about the polygon in the layer, say a village in the village layer would be displayed. The icon 'SQ' is for obtaining a spatial query such as the child population and the villages falling under a particular dose range. In order to make the decision making process easy, the display and queries are structured with the response zones like evacuation zone, food control zone etc. using derived intervention (dose) levels DIL. Fig.2 also shows the evacuation zone based on dose due to ground deposited activity for a spatial query for long range (100km) dose forecasted for 15h of a hypothetical accidental day. The details of the villages, the nearby shelters, roads etc. are also provided to the client. The Computer Division has enabled the availability of ONERS on ANUNET so that it is accessible by the DAE Crises Management Officials.

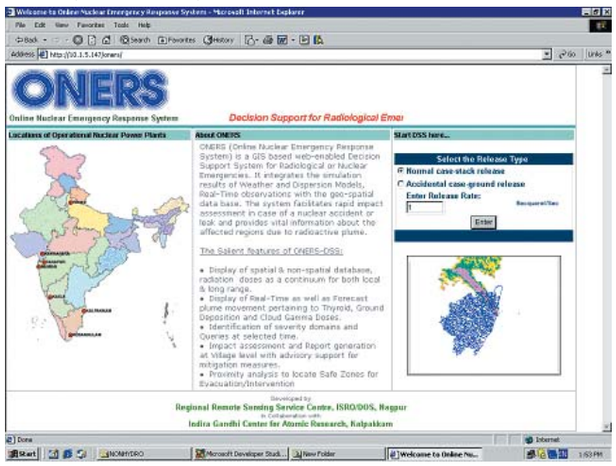

Fig.1
Typical Display Contents of Oners System

Another important requirement during emergency response management is the identification of the source term. Off-site radiation monitoring data is the readily available source for on-line estimate of the source term. A novel method of mapping of the site environmental radiation is initiated using a GIS so that visual identification of the source is possible. For validating the methodology, the Argon-41 release from the 100m stack of the MAPS is used. It is to be noted that the release is designed for operational condition and is well within the limit of occupational exposure. A portable monitor which will estimate the dose rate due to Ar-41 alone was designed and developed at Radiological Safety Division. Environmental survey at selected locations inside IGCAR premises has been done using the instrument with and without the presence of Ar-41 ie, during sea breeze and land breeze situations. Dose rate due to Ar-41 was measured at the selected locations along with recording their geographical co-ordinates using GPS. All the data are exported to GIS software and the intensity map is generated using the

method of Triangulated Irregular Network. Ar41 radiation dose rate map for the site indicated relatively higher dose on the NW sector of the MAPS stack. This is due to the onset of the sea breeze and the inhibition of vertical diffusion due to formation of Internal Boundary Layer. Thus, the geo-referenced radiation data can serve as input to an on-line numerical source term assessment model.

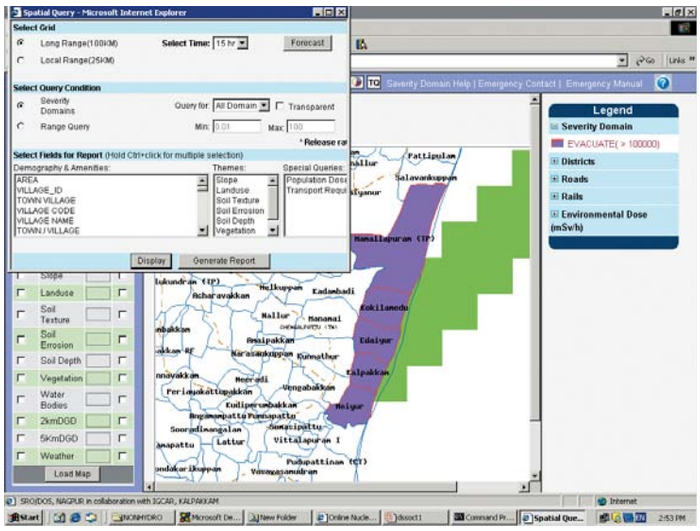

Fig.2
On-line Display of the Evacuation Zone and the Interactive Query Module

III.32 Database Management Software for Wholebody Counting Facility

RSD has a comprehensive internal monitoring program as per AERB requirement catering to the needs of all the active facilities of IGCAR. Management of dose records of the individuals is also equally important as periodic monitoring. About 700 workers are being monitored for internal contamination annually. The monitoring program has many components like preparation of periodic counting schedules, recording of personnel details of the workers, counting procedure, spectral analysis, activity estimation, intake calculation, dose evaluation, record keeping, reporting and quality assurance of data. To begin with, all these were being manually carried out. Later, the electronic spreadsheet applications like Lotus, Excel were used for data base generation with manual data entry that was prone to errors. To overcome these, an in-house software was developed using Visual Basic as front end and Microsoft Access in the back end, and is being used for whole-body counting program of RSD.

Fig.1
Personnel Data Handling Module

Software Design and Development

Personnel Data Handling Module:

Personal details of the occupational workers can either be added or edited. The personal data includes the name, institution, IC number, designation, TLD number, date of birth, date of joining, height, weight, nature of job, year of counting, native State and dietary habit. These details are stored in a separate table as an Access file. Queries are also designed for the easy access of a particular worker's data. When a person's data is edited, his counting sequence number is automatically stored in the database, which makes, accessing of his spectrum data easier at anytime later. This module has built-in option to indicate the history of any earlier intakes. Since most of the data are being fed by "list & check" box options, error due to manual data entry is minimized. Duplication of data is totally avoided.

Spectrum Data Uploading & Dose Estimation Module:

An ASCII output file from Nucleus and Aptec gamma spectrum analysis softwares can be directly uploaded to this module for estimating the intake. Standardised set of radionuclides are selected in this spectrum for quantification. The analysis module gets the net counts under each specific radionuclide and estimates the activity using the pre-set calibration factors. This module uses the calibration factors and retention functions that are stored in a

database. If the estimated intake is above the minimum detectable activity, this module corrects for the residual activity of any previous intakes and re-estimates the current intake. Using the dose conversion factors stored in the database, the committed effective dose (CED) is calculated and stored. Also a separate data report is generated in parallel for every confirmed intake.

Module for Reports Generation:

The types of reports that can be generated by the software are: a) List of persons counted from a particular institution during a year, b) List of persons counted from a particular institution during any particular period, c) List of persons counted during a particular period irrespective of the institution to which they belong to and d) Section-wise report for a particular institution. Reports are generated by pre-designed queries that extract data from various tables and present them in a single report. These reports in the form of tables would contain all the essential information about the personnel including the intake particulars and CED.

Data Environment and Data Report components of ActiveX Designer are used to generate the above reports. The Data Environment component helps in establishing the connection between the database and the software and retrieving the desired records. The Data Report component brings out the reports. The data needed to be printed in the report has been chosen in the report design view. The parameters needed for report query are chosen online using list box option. The software has been made user-friendly that the reports can be generated in Excel format too.

Module for Quality Assurance (QA) Data Storage & Display :

The components of QA such as efficiency factors, background counts in various energy regions of interest for different types of whole body counting systems are given as input to this module. It stores the data and estimates the average, standard deviation and relative error. Any fresh QA input value, as and when given, is immediately compared with the previously stored data and accepted only if it is falling within 3σ range. Otherwise, the user is alerted before accepting the fresh input. This module has graphical display feature too to enable the user to see the trend in QA values. Options are built-in to the module to add more systems as well as additional QA parameters.

Future Improvements:

The deployment of such application oriented software helps in storing and archiving of all pertinent data for the occupational workers and contract workers upto a defined period of time as per regulatory requirement. The software has been made user friendly and database is free of manual entry errors. It also fulfills the requirements of ISO 9000:2001.

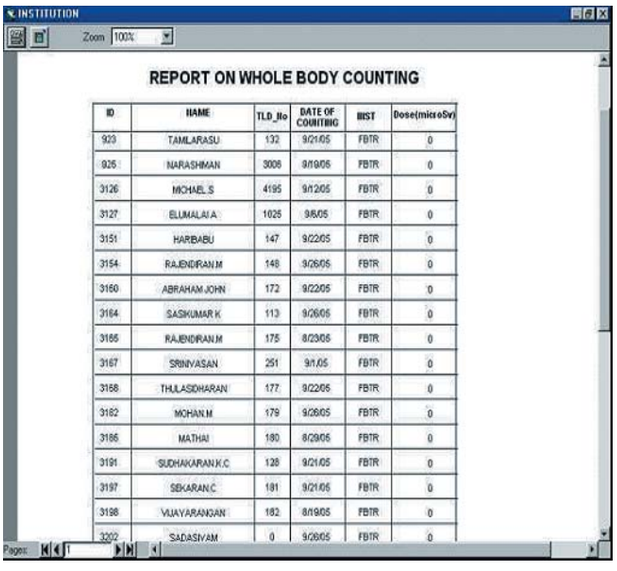

ID	NAME	TLD_No	DATE OF COUNTING	INST	Dose(microSv)
923	TAMILARASU	132	9/21/05	FBTR	0
926	NARASHIMAN	3006	9/19/05	FBTR	0
3126	MICHAEL S	4195	9/12/05	FBTR	0
3127	ELUMALAI A	1026	9/6/05	FBTR	0
3151	HARIBABU	147	9/22/05	FBTR	0
3154	RAJENDIRAN.M	148	9/26/05	FBTR	0
3160	ABRAHAM JOHN	172	9/22/05	FBTR	0
3164	SASIKUMAR K	113	9/26/05	FBTR	0
3165	RAJENDIRAN.M	175	8/23/05	FBTR	0
3167	SRINIVASAN	251	9/1/05	FBTR	0
3168	THULASIDHARAN	177	9/22/05	FBTR	0
3182	MOHAN.M	179	9/26/05	FBTR	0
3186	MATHAI	180	8/29/05	FBTR	0
3191	SUDHAKARAN.K.C	128	9/21/05	FBTR	0
3197	SEKARAN.C	181	9/21/05	FBTR	0
3198	VIJAYARANGAN	182	8/19/05	FBTR	0
3202	SADASIVAM	0	9/26/05	FBTR	0

Fig.3
Module for Reports Generation

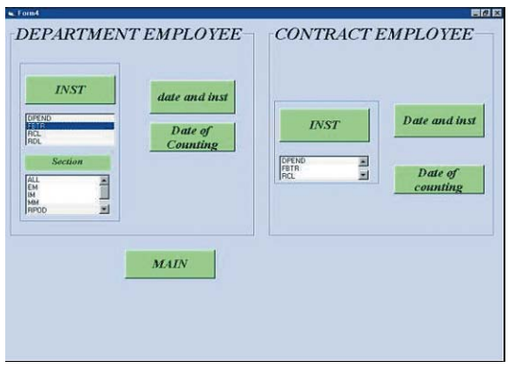

Fig.2
Spectrum Data Uploading & Dose Estimation Module

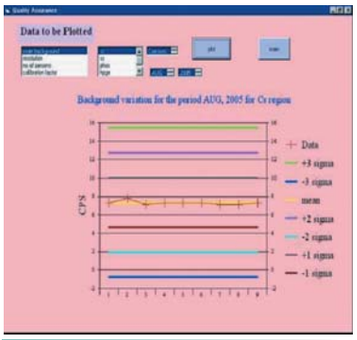

Fig.4 (a)
Module for Quality Assurance (QA) Data Storage & Display

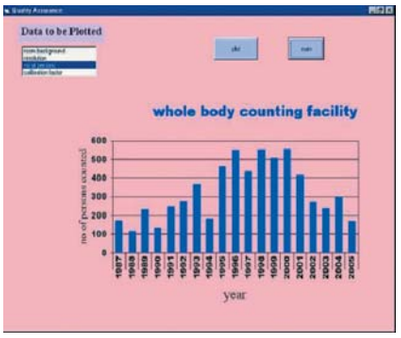

Fig.4 (b)
Module for Quality Assurance (QA) Data Storage & Display

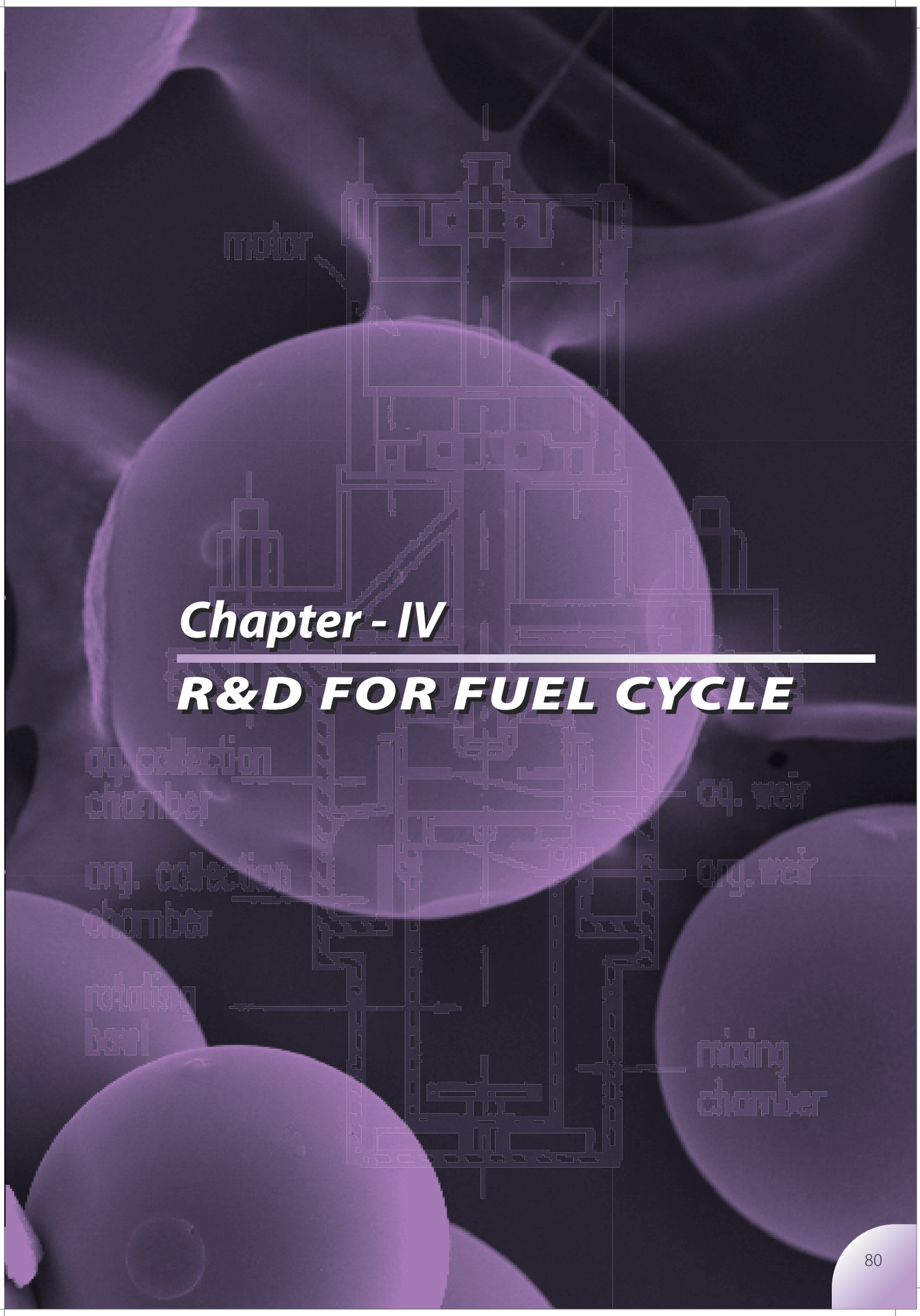

Chapter - IV

R&D FOR FUEL CYCLE

CHEMISTRY OF FUEL AND FISSION PRODUCTS

IV.1 Thermophysical Property Measurements on Nuclear Materials

Uranium-plutonium mixed oxide containing 45% PuO_2 has been proposed as the fuel for the expanded core for the operating FBTR. Uranium-plutonium mixed oxides containing higher amounts (>40%) of PuO_2 are being considered as potential fuels for the plutonium burner reactors. Heat capacity is an important thermodynamic property, which is required for understanding the various chemical interactions that are likely to occur during the irradiation of the fuel and thus for modeling the behavior of the fuel. No experimental data are available in the literature for the mixed oxides of $U_{0.55}Pu_{0.45}O_2$, $U_{0.45}Pu_{0.55}O_2$ and $U_{0.35}Pu_{0.65}O_2$. Hence, enthalpy increment measurements on these mixed oxides in the temperature ranges 956-1803 K, were carried out by the inverse drop calorimetry using a high-temperature differential calorimeter. The heat capacity data were computed from the measured enthalpy increments.

It can be seen from Fig.1. that the heat capacity data of all the three mixed oxides are indistinguishable within the experimental uncertainty of our measurements. It is to be expected since the heat capacities of UO_2 and PuO_2 at 298 K are within ± 5% of each other. They are also in agreement with the values computed using Neumann-Kopp's rule.

High temperature X-ray diffraction studies on the solid solutions of ThO_2 - $LaO_{1.5}$ and ThO_2 – $NdO_{1.5}$ were carried out to determine the solubilities of these rare earth sesquioxides in thoria. The solubility of $LaO_{1.5}$ in thoria varies from 49.7 to 50.3 mol % and that of $NdO_{1.5}$ from 45.7 to 46.2 mol %, respectively, from room temperature to 1473K. The lattice parameter, instantaneous (α_i instantaneous), mean (α_m mean) and linear percentage thermal expansivities thermal expansion coefficients for two compositions for each solid solution were also determined as a function of temperature using the high temperature X-ray diffractometry. Fig.2 shows the percentage thermal expansion of ThO_2 - $LaO_{1.5}$ solid solutions.

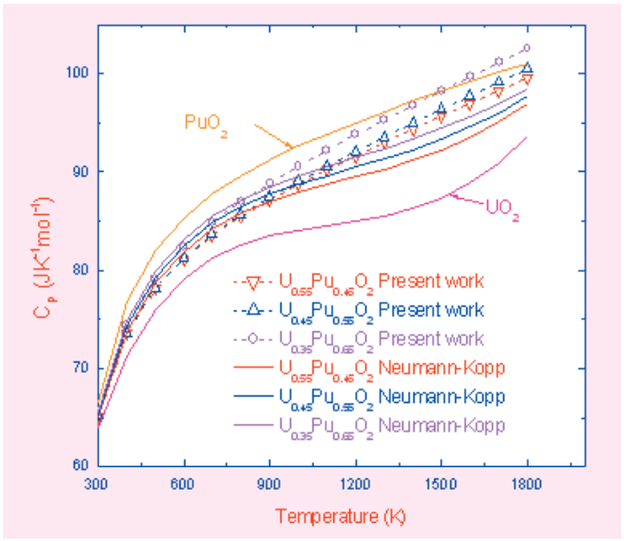

Fig.1
Comparison of the Present Heat Capacity Data of $(U,Pu)O_2$ Solid Solutions with Those Calculated using Neumann-Kopp's Tule.

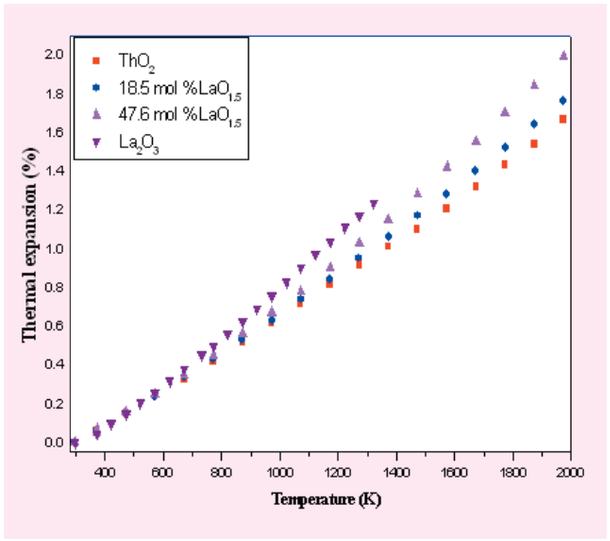

Fig.2
Thermal Expansion (%) as the Function of Temperature for ThO_2-$LaO_{1.5}$ Solid Solutions

IV.2 Formation of Ternary Mn-Te-O Phases on SS Clad of MOX Fuelled FBRs: High Temperature Mass Spectrometric Investigation

For a better understanding of fission-product tellurium assisted clad corrosion in mixed-oxide fuelled fast breeder nuclear reactors, one needs to consider formation of ternary oxide phases involving tellurium and stainless steel (SS) clad components also besides that of binary tellurides. This is particularly important, if the O/(M=U+Pu) of the fuel outer-surface were to ever become hyper-stoichiometric, that is > 2. Since our previous investigations on many binary metal tellurides led us to infer that the lowest tellurium activity is required for formation of manganese telluride, ternary system viz. Mn-Te-O system has been investigated first.

After establishing the ternary phase diagram of this system at 950 K in the composition range in and around the MnO-TeO_2 pseudo binary line, and performing a number of isothermal vaporization experiments that could confirm the existence of a quasi-congruently vaporizing three-phase equilibrium ($MnTeO_3 + Mn_3TeO_6$ + vapor), systematic high temperature mass spectrometric vaporization studies were conducted over the four three-phase regions (Mn_3O_4 + MnO + $Mn_6Te_5O_{16}$), (Mn_3O_4 + $Mn_6Te_5O_{16}$ + $MnTeO_3$), (Mn_3O_4 + Mn_3TeO_6 + $MnTeO_3$), and (Mn_3TeO_6 + $MnTeO_3$ + $Mn_2Te_3O_8$) in the temperature range 850-950 K. The p-T relations for the gaseous species TeO_2 (g), TeO(g), and Te_2(g) in the equilibrium vapor over these phase fields were obtained. Thermodynamic data for various heterogeneous reactions in each phase field as well as for the homogeneous gas-phase reaction TeO_2 (g) + 0.5Te_2 (g) = 2TeO (g) were deduced. Finally the Gibbs free energy and enthalpy of formation for the ternary phases $Mn_6Te_5O_{16}$, $MnTeO_3$, Mn_3TeO_6, and $Mn_2Te_3O_8$ were approved. A thermochemical assessment was then made to examine the conditions under which the ternary Mn-Te-O phases could be formed on SS clad of mixed-oxide fuelled (MO_2 ; M = U+Pu) fast breeder nuclear reactors. Three Pu/U+Pu ratios (0.20, 0.25, and 0.30) and four O/M ratios (1.9998, 2.0000, 2.0002, and 2.0004) were considered.

Fig.1 shows tellurium potentials Δμ(Te) that can exist in the fuel-clad gap as well as the threshold values required for formation of Mn-Te-O phases and binary M-Te phases. If threshold Te-potentials for formation of Mn-Te-O or M-Te phases are less than available Te-potentials in fuel-clad interface, then clad attack by tellurium can take place. (Positive values of Δμ(Te) are also shown in the figure only to enable comparisons amongst different phases) Amongst the four ternary phases considered, threshold Δμ(Te) values are the least for Mn_3TeO_6 and the greatest for $Mn_2Te_3O_8$. The values for $Mn_6Te_5O_{16}$ are less than for $MnTeO_3$ when O/M ≥ 2 and vice versa when O/M <2. Negative Dm(Te) values exist only for Mn_3TeO_6 (at all three Pu/U+Pu ratios and at O/M = 2.0002 and 2.0004) and for Mn_6Te5O_{16} (at Pu / (U+Pu) = 0.30 and 0.25 and at O/M = 2.0004). When compared with binary tellurides, the values for Mn_3TeO_6 at O/M = 2.0004 are more negative than that for tellurides of Fe, Ni, and Mo. Since it is known that O/M as well as oxygen potential of a MOX fuel increases with burn-up and that the oxygen potential would continue to increase even when the rate of increase in O/M would decrease drastically after a burn-up of 6 at.% it can be concluded that probability of formation of ternary phases Mn_3TeO_6 and $Mn_6Te_5O_{16}$ on SS clad there is a clear.

While the threshold Te-potential values for formation of M-Te phases do not depend on values of oxygen potential of the mixed-oxide fuel (and thus on Pu/U+Pu ratios), those for Mn-Te-O phases obviously do. This makes it important to study other M-Te-O systems also for a fuller understanding of Te-attack of SS cladding in MOX fuelled FBRs.

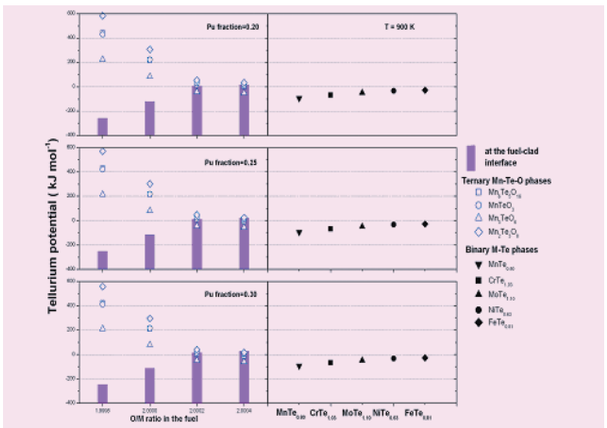

Fig.1
Comparison of Tellurium Potentials in Fuel-clad gap (filled bars) with Those Necessary for Formation of Mn-Te-O (open symbols) and M-Te (filled symbols) Phases (T=900 K)

IV.3 Development of a Rapid Separation HPLC Method for the Determination of Lanthanides in Uranium Matrix of Pyroprocessing Samples

Reprocessing is aimed at the separation of actinides such as uranium and plutonium from the spent fuel containing fission products, e.g. lanthanides and transuranium elements. In the evaluation of pyrochemical reprocessing methods using $MgCl_2$ based salts as electrolytes, analysis of lanthanide fission products in a uranium matrix (e.g. 1:10,000) is indispensable. In these studies, analysis of lanthanides such as La, Ce and Nd in trace levels is needed, as encountered in the cathode deposit of uranium. Thus, the separation and determination of lanthanides in large quantities of uranium is challenging and there is no report in the literature of a simple chromotive graphic technique to meet this requirement.

High Performance Liquid Chromatography (HPLC) has revolutionized as a powerful separation and analytical tool. Major advantages of HPLC are its ability to provide rapid and high performance separations. In the recent past, amide based modifiers have been shown to be promising candidates for actinide recovery. Since their solubility in aqueous phase is very low, they are attractive candidates for actinide separations employing extraction chromatography. Considering the desirable features of these modifiers, an extraction chromatographic technique was developed using bis-2-ethylhexyl succinamic acid (BEHSA) as the column modifier for separation of lanthanides from uranium matrix.

The retention behavior of uranium and lanthanides was investigated on C18 support modified with BEHSA as the modifier and α-Hydroxy isobutyric acid (α-HIBA) as the complexing reagent for elution. BEHSA solutions of appropriate concentrations were dissolved in methanol-water mixture and passed through the C18 column for the preparation of supports. After the completion of coating, the column was pre-equilibrated with about 60 mL of mobile phase prior to separation. Elution profiles of uranium and lanthanides were obtained as a function of the modifier concentration, mobile phase composition and its pH. A 5 mM BEHSA modified support was chosen for the quantitative analysis even though a good separation was established at 1mM support. This is for accommodating lanthanides during analysis, in the presence of large quantities of uranium. The BEHSA modified support offered an excellent base-line separation of lanthanides from uranium. Lanthanides could be accurately estimated in the presence of about 20,000 times of uranium. Based on the investigations with BEHSA support, an advanced characterization method has been developed for the rapid and accurate analysis of lanthanide elements in uranium matrix.

A large number of samples from pyrochemical process were analysed for their lanthanide contents (e.g. La, Ce, Nd) in uranium matrix. Uranium contents of these samples were also determined directly or with suitable dilution. For example, a separation of Nd (3 ppm) from U matrix (18 mg/mL) is shown in Fig.1. The results of these investigations were compared with standard analytical methods. For example, in one study, the lanthanide contents were measured using ICP-OES after removing uranium matrix with solvent extraction and the results were compared with HPLC. The concentration of uranium was also measured by standard analytical method, Davies and Gray and compared with HPLC. The lanthanide as well as uranium values were found to be in good agreement (within ± 2%). These studies established that the HPLC method is found to be fast, reliable and can provide accuracy required for a typical regular analysis. It is to be noted that the HPLC technique does not require pre-separation of uranium for the assay of lanthanides, whereas it is a pre-requisite with other analytical techniques.

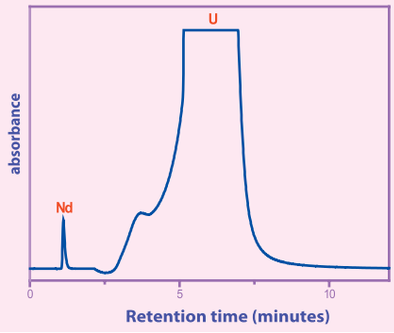

Fig.1
Separation of Nd from U Matrix of Pyrochemical Sample. Column: C18 (250 x 4.6 mm, 5m, Hypersil) coated with 5 mM BEHSA. Mobile phase: α-HIBA (0.1 M, pH 2.5), flow rate: 2 mL/min, PCR: Arsenazo(III), flow rate:1.5 mL/min, detection: 655nm. Sample injected: 20mL. Determined amounts: U(VI): 18 mg/mL and Nd(III): 3 ppm.

FUEL REPROCESSING
IV.4 Indigenous Anion Exchange Resins for Plutonium Purification

Ion exchange has been widely applied to various stages of the nuclear fuel cycle such us uranium milling, removal of contaminants from the primary coolant circuits, condensates and fuel storage pond water in water reactors, recovery of plutonium and other transuranics, and radioisotope production. Anion exchange process is being commonly used by most of the nuclear plants and laboratories for plutonium processing or purification. The inability of several elements to form the anionic complexes in nitric acid solution makes it possible to get a better decontamination factor. In the anion exchange process, plutonium is sorbed onto a strong base resin from a nitric acid concentration of around 7 M and eluted with dilute nitric acid.

In India, the purification and concentration of plutonium is carried out presently with an imported gel type anion exchange resin Dowex 1X4. To explore the suitability of the alternative indigenous anion exchange resins, Tulsion A-PSL 4 and Tulsion A-PSL 6, a program has been initiated at our centre in collaboration with M/s Thermax Pvt. Ltd., Pune, India. In order to make the resins withstand thermal or osmotic shocks and also to improve the radiation stability for nuclear applications some important features such as optimization of degree of cross-linkage, modified methods for curing copolymer beads, controlled chloromethylation and amination reactions have also been considered in the process of manufacture of the Tulsion resins. Tulsion A-PSL 4 and Tulsion A-PSL 6 are strong-base gel-type resins of 4% and 6% cross-linkage respectively with particle size in the range of 50-100 mesh.

Before plant scale operations, these resins should be evaluated for kinetics of sorption, stability in strong nitric acid medium and radiation fields, and ability to withstand osmotic shock due to alternating acidity in the loading and elution cycles environments used for the plutonium processing. Accounting for all the above-mentioned points, the experiments were designed for the evaluation of resins for plutonium processing.

Sorption Kinetics and Variation of $D_{Pu(IV)}$ as a Function of Acidity:

Distribution ratio for Pu(IV) was measured as function of time for all the three resins up to 24 hours. As shown in the Fig.1, both Tulsion A-PSL 6 and Tulsion A-PSL 4 were found to attain equilibrium within four hours whereas Dowex 1X4 was found to attain equilibrium after six hours. The values of $D_{Pu(IV)}$ increase with increasing nitric acid concentrations and reach a maximum at 7-8 M for all the three resins. Tulsion A-PSL 6 exhibited higher $D_{Pu(IV)}$ value at all acidities compared to Dowex 1X4 and Tulsion A-PSL 4, whereas the $D_{Pu(IV)}$ values of the latter resins were comparable with each other.

Gamma irradiation and Osmotic Shock:

The resins were moderated in 60-60 gamma chamber in presence of 8 M HNO_3, after irradiation the resins were analyzed for capacity, moisture content and Pu distribution ratio. Tulsion A-PSL 4 showed the minimum loss in total capacity (~14%) compared to Dowex (~21%) and Tulsion A-PSL 6(~22%). Dowex 1X4 exhibited severe damage in the polymer matrix compared to PSL 4 and PSL 6. Tulsion A-PSL 6 exhibited the minimum damage. At 200 MRad, Dowex 1X4 was completely dissolved in acid solution, whereas PSL 4 and PSL 6 became very soft and broke into smaller particles. The electron micrographs of the unirradiated and 100 MRad irradiated Tulsion A-PSL 4 is shown in Fig. 2. The extent of damage is comparable for all the three resins, with Tulsion A- PSL 6 showing marginally lesser damage over the other two resins. Osmotic shock experiments were done for the three resins by passing alternatively 8 M and 0.5 M nitric acid with flow rate of 2 bed volumes per hour. Even after 30 repeated cycles, no significant physical damage and breakage of beads was observed with all the three resins.

Loading and Elution:

The performance of the resins Tulsion A-PSL 4 and Tulsion A-PSL 6 were compared 7.2M HNO_3, washing with 7.2M HNO_3 and elution with 0.5M HNO_3. The loading and washing effluent samples collected at frequent intervals were analyzed for plutonium content. The data obtained on the plutonium loading and elution behaviour are summarized in Table 1 and Table 2. The loading behaviour of PSL 4 & PSL 6 was found to be same and were comparable to Dowex

1×4 (the performance of Dowex studied in earlier runs) under identical condition. The results indicate that due to its higher cross-linkage, PSL 6 shows tailing in elution compared to PSL 4 and Dowex 1×4. On the other hand elution behaviour of PSL 4 was found to be comparable with Dowex 1×4.

Tulsion A-PSL 6 was found to have higher plutonium sorption capacity and polymer matrix stability than the other two resins, while Tulsion A-PSL 4 and Dowex 1X4 were found to have comparable sorption capacity, kinetics, and resistance to chemical and radiation degradation. Preliminary experimental results on the evaluation of the two indigenous anion exchange resins namely Tulsion A-PSL 4 and Tulsion A-PSL 6 indicated that these indigenous resins can be used for the purification and concentration of plutonium.

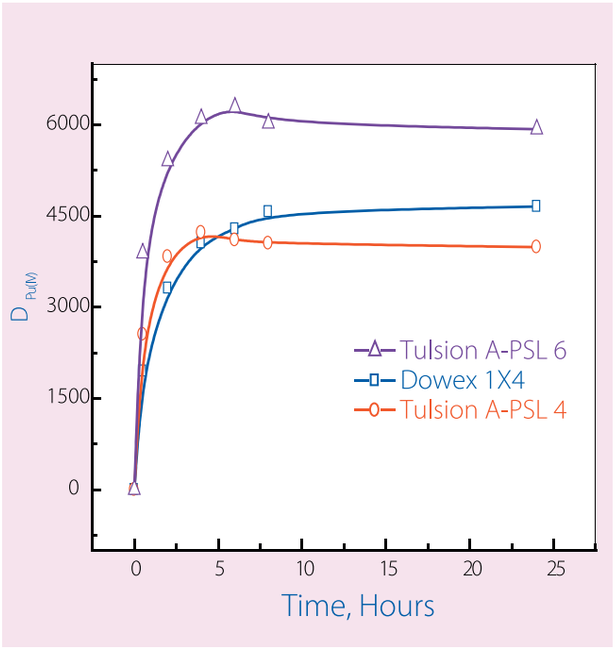

Fig.1
Variation of $D_{Pu(IV)}$ as a Function of Time

Table 1 - Loading

	PSL 4	PSL 6
Total amount of Pu loaded	4 g	4 g
Total Pu in the effluent (loading breakthrough)	8 mg	8 mg
Total Pu in washing	6 mg	6 mg
Net Pu loaded	3.986 g	3.986 g
% Pu loaded	**99.6**	**99.6**

Table 2 - Elution

Bed Volumes	Tulsion A- PSL 4	Tulsion A-PSL 6
1	169 mg	132 mg
2	1815 mg	1474 mg
3	1484 mg	1434 mg
4	311 mg	489 mg
5	65 mg	143 mg
Total Pu eluted	3.844 g	3.672 g
% Plutonium eluted	**96.4**	**92.0**

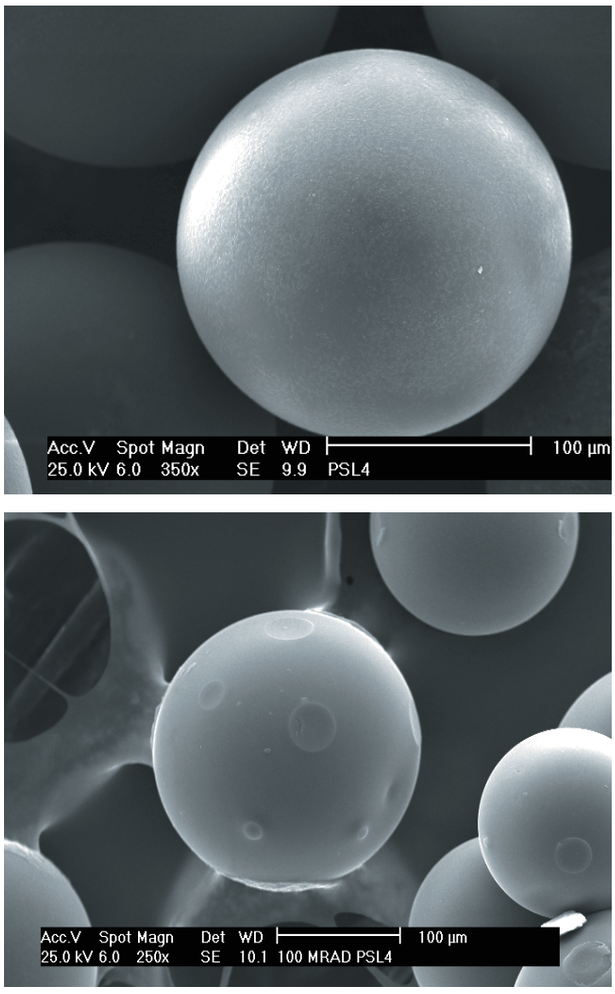

Fig.2
Scanning Electron Micrographs of Unirradiated and100 MRad Irradiated Tulsion A-PSL 4. Magnification: 350X and 250X.

IV.5 Electrochemical Behaviour of La, Ce, Nd Oxychlorides in $MgCl_2$- NaCl- and KCl Eutectic Salt

Oxide electrowinning is a pyrochemical method for the reprocessing of spent oxide fuels and production of fuel materials in granulated form for subsequent vipac fuel pin fabrication. 2CsCl-NaCl or NaCl-KCl is used as the electrolyte in this process flow sheet. Systematic investigations on the use of 50% $MgCl_2$-30%NaCl-20%KCl as the alternate electrolyte for the oxide electrowinning process are being carried out. As a part of these investigations, electrochemical studies were carried out on this $MgCl_2$- NaCl- KCl eutectic salt. The electrochemical window of the electrolyte was determined, to establish its utility as electrolyte for this process, to be from -1.2 V to 1.1 V vs Ag/AgCl reference electrode at 823 K. The valence state of Ce in the electrolyte was established using X-ray photoelectron spectroscopy. The redox behaviour of the lanthanide elements La, Ce and Nd in the electrolyte was studied using cyclic voltammetry and impedance spectroscopy. It has been deduced that the lanthanides are present as ROCl in the electrolyte and the reduction of oxychloride takes place in a single step according to the reaction

MeO+ + 1 e ß MeO

Figure1 shows two cyclic voltammograms, one when CeOCl alone is present in the electrolyte and the other when both UO_2Cl_2 and CeOCl are present. As can be seen, the reduction peaks corresponding to UO_2Cl_2 and CeOCl are well separated, which shows that CeO_2 can be separated from UO_2 by electrorefining process using this electrolyte. Fig.2 shows the cyclic voltammograms for a glassy carbon electrode in this electrolyte containing LaOCl at various scan rates. Analysis of the cyclic voltammograms has shown that the reduction of ROCl is quasi-reversible for scan rates in the range of $25 \leq v \leq 125$ mVs^{-1} and at higher scan rates it becomes irreversible.

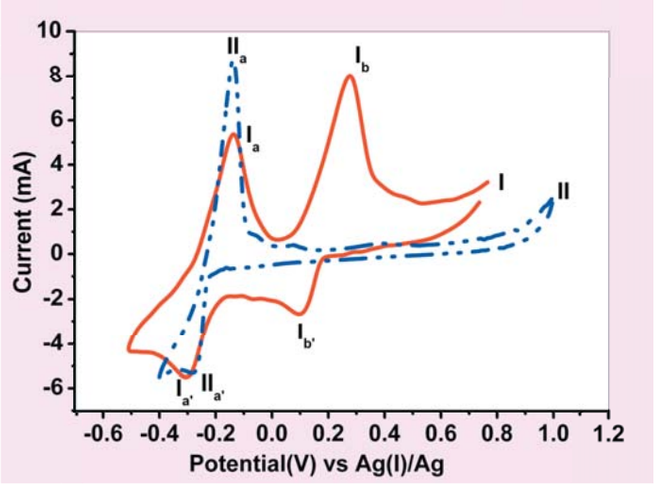

Fig.1
I). Cyclic Voltammogram for a Glassy Carbon Electrode in the $MgCl_2$-NaCl-KCl Eutectic Melt at 823K containing 0.305 mol% UO_2Cl_2 and 7.41 x 10-4 mol% CeOCl;

II). Cyclic Voltammogram for a Glassy Carbon Electrode in the $MgCl_2$-NaCl-KCl Eutectic Melt containing 1.60 x 10^{-8} mol cm^{-3} CeOCl at 823 K; Apparent Electrode area: 0.03926 cm^2 for I and II; Scan rate: 100 mVs^{-1}.

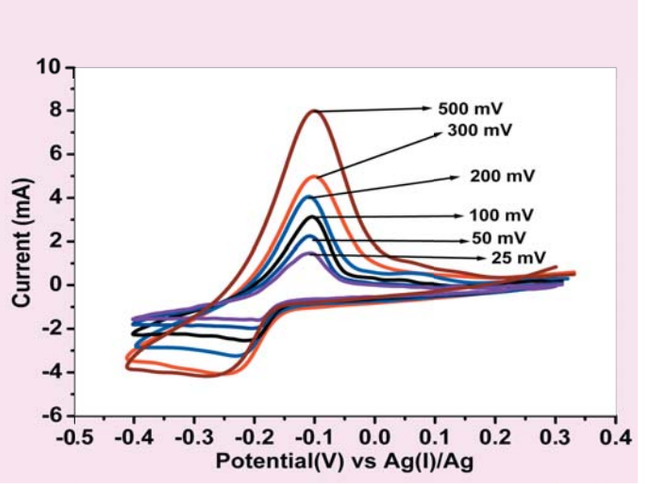

Fig.2
The Cyclic Voltammograms for a Glassy Carbon Electrode in $MgCl_2$-NaCl-KCl Eutectic Melt containing 9.47 x 10^{-6} mol cm^{-3} LaOCl at 873 K. Apparent Electrode area: 0.346 cm^2

IV.6 Modelling the Electrorefining Process

Molten salt electrorefining is a pyrochemical method considered to be ideally suited for reprocessing metallic fuels because, besides the advantages of other pyrochemical methods, it entails minimum number of process steps owing to the fuel remaining in the metallic state throughout the process. In this process, the spent metallic fuel is made the anode of an electrorefining cell having LiCl-KCl eutectic salt as the electrolyte and operating at 773 K and the actinides U and Pu are selectively electrotransported to a solid or a liquid cadmium cathode. Studies on the molten salt electrorefining process have been carried out for about a decade at our centre. Modeling the molten salt electrorefining process is necessary not only for understanding but also for predicting the behaviour of the system under various process conditions. Two groups of models, bone based on thermochemistry and the other based on electrokinetics have been reported in the literature. A code PRAGAMAN has been developed for the numerical simulation of the electrotransport behaviour of uranium and plutonium in the electrorefining cell. It is considered that in the electrorefining cell, equilibria exist among a pair of metals in the anode/cathode and their respective chlorides in the salt phase and a system of non-linear equations is set based on mass balance and thermodynamic equilibria consideration which are solved using MATLAB to arrive at the concentration profiles of eight elements and their chlorides in the anode, salt and cathode phases. It takes into account the different features that are possible in the electrorefining process: (a) various combinations of solid anode/cathode and liquid cadmium anode/cathode; (b) the sixteen different possibilities of anode and cathode combinations with respect to solubilities of uranium and plutonium, especially when both the electrodes are liquid cadmium and (c) the effect of applied potentials on the equilibrium constants and in turn their influence on the electrotransport behaviour.

Fig.1 and 2 show the results of computation using the code for a typical scenario in which the anode cadmium is initially saturated with U but unsaturated with Pu. Under these conditions, rate of U transport to cathode dominates over that of Pu, as is evident from the Pu/U ratio in Fig.2. Between point(a) and (b), both the electrodes are saturated with U and during this time only U gets transported , as is evident from both the figures. After (b), the anode becomes unsaturated with U and again the transport of Pu commences. But still the rate of transport of U dominates over that of Pu to the cathode. The computations also show that the amount of U and Pu transported to the cathode get slightly enhanced in the presence of lanthanide fission products and minor actinides.

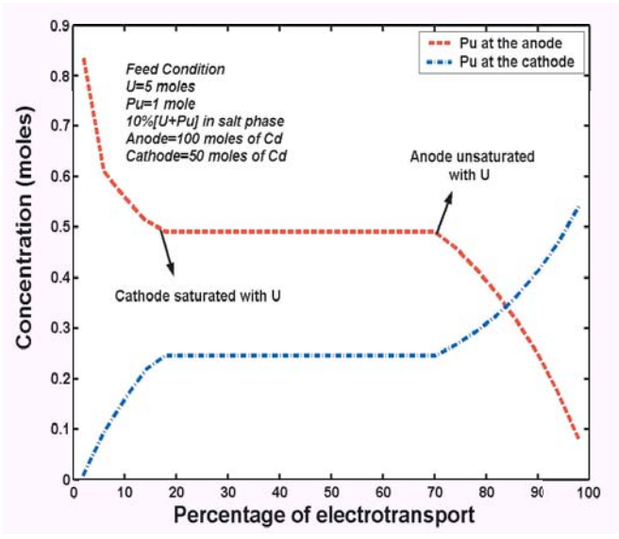

Fig.1
Variation of Concentration of Pu at the Liquid Cadmium Anode and Liquid Cadmium Cathode

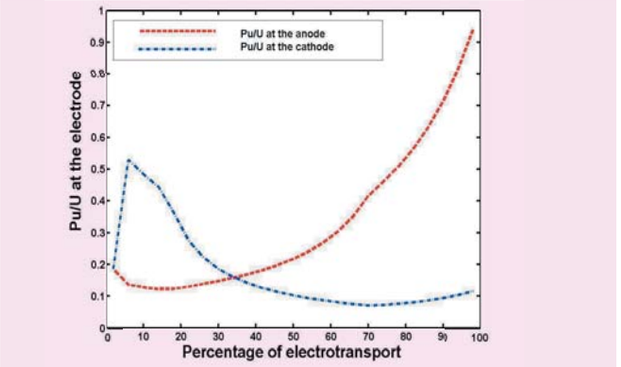

Fig.2
Variation of Ratio of Pu/U at the Liquid Cadmium Anode and Liquid Cadmium Cathode

IV.7 Room Temperature Ionic Liquids for Non-aqueous Reprocessing

Room temperature ionic liquids (RTIL) as the name implies are comprised entirely of ions and molten at temperatures lower than 373 K. Of late they are being studied extensively for various separation processes, especially applicable to the nuclear fuel cycle. Inorganic molten salt eutectics such as alkali/alkaline earth chlorides are employed as the electrolytic medium in non-aqueous pyrochemical reprocessing, at temperatures above 800 K. Substitution of the metal cation present in the electrolyte by unsymmetrical organic cations such as the 1-butyl-3-methylimidazolium ion (bmim+), results in substantial lowering of the melting point of the resultant organic chloride to 340 K. Employment of such organic chlorides as an alternative to the traditional high temperature inorganic molten salts in non-aqueous reprocessing may lead to the operation of the entire process at ambient conditions. In addition, the management of the spent electrolyte may be much simplified, as these organic electrolytes can be tuned to be completely incinerable.

The present studies investigating the suitability of RTILs for non-aqueous reprocessing focussed on the electrochemical stability of systems such as bmimCl, bmimPF6 etc., and the electrochemical behavior of strategic elements (for example, U(VI)) and potentially useful fission products (like Pd(II)) in different ionic liquids.

Palladium (II) in bmimCl was found to be speciated as $[PdCl_4]^{2-}$ and other stable square planar complexes. The cyclic voltammogram of palladium (II) indicated a surge in reduction current at -0.5 V due to palladium deposition. A nucleation phenomenon observed for palladium deposition was studied in detail by chronoamperometric methods. Instantaneous and progressive nucleation models were employed for describing the kinetics of nucleation. The diffusion coefficient of palladium (II) in bmimCl was found to be ~10^{-7} cm2/s. These studies indicated the feasibility of electrodepositing palladium from the RTIL medium. Electrowinning of palladium from bmimCl revealed the formation of dendrites and also exhibited dependance on the applied potential.

Similarly, the rate of dissolution and the electrochemical behavior of U(VI) in bmimCl was studied using various electrochemical techniques. Dissolution of uranyl chloride (taken in the form of $M_2UO_2Cl_4$, M = Cs or Na) in bmimCl was studied at 343 K by monitoring the amount of uranium dissolved using a spectrophotometric method. Rapid dissolution (>50%) occurred within 30 minutes and more than 70% dissolved in 5 hours. The cyclic voltammogram of uranyl chloride in bmimCl medium indicated an onset of reduction current at –0.5 V (Vs Pd) with a maximum at -0.7 V (vs Pd). The reduction of U(VI) ion (UO_2^{2+}) to U(IV) (as UO_2) as shown in equation 1 below is responsible for the surge in reduction current at -0.5 V.

$$UO_2^{2+} + 2\,e^- \leftrightarrow UO_2 \text{ (at cathode)} \quad (1)$$

$$2\,Cl^- \leftrightarrow Cl_2 + 2e^- \text{ (at anode)} \quad (2)$$

In order to confirm the nature of the reduced product, the uranium-loaded bmimCl was electrolysed at a controlled potential of -0.8 V (vs Pd) with a platinum plate as cathode and glassy carbon as anode for 18-20 hours. A black dense, fine particles got deposited all over the surface of the platinum plate with aggregation in some places, as shown in Fig.1. The Faradaic efficiency of electrodeposition was 80-86%. Thus, the electrowinning of uranium as UO_2, and palladium as metal has been demonstrated at near-ambient conditions from bmimCl medium.

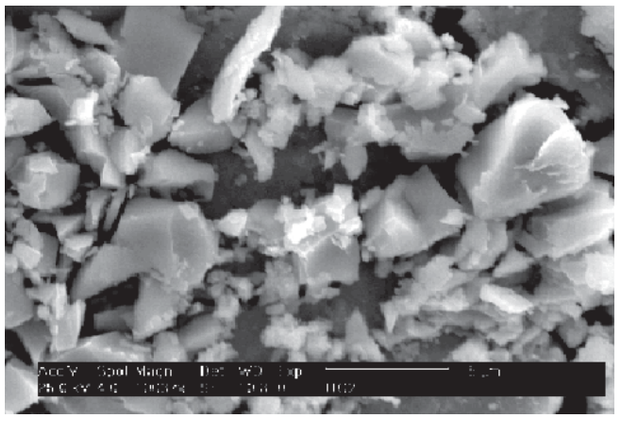

Fig.1
SEM Micrographs of UO_2 Deposit Obtained by Controlled Potential Electrolysis of 40 mM Solution of Uranyl Nitrate in bmimCl on a Pt plate (1cmx 1 cm) at -0.8V for 18-20 hrs.

IV.8 U/Th Separation by Counter-current Liquid-liquid Extraction with Tri-sec Butyl Phosphate by using an Ejector Mixer-Settler

Conventional U/Th separation process (THOREX process) uses either low concentration of tri-n-butyl phosphate (TBP) such as 5% or higher concentration of 30% or more as extractant depending on whether uranium is to be separated alone or along with thorium. As the typical composition of THOREX feed solution is about 200 mg Th/mL and about 240 µg U/mL in 4M HNO_3, use of TBP leads to third phase formation due to the limited solubility of the $Th(NO_3)_4$.3TBP complex in a non-polar diluent. Due to low separation factor evens in the process with 5% TBP, uranium product is contaminated with thorium, which demands several stages of scrub for its removal and needs to be purified further by ion-exchange or precipitation.

This has influenced the need to develop novel extractants to improve the performance of the process. In this connection, several trialkylphosphates have been synthesized and some of them have been tested by batch equilibration experiments. Studies revealed that distribution ratios for the extraction of Th(IV) and third phase formation tendency could be drastically reduced by the introduction of branching at the first carbon atom of the alkyl group, at the same time enhances the distribution ratios for the extraction of U(VI). Thus tri-secbutyl phosphate (TsBP) has been found to give higher U/Th separation factor as compared to TBP in batch equilibration experiments. The separation of U and Th can therefore be more effectively accomplished using TsBP as the extractant.

To demonstrate the performance of TsBP, countercurrent liquid-liquid extraction runs were camed out using a high efficiency air pulsed ejector mixer-settler. A photograph of the fume hood housing the mixer-settler is shown in Fig.1 The unit used for the present runs has 16 stages with mixer having a volume of 10 mL and settler having a volume of 25 mL and is made of a monolithic block of polypropylene. The nozzle and diffuser are 1.5 and 2 mm in diameter. Each mixer is connected to three settlers and each settler is connected to three mixers in such a way that the dispersed phase from n^{th} stage mixer enters the n^{th} stage settler where separation of organic and aqueous phases takes place. The organic and aqueous phases from the n^{th} stage settler are flown to $(n-1)^{th}$ and $(n+1)^{th}$ stages respectively. The counter current flow of organic and aqueous solutions in mixer-settler is represented in Fig.2.

Extraction behaviour of TBP and TsBP with respect to U/Th separations, has been compared by carrying out counter-current liquid-liquid extraction runs with the mixer-settler employing TBP and TsBP as extractants. A feed solution of around 200 mg Th/mL and 240 µg U/mL in 4M HNO3 and 0.183M Trialyl Phosphate dissolved in heavy normal paraffin (which corresponds to 5% TBP (v/v)) has been used to simulate the process conditions. These runs confirmed that TsBP requires lesser number of stages for scrubbing as compared to TBP. Based on these runs, a new flow sheet (Fig. 3) (for U/Th separation by 0.183M TsBP/HNP has been designed and employed by integrating extraction, scrubbing and stripping.

Integral process consisted of five stages of extraction, four stages of scrubbing and seven stages of stripping. After confirming the attainment of steady state, organic and aqueous stage samples were collected from settlers. All organic and aqueous stage samples were analysed for free acidity, uranium and thorium. The performance of the integral process was validated by repeating the runs under identical conditions.

The profiles for the extraction of thorium and uranium in the integral U/Th separation run are shown in Fig.4. The data indicate that concentration of thorium in the organic phase in the extraction section is less than 2 µg/mL and thorium concentration in the scrub section decreases with stage number towards the strip section. The concentration of thorium in the aqueous sample collected from the 16^{th} settler (raffinate) was around 149.3 mg/mL and uranium was found to be below detectable limit. Concentration of uranium in the 8^{th} stage organic phase leaving scrub section was around 163 mg/mL with a very small amount of thorium (8 mg/mL). In the strip section, concentration of uranium in the aqueous product collected from the 7^{th}

settler was about 649 µg/mL with a small amount of thorium (9 µg/mL). Hence, thorium and uranium present in the feed solution with a ratio of 823:1 got separated in to, uranium with a small amount of thorium (Th:U = 1:72) and $Th(NO_3)4$ solution with negligible amount of uranium as shown in Fig.3. The uranium product was decontaminated from thorium by a factor of $5.9*10^4$. The concentration of uranium in the lean organic, collected from the 1st stage was below detectable limit, indicating no loss of uranium.

The above studies indicated that TsBP can be employed for U/Th separation with lesser number of stages and the uranium product would achieve a high decontamination factor from thorium. TsBP is a promising extractant for the processing of irradiated 232_{Th} for the recovery of 233_U and also for the processing of certain ores of thorium containing uranium.

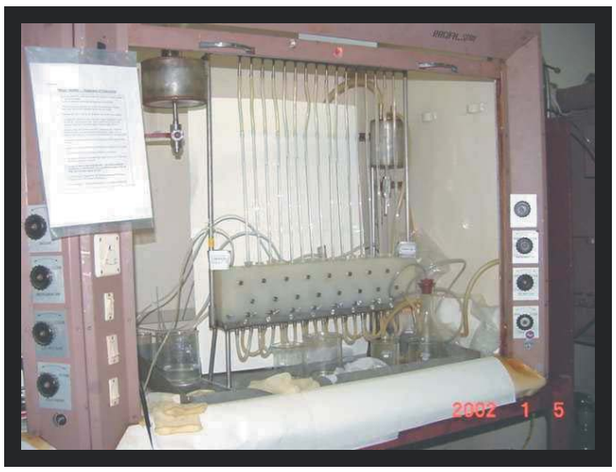

Fig.1
Fume Hood Housing the Ejector Mixer-settler

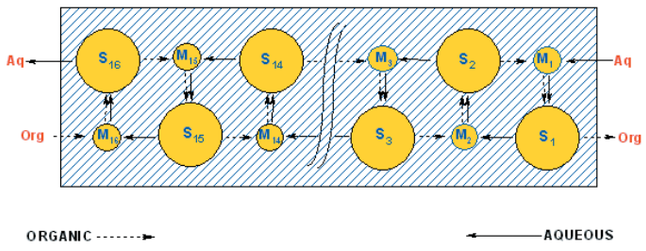

Fig.2
Counter-current Flow of Organic and Aqueous phases in a Mixer-settler

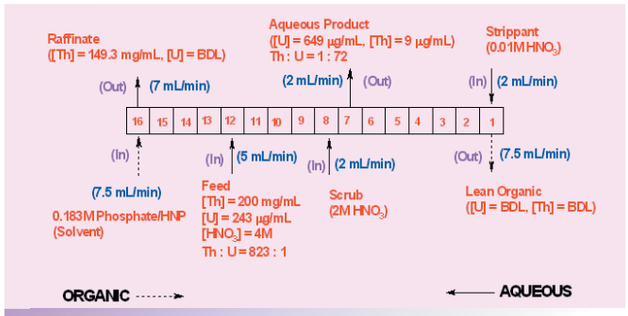

Fig.3
Flow Sheet for the Integral U/Th Separation Experiment with 0.183M TsBP/HNP

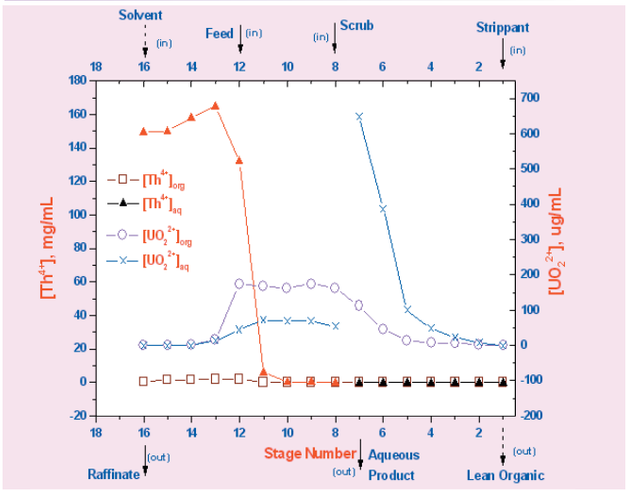

Fig.4
Stage Profiles for the Separation of U (VI) and Th(IV) by 0.183M TsBP/HNP in an Integral run.

IV.9 Uptake of Strontium from Aqueous Chloride Solutions using Crown Ether Bonded Hydrogel

Hydrogel is a three-dimensional network of hydrophilic polymer chains that holds water. It has widespread applications in biomedical, pharmaceutical, food and environmental fields due to its biocompatibility, drug permeability, easy deliverability and disposal. Crown ethers (CE) are extensively studied for the uptake of specific metal ions from the aqueous solutions mainly by solvent extraction. A novel technique has been used to chemically bond CE in hydrogel to trap specific ions. Studies have been undertaken to use crown ether functionalized hydrogels for uptake of strontium (Sr) from the effluents generated during reprocessing of Fast Reactor Fuels.

The extraction and stripping processes would be highly efficient and simple if the crown ethers are covalently bonded to the polyacrylamide hydrogel backbone. This is achieved if the crown ether is coupled with acryl group that can be co-polymerized with acrylamide during the photopolymerization process. CE functionalized hydrogel extracts specific ions from the aqueous solution. These ions are stripped from the hydrogel by water or nitric acid. Same hydrogel can be used for many cycles of extraction and stripping since CE is covalently bonded to the hydrogel. Specificity of a crown ether for ion can be improved by tailor making the crown ether with suitable attachments.

Experiments have been carried out at IGCAR for uptake of Sr using specific CE chemically bonded to hydrogel. Polyacrylamide hydrogels were prepared by photopolymerization of 10% w/w acrylamide (AAM) and 1% w/w N, N'-methylene bisacrylamide (MBA). After photopolymerization, the hydrogel was washed and immersed in deionized water to reach equilibrium. Volume of these hydrogels changes when they are soaked in solution of an acid, base or an electrolyte or kept in an irradiation chamber but no degradation was observed. There are several factors such as ionic strength, temperature, electric field, radiation, acidity, basicity and charges on the network that affect the swelling of a hydrogel. Hydrogel swells by 25, 150 and 18% in 3M NaCl, NaOH and HNO_3 respectively. Fig.1 shows the degree of swelling of the hydrogel in nitric acid at different concentrations. This swelling is due to ionic screening of dipole-dipole interaction of the polymers that result in the network expansion. This swelling was observed to be reversible when the gel was placed back in water.

At longer times, the gel in HNO_3 deswells linearly as shown in Fig.2 due to chemical modifications of the amide groups to aldehyde and carboxylic acid by HNO_3. In NaCl, the gel volume remains the same at longer times whereas, in NaOH, gel swells linearly due to hydrolysis. This longtime volume change is not reversible. Radiation and acid can break some of the C-C bonds. 10 Mrad γ irradiation deswells the gel to 45% of its volume. Diffusion coefficient of water in the gel was estimated as $4x10^{-7}$ cm^{-2}/s that is 60 times lesser than that of water self-diffusion.

4-acrylamidobenzo 18-Crown -6 (18C6) bonded hydrogel, shown in Fig.3, was cut into 4mm cubic pieces and taken in a bottle. 10mL of 1000 ppm $SrCl_2$ aqueous solution was added to the bottle. The ionic conductivity was measured from time to time. It reached steady state in 2h and this time depends on the size of the gel piece. Gel beads of 4μm diameter would need 7s to reach steady state. Sr^{++} concentration in the solution decreased due to the extraction of Sr^{++} by CE. Trapped Sr^{++} was stripped by repeated washings with DM water or 2N HNO_3. Same hydrogel was used for more than 20 cycles of extraction and stripping with identical results. Extraction efficiencies of various ions in aqueous solution in chloride form were estimated. The gel without any crown ether did not extract any ion. CE in the gel extracts Sr^{++}, Cs^{+}, K^{+} and Na^{+} with 17, 4, 38, and 21% loading; the corresponding mass distribution coefficients are 5.4, 1.9, 5.4 and 1.7 respectively. However, there was no uptake of H^{+} ions from the solution. As a part of R&D, it is planned to prepare many derivatives of 18C6 and test them for selectivity of Sr^{++}.

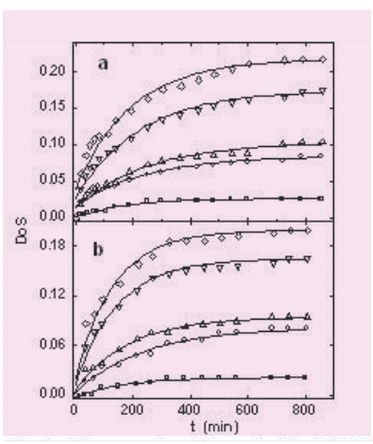

Fig.1
Degree of Swelling (DoS) a) 0.5% and b) 1% MBA gels. □ - 0.1N, O-0.5N, Δ1N, ▽-2N & ◊ - 3NHNO$_3$

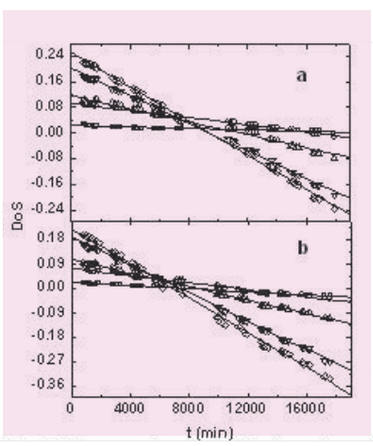

Fig.2
Degree of Swelling (DoS) at Longer Times. □ - 0.1N, O-0.5N, Δ1N, ▽ -2N & ◊ - 3NHNO$_3$

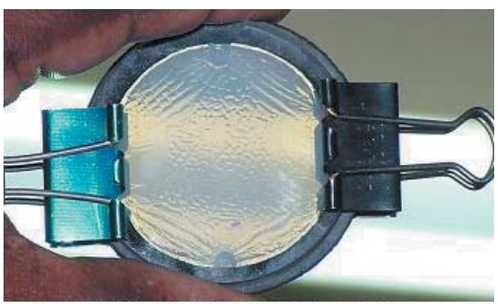

Fig.3
CE Gel Formed in the Quartz Cell

IV.10 Reprocessing of Spent FBTR Fuel in CORAL

After demonstrating the reprocessing of FBTR spent fuel with a burn-up of 100 GWd/t, the reprocessing of additioal pins with 25 and 50 GWd/t burn-up, was taken up in CORAL (COmpact Reprocessing facility for Advanced fuels in Lead cells, hitherto known as Lead Mini Cells). In this phase of the campaign, the impact of several process flowsheet parameters were studied apart from carrying regular production. These studies have enabled fine-tuning of the process flowsheet of the Demonstration Fast Reactor Fuel Reprocessing plant (DFRP).

Based on the operational feedbacks, a new facility for spent solvent treatment is being added to enable studies with various washing reagents. This will enable better understanding of the behaviour of solvent during reprocessing with high burn-up fuels. Another important activity taken up was the replacement of one of the banks of centrifugal extractors.

In CORAL facility, there are banks which are of fixed weir as well as variable weir for controlling interface. In variable weir type, over and above the fixed weir, air pressure is provided to alter the interface location. In the fixed weir type banks, the interface location cannot be altered. For this purpose, each stage is provided with air pressure over the weir by suitable tappings for air. Variable weir is required for handling systems of widely varying densities of fluids. Even though the weir heights can be pre-determined based on the chosen process flow sheet conditions of CORAL, to evaluate the performance, both the two types were deployed.

During the operation of the extractors over the last three years, it has been seen that maintenance requirement of variable weir type centrifugal extractor is higher than that of the fixed weir type. These problems are mainly due to the swelling of the PVC gasket between the drive shaft and the rotating bowl leading to the blockage of inter-phase air line of that particular stage which leads to aqueous phase flowing along with organic phase and subsequent build up of the level in the aqueous upstream stages leading to dripping from the bank. Drilling a hole with a long drill bit cleared the blockage in the affected bowl. Since the problem was recurring it was decided to replace the adjustable weir type CE units with the fixed weir type CE units since this will enable uninterrupted operation of the plant. Studies are separately being conducted to overcome the problem faced in variable weir type units.

Remote removal and replacement of the bowls in a constricted space is a challenging task. Each stage of the rotating bowl assemblies was remotely removed and taken to a-tight maintenance glove box. It was dismantled to remove the variable interface bowl from the motor. Subsequently all the bowls were replaced with fixed weir type bowls to the existing motor. Additional gadgets were fabricated for remote handling of the assembly. All the airlines of variable interface type bowls were removed remotely using a pneumatic grinder with cut off wheel. This was a difficult task to carryout with the help of manipulator and in-cell crane. After this, all the variable weir bowl assemblies were placed in respective stages and tightened remotely by a pneumatic wrench. The task was completed successfully and the unit was commissioned to take up further reprocessing campaigns.

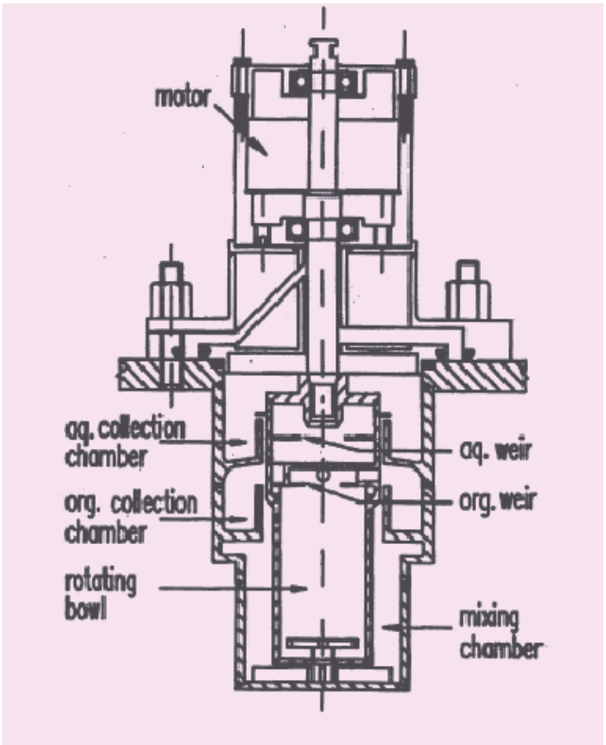

Fig.1
Schematic of a Centrifugal Extractor Stage

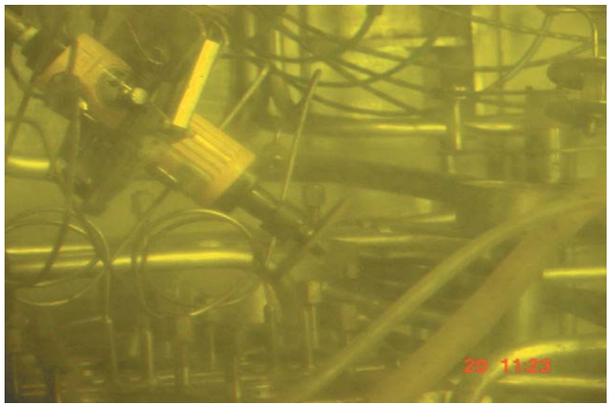

Fig.2
Remote Cutting of Interface Airline.

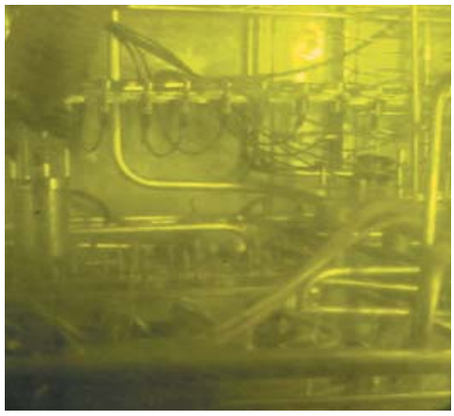

Fig.3
Replacement of the New Bowl

IV.11 CFD Simulation of Flow Fields in Vortex Diode

Pumping radioactive liquids in reprocessing plants is a problem of long standing due to requirement of a no moving part, maintenance free and highly reliable pumping system. Recently liquid transfer systems using fluidic devices like vortex diodes and Reverse Flow Diverter (RFD) are finding application in reprocessing and waste management facilities. The key feature of a fluidic device is that it does not contain moving parts, which are in contact with the process stream. This confers inherently high reliability, maintenance free operation and long life for radioactive liquid transfer applications.

Vortex diode is basically a disc-shaped chamber with a tangential port and an axial port. Flow entering the tangential port sets up a vortex and establishes a large pressure drop across the device (Reverse flow mode). However, if the flow enters the axial port it creates a substantially radial flow distribution and only a modest pressure drop equivalent to two 90° bends (Forward flow mode). The ratio of these two pressures for a given flow rate is the performance index of the diode which is termed as diodicity, $D = Eu_r/Eu_f$. (Eu is the Euler number, which represents pressure drop in dimensionless form). The device thus acts as a leaky non-return valve and can be incorporated in single and double acting fluidic pumps. A schematic of vortex diode is shown in Fig.1.

Though the concept of vortex diode is not new, adequate design guidelines are not available in open literature. The flow in the fluid system like vortex diode comes under confined vortical flow and the performance of the diode is largely dominated by the turbulent vortex. In order to understand the physics of confined vortical flow and to formulate design guidelines, a collaborative project to simulate the flows in vortex diode was taken up with NCL, Pune. Selected diode geometries along with the pressure drop – flow data were given as input to NCL for CFD simulation with Fluent 6.0. IFMG has identified that a laminar model describes the flow fields in diodes better than turbulent models during reverse flow mode. The results of simulation with laminar and κ-ε models for both forward and reverse flow mode are shown in Fig.2.

Profiles of tangential velocity over diode chamber cross section has revealed that the vortex created during reverse flow mode consist of a free vortex region where circulation ($\Gamma = \omega r$) is constant and a forced vortex region where tangential velocity is proportional to radius. The simulation showed that the transition from free to forced vortex region is not symmetric for both halves of diode chamber due to the presence of tangential port at one of the halves. Tangential velocity profiles for 125 and 150 mm diode for three different tangential inlet velocities chamber depicting the two vortex regions are shown in Fig. 3.

The velocity vector plot and static pressure contour plot for 125 mm diode corresponding to a flow rate of 2600 lph are shown in Fig.4 and Fig.5. The radial pressure distribution

across the diode chambers showed sub-atmospheric pressures at the center of the vortex and there can be incipient cavitation at very high inlet velocities. The radial pressure distributions for 125 and 150 mm diode chamber at three tangential velocities are shown in Fig.6.

IFMG has validated our experimental data by running CFD simulations for 30, 70, 100 and 125 mm diodes for the tested Reynolds number range. A comparison of our experimental data and the CFD predictions is shown in Fig.7.

Our present design of vortex diodes has yielded a maximum diodicity of 50 for 125 mm chamber at 2600 lph. To explore the possibility of attaining higher diodicities, simulations are carried out at IFMG with design modifications in axial and tangential port nozzles. Simulations predicted higher diodicity of around 60 at an inlet velocity of 1.4 m/s when the divergence angle of the tangential nozzle is changed from 5° in the present design to 7°. . Simulations with an axial port having higher radius of curvature (RC=32 mm instead of 16 mm in the present design) also yielded diodicity of the order of 65 at high Reynolds numbers as shown in Fig. 8.

Diodicity experiments need to be conducted incorporating these changes in divergence angle and radius of curvature of the port nozzles to verify the CFD predictions. Simulations revealed periodic oscillations in steady state pressure drop created by the vortex, which may be attributed to the precession of vortex centre. To throw more light into this phenomena and to identify location of free to forced vortex transition for a given design of vortex diode, velocity field measurements need to be carried out. These studies will provide better understanding of confined vertical flow, which will lead to better design of diodes. Ultrasound Velocity Probe (UVP) measurements within the diode chamber will be taken up by NCL along with exploring the possibility of diode chamber design modifications for bettering the performance in the next collaborative project.

Fig.1
Schematic of Vortex Diode

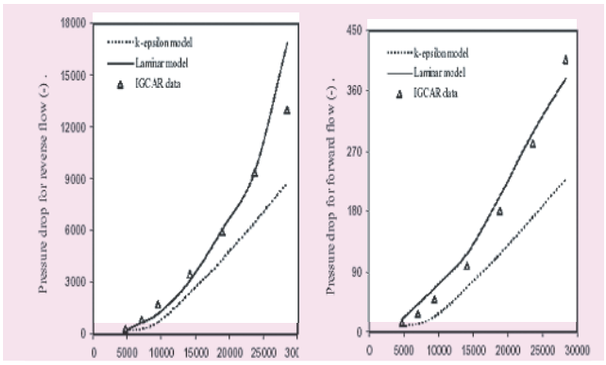

Fig.2
ΔP - Re Plot for Reverse Flow & Forward Mode for the case of 90mm Diode with Different Flow Models

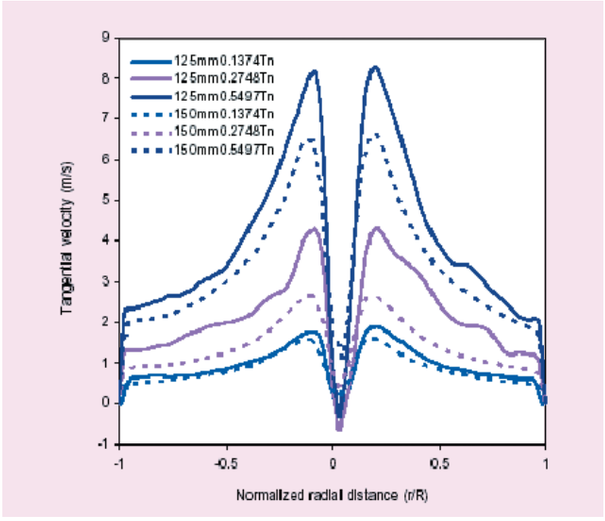

Fig.3
Tangential Velocity Profiles for 125 & 150mm Diode for Three Inlet Velocities

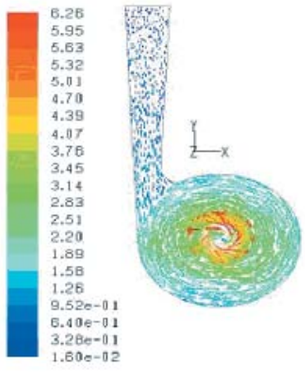

Fig.4
Velocity Vector Plot for 125mm Diode - Tangential Entry - Flow Rate 2600 L/hr

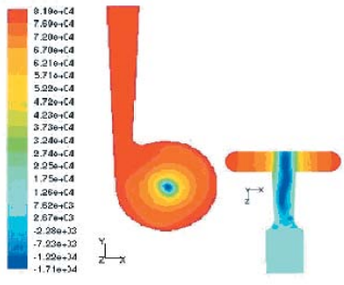

Fig.5
Static Pressure Contour Plot for 125mm Diode - Tangential Entry- Flow Rate 2600 L/hr

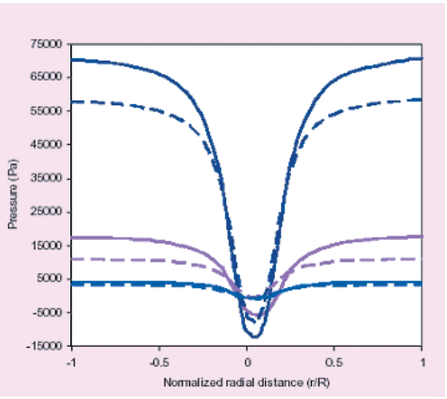

Fig.6
Radial Pressure Distribution for 125 & 150mm mm Diode - Three Inlet Velocities

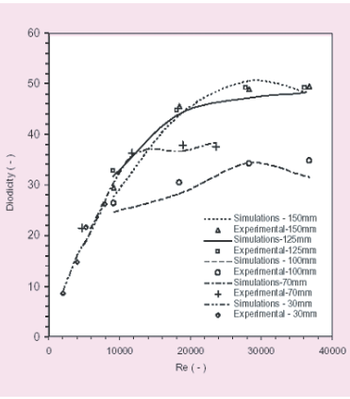

Fig.7
Experimental Data & CFD Predictions for Different Diodes

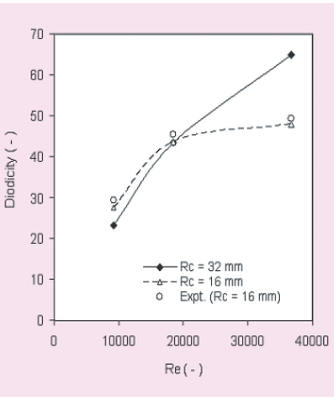

Fig.8
Variation of Diodicity with Re for Different Radius Curvatures (Rc) of Axial Port Nozzle

IV.12 Modelling Activities in Nuclear Fuel Reprocessing

Aceto-hydroxamic acid (AHA) is a novel reductant and complexant for several tetravalent and hexavalent actinides e.g., plutonium(IV) and neptunium(IV). It makes separation processes for these actinides quite simple and results in a simpler plant design. At present, its use has been proposed in the new processes for reprocessing the spent nuclear fuel such as UREX (URanium EXtraction process) and UREX+ (UREX process with additional enhancements). Considering the potential application of AHA in the nuclear fuel reprocessing, extensive studies on modeling of AHA behaviour in the PUREX (Plutonium URanium EXtraction) process and its thermodynamic parameters have been initiated at the Centre. Information on the thermodynamic parameters for AHA-water system is scarce. Recently the measurement of densities and water activities of AHA-water solutions at several temperatures has been carried out at the centre. Based on these studies, apparent molar volumes, activity coefficients, osmotic coefficients and excess Gibbs energy of AHA-water solutions have been predicted. Fig.1 shows a plot of error surface for the prediction of prediction of aqueous density of AHA solutions at several concentration and temperature levels

Hexavalent plutonium is an important non-key species in the PUREX (Plutonium URanium EXtraction) process. A significant quantity of Pu(VI) is generated during the dissolution of the high Pu content fuel of fast reactors. As it is extracted at a lesser rate than the key component Pu(IV) by the PUREX solvent, there is a risk of loss of valuable Pu to aqueous raffinate waste leading to subsequent extra operation for recovery and rework. In the recent past, experimental data on Pu(VI) extraction related to PUREX process was reported by BARC researchers. Combined with the archival data in the literature, reported data were analyzed and an extraction model was developed at our centre. The developed model is being integrated with the in-house developed computer code SIMPSEX (SIMulation Program for Solvent EXtraction) for the flowsheet analysis and simulation. Fig.2 shows a parity plot between experimental data reported by BARC researchers as well as archival data and the predicted values from the model developed at IGCAR and agreement is good. Fig.3 shows variation of Pu(VI) distribution coefficient with the aqueous acidity which indicates satisfactory fitting to the experimental data.

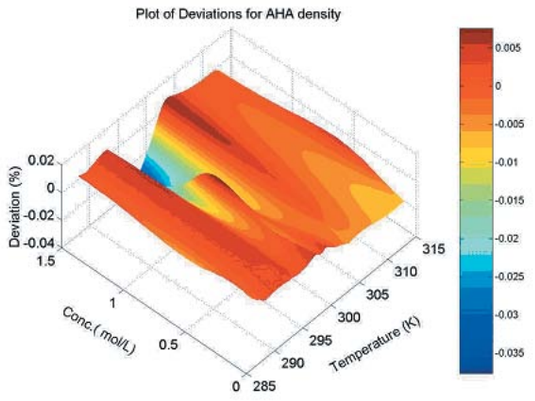

Fig.1
A Pictorial Representation of the Error Surface for Prediction of Aqueous Density of AHA Solutions at Several Concentration and Temperature Levels

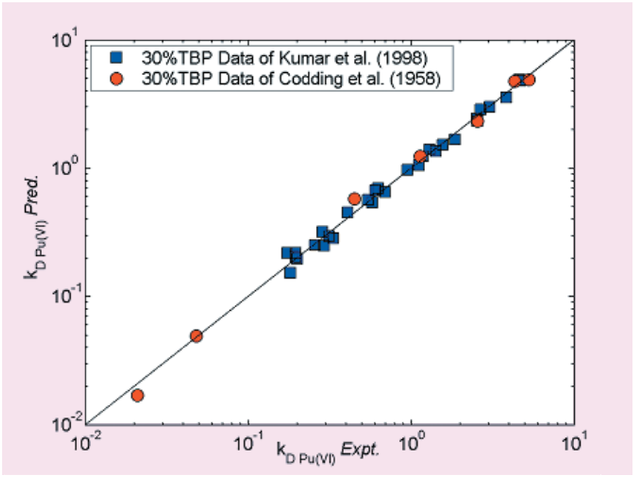

Fig.2
Parity Plot for Pu(VI) Distribution Coefficients in PUREX Process.

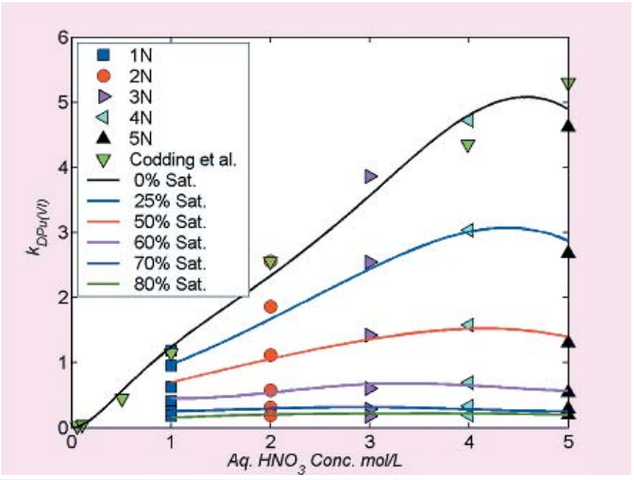

Fig.3
Variation of Pu(VI) Distribution Coefficients with Aqueous Acidity in PUREX Process. Experimental Data for 1-5 N Acidity was generated at BARC.

IV.13 Materials and Coating Technology Development for Pyrochemical Reprocessing Applications

Pyrochemical reprocessing in molten chloride salt medium has been considered for the reprocessing of metallic fuels envisaged for the future fast breeder reactors. For undertaking various unit operations like salt preparation, electrorefining, cathode processing etc. components made of type 316L SS, Ni-base alloys, high alloy steels and high density graphite will be utilized in the high temperature molten chloride salt environment. Development of materials and coating technology is important, and the manufacturing route for engineering components needs to be established. In collaboration with a private industry, attempts have been made to cast a seamless vessel of type 316L SS for application in salt preparation unit. The investment casting mould was designed and optimized, and casting route was established with a prototype vessel. Currently, the vessel is under finishing operation, and will be evaluated for integrity and chemical composition.

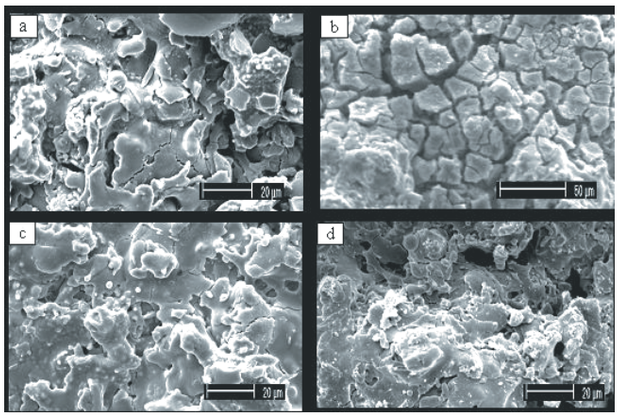

Fig.1
SEM Micrographs of Partially Stabilized Zirconia Coated over type 316L SS in (a) as-coated, (b) 5 h exposed, (c) 100 h exposed, and (d) 500 h exposed to molten LiCl–KCl salt

For better service and life, zirconia based ceramic coatings with a bond coat of MCrAlY has been proposed over the components employed towards this purpose. An attempt was made to study the plasma spraying of such coatings on type 316L SS, and enhancing their property through laser surface treatment. Type 316L SS rod of 100 mm length was coated upto 40 mm with 300 micron thick Yttria stabilized zirconia (8% Y_2O_3) by plasma spraying over a 50 micron metallic bond coating of NiCrAlY using the facilities in the industry. The as-coated sample was characterized for porosity and surface morphology by optical microscopy. The coated samples were assessed for corrosion behaviour in molten LiCl+KCl medium at 873 K for periods of 5 h, 100 h, 250 h and 500 h. Corrosion tests in molten LiCl-KCl salt were carried out in a molten salt test assembly (MOSTA) specifically designed and fabricated inhouse. The as-coated and tested samples were examined by optical microscopy and SEM for homogeneity and integrity, and corrosion of type 316L SS substrate. Area percentage porosity measured by following ASTM E 2109 indicated the porosity of the coatings around 10 %. The cross-section micro hardness

indicated fairly high hardness values (1100 VHN) in the ceramic region, a hardness value of 249 VHN in the bond coat region, and a hardness value of 283 VHN in the substrate. The percentage weight loss of the samples exposed in molten chloride medium at 873 K for 100 h and 500 h was about 0.3 %. Except for the sample exposed to LiCl-KCl for 5 h, the SEM micrograph of the 100 h, 250 h and 500 h exposed samples are similar in appearance to that of the as-coated surface (Figs 1 (a-d)). The surface of such samples showed little or no degradation of the coating after exposure to molten salt up to 500 h. This indicated better corrosion resistance of ZrO_2 in molten LiCl-KCl. The yttria stabilized zirconia coating performed well without significant degradation and corrosion attack.

Air Plasma Spraying results in the presence of limited porosity and micro-cracks in the coating. In order to eliminate such porosity and micro-cracks laser treatment was pursued by using a continuous wave (CW) CO_2 laser. The coated samples were laser treated at 50 and 100 W power using a 3-axis Computer Numerical Controller (CNC) workstation. The as-coated and laser treated samples were characterised by using XRD, cross sectional micro structural studies, microhardness and porosity. Surface morphology was examined using optical microscopy and SEM. The porosity in the as-coated sample decreased from 10% to 0.5% in the laser treated sample. Segmented cracks were formed due to residual stresses developed during laser melting and solidification. The melted thickness increased marginally as the laser energy increased. Delamination existed near the bond coat/ceramic interface in the coating as the melted thickness was higher for higher laser energy. Microhardness measurements indicated higher hardness in the laser treated region. Optical and SEM examination revealed the polygonal grains of zirconia formed during laser remelting in all the laser treated samples. The detailed analysis of the XRD of laser treated samples in the range 72-76° showed that doublets are forming after laser melting revealing the formation of tetragonal, non-transformable tetragonal and cubic phases. With the increase of laser power, the non-transformable tetragonal phase increased marginally. Further work is in progress to establish and optimize the procedures for component manufacturing.

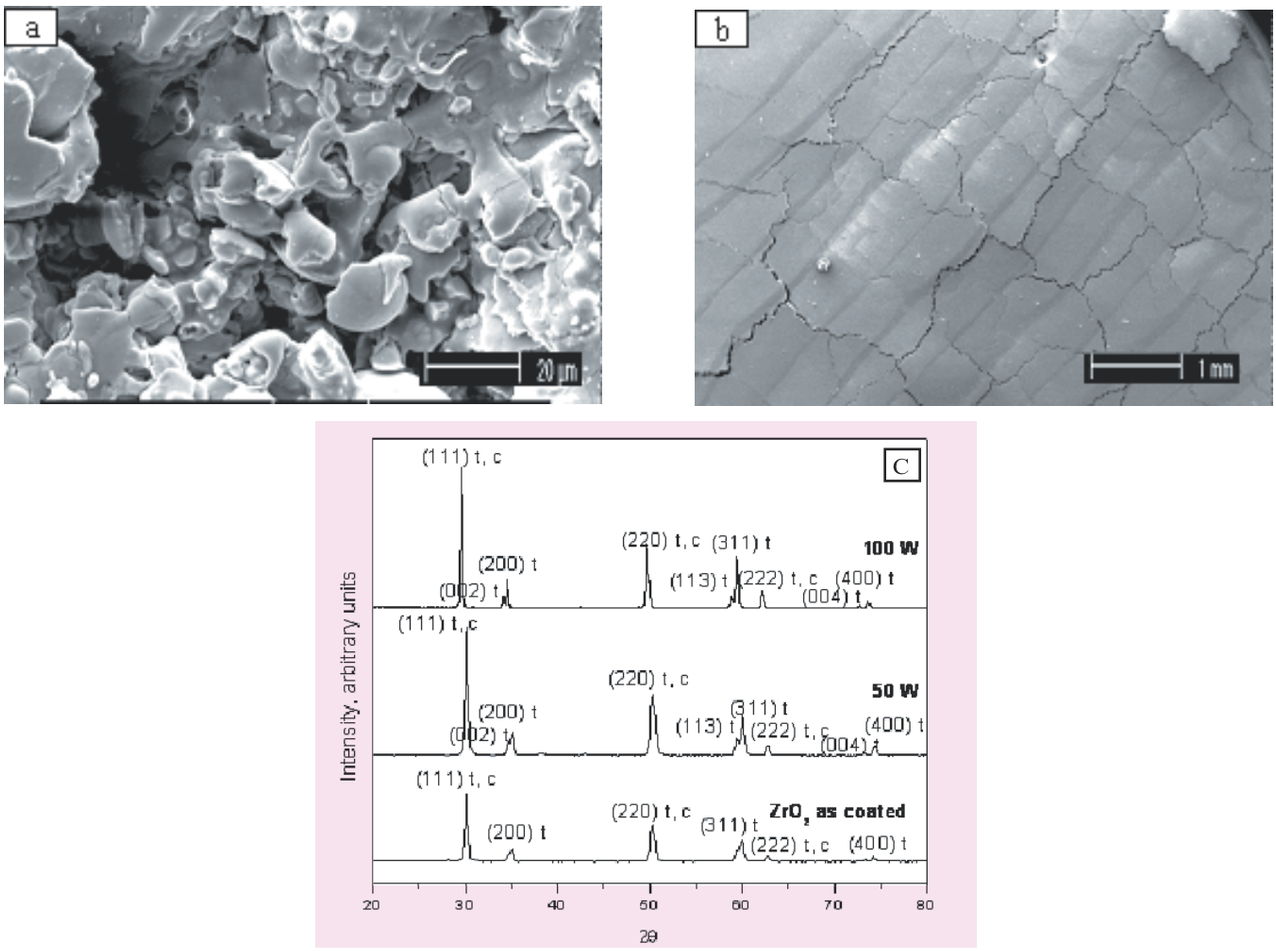

Fig.2
SEM Micrographs of PSZ Coating on type 316L SS, (a) As-coated, (b) Laser Melted at 100 W, and (c) XRD pattern of Laser Melted Samples.

IV.14 Evolution of Design of Choppers for Fast Reactor Fuel Reprocessing

Based on the feed back from the first-generation chopper used in CORAL, a single pin chopper has been designed for FBTR fuel chopping in DFRP. In the second generation, this design has been simplified from rotary movement of the magazine to linear movement. To avoid the problem of entangling of spacer wire in the earlier design, positive shearing of spacer wire in each cut is ensured. The prototype of this chopper is in advanced stage for testing. To enable a compact design with high throughputs, a third generation-chopper design is being conceived. This chopper will be used for PFBR fuel pins in DFRP.

The schematic of the second-generation chopper is given in Fig.1. In this, magazine movement for pin selection is carried out through a linear slide mechanism. This enables precise movement and better alignment with the chopper unit. There is no modification in the pin feeding mechanism. The profile of the gripper and cutter have been modified to keep the spacer wire intact even after a cut thereby avoiding entanglement, which was a major difficulty in the operation of CORAL chopper.

For PFBR fuel pins, the capacity requirements are much higher than that of FBTR. Hence multipin chopping is conceived. Since PFBR fuel pins are very lengthy, modification in pin feeding is also required. These issues are addressed in the third generation choppers. Fig 2 gives the schematic of this design. In this chopper design, because of the slender nature of the pin, to avoid crimping of the cut section, cutting blade profile is so chosen to emulate single pin chopping. Also to reduce the load on the cutter, two pins at a time are cut during the partial movement of the drive. With the total movement of the drive all the ten pins are cut. A pusher makes feeding of all the ten pins at a time initially. Later, a wedge arrangement with a drive enables further feeding and gripping. This eliminates the fuel pin selection mechanism used in the second-generation chopper. This also reduces the total length of the chopper. Cutting is carried out vertically compared to the hozontal action as used in the second generation chopper thereby eliminate the shunter mechanism, required to avoid the flying of chopped pellets in the horizontal design.

All the parts of the chopper, which undergo wear and tear, are designed for remote maintenance and can be replaced remotely with the help of manipulator and in-cell crane. Also all the operations can be sequenced through a microprocessor based control unit kept outside the cell.

The second generation FBTR chopper can handle all the three types of fuel pins of FBTR (two types of mixed carbide and one of mixed oxide). This will be commissioned prior to PFBR chopper. This is possible since these two systems are located in separate cells. The feedback from the hot operations of the second-generation chopper will be available for incorporation in the third generation design, which will be tested in DFRP itself. Hot experience of the third generation chopper in DFRP will enable fine-tuning of the chopper design for the PFBR reprocessing plant to ensure improved availability.

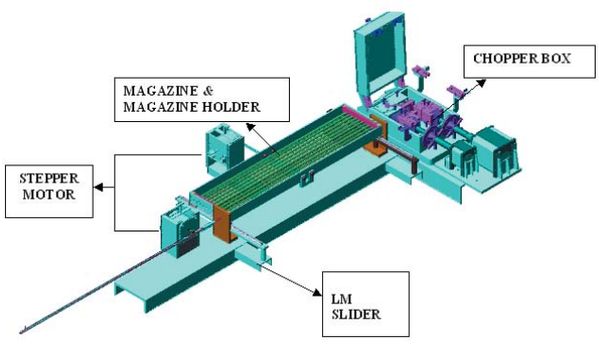

Fig.1
Schematic of Chopper for FBTR Fuel.

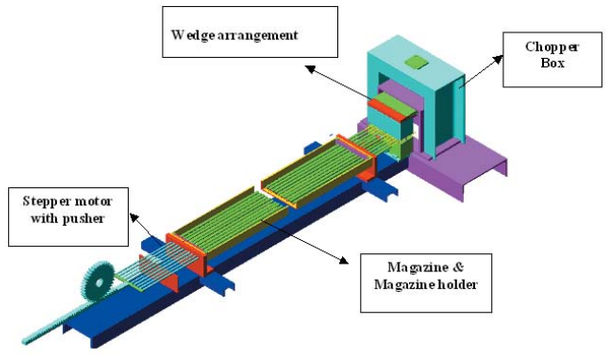

Fig.2
Schematic of Chopper for PFBR Fuel.

IV.15 Studies on the Fabrication and Thermal Diffusivity of Simulated Synroc Waste Forms

Crystalline ceramic matrices are emerging as an alternative to the presently employed borosilicate glass matrix for the immobilization of radioactive wastes. This is mainly due to the superior chemical durability of crystalline ceramics. Synroc (synthetic rock), an assemblage of four titanate minerals, is well known system among the ceramic waste forms. It is especially suitable for fixing large amounts of actinide and noble metal elements expected in the high level wastes (HLW) from fast reactors.

Synroc waste forms were fabricated using an inexpensive nano-anatase as the source for the major matrix material, TiO_2. The simulated HLW used were of fast reactor origin, including the one expected from the FBTR fuel after a burn-up of 50 Gwd/t with a cooling period of 3.5 years. Three different consolidation methods were employed, viz., cold uniaxial pressing and sintering (CUPS), hot isostatic pressing (HIP) and hot uniaxial pressing (HUP), to fabricate monoliths of high density (15 wt% waste loading).

In the CUPS method, the powders were cold uniaxially pressed into 10 mm diameter pellets and sintered at 1473 K for 2 h in Ar/4%H_2. In the second method, the powders were made into pellets of 25 mm diameter and about 2 mm thickness having ~ 45% theoretical density. They were stacked in one-end-closed stainless steel (SS) tubes of 28 mm internal diameter and 2 mm wall thickness, and subjected to HIP at 1473 K and 118 MPa for 3h in argon at DMRL, Hyderabad. In the third method, the powders were compacted by HUP in 10 mm diameter graphite dies at 1423 K and 30 MPa for 2 h in argon at MPD, BARC. Fig. 1 shows the photograph of a batch of three isotropically compacted SS capsules after HIP. The products were characterized for density, surface area, phase composition and microstructure. XRD showed satisfactory phase formation in all cases. CUPS yielded pellets of 85-90% density. The HIP and HUP methods gave monoliths of near theoretical density (4.2 g/cm^3) and they also showed a dense and fine-grained microstructure. Surface area estimation by gas adsorption showed practically nil adsorption, indicating the absence of any open porosity.

Thermal diffusivity is a critical property of any waste form, and very little information exists in the literature on the high temperature data. So, measurements were carried out with high density synroc pellets by a laser flash technique. The thermal diffusivity values were found to vary very slowly from 8.2 x 10^{-3} cm^2/s at 673 K to 7.2 x 10-3 cm^2/s at 1373 K (Fig. 2). Only limited measurements at room temperature are available for comparison. The presently measured thermal diffusivity extrapolated to the room temperature (0.9 x 10^{-3} cm^2/s), agrees with the literature value for a typical synroc assemblage.

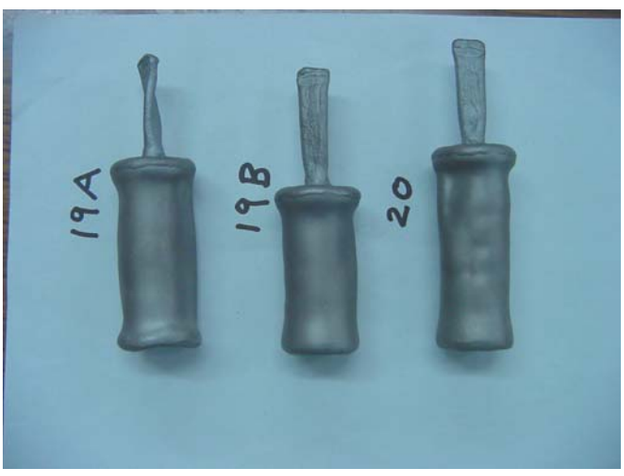

Fig.1
SS Capsules Containing TiO_2 after Hot Isostatic Pressing

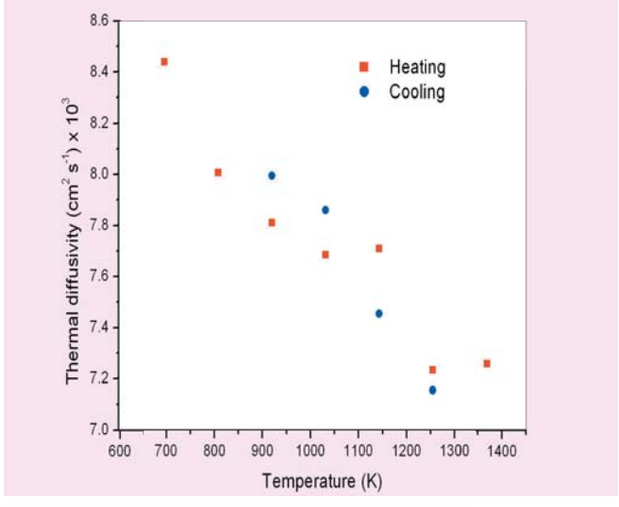

Fig.2
Variation of Thermal Diffusivity as a Function of Temperature

IV.16 Current Status of Demonstration Fast Reactor Fuel Reprocessing Plant

With the successful completion of the engineering R&D and the Pilot plant (CORAL) operation, Demonstration fast reactor fuel reprocessing plant (DFRP) represents the third phase of the four phase development strategy being adopted for mastering fast reactor fuel reprocessing technology. It serves a strong foundation to embark on the fourth phase, which is the commercial reprocessing plant for PFBR (PFRP).

The primary objective of DFRP is the demonstration of regular reprocessing of FBTR fuel in a sustained manner with high availability and capacity factors. DFRP will also demonstrate reprocessing of PFBR core till the commissioning of PFRP. All vital feedbacks obtained from the operational experience of CORAL with respect to critical equipment like single pin chopper, thermosyphon dissolver, feed clarification centrifuge, centrifugal extractors, sampling systems and remote analytical systems will be incorporated in the DFRP.

It is planned to implement novel features in DFRP, namely, (a) laser dismantling of hexagonal wrapper of fuel subassemblies, (b) hull monitoring using HPGe/La Br_3 detectors, (c) on-line monitoring of plutonium in raffinate and lean organic streams from centrifugal contactors based on indigenously developed fiber-optic spectrophotometric (FOS) instruments, (d) process analysis of high active solutions using FOS generating nil/minimum analytical waste, (e) demonstration and validation of indigenously developed detectors viz., On-Line Alpha Monitors (OLAM) for monitoring low level plutonium concentrations and Neutron Collars for high plutonium concentration in product streams. Validation of these devices in DFRP is very important since these have to be deployed in large numbers in PFRP.

The cell piping works is being taken up in several packages. With the major design inputs available from CORAL campaigns, the piping engineering of complex cells such as sampling, contactor, chopper and dissolver are in full swing. The piping in the rest of the cells is in progress. All the major equipment such as chopper, dissolver and centrifugal extractor banks are in various stages of fabrication. The in-cell crane development has been completed and it is being fabricated. Major works in high active storage vault have already been completed.

In order to demonstrate the PFBR spent fuel subassembly reprocessing, it is planned to add a head-end facility to the one constructed already. This facility will have cells for receiving PFBR fuel subassembly, dismantle the pins and transport them to the already constructed cells. By integrating these two facilities, it will be possible to not only close the FBTR fuel cycle but also demonstrate and reprocess the initial discharges of PFBR. Atomic Energy Regulatory Board has cleared the construction of the facility.

IV.17 Seismic Refraction Survey at Fast Reactor Fuel Cycle Facility Site

Seismic refraction survey is a geophysical method based on the property of seismic waves, which travel through different soil media in different velocity. Seismic refraction methods are used to determine the depth and structure of geological units, detect cavities or voids and fractures and fault zones. Purpose of the survey is to explore the subsurface stratigraphy including rock topography. The subsurface strata information helps in deciding founding levels and finalizing design parameters of various civil structures. Results of the seismic refraction survey supplement the data from geotechnical investigations.

Seismic refraction survey was carried out at Fast Reactor Fuel Cycle Facility (FRFCF) site. Traverse spacing is one of

the important parameters in Seismic Refraction Survey. Factors that affect the traverse spacing are the geology of the site, importance of the project, time required for survey and the features like fault and fractures to be identified. A grid spacing of traverse will give a fair idea of the geological units of the site.

A Continuous seismic refraction technique was used for data collection and the same was interpreted by `Generalized Reciprocal Method'. The survey was conducted along eleven N-S profiles and 44 east-west profiles on both sides of the main road. Length of N-S profiles was 445m and the same for E-W profiles on east side of road was 180m. Lengths of E-W traverses on west side of road varied between 90m and 138m depending on the spread lengths available. Location of the seismic refraction traverse is shown in Fig.1. Geophones for the survey were kept at 5m/ 6m interval. 24-channel signal enhancement seismograph was used for data collection. Seismic waves were produced by exploring a small charge buried in a hole of about 1.5m depth. Seismic waves were picked up by geophones having 8 Hz natural frequency.

Results of the continuous refraction survey revealed that the sub-surface at the site comprises of three layers including rock. These layers, depending on their compressional wave velocities, were interpreted loose sand (velocity 300m/ sec to 500m/sec) followed by compact sand/ weathered rock (velocity between 1400m/sec and 2000 m/sec). These layers overlie the granite gneiss rock, the velocity for which was evaluated to be between 4000m/ sec and 5800m/ sec. This order of the rock velocity for granite gneiss indicates good quality of rock. Narrow range of velocity variations in overburden indicated uniform nature of the layers. Variation in depth to bedrock along various traverses is small, indicating that weathering in the rock is uneven. In general, bed rock was available at a depth of 14m to 20m below the ground level. A few zones in bedrock having wave velocity less than 4000m/sec were delineated. These zones were interpreted to be weak/ shear zones in bedrock. A typical profile from seismic refraction survey is shown in Fig.2.

The depth to rock evaluated by refraction technique agreed remarkably well with those inferred in boreholes. It is generally seen that the rock depths evaluated by refraction survey matched with the level of rock inferred in boreholes where RQD is more that 50 percent and the same continues to improve with the depth. The RQD value obtained from geotechnical investigation varies from 50 to 100 which indicates that compression wave velocity of bed rock obtained from seismic refraction survey and RQD value of rock cores obtained from site specific geotechnical investigation are matching. A typical comparison of bore hole details and seismic refraction details is shown Fig.3.

A 3-D rock profile was generated from the seismic refraction traverse for the rectangular area of FRFCF site. The 3 –D profile of the rock surface along with the contour map is shown in Fig.4. In general bed rock is available at shallow depth along the western side and deeper towards eastern side. Results of the survey did not reveal any major shear or fault zone which might have posed foundation problems. Thus, the selected site is geologically suitable for the construction of FRFCF.

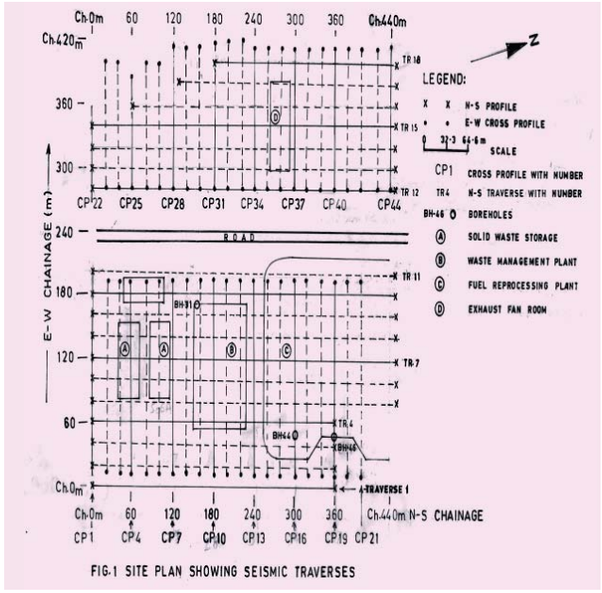

FIG.1 SITE PLAN SHOWING SEISMIC TRAVERSES

Fig.1
Site Plan Showing Seismic Traverses

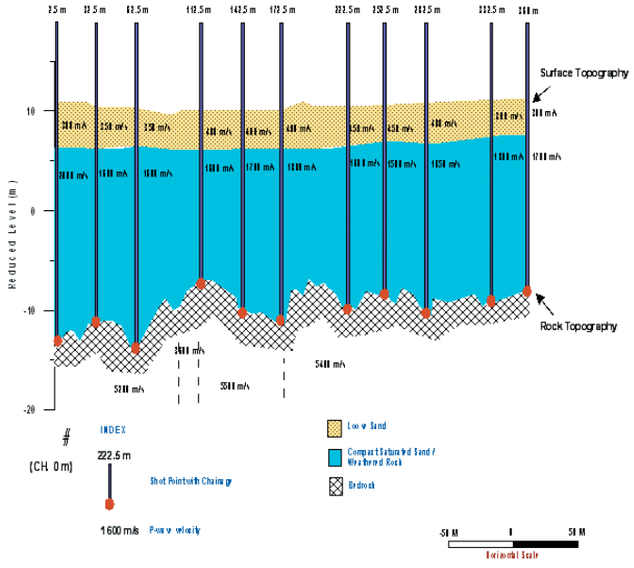

Fig.2
Depth-Section along Traverse-1 (Ch.0-360m) at FRFCF Site, Kalpakkam

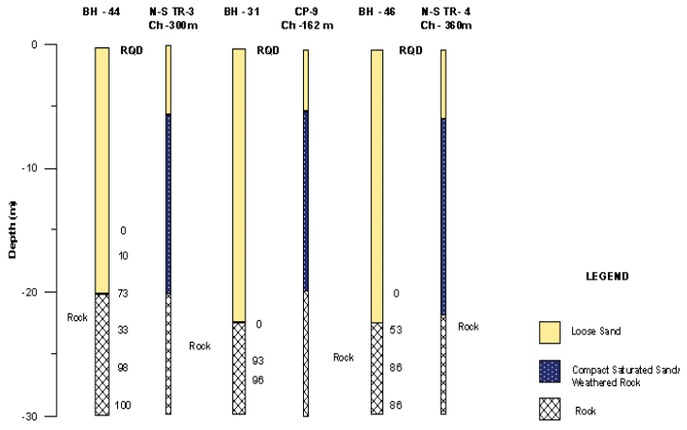

Fig.3
Comparison of Seismic Refraction Profile and Site Specific Geotechnical Investigation

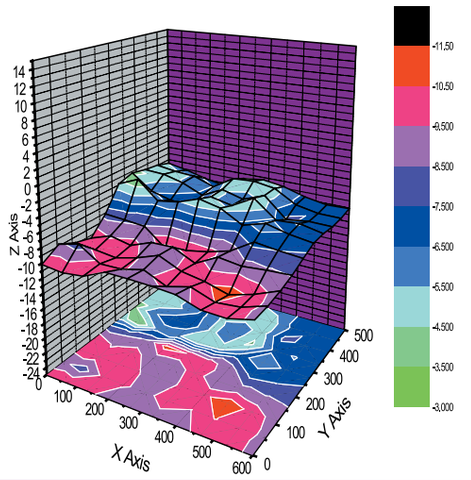

Fig.4
3-D Profile of Rock Surface along with Rock Contour

IV.18 Design and Development of A 250 kg Capacity, Low Headroom, Stainless Steel Special Mini Crane for Hot Cell Application

A typical 50 kg capacity stainless steel mini crane was designed and deployed at CORAL successfully. Based on the feed back and experience gained from this in-cell crane, a 250 kg capacity, low headroom, stainless steel special mini crane for hot cell application has been developed for holding, lifting, turning, shifting, lowering and moving of different types of loads remotely. A schematic of the specially designed crane is shown in Fig.1. This crane will play a significant role in fuel handling, hull transferring and remote maintenance of equipments such as single pin chopper, centrifugal extractor and centrifuges inside the hot cells of DFRP, where radioactivity and acid environment prevail. Since this crane performs critical job in a limited space the hook approaches are more critical. Moreover with the aid of master slave manipulators it serves like a power manipulator. All the travels are motorized and because of high acidic environment the drives selected are compact package drive with special coating for corrosion, humidity and acidity protection features for the winding. As a measure of redundancy to the inbuilt disk brake drive, a worm and worm gear is provided for the hoisting motion so as to self lock the lifting load under the failure of drive. Hoisting, cross travel, long travel drives along with respective brakes and circuit switches are located outside the cell inside maintenance box without breaking alpha-tight containment for contact maintenance. All motion transmissions from the drives to the cell are positive. Worm and worm wheel is provided for hoisting so as to provide self-locking system. Hook block assembly is designed with two pulleys one above other so as to provide single failure proof to the rope.

A mathematical model of the main girder was developed using ANSYS-8 FEM package and analyzed for deflection, shear force and bending stress developed under the combination of dead load, live load and seismic load. A prototype crane is under fabrication and testing.

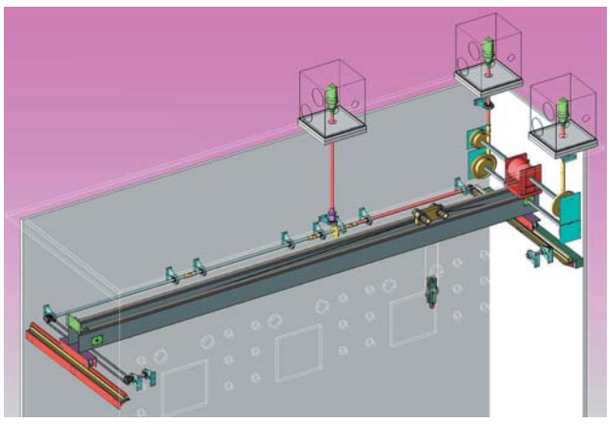

Fig.1
Schematic of a Special Mini Crane for Hot Cell Application.

IV.19 A Remotely Operable Welding Facility for the Fabrication of Fuel Pins for Test Irradiation

Encapsulation of fissile materials in the fuel tube is an important step in the fuel fabrication process. In the Sphere–Pac route fuel fabrication process, the fissile material is filled in a one-end closed fuel tube in the form of micro spheres and vibro-compacted. The tube is then fitted with hardware including a spring before closing with an end plug by welding. The welding is carried out remotely by the Pulse TIG welding process in a helium gas filled chamber which is housed in a glove box. The welding chamber is a leak tight hollow cylindrical block fitted with collets for holding the fuel tube and the plug, in position. The collet holder is rotated by means of a stepper motor drive against a stationary torch which is fixed horizontally in the chamber. The facility consists of an automated tube loading mechanism which transports the fuel tube from the vibro-compaction station and elevates the tube for insertion into the welding station. The fuel tube after insertion is held by the collet and the end plug is rammed on the tube pneumatically to achieve an interference fit. The welding chamber is evacuated & back filled with helium and while the fuel tube is rotated, welding is carried autogenously. The electrode position, orientation, arc gap adjustment and joint fit-up are carried out remotely and monitored by a CCTV camera. Dummy fuel pins have been successfully welded using this facility and the weld joints have been qualified by radiography & metallographic examinations. A photograph of this special facility is shown in Fig.1.

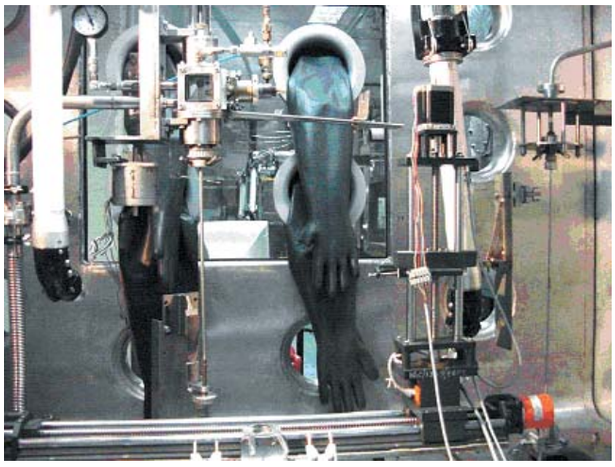

Fig.1
Photograph of Remotely Operable Welding Facility

IV.20 In-Service Visual Examination of CORAL Vessel

As part of the program for comprehensive in-service inspection of critical components of CORAL, the dissolver vessel was required to be inspected using NDE techniques to assess its healthiness and integrity. One of the NDE techniques envisaged is visual examination of the inner surface of the vessel and nozzle welds.

A remote inspection device using a camera was conceived, fabricated and used to carry out the visual inspection of the inner surface of the dissolver vessel. The dissolver vessel is oriented with its longitudinal axis normal to the floor of the containment box and the vessel is extending below the containment box. The vessel has a number of ports which require to be inspected for clogging to the extent possible. The dissolver vessel is located inside a lead-cell containment box and the device has to be posted into it through a double door port. The location is accessible by only one arm of the in-cell articulated MSM necessitating motions of the device to be self-locking. The device had to be designed taking into consideration of MSM load handling capacity which is 4 kg only.

The remote inspection device is basically a 2-axis telescopic scanner having two degrees of freedom (DOF), namely a vertical telescopic movement and an azimuth motion. Collapsible feature is incorporated to facilitate its posting into the containment box through the double door port. The telescopic stage consists of 5 stages having a total travel range of 430 mm and the azimuth motion has 360° travel. Overall size of the scanner in the collapsed state is

Æ195 X 305 mm. Fig.1(a) & (b) show the photographs of the scanner in collapsed and expanded states respectively. The scanner has the provisions for lowering and orienting the camera for radial and axial viewing with read-outs for relative position / orientation of the camera. A ¼" CCD-based camera with 290 k pixels and resolution over 320 TV lines was used for examination of the dissolver vessel. A light source consisting of an array of 11 white LEDs (Fig.2) around the camera was provided integral with the camera. The complete inspection campaign has been recorded in a movie format which can be used as a baseline data in subsequent ISI campaigns.

Visual inspection of the dissolver vessel limb in LMC was successfully carried out after testing the device thoroughly in a full scale mock-up vessel. It was seen that the vessel remained free of remnants after dissolution of the fuel and there was no clogging of chute. All accessible welds and inner surface of the vessel were examined closely and no degradation or corrosion was observed. Visual inspection of the LMC dissolver vessel did not reveal any significant degradation of the inner surfaces or weld joints. The dissolver vessel had been in operation for the last two years and had seen several campaigns under severe environments with nitric acid concentration and high levels of radiation. Images of a few locations inside the dissolver vessel acquired during the inspection campaign are shown in Fig.3. No unwanted material or debris are trapped or blocked inside the vessel or various openings of the vessel. This inspection campaign provided the plant personnel with required confidence level to undertake further reprocessing campaigns. Results obtained from this campaign could form a baseline data for future inspection campaigns of the dissolver vessel limb.

Fig.1 (a)
2-Axis Telescopic Scanner (Collapsed State)

Fig.1 (b)
2-Axis Telescopic Scanner (Expanded State)

Fig.2
CCD Camera with LED Lighting

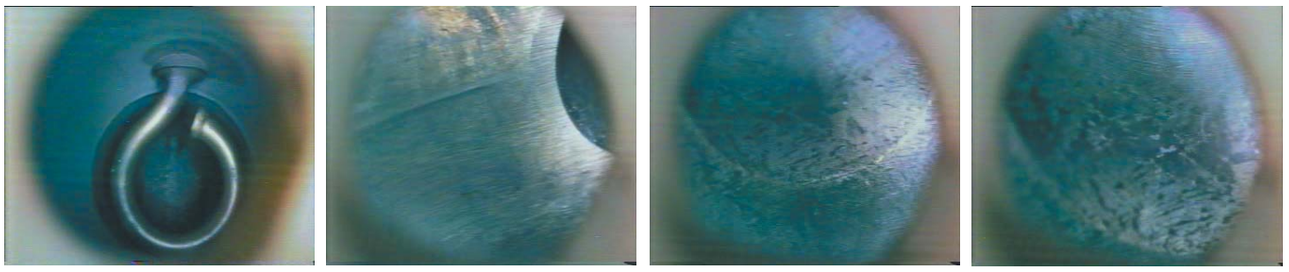

Axial View Showing Sparger Pipe

Location Near the Top Interconnecting Pipe

Chute

Close-up View of the Chute

Fig.3
Images of the Various Locations Inside the Dissolver Vessel Acquired During the Visual Examination Campaign

IV.21 Indigenous Development of Disk and Doughnut Columns for Fuel Reprocessing Applications

Conventionally, pulse columns with perforated plates or nozzle plates have been used in the fuel reprocessing applications. However these columns have a significant amount of back-mixing which reduces the efficiency of the column for the separation of valuable material from the waste fission products. Disk and doughnut columns have been proposed to overcome this problem as these columns have less back-mixing as compared to the conventional pulse columns.

Till now no indigenous studies were available on disk and doughnut columns. As a part of MPCTR (Mini-Pulse Column Test Rig consisting of 10 mm, 25 mm and 50mm diameter DD columns) development, 25 mm disk and doughnut column (of glass) of 2 m active height has been erected Fig.1 shows a view of the PMCTR with the 25 mm column in operation. The experimental runs with 30%TBP/NPH-0.5N HNO3-water system were conducted for checking the flooding throughput. Organic dispersed as well as aqueous dispersed systems were investigated. Fig.2 shows a view of the dispersion inside column section. For organic dispersed systems, hold up values were more than 30%. For conventional pulse column, hold up is typically limited to 20% maximum. For aqueous dispersed systems, holdup values were in 45-54% range. It may be noted that that higher value of hold up results in higher mass transfer resulting in better operation.

Fig.1
A view of Mini Pulse Column Test Rig (MPCTR) with installed 25mm dia pulse-column. Two more columns of 10 mm and 50 mm dia are being erected.

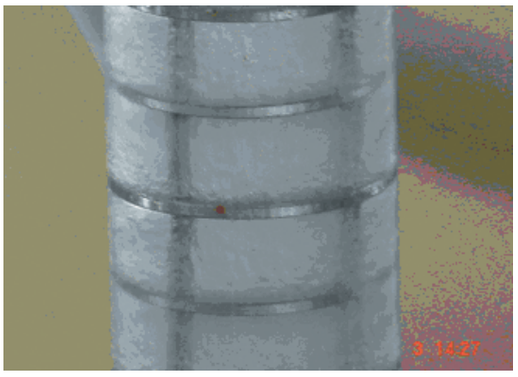

Fig.2
A view of Dispersion inside the 25mm dia Pulse-column Section. System was 30%TBP/kerosene-0.01 N nitric acid.

Chapter - V

ENABLING TECHNOLOGIES

INSPECTION TECHNIQUES

V.1 Development of Comprehensive Technology for In-service Inspection of Steam Generator Test Facility

Steam generator test facility (SGTF) has been established to verify the complete thermal hydraulic performance and to generate data for validation of multi-dimensional thermal hydraulic codes. The SGTF is a vertically mounted 1:1 model of the PFBR steam generator with 19 tubes installed (Fig.1). The facility is instrumented with sensors for detection of sodium-water reaction. The material of construction of steam generator is modified 9Cr-1Mo ferritic steel. Stringent quality assurance of manufactured tubes using saturation based eddy current non-destructive technique was carried out at NFC, Hyderabad. As the saturation based technique cannot be applied for in-service inspection (ISI) of installed SG tubes, remote field eddy current technique has been proposed. The challenges for development of ISI technology include high magnetic permeability of modified 9Cr-1Mo steel, smaller tube diameter (17.2 mm), limited top-side access, probe negotiation in the expansion bends of the tube, detection of defects under support plate regions, and presence of sodium deposit on outer surface. For ISI purpose, comprehensive technology comprising of RFEC instrument, sensor, winch mechanism and signal processing method has been developed in-house after detailed finite element modelling, studies in sodium test vessel and trials in a mock-up facility. This technology has been successfully demonstrated on SGTF for assessment of health of the tubes and to generate the baseline data.

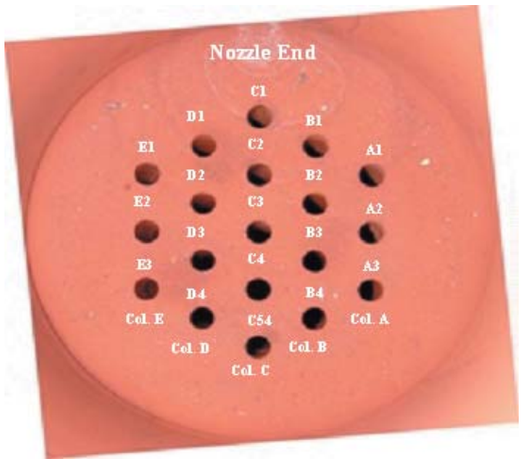

Fig.1
Tube Sheet Layout of the SGTF with Tube Numbering

A flexible sensor head comprising of 15 mm long high density depleted uranium and tungsten carbide rings on either side of exciter and receiver coils was developed to enable easy negotiation through the bend regions. A specially designed, computer controlled winch as shown in Fig.2, with a coil drum was used for insertion and retrieval of the RFEC probe. The winch was mounted on the top tube sheet of the steam generator. The probe was lowered by gravity and pulled up using the winch. ISI was carried out at 900 Hz and 1500 Hz from the top of the SGTF tube sheet. The RFEC measurements were set to zero when the probe was at the extreme end of the tube (deep bottom). The probe was retrieved at a constant speed of 25 mm/sec and the RFEC data was simultaneously acquired at a sampling rate of 200 samples per second. The digitized RFEC data was stored in binary format for each tube for further analysis.

All the 19 tubes were inspected using the RFEC technique and using the optimised test parameters (Figure 3). Large amplitude signals were observed from Inconel support plates and bend regions. Further, signals from two close-by supports on either side of the bend region and at the center of the bend region were also observed. The locations of these signals matched exactly with the actual locations of the support plates and bend regions, as per the SGTF drawings. The phase of the signals from bend regions and support plates is opposite to each other (180 degrees apart) which is a unique characteristic for differentiating these two. A positive signal corresponding to the transitions from straight and bend portions was observed for the bend regions. Similarly, a negative valley was observed for the support plates. Detailed analysis of the stored RFEC data of the tubes obtained at both the frequencies compared with the calibration tube signals. Characteristic double peak signal, typical of a localized wall loss or defect (as found for calibration defects), is not observed for any of the tubes, indicating that none of the 19 tubes had any defect comparable to the 10% wall loss reference defect. The inspection data and processed results were stored for comparison with RFEC data of future in-service inspections.

Fig.2
Specially Designed Computer Controlled Winch with Cable Drum for Insertion and Retrieval of RFEC Probe having Exciter Coil, Receiver Coil, and Depleted Uranium Rings.

Fig.3
Remote field Eddy Current Inspection at SGTF

V.2 Impact Echo and Low Frequency Ultrasonic Studies for Assessment of Damage to Concrete Blocks Exposed to Sodium Fire

Sodium-resistant lime stone aggregate concrete is used as sacrificial layer over the structural concrete in the steam generator building floors of PFBR, where hot sodium is likely to spill during any leakage. It is required to optimize the thickness of the sacrificial layer and develop a non-destructive methodology for assessment of damage to concrete structures due to sodium fire in case of any sodium leakage. With these objectives in view, systematic studies have been undertaken to develop impact echo and low frequency ultrasonic based non-destructive methodologies for assessment of damage to concrete structures due to sodium fire and also to determine the depth of damage consequent to sodium fire. This in turn would also provide the information about the thickness of the sodium resistant sacrificial layer required.

A set of lime stone aggregate concrete blocks of dimensions 600 x 600 x 300 mm having a cavity of dimension 300 x 300 x 150 mm at the center of the larger area side (Fig.1a and b) was cast. After 28 days of curing of the concrete blocks, 25 kg of sodium at about 723 K was poured in the cavity. Sodium was burnt in the cavity for about 30 minutes. The concrete surface temperature in the cavity increased to about 1073-1173 K consequent to the sodium fire. After 30 minutes of the sodium fire, the remaining sodium and byproducts were sucked out. Impact echo studies were carried out on these concrete blocks before and after the sodium fire exposure. Ultrasonic velocity measurements were carried out on back surface of the blocks using double transducer impact echo technique and impact echo testing was carried out at centre of 75 mm square grids, marked on all surfaces of the blocks. Low frequency ultrasonic velocity and attenuation measurements were carried out on the cylindrical core specimens of 50 mm diameter extracted from the as-cast and sodium fire exposed blocks as shown in Fig.1c. Compressive strength measurements have been carried out on 80 mm long core specimens and these were correlated with the ultrasonic parameters.

All the cubes exhibited similar acoustic properties in the as-cast condition. Both impact echo testing and low frequency (500 kHz) ultrasonic measurements indicated decrease in ultrasonic velocity and increase in attenuation to different extent in different blocks upon exposure to sodium fire. The decrease in velocity and increase in attenuation are attributed to damage to the concrete blocks, in terms of generation of micro-cracks and decrease

in moisture content. Compressive strength was also found to decrease to different extent in different core samples. The decrease in the ultrasonic velocity (Fig.2) and the compressive strength were found to be more for the core specimens extracted from the regions near to the sodium exposed surface.

The ultrasonic velocity could be correlated linearly with the compressive strength in the core specimens. The present study demonstrated that for thin specimens (~150 mm thickness), impact echo technique can be used for in-situ assessment of the extent of damage to concrete structures consequent to exposure to sodium fire, with requirement of access to any single side only. However, for thicker structures, reliable assessment of damage can be made only from the exposed surface using double transducer impact echo technique due to the graded damage. By using different frequency waves generated by balls of different diameters, the depth of damage can also be determined. Further, the ultrasonic measurements on the core specimens extracted from different depths from the surface exposed to sodium fire indicated that the maximum damage due to the sodium fire is confined to the top 70 mm only. This clearly demonstrates that the required thickness of the sodium resistant sacrificial layer is about 70 mm.

Fig.1 a
Photograph of a Typical Concrete Block

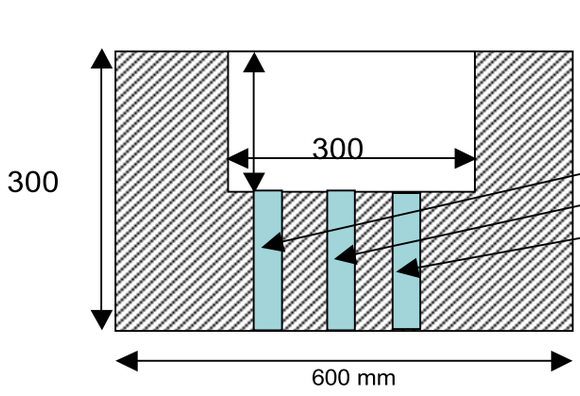

Fig.1 b
Schematic of the Cross Section of the Concrete Blocks

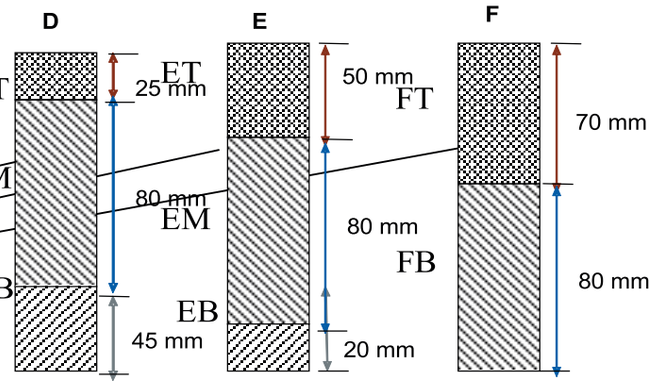

Fig.1 c
The Extracted Core Specimens along with Identification Numbers

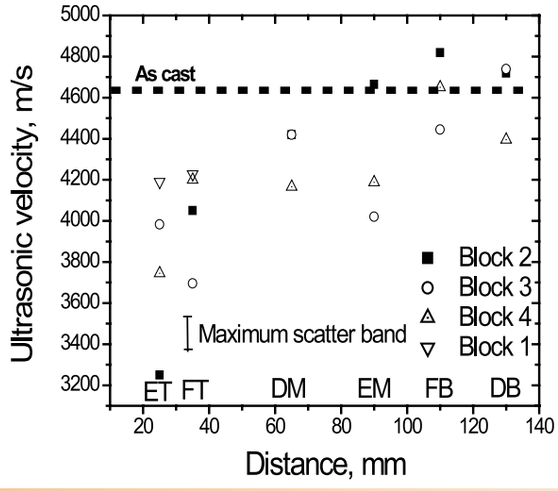

Fig. 2
Variation in Ultrasonic Velocity with Average Distance from Centre of Core Specimen to the Surface Exposed to Sodium Fire for the Four Blocks (ET, FT, DM, EM, FB) and DB indicate the Core Specimens Extracted from Different Depths, as shown in Fig. 1b.

V.3 Ultrasonic TOFD and SAFT for Evaluation of Flaws in Weldments: An Alternative to Radiography

The qualification of components based on different non-destructive evaluation (NDE) methods is found to have varying sensitivity and reliability. The limits of flaw detection by NDE methods are based on the interaction of the applied probing medium with the material. Ultrasonic and radiographic NDE techniques are employed widely to qualify the fabricated components. In general radiography technique finds application during the fabrication and the ultrasonic technique during in-service inspection of components. The demand for use of ultrasonic technique for assessment of fabrication quality arises because of easy amenability, and less complexity, in comparison to hazardous radiography in the shop floor and field environment. The added advantages in use of ultrasonic technique include, increased confidence in fitness-for-service based evaluation, compatibility with pre-service and in-service inspection methods, imaging and quantitative characterization of defects, and potential for significant cost savings. In order to assess the usefulness of the ultrasonic technique in lieu of radiography, a systematic comparative study has been made among the radiographic and two advanced ultrasonic techniques i.e. Time-of-Flight Diffraction (TOFD) technique and Synthetic Aperture Focusing Technique (SAFT). The studies were carried out on a 18 mm thick carbon steel weld pad with natural defects introduced at predetermined locations, as shown in the radiograph (Fig. 1).

The TOFD technique is based on diffraction of ultrasonic waves at tips of discontinuities instead of geometrical reflections from the interface of the discontinuities. As TOFD technique relies solely on the time separation between signals diffracted from the edges of the defects, it can be performed almost independent of amplitude response and thus the coupling quality, material attenuation and defect orientation are much less critical than with conventional pulse-echo methods. SAFT is a signal processing tool that aims at improving the accuracy of ultrasonic signals, thus leading to better sizing capabilities. SAFT synthesizes a large focused transducer by gathering data at various positions using a small unfocused transducer. A synthetic aperture focusing system will produce a narrow synthetic beam by means of a coherent summation of phase adjusted pulses (A-scans), which results in greatly improved lateral resolution and the signal-to-noise ratio of the raw B-scan. The SAFT based reconstruction provides detailed information about the spatial location and extent of flaw contained in the inspected object.

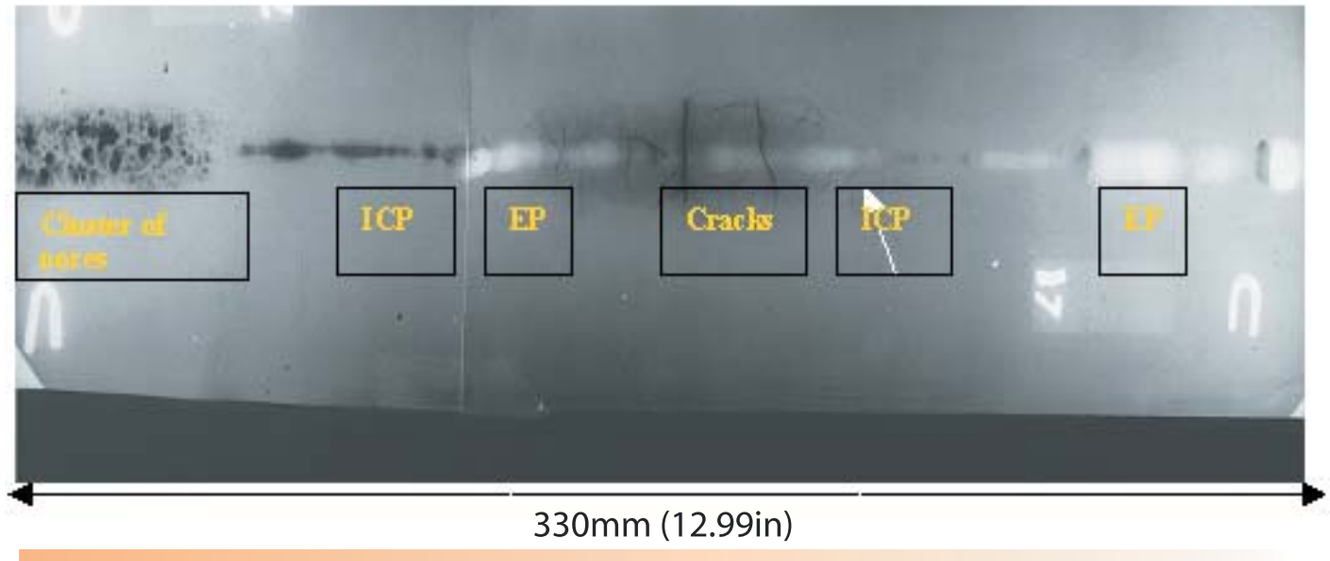

Fig.1
Radiograph (1:1 Scale) Showing Planar Location of Different Defects in the Weld pad : ICP (Incomplete penetration), EP (-Excess Penetration)

The systematic studies carried out indicated that, while the TOFD technique could detect most of the defects, it was not possible to clearly resolve and characterize the cluster of pores and group of cracks. Cracks with cleft edges were almost impossible to be identified. The experimental results revealed that TOFD, as a minimum meets the codal requirements for detection of flaws. Sizing of length and through-wall extent can be carried out using the initial TOFD data as shown in Fig.2. However it is found that, the TOFD has serious limitation with respect to identifying defects close to scanning surface (top 6 mm) due to the merging of lateral wave with diffracted waves from defects. By employing SAFT, it is possible to resolve and characterize all the defects on-par or even better in comparison to the radiographic information. In addition, two clusters of porosity were distinctly seen which were separated by 7 mm and 9 mm below the scanning surface, as shown in Fig.3, demonstrating the spatial resolution as well as depth resolution of the technique. The SAFT has also provided better detection and characterization of oriented cracks which were missed by radiography. Figure 4 shows the SAFT image corresponding to defects (P and Q) which were missed by radiography, whose presence were later confirmed by destructive tests as shown in Fig.5. Hence, the inspection criteria of ASME code can be satisfied using ultrasonic imaging techniques such as TOFD and SAFT for detection, sizing and characterization of flaws in weldments, in lieu of Radiography.

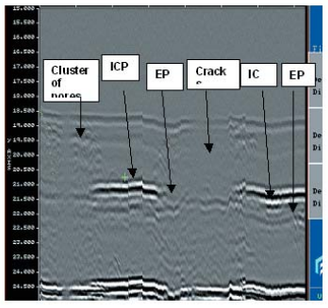

Fig.2
TOFD Image for Different Defects in Weld Pad

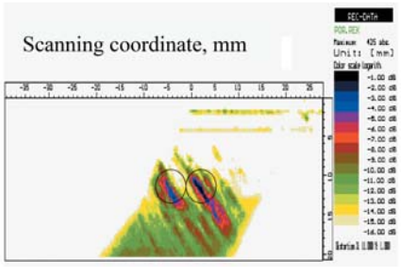

Fig.3
SAFT Image Showing two Clusters of Porosity Separated by 7mm apart 9 mm below Scanning Surface

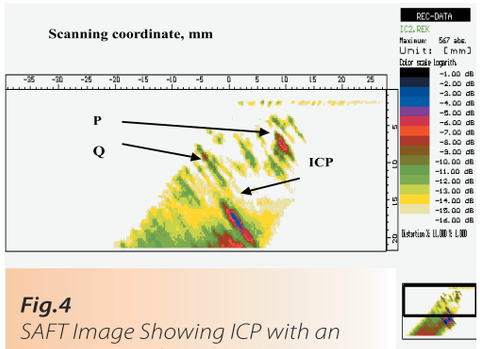

Fig.4
SAFT Image Showing ICP with an Additional Defect Missed by Radiograph

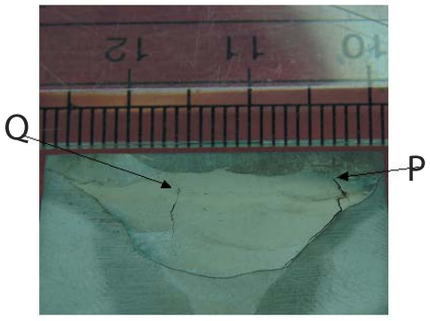

Fig.5
Image of Defects Missed by Radiography but Picked by SAFT

V.4 Development of Electromagnetic Techniques for Non-destructive Detection of Sub-surface Defects

Non-destructive detection of surface and sub-surface defects in components is essential for ensuring structural integrity. In general, radiography and ultrasonic techniques are employed for detection of sub-surface defects in thick components, especially welds. While radiography techniques require double-side access, ultrasonic techniques are done in contact mode and require the use of couplant. In this regard, electromagnetic techniques such as magnetic flux leakage (for ferromagnetic materials) and eddy current are attractive. Traditionally, these techniques are recommended for detection of defects upto a depth of 5 mm. Availability of efficient field-detection sensors such as SQUIDs, Hall, Giant magneto resistance (GMR) and Giant magneto impedance (GMI) sensors, enhances the scope of these techniques for reliable detection of defects located 10 mm below measurement surface. These sensors can be integrated with magnetizing yokes or exciter coils for ease of measurement. In this direction, for detection of sub-

surface defects in thick carbon steel plates (ferromagnetic), micro-Hall based magnetic flux leakage technique has been developed and GMR based eddy current technique has been developed for detection of sub-surface defects in stainless steel plates.

The leakage magnetic field from sub-surface defects in carbon steel is of the order of a few Gauss. In general, Hall sensors are widely employed for detecting the leakage fields. For enhanced performance, 2-dimensional electron gas (2DEG) micro-Hall sensors with GaAs/AlGaAs multilayers have been fabricated using a 5-mask photolithographic process. These sensors have shown an order of magnitude higher sensitivity than the conventional Hall sensors. The active area of the sensor is 50µm x 50µm. These sensors have been used to detect the normal component of leakage flux from machined notches (length, 15 mm, width 0.5 mm and depths 1, 2, 3, 4, 6 and 9 mm) on the far-side of a 11 mm thick carbon steel plate. The experimental setup comprising of magnetic yoke, sensor, scanner and personal computer is shown in Fig.1. The output voltage of micro-hall sensor from EDM notches at different depth locations is shown in Figure 2. As can be seen, the EDM notch located 6 mm below the surface is reliably detected with good signal to noise ratio.

Giant magneto-resistive (GMR) sensor with multilayer structure having ferromagnetic layers (Ni/Fe, Co/Fe) anti-ferromagnetically coupled with non-magnetic layer (Cu, Au) has also been used to measure the leakage field from sub-surface notches. GMR sensors are known for their high sensitivity at low magnetic fields and high spatial resolution. GMR sensor measures the tangential component of magnetic field and as can be seen in Figure 3, GMR sensor could successfully detect leakage fields from a notch located at 9 mm below the surface. Finite element modelling has been carried out to optimise the parameters such as magnetizing current and sensor orientation. The experimental and predicted leakage fields are in good agreement, as typically shown in Fig.3.

For detection of sub-surface defects in thick non-ferromagnetic materials, an integrated probe that uses eddy current coil as exciter and GMR as detector has been developed. The integrated probe has a feature that the secondary magnetic field induced in the material by eddy current coil (low frequency, 1 kHz) is detected by GMR. The performance of the integrated probe has been evaluated on a stainless steel plate of 6 mm thick having notches at the depth locations of 4, 4.5 and 5.25 mm below the surface. Typical image of a sub-surface defect in a 6 mm thick stainless steel plate is shown in Fig 4. Comparison of performance of eddy current and integrated probe outputs revealed that the integrated probe exhibits higher detection sensitivity for sub-surface defects, sensitivity for surface defects being equal. The studies also revealed that the integrated probe can be used for detection of far-side corrosion in waste vault tanks of reprocessing plants.

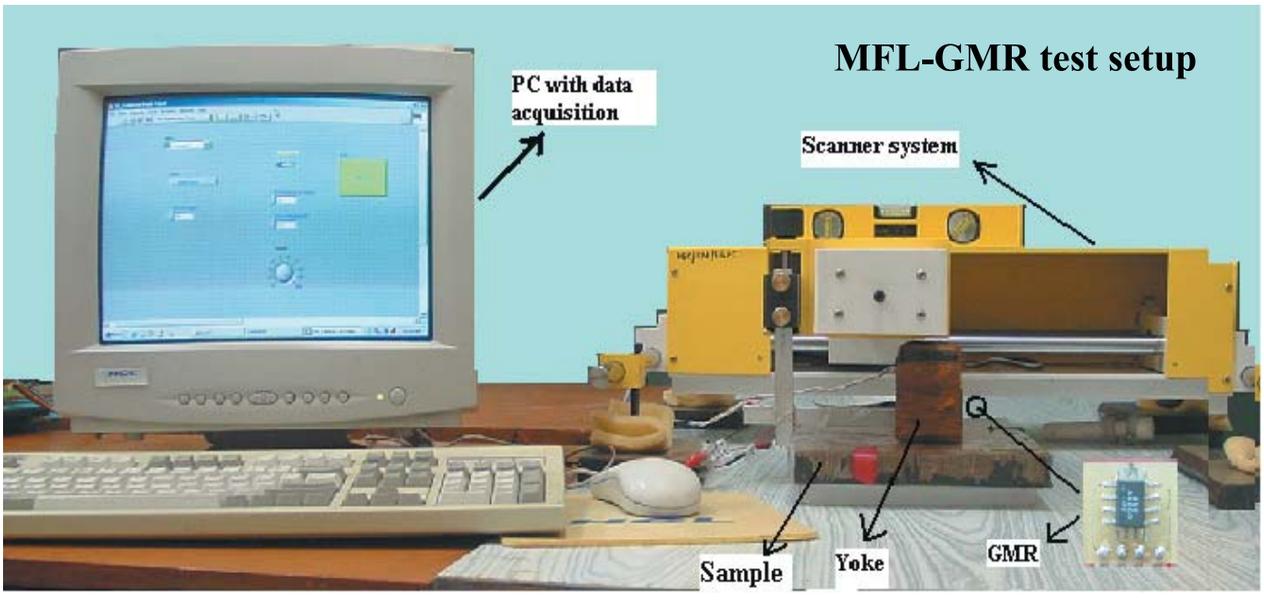

Fig.1.
MFL Test Setup Comprising of Computer Controlled Scanner for Scanning Surface of the Material with Magnetic Yoke and Sensor Setup.

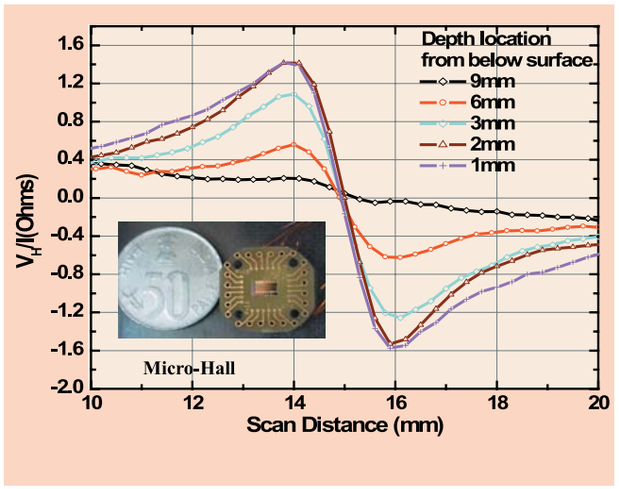

Fig.2
Typical Voltage Signal (tangential component of magnetic field) of Micro-Hall Sensor for Sub-surface Notches at Different Depth Location in Carbon Steel Plate.

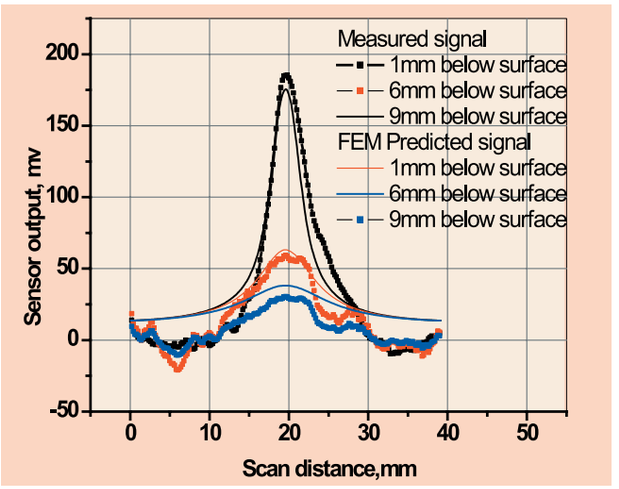

Fig.3
FEM Simulated and Experimentally Measured Response of GMR Sensor for Sub-surface Notches in Carbon Steel Plate.

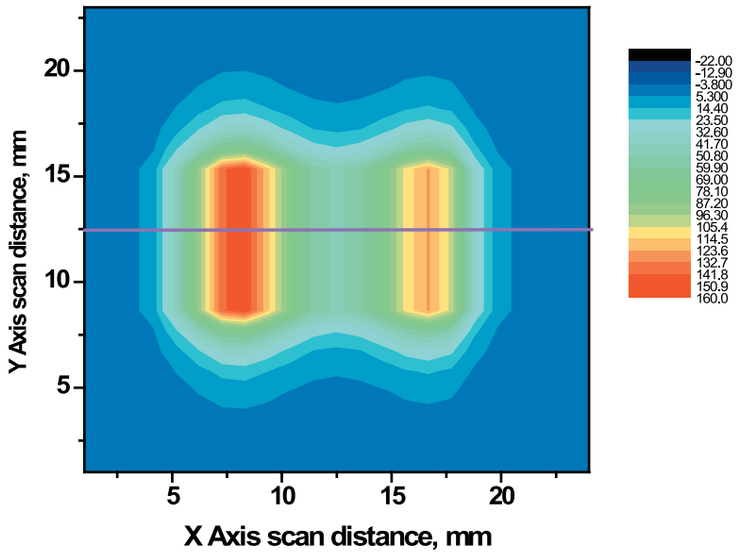

Fig.4
The image of Sub-surface Defect (EDM notch, 5 mm below surface) in a 6 mm thick Stainless Steel plate, Generated by the Integrated EC-GMR Probe

V.5 Eddy Current Inspection for Detection and Characterization of Scratch Marks in Calandria Tubes at NAPS-1

During the en-masse replacement of coolant channels of Narora Atomic Power Station -1 (NAPS-1), scratches were suspected to be formed inside the calandria tubes. Since the wall thickness of the calandria tube is only 1.25 mm, it is necessary to find out the scratches formed and its depth before inserting new coolant channels inside calandria tubes. For detection of scratches, Inspection Technology Group (ITG), designed and developed a very high sensitive focussed differential surface eddy current sensor. A sensor head with special design features was fabricated for the purpose of inserting and positioning of the sensor precisely inside the calandria tube at various locations. The special features of this system are spring loaded sensor to minimise lift off variations and special mechanical fixtures with reduced weight for smooth passage of the sensor assembly inside the tube. Fig.1 shows the photograph of the sensor head assembly and Fig.2 shows the sensor head assembly inserted inside a mock-up calandria tube.

For optimising the instrument settings and to establish calibration graph a zircalloy-2 calibration tube having reference notches of depths 0.015 mm, 0.025 mm and 0.0450 mm and width 0.050 mm was used. The calibration notches were made using electro-discharge machining (EDM) process and their dimensions were characterized by replica measurement technique with a resolution of 0.005 mm. Table I gives the dimensions of the notches and the corresponding peak-to-peak amplitudes of the eddy current signals obtained using the differential eddy current probe.

Table 1. Depth and EC response of EDM notches

SCRATCH DEPTH	EDDY CURRENT SIGNAL AMPLITUDE (mV)
0.015 = 0.005	1600 = 400
0.025 = 0.005	3600 = 400
0.045 = 0.005	4400 = 400

Repeated measurements were carried out on the calibration tube to establish a reliable pattern recognition methodology for distinguishing signals of notches from that of weld seam. A typical eddy current signal pattern recorded in one of the NAPS -1 calandria tubes is shown in Fig.3. Subsequently, mock up studies were carried out in a full length calandria tube available at the mock up facility of NAPS. All the inspection parameters including instrument settings, scanning speed, mode of interconnection of extension pipes etc., were once again standardised for field

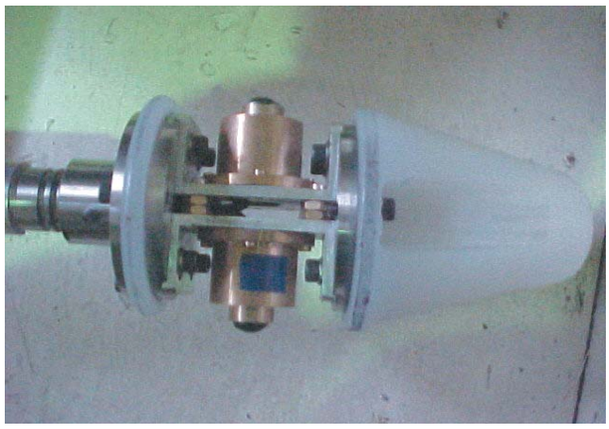

Fig.1
Eddy Current Sensor with Head Assembly

implementation. A detailed procedure for inspection of the selected calandria tubes was established, subsequent to satisfactory mock-up trials .

Eddy current inspection was carried out on the full length of six selected calandria tubes of NAPS-1. During this inspection, the sensor head was inserted into the calandria tubes from the north end of the FM vault and positioned in the area just beyond the bell-mouth region. The sensor head was then linearly translated by 100 mm manually with the help of measuring scale and then, rotated at each axial location, by 360 degrees in clockwise and anticlockwise directions. During the rotational scanning of the

sensor head, eddy current signals were recorded on a strip chart recorder.

A few signals observed during the inspection of the calandria tubes were attributed to scratch marks, based on the signal patterns of reference notches in mock-up tube. On evaluation of these signals with that of the reference signals, it was inferred that the depth of scratches corresponding to these signals was in the range of 0.015 mm to 0.020 mm. The locations of detected signals and their equivalent depth based on the calibration graph for all the 6 calandria tubes were observed and recorded. The overall accuracy in sizing the scratches using the eddy current test procedure is ±0.005 mm. Detailed analysis using calibration graph revealed that all the scratches detected are of depth less than 0.025 mm and length less than 200 mm. These values are within the acceptable limits set by NPCIL.

Fig.2
Sensor Inserted inside a Mock-up Tube

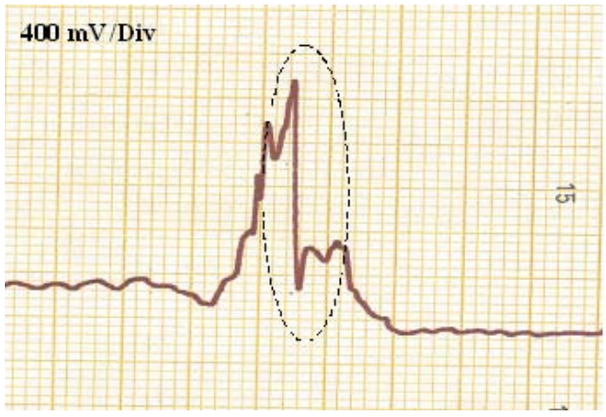

Fig.3
Signal Detected in Calandria Tube no H-02 of NAPS-1, at 1800 mm from the North End of the Bell-mouth Region.

SENSORS

V.6 Performance of Electrochemical Hydrogen Meters in SGTF, SOWART and FBTR

Electrochemical hydrogen meters using CaBr2-CaHBr as electrolyte were developed for detecting any steam leak into sodium at its very inception during operation of fast reactors. The meters were incorporated for evaluating their performance in plants with large sodium inventory such as SGTF, SOWART and FBTR after their satisfactory performance during laboratory testing and calibration. The performances of these meters in all these plants were satisfactory for hydrogen detection. Subsequently, ECHM signal has been taken for safety logic in SGTF. Response of ECHM in SOWART to experiments involving hydrogen injections at different sodium temperatures, steam injections of different leak rates and cold trapping of sodium containing high hydrogen levels (of a few ppm) established ECHM as a reliable steam leak detector. Subsequently, another meter of the same design, complete with instrumentation for plant adaptation was installed in FBTR west sodium circuit in January 2006 in the new location. The instrumentation displayed directly the concentration of hydrogen in ppb as measured by the meter and the same output is made available for recording. The meter response to three hydrogen injections of ~40 ppb each made on 20/02/06 in west sodium circuit of FBTR is shown in the Fig.2. The meter output shows that the hydrogen level had increased from the starting value of ~90 ppb to ~200 ppb at the end of the three injections. The figure also shows that the output (in Volts) of SIP based detector is in phase with ECHM output during hydrogen injections. Similar experience of ECHMs in all these plants validates its performance as a reliable steam leak detector. Currently efforts are on to incorporate 10 Nos. of calibrated ECHMs in the hydrogen leak detection (HLD) system of PFBR.

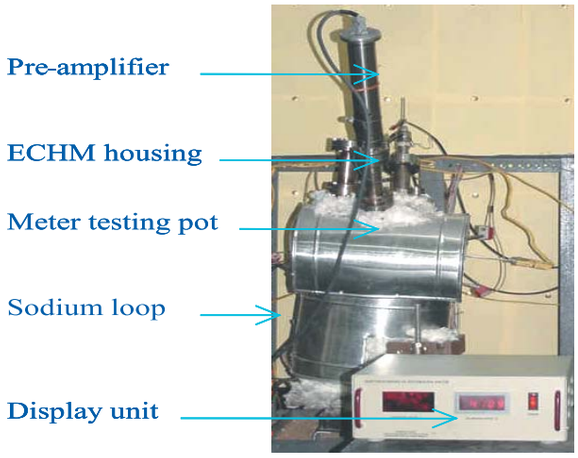

Fig.1
Calibration Setup in Laboratory

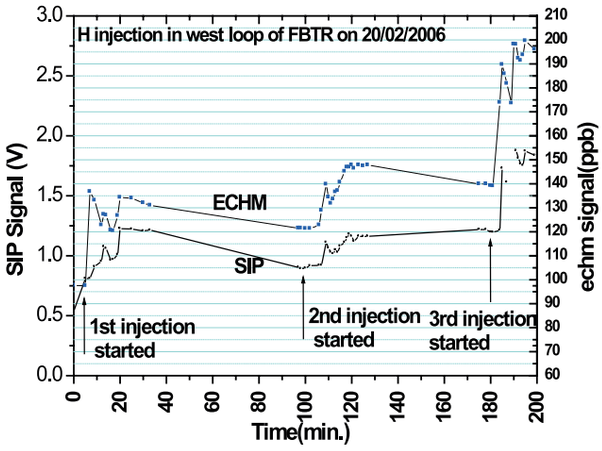

Fig.2
Response of Electrochemical Hydrogen Meter to Hydrogen Injections in FBTR

V.7 Development of Yttria Doped Thoria Based Oxygen Meter for Sodium

Accidental leakage of air into sodium circuits of fast breeder reactors can be detected by continuous monitoring of dissolved oxygen concentration in sodium and this monitoring can also be used for detecting a steam leak in the steam generators. An oxygen sensor using yttria doped thoria (YDT) solid electrolyte (oxide ion conductor) is being developed for this application in collaboration with CGCRI, Kolkata. These YDT based sensors can also be used for measuring oxygen potentials corresponding to different chemical equilibria in sodium systems.

YDT ceramic wares fabricated from the powders prepared by conventional methods require very high sintering temperatures (1850 - 2200°C), and this results in large grain size and poor mechanical strength. A novel combustion method was developed in-house to obtain nanocrystalline powders. These powders on compacting and sintering at relatively low temperatures (1500°C for 2h) resulted in products with 99% of theoretical density. About 2.5 kg of electrolytic grade YDT powders were prepared in 50 g batches for device fabrication studies.

YDT in the form of thimbles and impervious (helium leak rate $<10^{-9}$ l/s) are required for their use as oxygen sensor in sodium systems. To achieve the specified leak tightness, selection of additives and their concentrations, sintering conditions and thickness of the sintered bodies were optimized. Thimbles were made by cold-isostatic pressing of the powders. It was found that YDT powder with 0.2 wt% ZnO sintering aid yielded thimbles with a leak rate of 5 x 10^{-10} l/s of helium when the compacts with a wall thickness of 1.5 mm were sintered at 1650°C. Scanning electron microscopic images of a sintered YDT thimble (both surface and cross section) are shown in Fig.1. As seen from the images (Fig.1(a) & (b)), the grains are well-formed with fine "neck connectivity" between them.

For the fabrication of oxygen sensor, the sintered YDT thimble needs to be attached to a low expansion alloy, Ferni (Iron-Nickel-Chromium) using a glass seal. Ten kg of suitable Ferni alloy whose thermal expansion coefficient is comparable to that of YDT was prepared by induction melting. The Ferni ingots were forged into rods to facilitate machining to suitable dimensions. A solder glass which is compatible in liquid sodium and adherent to both YDT and Ferni was developed. The thermal expansion properties of both Ferni alloy and glass powder were evaluated. The conditions for glass soldering between YDT pellet and Ferni alloy have been optimized. Twenty numbers of oxygen sensors are currently being assembled in collaboration with CGCRI, Kolkata.

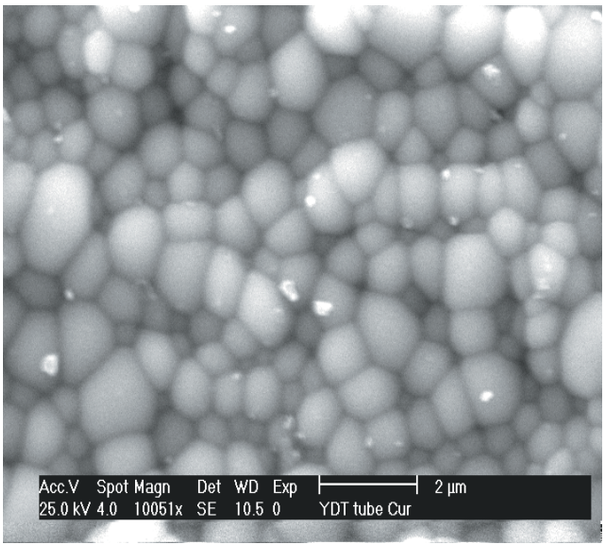

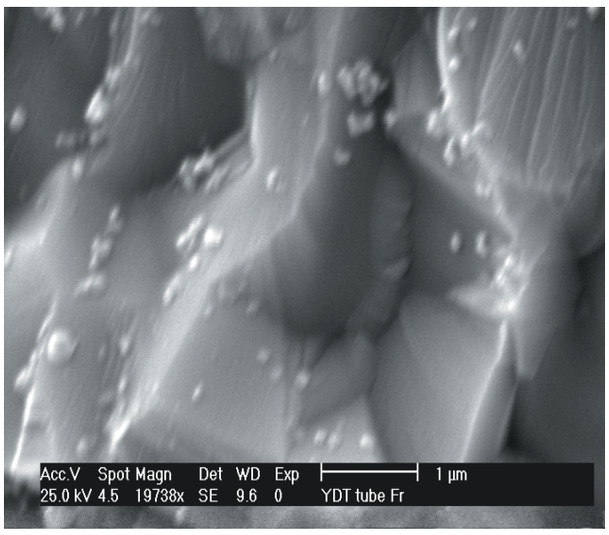

Fig.1
Scanning Electron Micrographs of YDT Pellet Samples Sintered at 1923 K: a) Surface Morphology and b) Cross Sectional View

V.8 Amperometric Hydrogen Sensor based on PEM Fuel Cell and its Applications

An electrochemical hydrogen sensor operable at room temperature has been developed in Chemistry Group. The amperometric sensor is a fuel cell type device with a mechanical barrier limiting the supply of hydrogen to the sensing side electrode. The counter electrode is exposed to air in the ambient atmosphere. NAFION, a proton conducting solid polymer electrolyte membrane (PEM) is used as electrolyte in the sensor. The electrolyte is sandwiched between thick films of platinum that serve as electrodes. The electrode catalysts are deposited on either sides of the membrane by transfer printing technology (decal method). The sensor operates in amperometric mode and the limiting current is linearly dependent on the hydrogen concentration. The schematic of the sensor with photograph of a compact sensor (Fig.1 and 2), cell configuration and electrode reactions occurring at the sensing and counter electrodes are given below.

Cell : H_2, / Pt // Nafion // Pt, air
Anode : $H_2 \rightarrow H^+ + 2e^-$
Cathode : $H^+ + 2e^- + ½\ O_2 \rightarrow H_2O$
Overall : $H_2 + ½\ O_2 \rightarrow H_2O$

The sensor can be used to monitor hydrogen in argon, carbon dioxide and air. Its operating range can be optimized to either ppm or percentage level of hydrogen

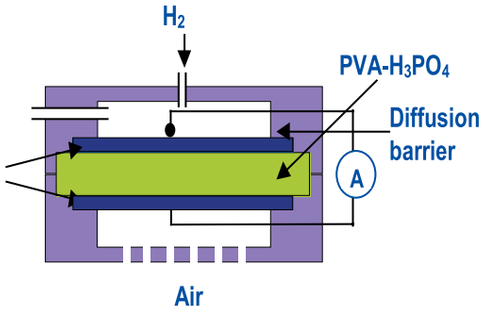

Fig.1
Sensor Schematic

and is a direct reading device with provision for interfacing to personal computer. User friendly calibration procedures have been incorporated by integrating the transducer to the direct readout device. The direct read-out device (developed in-house) stores the calibration parameters. The concentration of hydrogen is estimated on-line using the calibration parameters and displayed directly. Figs.3 and 4 show the response of the sensor for hydrogen additions in carrier gas and calibration respectively. The response time for hydrogen is about 40 s in readout mode. The sensor is compact, cost effective and suitable for field applications (Fig. 5). The present sensor is being upgraded to a potentiostatic three electrode device with better long-term stability and selectivity.

The sensor was successfully used for monitoring hydrogen in simulation studies on sodium cleaning and decontamination of sodium exposed fast reactor components. Fig.6 shows application of the sensor for hydrogen monitoring during sodium cleaning by water vapour-carbon dioxide process. The sensor is also used in simulated experiments to monitor the progress of dissolution of the degraded layer of sodium-exposed fast reactor components during decontamination by sulpho-phosphoric acid method by measuring the hydrogen evolved as shown in Fig. 7. This sensor was also used to study the decontamination of primary heat transport system components of PHWR and this yielded valuable information on the mechanism and kinetics of decontamination. Comparison of H_2 evolution behaviour of Fe_3O_4 coated carbon steel (CS) and polished CS in decontamination (EAC) formulation is shown in Fig.8. Region (1) shows the base metal aided Fe_3O_4 dissolution, region (2) shows the base metal aided Fe_3O_4 dissolution and corrosion reaction while region (3) shows only the base metal corrosion represented by the reaction $Fe + 2H^+ \rightarrow Fe^{2+} + H_2$. The sensor was also used in the set-up for measurement of diffusible hydrogen in weldment developed and patented at IGCAR.

Fig.2
Sensor Transducer

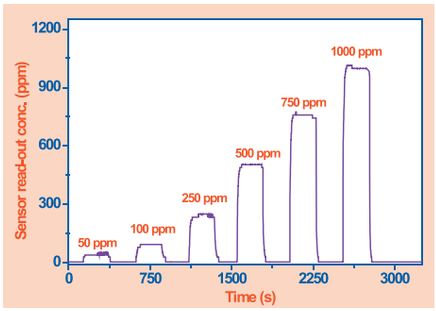

Fig.3
Sensor Readout for Set Conc. of Hydrogen

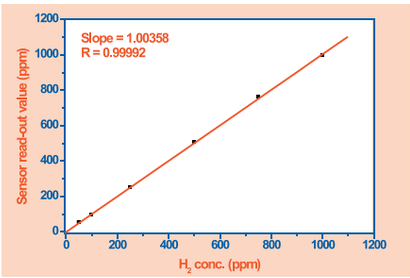

Fig.4
Plot of Sensor Readout vs Actual Conc. of Hydrogen

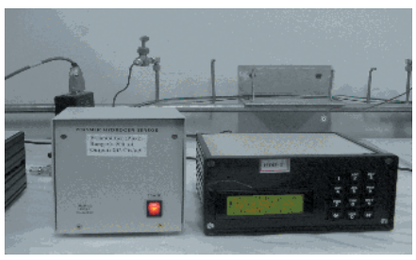

Fig. 5
Sensor with Preamplifier and Readout Unit

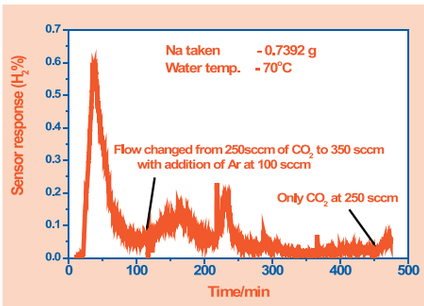

Fig. 6
Monitoring of Hydrogen in Sodium Cleaning Process

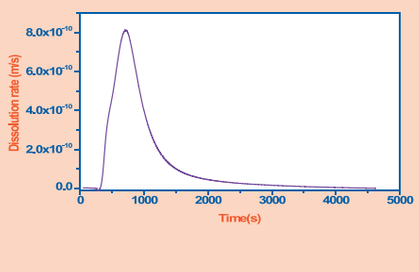

Fig.7
Dissolution Rate of Depleted Surface of Sodium-exposed SS 316LN

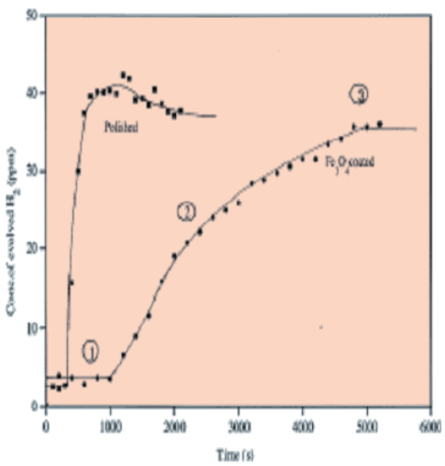

Fig.8
Decontamination of Carbon Steel

V.9 Development of Automated Test Facility for Sensor Characterisation

An automated test set up has been standardized for the rapid and in-depth study of the characteristics of electro-chemical sensors that are being developed as part of the Chemistry research on sensors. The heart of the hardware is a multi-channel high impedance electrometer of an international make, which measures with negligible interference, the voltage, current, resistance etc., from electrochemical sensors/cell. The multi-channel feature is useful in acquiring the signals from an array of sensors. The electrometer has a GPIB interface that interfaces to a computer, which runs the software on the versatile LABVIEW package.

The software has been developed to acquire the data from the electrometer, store the same and generate an online plot. The software affords channel selection and assigns a function for each channel. At present the software is able to measure Voltage, Current, Resistance and Charge. Additional functions can be implemented on demand. It also provides powerful online plotting with many levels of zoom facility (both X-axis and Y-axis), also providing a facility to store the data in a file. The software stores the data continuously and makes separate files for each day to avoid huge sizes of data files. Fig.1 shows the main menu (a) and online plot (b) using this software.

Features:

- Data Acquisition
- Graphical User Interface
- Multiple Channel selection
- Function Selection for each channel
- Online plotting of all selected channels
- Zooming of the plot (many levels)
- Store the acquired data in the file

(a) Main Menu

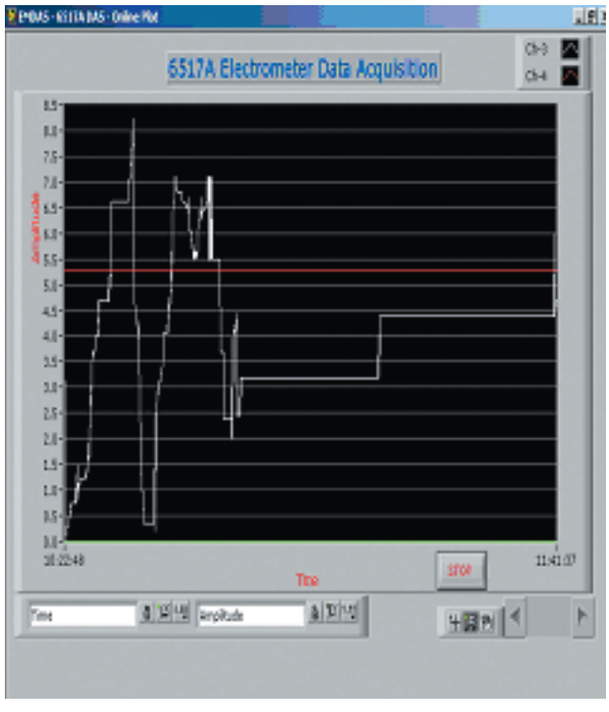

(b) Online Plate

Fig.1
Display System of the Software

V.10 Modified Design and Modelling of Eddy Current Position Sensor

During normal operation, the diverse control rods (DSR) are held above the active fuel zone by an electromagnet, at the bottom end of Diverse Safety Rod Drive Mechanism (DSRDM). On receiving SCRAM signal, the electromagnet de-energizes and drops the DSR, which falls under gravity. Eddy Current Position Sensor (ECPS) has been conceptualized to detect whether the DSR has reached its bottom most deposited position. The circuit diagram of conceptual ECPS is shown in Fig.1.

There are five coils in ECPS. Three coils are connected in series on DSR sheath side. These are secondary coil (S1) placed concentric to primary, signal transfer coil (S2) concentric to pick-up coil and sensor coil (S3) concentric to the deposited position of the piston. A pick-up coil is also placed below the primary coil in same axis for getting the output signal. The induced voltage in secondary drives a circulating current in the entire three coils. The impedance of sensor coil increases considerably when the piston, having ferromagnetic material, is in the deposited condition. The variation in pick up voltage is the measure of DSR in lifted position or DSR in bottom most position. Sensitivity in ECPS is defined as the ratio of change in pick up voltage (from DSR lifted position to DSR bottom most position) to the pick up voltage at DSR lifted position. Earlier tests had indicated a low sensitivity and the design was improved by reducing the cross coupling between the pickup and primary coils by provision of a copper disc spacer in between.

A preliminary model of modified ECPS was studied using finite element analysis. The analysis was done for 20 mm and 10 mm copper spacer between primary and pick-up coil. Simulation was done for non-sodium model of ECPS simulating sodium by stainless steel target and simulating annular sodium by 0.8 mm thick aluminum sheet in annular gap. Simulation results and experimental air test results are shown in Table 2 and compared with actual sodium test results carried out. It is seen that the sensitivity by analysis and the experiments are matching. It can be seen that tests in sodium can be avoided by simulating sodium by SS and aluminum.

Table.2

S.No.	Configuration	Numerical Simulation	Experimental air -test Results	Experimental Sodium-test Sensitivity (%)
1	20 mm copper spacer	20.3%	21.5%	22 %
2	10 mm copper spacer	10.5%	14.37%	12 %

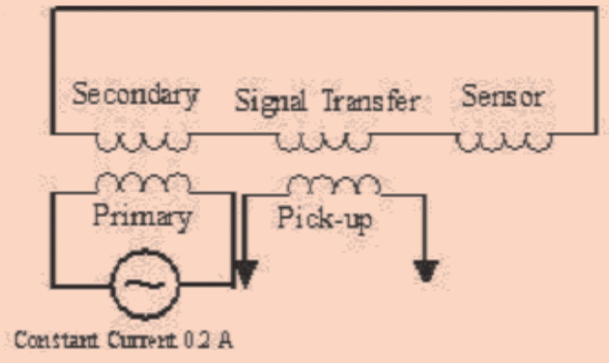

Table- 1

Primary (P1) Secondary (S1)	1.5 mm copper core MI cable 1.5 mm copper core MI cable
Signal transfer (S2)	1.5 mm copper core MI cable
Pick-up coil	1.0 mm copper core MI cable
Sensor Coil (S3)	1.5 mm copper core MI cable

Fig.1
Circuit Diagram of Prototype ECPS

V.11 In-house Developed Level Sensors for Sol-gel Facility

A laboratory scale sol-gel facility is getting ready for production of fuel micro-spheres. Unique pulsating type level sensors have been developed for a good number of the aqueous and non-aqueous process tanks. The liquids for which the levels are to be sensed are of different types - water, acids, uranyl nitrate solution, HMTA with urea solution, ammonia, CCl_4 and silicon oil. Thirteen tanks are provided with such level sensors -nine of them being discrete two-level conductance based for aqueous media, and four being continuous type of capacitive nature for non-aqueous media.

The level sensors for all the conducting ionic liquids for this application are discrete dual-level sensors, design of which stems from the generalised approach for discrete multi-level detection developed in the laboratory. Multi-level sensing is effected by a set of chemically compatible electrodes of different lengths corresponding to the desired discrete levels to be sensed within a given vessel. A network of resistors, which is connected appropriately to the set of electrodes, is placed in the timing circuit of a suitably designed oscillator in such a manner that, on progressive attainment of every discrete level, the conducting medium acts as the shunt and reduces the effective resistance by a fixed and desired quantity. Thus, there is a sharp change in pulse frequency at the output of the oscillator at every discrete level. Beyond a certain minimum value of ionic conductivity of the liquid, the output frequency and magnitudes of step jumps are practically independent of conductivity and, hence, independent of the nature and composition of the liquid.

The schematic diagram of a dual-level sensor is shown in Fig.1. Sharp changes in frequency with the attainment of 1st and 2nd levels for two liquids, differing by ten fold in conductivities are shown in the same figure. Measured frequency profiles as functions of respective level heights in two cases match closely. Absolute values of frequencies and their shifts on attainment of fixed levels are practically similar.

Continuous type level sensors have been developed for precise determination of levels of non-conducting liquids such as CCl_4 and silicone oil in respective process tanks of the sol-gel plant. The non-conducting liquid pool, whose level is made to sense, acts as the dielectric medium within an appropriately designed capacitive type detector. It responds to minute changes in liquid level by monitoring

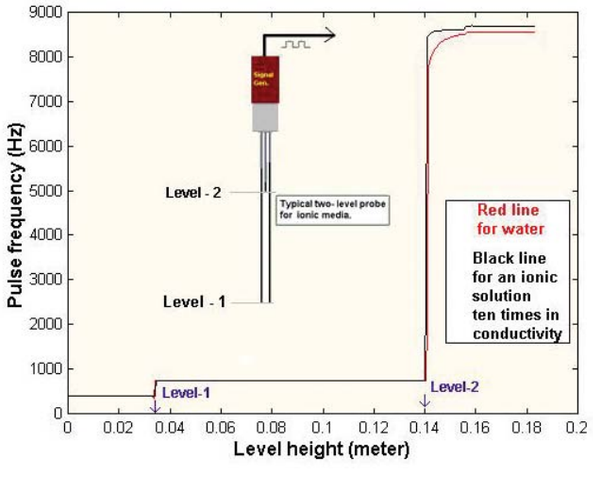

Fig.1
Schematic Representation of a Typical Pulsating type Dual-level Sensor with its Response to Discrete Level Detection of two Ionic Liquids Differing in Conductivity by Ten Times.

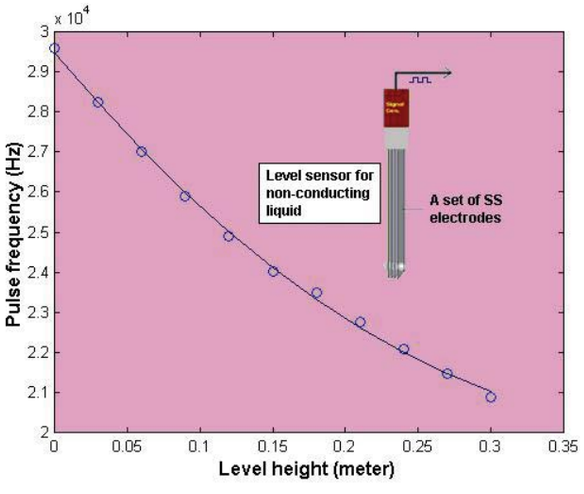

Fig. 2
Schematic Representation of a Continuous type Pulsating Level Sensor for Non-conducting Liquids and its Response to Level of CCl_4.

Fig. 3
Long-term Performance Test of all the Sensors together in the Laboratory with an Indigenous PC based Instrumentation.

shifts in capacitance. An assembly of uniformly spaced multiple number of rectangular stainless steel plates is the capacitor assembly whose capacitance changes with the change of liquid level on account of change in fractions of two dielectric media, namely the liquid and air, within the electrode gaps. The capacitor is in the timing circuit of a compact logic gate oscillator mounted on the probe head. The shift in digital pulse frequency at the output of the oscillator is directly related to change in the liquid level. A level sensor of this type along with a typical pulse frequency to level height relationship is given in Fig. 2.

All the thirteen level sensors (9 dual-level discrete type and 4 continuous type) were fabricated, tested over a long period in the laboratory using in-house developed 24-channel PC based signal handling and data acquisition system (Fig. 3) and, subsequently, handed over for installation in the process tanks.

ELECTRONICS AND INSTRUMENTATION

V.12 Time Domain Electromagnetic (TDEM) System for Remote Sensing of Conductive Ore Body Deposits

DAE has embarked on a program to develop indigenous technologies for prospecting the uranium. As uranium ore deposits may be found along with the deep-seated conductive deposits, the need of development of a system to locate conductive deposits at the depth of more than 300 m is envisaged. Electromagnetic survey is the rapid and cost effective geological exploration method for prospecting the conductive deposits buried in bedrocks. Electromagnetic methods can be classified as Frequency Domain (FDEM) or Time Domain (TDEM) system depending on the principle of excitation and measurement. The TDEM system is mostly preferred over FDEM for the deeper exploration.

Time Domain (TDEM) system:

The Time Domain Electromagnetic system consists of a concentric transmitter-receiver coil assembly. The transmitter coil is excited by a periodic bipolar current pulse whose fall time is controlled. The changing primary field created during the transmitter current fall induces eddy currents to

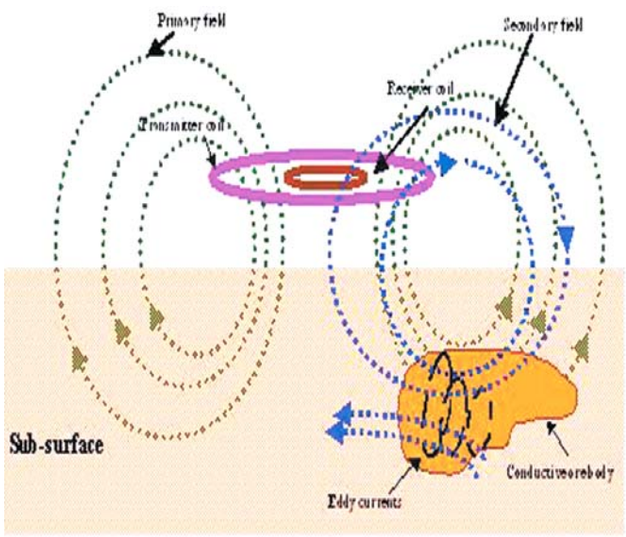

Fig. 1
Principle of Time Domain Electromagnetic Method

flow in the surface, which decay due to the finite ohmic resistance of the layer. The decaying currents produce a changing secondary magnetic field. This induces voltage in the subsurface layer as shown in fig. 1. The time constant of eddy current decay in the ore body depends on its conductivity and geometry.

The time rate of change of secondary magnetic field generated by the eddy current decay in the layer and ore body is measured by the receiver coil as induced voltage during the transmitter off-time. From the induced voltage data a conductivity map of the subsurface geology can be obtained using suitable interpretation software.

To explore the deposits at the depth of more than 300m, the system requirements are as follows:

- High Dipole moment of the transmitter coil (of the order of 10^6NIA)
- High excitation current (of the order of 300A) is to be switched off abruptly
- The receiver electronics is capable of measuring the signal of the order of nano volts buried in noise.
- The system is to be designed for its airworthiness so that it can be airborne.

Complex design of this kind needs to be preceded by the simulation and modeling to fetch right results within reasonable time and cost. Hence, it was decided to simulate the EM system first using the Magnet3D software by employing a suitable model with varying modeling parameters. Compilation and analysis of such results would give proper direction to the hardware and software design.

The design and development of the system is proposed to be taken up in stages achieving higher dipole moment and larger size in each stage. Initially, a laboratory model was conceived, designed and developed to conduct in-house experiments. The setup consists of a concentric transmitter (dia. 25 cm)-receiver coil (dia. 2.5 cm) assembly hung from a wooden support. The conductive target, placed on the ground surface, was excited with 3A, 25 Hz and trapezoidal current waveform. The induced voltage in the receiver coil was recorded after suitable amplification.

Experiments were conducted with targets of different conductivity with a nominal fixed height between the coil assembly and target. The apparatus used for the experiments and the compiled data are shown in figure 2. The above setup was also modeled and simulated using a Finite element method (FEM) based electromagnetic software. Simulation results matched quite well with the experimental data.

As part of the next stage development, a 30A, 25Hz, Trapezoidal current source along with the transmitter-receiver coil assembly was designed and developed in collaboration with IITM, Chennai. The setup consists of a transmitter coil (dia. 2.5 m) hung from a cantilever support with a concentric receiver coil (dia. 0.25 m). In this setup the cantilever support had a small pulley through which the distance between the coil and target was varied and receiver voltage was recorded at different heights. The response of earth surface was also measured at different heights. The experimental setup and compiled results are shown in Fig.3.

At a given depth, with the increase in conductivity, the decay time of induced voltage in the receiver coil is longer. Again after the primary current is switched off, after a delay time 'τ', the amplitude of the induced voltage increases in the receiver coil with increase in conductivity. Thus the experiments conducted so far on prototype systems have given confidence to develop the final system.

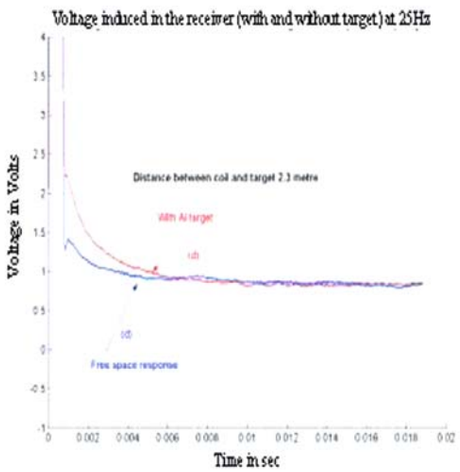

Fig.2
In-house Experimental Setup and Results

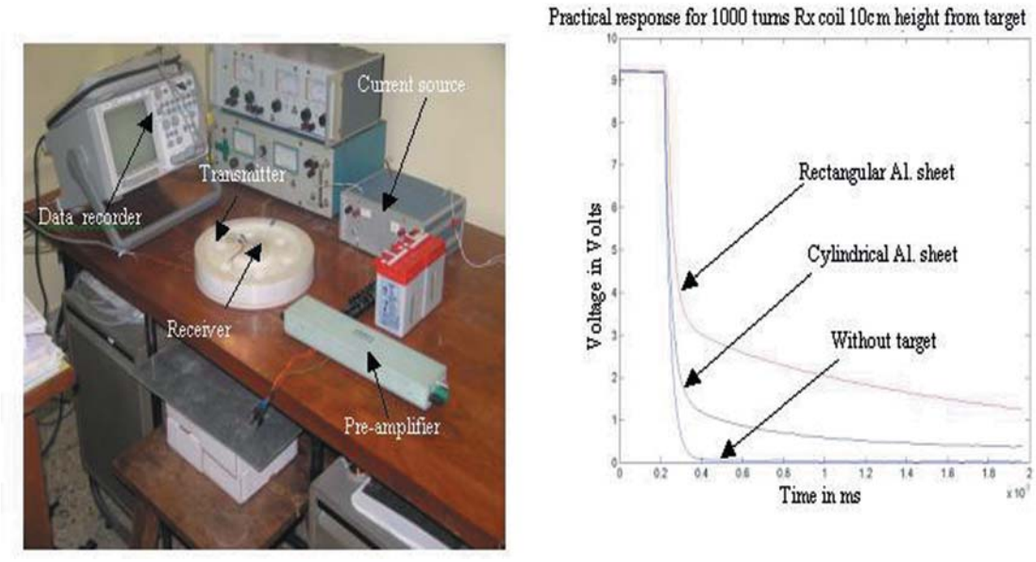

Fig.3
Experimental Setup at IITM and Results

V.13 Bubble Detector based Criticality Incident Detection and Alarm System

The installation of criticality accident alarm system is recommended by ANSI (1986) for all activities in which the inventory of fissionable materials represents a non-trivial risk of a criticality accident. Such an alarm system can provide a significant reduction in radiation exposure for personnel in the vicinity of an accident by signaling a person for evacuation.

Various types of radiation monitors are currently being used as criticality monitors in nuclear facilities. These are essentially gamma monitoring systems. In fast reactor reprocessing facilities, the gamma radiation background is high due to larger radioactivity of the fuel pins. Hence it is required to use neutron monitors as criticality monitors. With this purpose, a bubble detector based criticality accident alarm system was successfully developed for detection of a criticality event. The device can be installed in reprocessing plants in the plutonium separation stage or in fuel fabrication facilities, where plutonium and enriched uranium are handled. These can be installed in operating areas in fuel processing plants and are insensitive to gamma background.

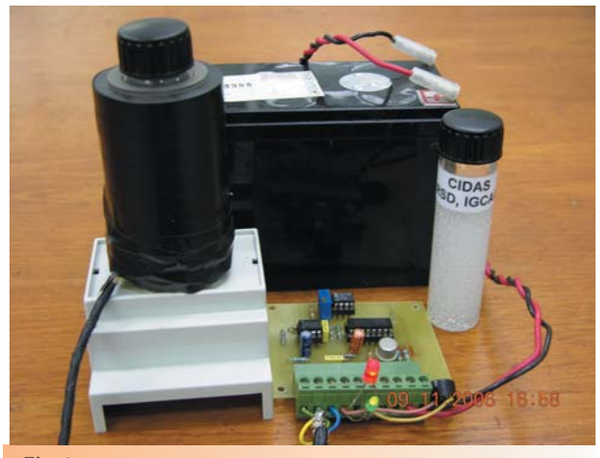

Fig.1
Photograph of CIDAS

The bubble detector consists of an elastic polymer (polyacrylamide gel) in which droplets of superheated dichlrodifluoromethane (CF_2Cl_2) liquid have been uniformly dispersed. These droplets are photon insensitive, whereas high linear energy transfer (LET) neutron recoils trigger the boiling of the drops, nucleating visible bubbles that remain fixed in the polymer. With increasing fluence of neutrons the scattering of light and opacity of the medium increases and a measure of this opacity is a measure of neutron fluence. The sensor consists of a set of Infrared diodes and photodiodes (BPW 34) as transmitter and receiver arranged in transmission-reception geometry in a cylindrical container with associated electronics. The bubble detector is placed at the centre of the container. The photographs of

the prototype criticality accident monitor and its associated electronics are shown in Figs. 1 and 2 respectively. When connected to a power source, light emitted by the IR diode transmits through gel matrix and gets collected at the photodiode. The neutron interaction with the emulsion results in increased bubble density which increases scattering of light. This process decreases the intensity of light reaching the photodiodes and activates the buzzer. The system is provided with a blinking green LED indicator showing the normal functioning while the presence of bubbles is indicated by continuous glowing of a red LED along with buzzer activation. Interference from ambient light is avoided by operating IR diode in pulsar mode. The sensitivity of the photodiode can be set to required values.

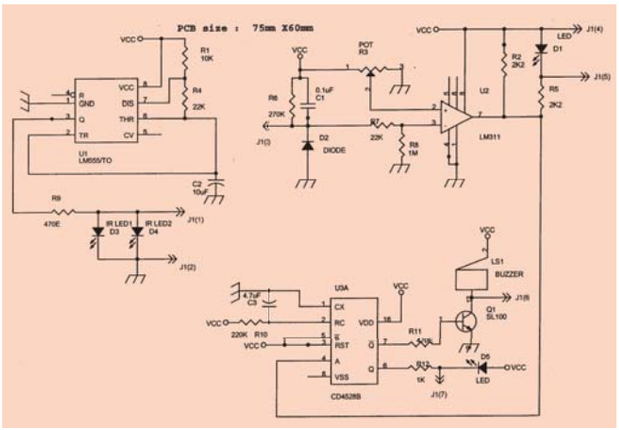

Fig. 2
Bubble Detector Based Criticality Incident Detection and Alarm System

The performance of the prototype system (CIDAS) was studied using 5 Ci Am/Be neutron source. Its response time to neutron fluxes of 10^3 to 10^3 n/cm^2/sec is given in Table 1. The activation of alarm occurs within 28 sec for the neutron flux of 10^5 and it is expected to get reduced further at higher neutron fluxes. In a criticality accident in a reprocessing facility, 10^{16} to 10^{17} fissions occur within a millisecond and the detector response is also expected to be in milliseconds.

Table 1. Response time of CIDAS to neutron flux

Neutron flux (n/cm ^{2}/sec)	Response time (sec)
10^3	180
10^4	58
10^5	28

Multiple numbers of such systems can be installed and networked with suitable networking techniques for monitoring a particular area. This system will be very useful in confirming the occurrence of a criticality event and also ensuring the absence of criticality during re-entry of personnel to the locations where criticality event might have occurred earlier. Such systems could be used as criticality accident dosimeter by using ultrasonic readout system.

V.14 Liquid Scintillation Coincidence Counting System using Particle Arrival Time Recording Module

A liquid scintillation counting system using a novel 'particle arrival time recording module' has been developed mainly for use in tritium assay. The LSC system uses the conventional two PMT configuration but proceeds to determine the coincidence by a diverse digital method. The arrival time of all the scintillation pulses from both the channels are logged in sequence and stored in memory independently. This data can then be used by off-line software analysis to obtain two fold levels of coincidence. One channel is used as reference and the software computes the number of pulses in the other channel, which arrive within the specified time window. The system is a software module, which runs on LABVIEW, using as the hardware platform, a PCI plug in card. Because most of the components are in software, a lot of flexibility is brought under the user's control. The complete data is always available in memory, and hence multiple analysis can be tried with different analytical parameters.

The block diagram is shown in Fig.1 .The module uses a PCI bus based plug-in-card to measure the arrival time. It has a set of 32 Digital I/O lines, a clock source and counters. A virtual instrumentation (VI) software in LABView configures and controls the card for the required operation. The software stores the data like pulse number, arrival time of the pulse, in a file in ASCII form. These files are the input data for the coincidence analysis in the next module. The

preset time can be varied from 10 – 1000 s; the pulse pair resolution is better than 1 µs and the count capacity of each channel is 10^7.

The analysis software has been developed in VB ver.6. The channel with lesser number of counts is used as reference. Twenty bins – each with a width of 250 ns – are used for accumulating the coincidence counts. The arrival time of the first count in the reference channel is compared with the arrival times of the pulses in the second channel up to a time period of 5000 ns. If the arrival time of any pulse in the second channel is found within this time period, the appropriate time bin is incremented by one. If there is no coincidence count within 5000 ns, the software exits from this loop and takes the next pulse in the reference channel for analysis. Table 1 presents efficiencies obtained using standards containing ^{3}H, ^{14}C and ^{241}Am.

Table 1. Typical count rates for 3H, 14C and 241Am.

Sr.no	Sample	Left Counts/10s	Right Counts/10s	Coincidence time spread (ns)	% Efficiency obtained
1	^{3}H	19540	18981	2500	14.3
2	^{14}C	21631	21937	2500	85.1
3	^{241}Am	8718	5857	750	100
4	Background	6451	3543	2500	

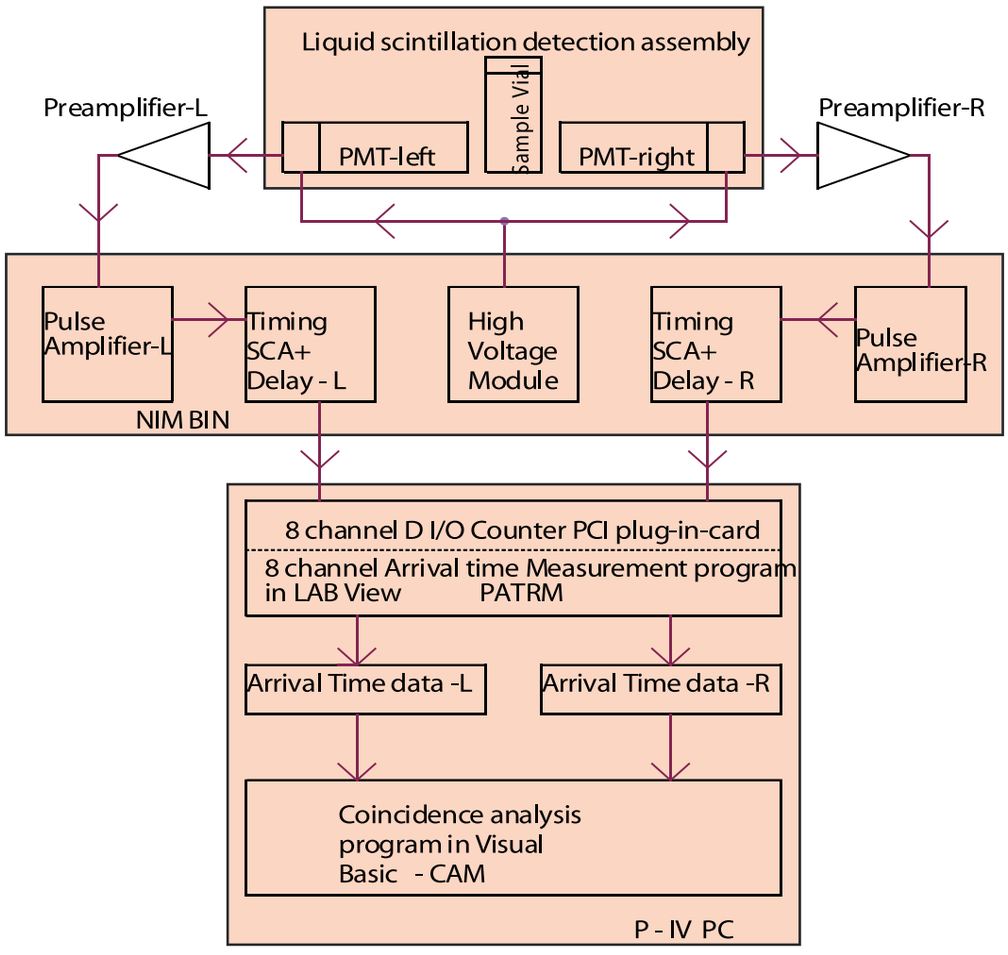

Fig.1
Liquid Scintillation Coincidence Counting System

V.15 Ion Source for Intense Pulse Neutron Source

An Intense Pulsed Neutron Source is being developed at RSD, Safety Group for assay of fissile materials in wastes.The neutrons are generated by T(d,n) ^{4}He reaction. The deuterons are accelerated to 150 keV potential and hit a rotating target of 150 Ci tritium generating a flux of 10^{10} neutrons/sec. The target being at ground potential imposes a constraint of maintaining a high power ion source at a high potential of 150 kV.

Various types of ion sources have been adopted for the DT neutron generators like Radiofrequency (RF), Penning (PIG) and Duoplasmatron (DP). RF ion source has the high monatomic ratio, while PIG and DP have high currents. For our DT neutron source, a single ring cusp magnetic field ion source has been chosen which satisfies both the reqirements of high mono atomic ratio and high currents. In this type of ion sources a discharge is struck between a hot filament and the anode. The electron confinement is aided by the presence of the magnetic field. The magnetic field is produced by placing permanent magnets along the circumference of the body. The body of the ion source is thermally shielded from the plasma by a floating electrode.

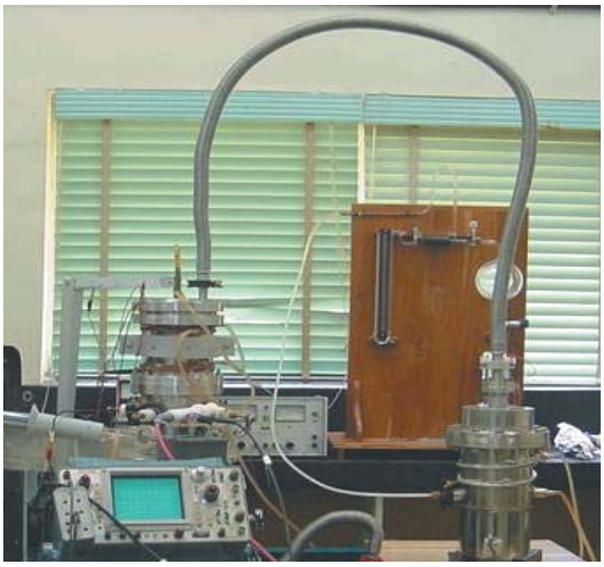

Fig.1
Ion Source for Intense Pulse Neutron Source

The source operates at a pressure of 0.1 Pa maintained by an oil diffusion pump based vacuum system. Deuterium produced by electrolysis of heavy water is introduced into the source by a heated Nickel leak. The gas feed into the vacuum system is automatically controlled by the electrolysis system as well as the Nickel leak system. The power supplies, the electrolytic deuteron production system and the Nickel leak system have been mounted in a high voltage dome. Experimental extraction of ions is being carried out using hydrogen. At the extraction point a beam current of 0.5 mA has been sustained. The ion source has been tested for continuous operation of 3 hours and the ion output was resonably stable.

V.16 High-performance Computing at IGCAR

A Cluster aggregates the computing powers of the interconnected nodes to provide more combined computing power, higher scalability, or to build in redundancy to provide higher availability. An High-Performance Computing (HPC) Cluster typically has a large number of computers (often called nodes) interconnected by high-speed, low-latency network. HPC Clusters are designed to use parallel computing to solve highly compute intensive problems.

A significant milestone has been achieved in scientific computing at IGCAR through the commissioning of a High-Performance Computing Cluster with 32 Itanium2 processors. This cluster delivers a maximal sustained performance of 156 GFlops with industry-standard HPL benchmark. The hardware environment is powered by the 16 Compute Nodes and a Management Node based on the state-of-the-art Itanium 2 processors in dual processor configurations. High-speed Gigabit Ethernet interconnects is used for communication between the nodes.

HPC Cluster System					
Cluster	Processor	Inter - connect	Memory / Node (GB)	Disk / Node (GB)	GFLOPS/ Cluster *
1 Management Node	Dual Itanium2 1.6 GHz	Gigabit Ethernet	4	1460	1P : 5.6
16 Compute Nodes	16 x Dual Itanium2 1.6 GHz	Gigabit Ethernet	4	146	32P : 156

*NOTE: Performance figures based on High-Performance Linpack N*N Calculations

Hardware Configuration:

The cluster infrastructure consists of Compute Nodes for intensive calculation and Management/Master Node(s) for management, storage and software development services.

Compute nodes are optimized for code execution and exclusively used for running parallel codes of users. The Itanium's 64-bit architecture with EPIC, SIMD and other pipelining technologies provides a significant performance increase by maximizing hardware-software synergy.

Management Node (Master Node) acts as a service node for administration and management of cluster hardware/software and data storage. Also it is the front-end node where users log in, develop and setup their applications, compile & link their code, test it and submit it. It takes care of job queuing and scheduling.

Gigabit Ethernet Networks, dedicated to specific functions, are used for communication: one for cluster administration & maintenance, and other for data transfer between compute nodes.

Software Environment for HPC Cluster:

HPC software component includes: operating system, middleware, compiler, parallel program development environment, debugger, performance analyzer, hardware/OS level node monitoring/management tool, cluster monitor/management tool and parallel applications. The cluster operating system is based on standard Linux distribution combined with a number of open-source applications. It provides a full environment for development including FORTRAN and C/C++ compilers, optimized scientific libraries, parallel libraries, as well as debugging tools and performance optimization tools. The following Compilers, Scientific Libraries and Tools are included in the HPC software suite.

- Intel C/C++ and Fortran Compilers
- GNU C, C++ and Fortran-77 Compilers
- Java BEA Weblogic JRockit VM
- Intel idb, GNU gdb, dmalloc, ElectricFence Debuggers
- Intel Trace Collector and Trace Analyzer
- PAPI, pfmon, cprof and gprof profilers
- Intel Cluster Math Kernel Library
- FFTW, Blacs, Scalapack, PETSc, Netcdf, BlockSolve95, and SuperLU scientific libraries

The system offers a choice of message passing libraries, including PVM, LAM-MPI and MPICH with common programming language interfaces. TORQUE is the resource manager used for batch job submission and queuing.

Applications:

The cluster system has been extensively used for solving very large computational problems in scientific research and engineering for variety of applications like Finite Element Analysis, Computational Fluid Dynamics, Computational Material Science/Molecular Dynamics, Monte-Carlo Simulation, and Weather Forecast Modeling etc. Parallel versions of CAE softwares namely LS-DYNA and

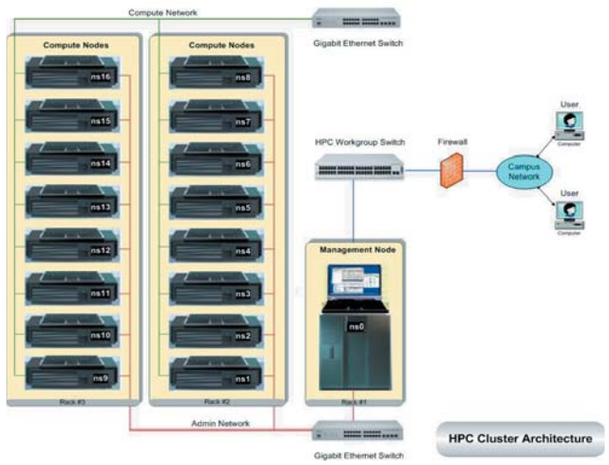

Fig.1
HPC Cluster Architecture

STAR-CD are installed in the cluster for FEA and CFD applications.

Two in-house developed reactor application codes namely SOLPREC and QAD-CGGP that were taking considerable amount of computing time were parallelized initially using the 8-way Intel Xeon Server System. The performance of a parallel program is stated in terms of speed-up. It is the ratio of the time taken for a program to execute in serial (with one processor) to that in parallel (with many processors).

The SOLPREC code developed at Safety Group (SG) estimates the radioactivity build-up due to the transport of activation corrosion products such as Mn-54 and Co-60 that get deposited in surfaces of pipes, heat exchanger and pumps in fast reactor along the flow path of coolant. The speed-up for the SOLPREC code was significant but not

linear as we increased the number of processors. There was much communication overhead involved in the program as the MPI Send/Recv calls were embedded within the time loop of the calculation. The speed-up realized was 1.8 employing 5 processors.

Detailed CPU-intensive gamma ray shielding calculations are being carried out using this computing facility. It computes the dose rate due to the volume source in arbitrary complex geometry of shielding configuration and involves ray-tracing technique. The speed-up obtained was 5.9 employing 6 processors. This code did not pose any communication overhead and a linear speed-up was obtained.

The high-performance computing cluster facility provides a reliable and scalable performance to meet the growing high-performance technical computing requirements of the users at a fraction of the cost of supercomputer.

V.17 Reliable Earthquake Notification System

An early Earthquake Notification System with a Tsunami warning system could reduce the possible damage and save many precious lives. Also, such an early warning system will help in taking the precautionary measures required in Nuclear Reactor sites like Kalpakkam. To enable this, an Earthquake Notification System (ENS) has been developed in-house. ENS is a software application program which scans the authentic geological websites periodically and checks if any new earthquakes occurred in our region, which may create a Tsunami. The new earthquakes which are of our concern are shown as notification at the client's PC.

Many innovative features have been added to make the ENS system more reliable and robust. The ENS has 2 components, namely, the server component and the client component. The server keeps scanning more than one geological website at a regular interval and updates its database with new earthquakes in our region and having a magnitude higher than some pre-fixed threshold. Two servers with identical capabilities and information are commissioned for higher reliability, to scan the websites and to respond to the clients. If the format of the information in the geological websites changes also which happens often, the server finds that and alerts the administrator. Fig.1 illustrates the operation of ENS schematically.

The client sits on the user computer located in different locations (MAPS and FBTR Control room) and keeps querying the server at regular interval for new notifications. If there are any new notifications, the application pops up and shows the notification with an alarm. The notification consists of earthquake details like magnitude, location, depth, region, and source of information. The user can click on individual notification and see the event location using online map or news from available search engines Fig.2 shows a typical screen shot during the occurrence of an earth quake.

The earthquake notification system can be used to initiate Tsunami warning siren, if required, to alert the families in the Kalpakkam Township and nearby villages. A system is also being installed at Nuclear Power Plant Township at Kudankulam.

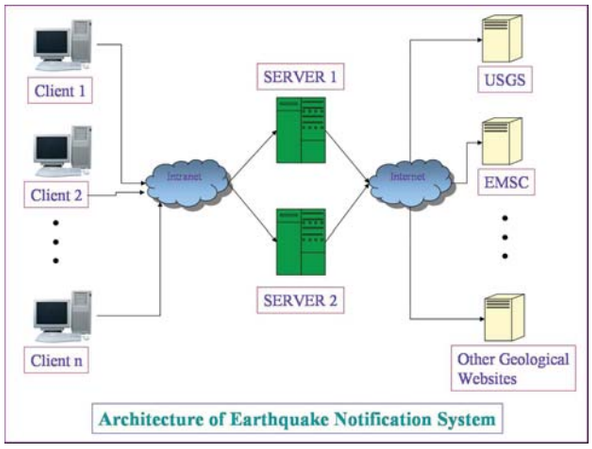

Fig.1
Operation Schematic of Earthquake Notification System

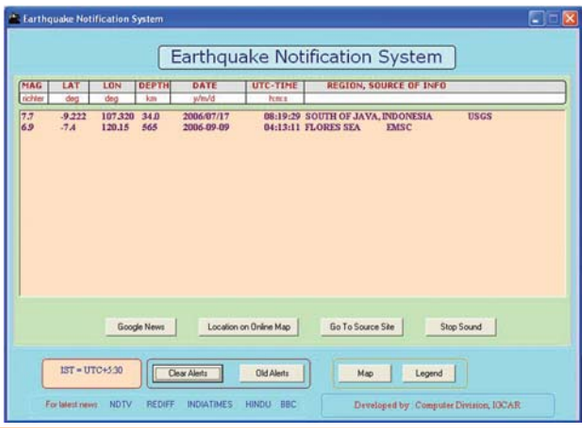

Fig.2
Screenshot of Earthquake Notification System in Control Room

Chapter - VI

BASIC RESEARCH

VI.1 Conformation Studies using Matrix Isolation Infrared Spectroscopy

Study of conformers is particularly important as many fundamental chemical processes can be understood on the basis of molecular structures. Various conformations of organic phosphates play an important role in its extraction chemistry. Factors affecting the structures, such as electronic and steric effects must therefore be clearly understood in order to unravel the role of molecular structures in extraction chemistry. Of the factors that affect the structure, the major contributor is the anomeric effect, which is basically a charge delocalization interaction between a non-bonded orbital of an electro-negative atom, such as oxygen, and an adjacent and suitably disposed antibonding sigma orbital. To study the role of anomeric effects in deciding conformational preferences in molecules, various studies have been performed using model compounds. Methoxymethanes and methoxysilanes are a class of components which possess a backbone structure similar to that present in organic phosphates, i.e. a C-O-X-O-C backbone, where X, may be C, Si or P. These model compounds were studied using matrix isolation infrared spectroscopy and ab-initio computations.

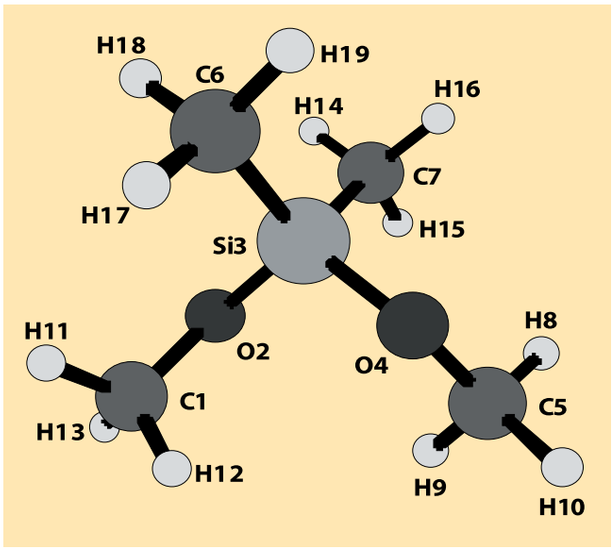

Fig.1
Structure of the Ground State Conformer in Dimethyldimethoxysilane, showing the Gauche Disposition of the C1 and C5

In matrix isolation infrared spectroscopy, the molecules were trapped in solid argon or nitrogen matrixes, at cryogenic temperatures (~12 K). When depositing the matrix, various nozzle sources, such as room temperature effusive, hot nozzle effusive and supersonic nozzle sources were used. The idea behind these experiments was to alter the ratio of the population of the different conformers in the matrix, which leads to a better understanding of the conformational picture. Calculations were performed at both HF and B3LYP levels of theory using 6-31++G** basis set to corroborate the experiments.

In all the methoxymethanes and methoxysilanes studied, it was found that the anomeric effect directs the carbons in the C-O-X-O-C backbone to adopt a gauche conformation; i.e. the dihedral angle between the C-O-X and the O-X-O plane is approximately 60° (Fig. 1). In compounds with extended chains, such as in structures with a C-C-O-X-O-C-C backbone, it was found that the carbon, attached to the oxygen, still retained the gauche orientation, but the terminal carbons adopted a trans orientation. This conclusion is of importance in understanding the structure of the organic phosphates, such as tributyl phosphate, where the carbon attached to the oxygen is expected to be gauche while the remainder of the carbons in the alkyl chain would be expected to be in a trans orientation. This conclusion has been confirmed in the case of triethylphosphate. These studies also show that the magnitude of the anomeric effect decreases on going from carbon to silicon. However, even though the effect decreases on going to silicon, it is still strong enough to retain the gauche orientation of these molecules, implying that the anomeric interactions would be important in the phosphates too. Natural bond orbital calculations on these systems also show that any alterations in the electronic distribution in the molecule may change the conformational preferences. This conclusion has far reaching implications in the extraction chemistry, as coordination of the phosphates with the metal, which can be expected to alter the electronic disposition in the molecule, altering conformational preferences.

VI.2 Laser Induced Breakdown Spectroscopy

Laser induced breakdown spectroscopy (LIBS) is a form of optical excitation in which the sample is vaporized by a high-energy laser pulse and forms a luminous plasma. The light from the plasma is temporally resolved to discriminate against the continuum emission from the plasma, and wavelength dispersed to obtain information regarding the composition of the material that is laser vaporized. This technique has received considerable attention in recent years as a versatile analytical technique, particularly in nuclear applications, as it offers several advantages: a) small sample size required for analysis, b) direct analysis of inhomogenous materials (without the need for any sample preparation), c) capable of analysis within a glove-box, and d) small turnaround time between sample submission and analysis. All the above advantages become particularly attractive in the analysis of radioactive samples.

In this method, the sample is first vaporized by a focused, high-energy laser pulse. Usually the fundamental (1064 nm) or the second harmonic (532 nm) of a YAG laser, with pulse energies in the realm of 20 to 50 mJ/pulse is used. Emission from the laser plasma is sampled through a collection lens and focused onto a spectrometer (Fig. 1). As emission in the first few hundred nanoseconds or so, after the laser pulse, is dominated by the continuum emission from the plasma, and it is only at later times that the emission is dominated by the elements constituting the solid sample (Fig. 2), the detection must be delayed. A spectrometer fitted with an ICCD (Intensified Charge Couple Device) is usually the detector of choice in such experiments.

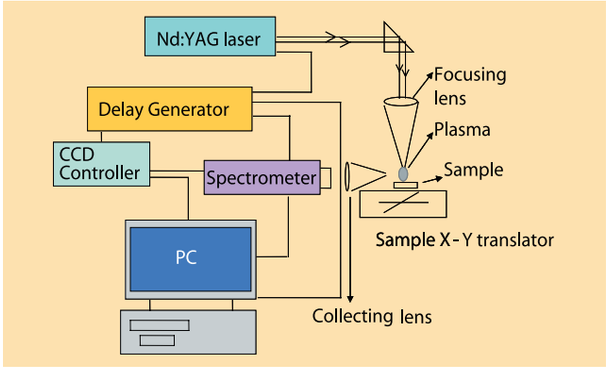

Fig.1
Experimental Set up of the Laser Induced Breakdown Spectrometer.

A LIBS facility has been set up using a Nd:YAG laser as the source and a Triax 550 monochromator (f = 0.55 m) fitted with a 2400 grooves/mm grating and an ICCD as the detector. The LIBS technique was applied to a number of stainless steel samples with a view to standardizing the technique. The LIBS signal of Cr, Ni and Mo, were recorded as a function of concentration for various samples (Fig. 3). Sharp emission lines were obtained and it must be noted that these spectra were recorded with no prior sample preparation, highlighting the ease in the application of this technique. The spectra were recorded using a gate width of 5000 µs and a delay of 7000 µs after the laser pulse. Typically the average signal of 15 laser pulses were obtained to achieve a good signal to noise. Plots of LIBS emission intensity against concentration of the anlayte element yielded linear plots. Using these calibration graphs, concentration of these elements in analyte samples can be determined. The precision of the LIBS data was observed to be 10% (RSD) which compares somewhat poorly with other spectroanalytical techniques such as AAS or ICP-AES. However, the simplicity of sample handling, particularly when handling refractory materials, renders the LIBS method superior. This work only represents the initial phase of setting up the technique and validation of the method. Our immediate future work would involve the study of the emission process in vacuum or in the presence of controlled pressures of inert gases and the eventual adaptation of this method for liquid samples.

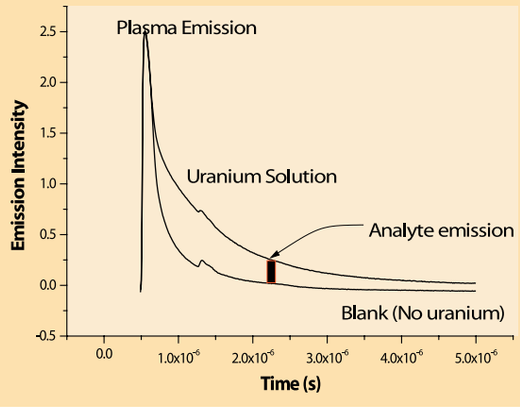

Fig.2
LIBS Temporal Emission Curves to Show Plasma and Analyte Emission.

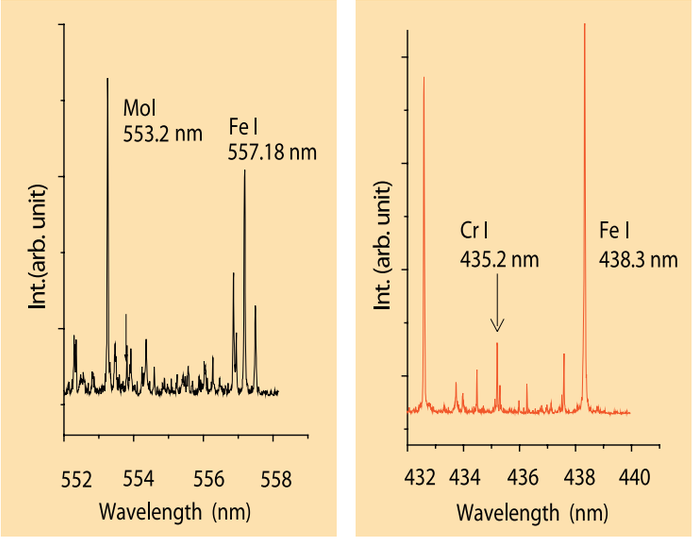

Fig.3
Spectrum Showing Mo and Cr Lines in Steel (BAS 475) Samples, Different Region was Shown to Highlight Emission from Different Elements.

VI.3 Monovacancies in Titanium Carbide: An ab-initio Computational Study

Titanium carbide has attracted attention in nuclear applications in view of its role in the form of nanoscale precipitates in austentic stainless steel to reduce void swelling at higher temperatures. Hence, it is imperative to understand the behaviour of TiC/austenite interfacial defects under various conditions. In general, metal carbides suffer from carbon off-stoichiometry, which is known to affect their mechanical properties. Positron annihilation spectroscopy is an excellent technique for studies of open volume defects like vacancies. We have carried out detailed positron lifetime measurements to understand the TiC precipitation behaviour in D9 alloys. Fig.1 shows the variation of positron lifetime observed after 1000 K annealing of pre-cold worked D9 samples with different Ti/C ratios. The sample without Ti shows a defect free lifetime of about 110 ps. With increasing Ti/C ratio, the positron lifetime increases to a maximum for Ti/C~6 and decreases thereafter. These variations are interpreted as due to variation in the number density of TiC nano particles. The inset in Fig.1 shows two major trapping sites for positron; viz., vacancy inside TiC and interfacial defects. In D9 alloy, positrons are expected to be trapped by vacancy type interfacial defects. Earlier positron experimental studies on transition metal carbides coupled with theoretical calculations were in agreement with experimentally observed carbon deficiency. However, TiC was observed to be an exception wherein Ti deficiency is inferred from Linear Muffin Tin Orbitals (LMTO) calculations of positron annihilation parameters. These earlier computational studies mainly suffer from a small supercell size, which leads to ordering of vacancies instead of simulating an isolated monovacancy and also lack of self consistent structural relaxation of the vacancy. With the recent developments in ab- initio electronic structure calculations and availability of 16 node parallel computing facility at Computer Division, self-consistent electronic structure calculations have been carried out using Projector Augmented Wave (PAW) pseudo potential as implemented in Vienna Ab initio Simulation Package (VASP) to address the carbon and titanium vacancies in TiC. The vacancy structure was relaxed and resultant electron density and relaxed structure were used to compute positron annihilation parameters.

In order to study mono-vacancies in TiC, a 3x3x3 super cell is constructed with 215 atoms and a vacancy at the body centre of the super cell. This system is relaxed to reduce forces on each atoms using VASP and resultant configuration is used to estimate positron density at and around vacancy as well as positron lifetime. Both Ti and C vacancies were studied using this scheme. Fig.2 shows the forces acting on neighboring atoms around a C-vacancy in TiC. Contrary to common expectation, both C and Ti vacancies are found to expand as compared to a vacancy in iron. The amount of outward relaxation of first neighbour atoms around C-vacancy is found to compare well with earlier experimental X-ray diffraction studies. Fig.3 shows the computed positron density profile along (110) plane of the

relaxed supercell with a carbon vacancy at the body centre. The colour grading is with blue and white representing minimum and maximum positron densities, respectively. Positron trapping at vacancy is evident from the confined nature of positron density profile as shown in Fig.3. These refined positron lifetime computations reveal that carbon vacancy is the one which correlates with the experimental observations in Titanium carbide. Detailed studies on interfacial defects and defect-helium interactions are planned with upcoming 64 node cluster computer facility.

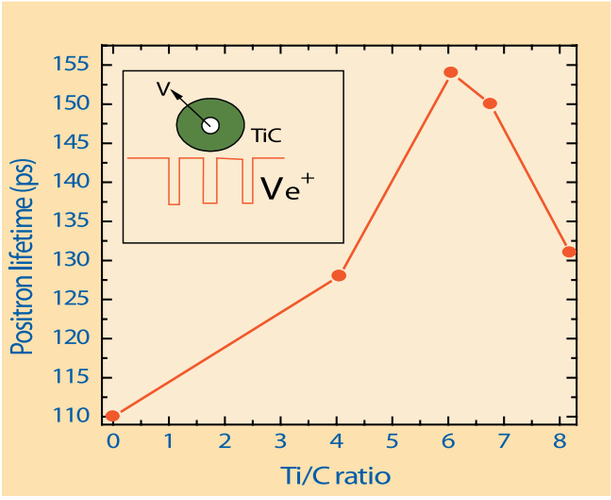

Fig.1
Variation of Positron Lifetime Observed after 1000 K Annealing of Pre-cold worked D9 Samples as a Function of Different Ti/C ratios. The inset shows two major trapping sites for positron; viz, vacancy inside TiC and interfacial defects between the matrix and TiC precipitate.

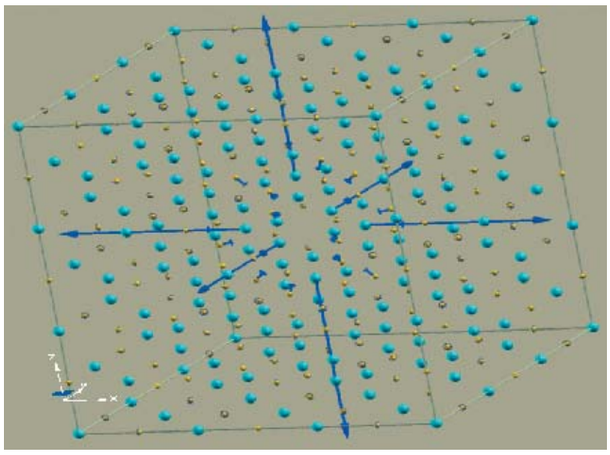

Fig.2
A 3x3x3 super cell of TiC with C Vacancy at the Body Centre. The arrows indicate the direction of force acting on each atom and the length is proportional to the magnitude of force. A maximum force of 1.85 eV/Å is experienced by first nearest neighbor Ti atoms, indicated by longest arrows.

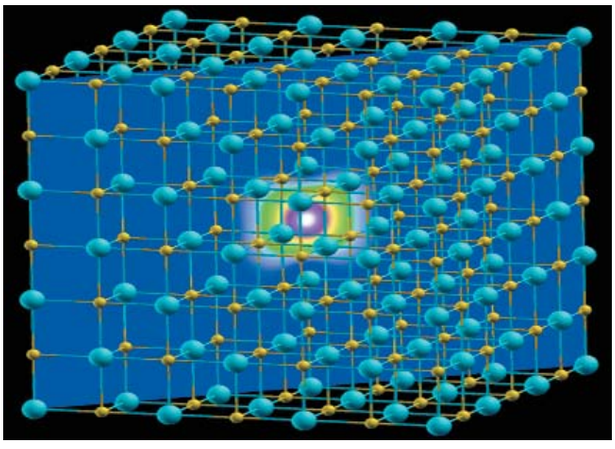

Fig.3
Computed Positron Density Profile along (110) Plane in the Completely Relaxed TiC supercell with C Vacancy at the Body Centre. The colour grading from blue to white is representing the increasing positron density.

VI.4 Positron Annihilation Studies of Metal-silicides

Metal-silicides find extensive technological applications in a variety of fields such as strengthening of alloys, ohmic contacts and interconnects in integrated circuits. There is also fundamental interest in studying silicide phase transformation in metal-semiconductor junctions, because diffusion and defects play a crucial role in determining the nature of silicide phases and the transformation temperature. Detailed experimental studies have been carried out on Pd/Si, Ni/Si and Co/Si thin film junctions, wherein a thin metal film (of the order of a few hundred nanometers) has been coated on Si substrates. These samples have been subjected to thermal annealing at successively elevated temperatures (300-1170 K) and corroborative experimental studies using variable low energy positron beam, Auger electron spectroscopy (AES), Glancing incidence X-ray diffraction (GIXRD), Rutherford backscattering Spectrometry (RBS) and Scanning electron microscopy (SEM) have been carried out.

Figure 1 shows the results of positron beam studies on Pd(10nm)/Si sample, subjected to various annealing temperatures. The most notable feature is that defect sensitive lineshape S-parameter shows distinct values attributable to the metal overlayer and the substrate, across the metal-semiconductor interface. This S-parameter Vs. positron beam curve suddenly changes at 570 K, due to silicide phase formation, which has been confirmed by GIXRD. Beyond 870 K, while GIXRD does not show any phase changes, noticeable increase in S-parameter is observed across the over-layer and the substrate, which are attributable to vacancy-defect production across the silicide-silicon interface. Figure 2 shows AES results in terms of the variation of Pd and Si surface atomic concentrations, which clearly indicate that Pd_2Si silicide phase forms at 570 K and beyond 870 K, there is enhanced Si segregation at the surface. Apart from this, corroborative RBS measurements have also confirmed Si-enrichment at the surface. Due to this enhanced Si diffusion from the substrate regions, vacancy defects are produced across the interface and Si substrate, which has resulted in the observed changes in the S-parameter, as shown in Fig.1. From these combined experimental studies, it is found that Si is the fast diffusing species for the silicidation to occur and further, subsequent to the silcidation, Si atoms diffuse from the substrate region to the surface of the silicide layer, giving rise to above experimental observations.

Fig.3 shows the schematic of phase transformations occurring at various annealing temperatures in Ni/Si thin film structures, obtained using the above experimental techniques. It is found that the sequence of silicide phases formed depends on the nature of diffusing species i.e., metal or silicon atoms, the thickness of the metal over-layer. In the case of Ni/Si system, it is found that Ni is the fast diffusing species and hence, initially it results in the co-existence of a series of silicide phases consisting of Ni_2Si, NiSi and $NiSi_2$ at various depth regions. Due to surface-sensitive nature of AES, depth-resolved nature of experimental techniques such as positron beam, GIXRD and RBS, these phases could be resolved. As the annealing temperature is increased, all the phases eventually get transformed to $NiSi_2$ phase.

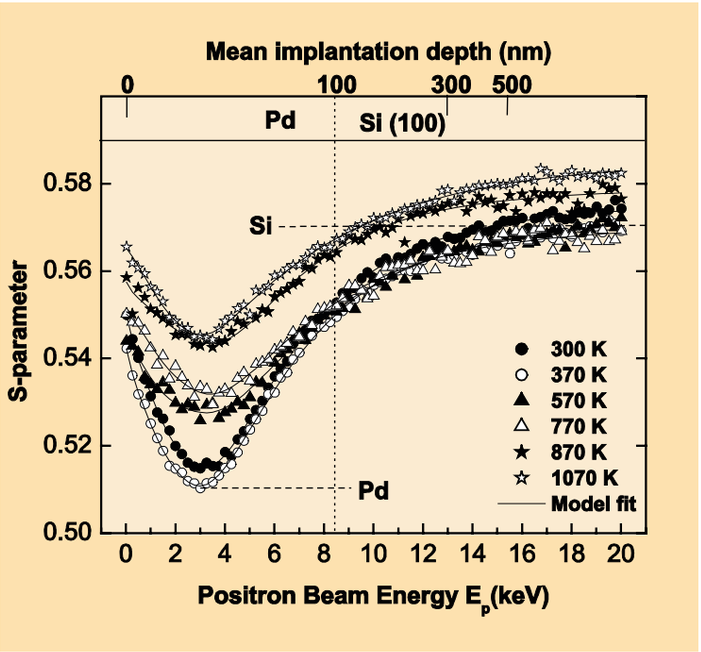

Fig.1
Defect-sensitive Positron Lineshape S-parameter Verses Positron Beam Energy Curves at Various Annealing Temperatures for Pd(100 nm)/Si System. The location of the interface is indicated by vertical dotted line and the mean depth probed by Positron Beam is shown on the top axis.

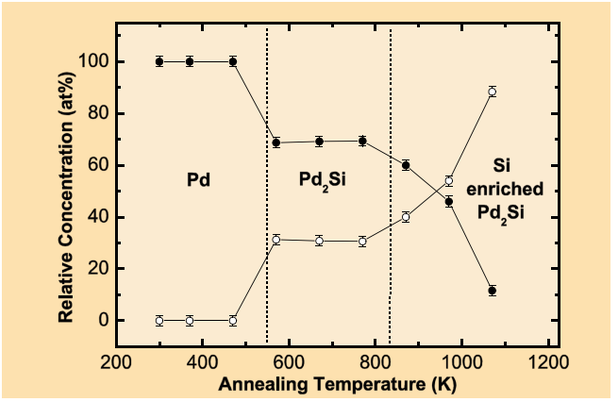

Fig.2
Auger Electron Spectroscopy Results in terms of Relative Concentration of Pd (solid circles) and Si (open circles) as a Function of Annealing temperature for Pd/Si System. The Temperature Regions Corresponding to the Transformation of the over-layer from Pd to Pd_2Si and Si-enrichment of Silicide are indicated by vertical dotted lines.

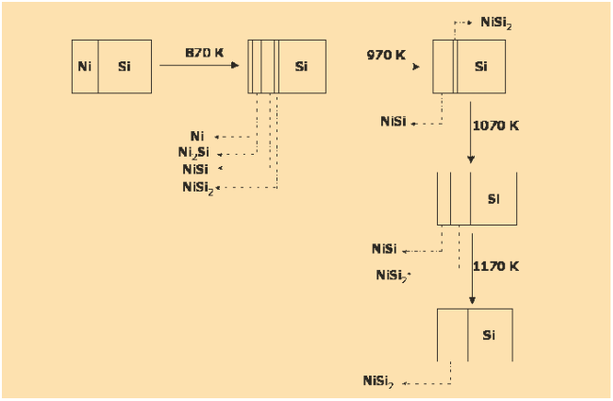

Fig.3
Schematic Diagram of Phase Transformations in Ni (100 nm)/Si System, showing the Evolution of Silicide Phases at Different Depth Regions Due to Annealing at Various Temperatures, obtained using Positron Beam, AES, GIXRD and RBS Techniques.

VI.5 A Novel Negative Thermal Expansion Material: $Zn(CN)_2$

Negative thermal expansion materials and zero thermal expansion materials are perceived to be of importance due to their anticipated applications and also from the point of view of understanding the origin of the novel behaviour. While most of the substances show a positive thermal expansion on heating, a few substances have shown negative expansion at least in a small range of temperature. The oxide framework material ZrW_2O_8 condensing in a cubic structure is a classic example of a negative thermal expansion material which has been studied extensively. It shows an isotropic thermal expansion co-efficient value of -0.5×10^{-5} K^{-1}. Much higher, and anomalously large, value of isotropic expansion co-efficient (α) has been reported on $Zn(CN)_2$ by neutron diffraction experiments carried out at two temperatures namely 14 K and 305 K. $Zn(CN)_2$ is characterized by the existence of diatomic linkage (M-C-N-M') between the metal atoms. Fig.1 shows the structure of $Zn(CN)_2$. In fact, based on the arrangement of C and N, Zn $(CN)_2$ can condense in an ordered structure with $P\bar{4}3m$ or in a disordered structure with $Pn\bar{3}m$ symmetry. Simulations carried out based on the density functional formalism to resolve the structure have not shown the structure of this material conclusively. Raman and IR measurements carried out and analysed using Factor Group analysis indicate that $Zn(CN)_2$ prefers the disordered structure. In the present study the aim was to find out if the negative thermal expansion continues beyond room temperature and also to check if the structure remains the same or undergoes a transition at higher temperatures. Polycrystalline and phase pure $Zn(CN)_2$ samples were loaded on a diffractometer with a high temperature attachment. The sample holder is a tantalum strip with a cup of about 6 mm dia and 0.5 mm depth at the centre of the strip. A Pt-Rh thermometer spot-welded at the back side of the cup

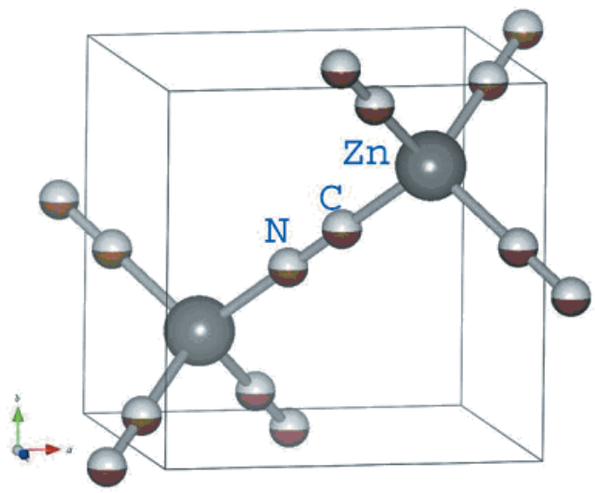

Fig.1
Structure of Disordered $Zn(CN)_2$

measures temperature with an accuracy of ±1°C. The diffractometer uses Cu Kv radiation and is aligned with NBS standard silicon powder. X-ray diffraction data are collected from 2θ = 20° to 70° from room temperature up to 600 °C

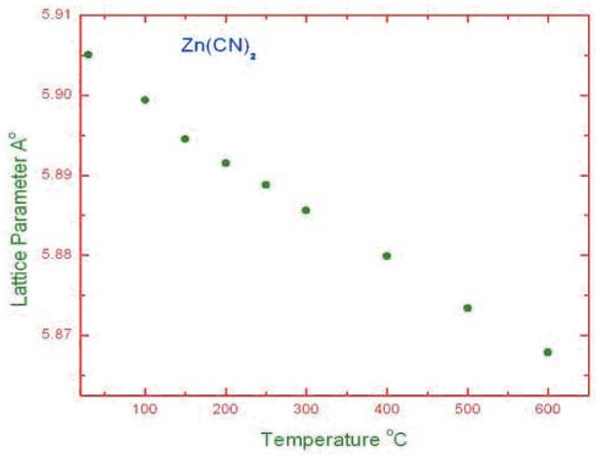

Fig.2
Lattice Parameter Vs Temperature Showing Lattice Contraction with Increasing Temperature

since it is known that the sample decomposes at 800°C. The data has been analysed with a disordered structural model (Fig.1) with $Pn\bar{3}m$ symmetry where Zn-C and Zn-N tetra hedra are stacked randomly. Figure 2 shows the lattice parameter plotted as a function of temperature indicating a negative thermal expansion. The coefficient of lattice expansion is calculated to be -1.046698 x 10^{-5} / K, which is almost twice as much as the negative expansion observed in ZrW_2O_8.

In $Zn(CN)_2$, the diatomic bridge formed by C and N connects the two Zn atoms. It is this diatomic feature that seems to give the extra flexibility for contraction due to the tilting of the C-N dumb-bell without any change in the bond length. The monotonic decrease in lattice parameter as a function of temperature clearly indicates that the mechanism of tilting of the C-N dumb-bells is robust even at high temperature. The present study has also shown that there is no structural phase transition in this material up to 600°C.

VI.6 Magnetoresistance in Cobaltites

Magnetoresistance(MR) as the name implies is the change in resistance brought about by an applied magnetic field. GMR and AMR are commonly used in devices such as read/write heads, where G stands for a Giant change as compared to ordinary MR and A for Anisotropic changes in resistance. To have practical use, MR should be observed for small changes in applied magnetic field. In the currently fashionable Collosal magneto resistance materials (CMR) even though the measured change in resistance is large, it occurs under high magnetic field and has thus not found many applications.

The oxygen deficient double perovskite $GdBaCo_2O_{5.5+\delta}$ termed cobaltite, shows a rich variety of phase transitions both as function temperature and oxygen stoichiometry δ. The δ=0 composition consists of a Co-O layer containing alternating pyramids of CoO_5 and octahedra of CoO_6, stacked along the b-axis (see Fig.1a). The competition between the crystal field splitting energy (Δ_{CF}) and Hund's coupling energy (J_H) leads to three spin configurations of Co^{3+} such as low spin LS ($t_{2g}^6, e_g^0, S=0$), high spin HS ($t_{2g}^4, e_g^2, S=2$) and intermediate spin state IS ($t_{2g}^5, e_g^1, S=1$). In the pyramidal site, Co^{3+} is in the IS spin state (S=1), whereas in the octahedral site Co^{3+} can be either in the LS or HS state. Since the energy difference between LS and HS for octahedral δ is very small, even a small thermal fluctuations can give rise to spin state transitions The transition from the HS to LS state at 360 K results in a transition from metallic to an insulating state. On lowering the temperature below 270 K, the ordering of these S=1 spins along a-axis results in the appearance of ferromagnetism in the insulating phase (FMI) below T_C. Inter-chain interactions leads to an antiferromagnetic (AFI) at T_N ~ 240 K. It has been shown by resistivity measurements in single crystalline samples that there is large negative MR associated with the FMI-AFI transition. In fact the FMI-AFI transition temperature is lowered in the presence of external magnetic field and since the FMI phase has lower resistivity, a negative MR ensues.

Chemical substitution at different sites in $GdBaCo_2O_{5.5}$ seems to have a significant effect on the various phase transitions in this system, depending on how the spin sublattice and the charge on the octahedral network gets affected, due to the substitutions. With Ni substitution at Co site the T_{MIT} decreases, T_C and also T_N decrease, the degree of orthorhombicity increases and the cell volume decreases. In

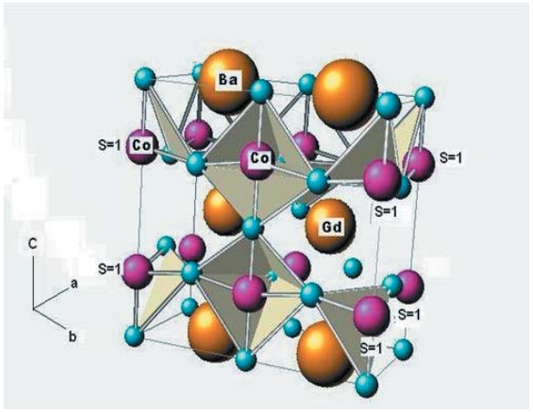

Fig.1 (a)
The Crystal Structure of Ideal $GdBaCo_2O_{5.5}$ Gd, Ba and Co are marked, the atoms marked blue are oxygen. The pyramids with Co in the S=1 spin state form chains along the a-axis The Co housed in the octahedral undergo the S=0 to S=1 transition at the insulator to metal transition.

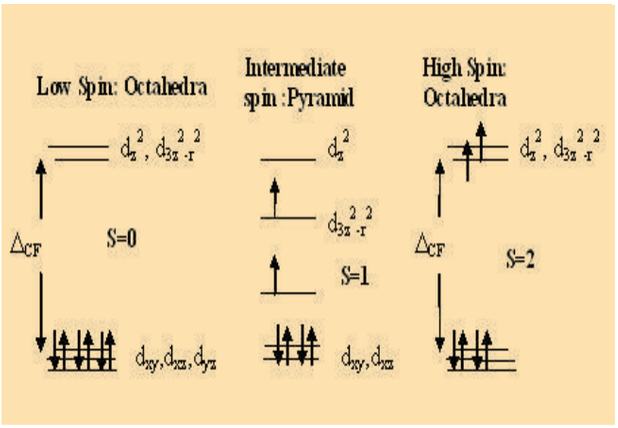

Fig. 1 (b)
The Schematic Diagram of Electronic Structure of the Co-O Octahedra and Pyramids, indicating the various possible spin configurations.

contrast, the T_{MIT} remains unchanged with Fe substitution, the T_C increases slightly but T_N decreases with Fe substitution, the cell volume increases with Fe and the degree of orthorhombicity remains unaltered with substitution. The observed MR for both Ni and Fe substitutions is larger than in the pristine sample. Ce substitution at the Gd site has also been carried out. T_{MIT}, T_C and T_N decrease with Ce substitution the degree of orthorhombicity decreases and cell volume increases and so does MR.

Magnetoresistance measurements were carried out using the four probe method in a temperature range of 4.2K to 300K, and in magnetic fields up to 12 Tesla. In Fig.2 is shown the resistance behaviour in pristine, Fe, Ce and Ni substituted samples for 0 Tesla and 6 Tesla in the 25 K-300 K temperature range. It is clear from the figure that a negative MR is observed over a limited temperature range in all samples, but the range over which negative MR is observed is larger in the substituted samples. The MR defined as (R(0)-R(H))/R(0) in percentage is shown in Fig.3 for the Ce series of samples as a function of magnetic field upto 12 Tesla, at different temperatures. The MR in the Ce substituted sample is seen to be much larger than the MR observed in the pristine sample. Even a greater decrease is seen in the Ni substituted samples at similar temperatures. It is interesting that MR as large as 10% has been observed even in the ferromagnetic phase. It is noteworthy that by Fe, Sr and Ca in $GdBaCo_2O_{5.5}$ substitution the T_C has shifted to higher temperature. Shifting T_C beyond room temperature may not be an impossibility in this system, making way for the observation of room temperature ferromagnetism. It may also be possible to obtain large MR at room temperature a property useful for applications.

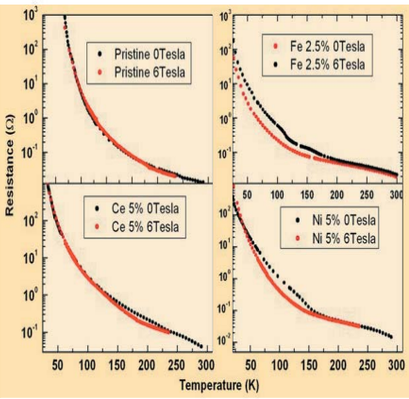

Fig.2
The Resistance in the Pristine, Fe,Ni and Ce Substituted $GdBaCo_2O_{5.5}$ Sample for 0 Tesla and 6 Tesla in the 4.2K-300K Temperature Range. The percentage of Fe and Ni substitution at the Co site and Ce at the Gd site are indicated in the respective panels.

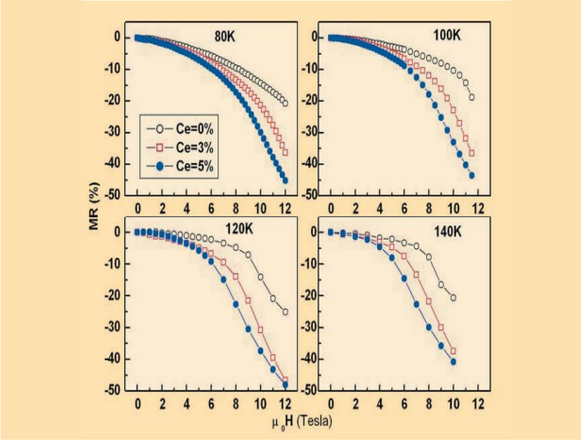

Fig.3
The MR Defined as (R(0)-R(H))/(R(0) in Percentage, Shown for Different amounts of Ce Substituted at the Gd site in $GdBaCo_2O_{5.5}$, Compared at Various Temperatures. The increase in MR arises due to the system undergoing a AFM to FM transition with increasing magnetic field.

VI.7 Measurement of δ-ferrite Content in Stainless Steel 316 L(N) Weld Joint through SQUID based Remanent Magnetization Measurements

Austenitic stainless steel 316L(N) is widely used in nuclear and non-nuclear power plants as a major construction material for the fabrication of large mechanical components. The welding process dominates in the manufacture of any large mechanical component and there is a high probability for a defect to be present in the welded joint and the heat-affected zone. This may lead to failure of the component during operation and service. It is known that the presence of a limited amount of d-ferrite, usually in the range of 3 to 5 FN (Ferrite Number), is favorable in reducing hot cracking and micro-fissuring during welding. However, exposure of the weld joints to fatigue deformation at high temperatures above 500˚C for extended periods causes transformation of the magnetic d-ferrite phase into various non-magnetic intermetallic phases including the hard and brittle σ phase. Superconducting Quantum Interference Devices (SQUIDs) developed indigenously represent the most sensitive magnetic sensors available today and are suitable for the detection of such changes in the magnetic content. A SQUID based technique has been developed for the Non-Destructive Evaluation (NDE) of δ-ferrite content in the stainless steel weld joint subjected to low cycle fatigue loading at 600ºC.

In this study, a single weld joint was selected for remanent magnetization measurements in the virgin state and subsequently after every additional 50 fatigue cycles using a homebuilt SQUID system as well as a Bartington flux gate sensor. 316L(N) stainless steel weldment specimens were prepared by welding 316 L(N) base metal with 316N electrodes by the manual metal-arc welding process. Welding was carried out on a 25mm thick plate with a double-V configuration with an included angle of 70°. The low cycle fatigue (LCF) tests were conducted at a strain amplitude of ±0.6% using an Instron servo-hydraulic fatigue testing machine under total axial strain control mode. A strain rate of $3x10^{-3}s^{-1}$ was employed for the test. At each stage prior to the commencement of the remanent magnetization measurement, the weld joint was properly demagnetized to eliminate the influence of the past history and then re-magnetized by applying a preset magnetic field for a preset time.

Fig.1.
Photograph of the Experimental Arrangement for SQUID-NDE. The SQUID sensor is mounted inside the liquid helium dewar. The specimen is scanned over the entire length by placing it on the sample stage of a XY scanner with a positioning accuracy of 25 microns.

The specimen was scanned over the entire length by placing it at the centre of the sample stage of a XY scanner with a positioning accuracy of 25 microns, which has been custom built avoiding the use of magnetic as well as metallic materials in the vicinity of the sample stage. Fig.1 shows the photograph of the experimental arrangement. The magnetic signal from the weld joint was coupled to the SQUID device using a superconducting pick-up loop in the form of a first order gradiometer in order to discriminate against distant sources of magnetic noise. The virgin weld joint gave a maximum SQUID signal of 15 F0 during scanning, which decreased rapidly to 6.67 F0 when the sample was subjected to LCF for 50 cycles at 600°C (Φ_0 is a quantum of magnetic flux which is equal to ~ 2.07×10^{-15} webers). Thereafter, no significant changes in the maximum SQUID signal could be observed up to 150 cycles. However, a change in the SQUID signal was noticed when the sample was subjected to LCF for 200 cycles; this was also accompanied by the initiation of a crack at the boundary of the weld joint. Micro-cracks were seen at the boundary of the weld

joint when the specimen was examined through a microscope. Fig.2 shows the variation in the maximum SQUID signal as a function of number of cycles of fatigue loading and portrays the progressive transformation of the magnetic δ-ferrite phase to nonmagnetic phases when the weld joint is subjected to LCF at 600°C. To corroborate the SQUID data, magnetization of the weld joint was also measured using a Barrington flux gate sensor operated inside the magnetically shielded environment provided by a set of three concentric μ-metal cylinders. The magnetic shielding was essential during the flux gate based measurements since the flux gate measures the magnetic signal directly as opposed to its axial gradient measured by the SQUID sensor. In this data, however, no significant change of magnetic signal could be observed after 200 cycles as seen in the SQUID based measurements. These results augur well for further development of the SQUID based NDE technique for applications, which require harnessing of the unparalleled sensitivity offered by the SQUID sensor.

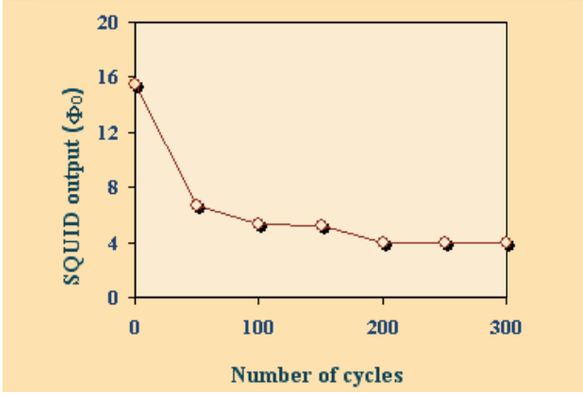

Fig.2
Change of SQUID Output Vs Number of Fatigue Cycles for the Weldment Specimen Subjected to Fatigue Deformation.

VI.8 Ergodic to Non-ergodic Transition in γ-ray Irradiated Polyacrylamide Solutions: A Light Scattering Study

Hydrogel is a three-dimensional network made up of polymer chains, which are weakly cross-linked together by covalent bonds and containing a large amount of water. They are used in a diverse range of technologies such as in controlled release systems, super absorbents, size-selective separators and so on. Further, colloidal crystalline arrays immobilized in a polymer hydrogel such as polyacrylamide have found high-tech applications such as tunable photonic crystals, chemical sensors and optical switches. Immobilization of colloidal crystalline arrays in a hydrogel involves growing a crystal first in aqueous polymer solution and then transforming the polymer solution to a gel by photo-polymerization or by γ-irradiation. The length scales and time scales involved in the sol-gel process are accessible to light scattering, hence we employ static and dynamic light scattering techniques.

Dynamic light scattering (DLS) probes density-density fluctuations. If the characteristic decay time of these fluctuations is smaller than the time taken for performing a single DLS experiment, the system explores complete phase space. Thus, for an ergodic system the time averaged $g^{(2)}(q,t)$ is identical to the ensemble averaged

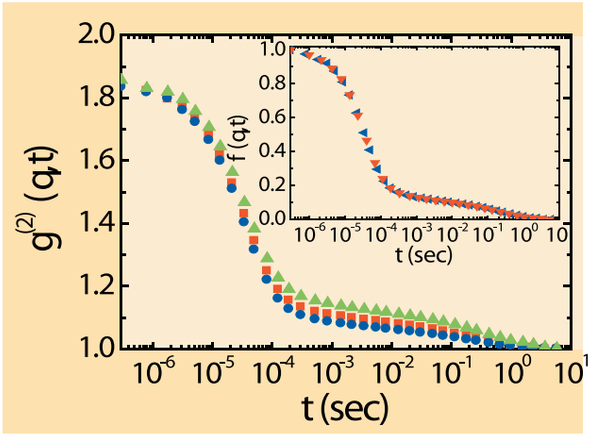

Fig.1
$g^{(2)}$ (q,t) Measured at Three Different Positions for 0.25 MRad Sample. Inset shows time averaged (B) and ensemble averaged (B) f(q,t)s. These two being identical implies that sample is ergodic.

$g^{(2)}(q,t)$, which is, related to the field correlation function f(q,t) by Eq. 1. In case of polymer hydrogels, the presence of frozen-in structures (inhomogeneties) formed during gelation complicates the DLS data. The static electric field from these inhomogeneties interferes directly with the electric field from gel modes. Since these inhomogeneties are static and random, the time-averaged $g^{(2)}(q,t)$

measured from one sub-region of the sample is not same as that obtained by ensemble averaging (measured from different sub regions of the sample and then averaged) i.e. the system is non-ergodic. A simple way of obtaining ensemble averaged field correlation function for non-ergodic systems such as gels and colloidal glasses is given by Eq.2.

Polyacrylamide solutions with 2.5wt% concentration were prepared by taking dust-free acrylamide solutions with photo-initiator and exposing them to UV radiation. These polymer solutions were irradiated with a γ-ray (^{60}Co source with average γ-energy 1.25 MeV) for different doses. Measurements were carried out using a DLS set-up equipped with multi-tau correlator and an Ar/Kr ion mixed laser.

For an ergodic system time averaged intensity correlation function is $g^{(2)}(q,t)$, which is related to the electric field correlation function by

$$g^{(2)}(q,t) = 1 + |\beta f(q,t)|^2 \qquad (1)$$

Where ß is the coherence factor (~1). Here, scattering wave vector q = [(4Лμ/λ) sin (q/2)]. For a non-ergodic system

$$f(q,t) = \frac{Y-1}{Y} + \frac{[g^{(2)}(q,t) - \sigma^2]^{1/2}}{Y} \qquad (2)$$

Where Y is the ratio of ensemble averaged scattered intensity <I(q)>E to time-averaged scattered intensity <I(q)>T and σ^2 is the mean square fluctuation in the scattered intensity. Both Y and σ^2 are experimentally accessible. <I(q)>E is measured by accessing different sub-regions of the sample through subjecting it to slow rotation.

Fig.1 shows the time averaged intensity correlation functions measured at different positions of polyacrylamide solution, which is irradiated, to a dose of 0.25 MRad. It can be seen that all correlations functions merge and decay from a value of approximately 1.9 to 1. The inset shows field correlation functions obtained using Eqs.1 and 2 and is identical. These observations imply that 0.25 MRad irradiated sample is ergodic. Further this sample is observed to be highly viscous yet flows (Fig.2 (a)) when inverted, suggesting that no gelation has occurred in this sample. However on exposure to doses of 1 MRad and 3 MRad no flow was observed when inverted (Fig.2 (b), (c)) indicating gelation upon irradiation. The time averaged intensity correlation functions measured at different positions on 3 MRad sample are shown in Fig.3 and they show strong position dependence. Inset shows field correlation functions obtained from Eq.1 (curve a) and Eq.2 (curve b). Unlike in 0.25 MRad sample (inset in Fig.1), these two curves differ widely; this suggests that system is non-ergodic. Similar behavior is observed in 1MRad sample. The ensemble averaged f(*q,t*) decays initially and saturates to a non-zero value at longer-times. The saturation in f(*q,t*) implies presence of frozen-in-fluctuations. Detailed studies of q-dependence of f(*q,t*) revealed that the dynamics in γ -irradiated gel is describable by a model that incorporates gel modes plus inhomogeneties.

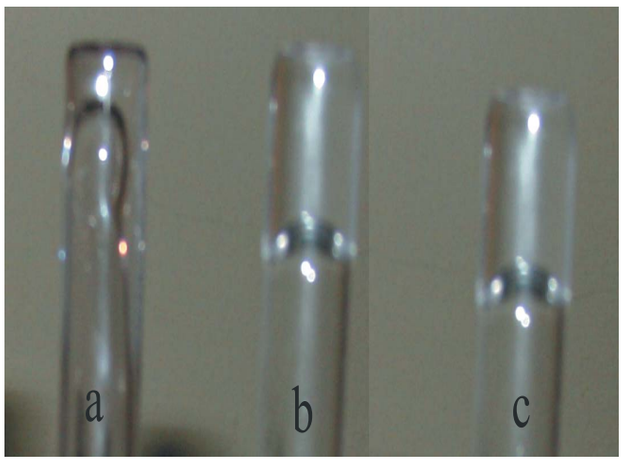

Fig.2
Photographs of Sample Cells with Polyacrylamide Solutions Irradiated to Different Doses: (a) 0.25 MRad, (b) 1 MRad and (c) 3 MRad. Sample irradiated to a dose of 0.25 MRad flows, but turn rigid (no flow) when exposed to higher doses.

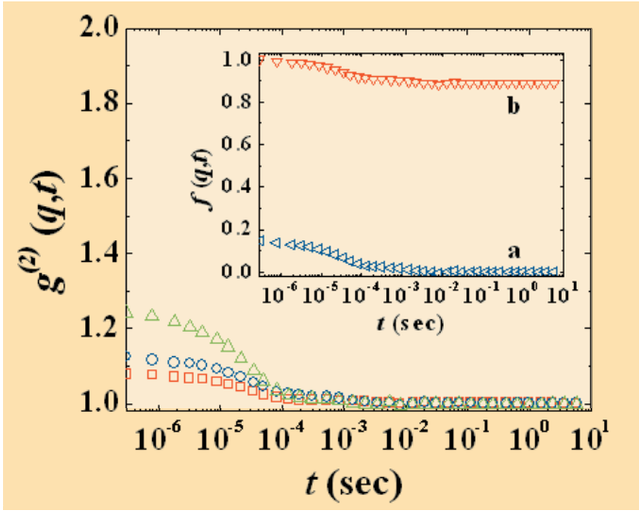

Fig.3
$g^{(2)}$ (q,t) Measured at Three Different Positions for 3 MRad Sample. Notice that they are all different. Inset shows f(q,t)s obtained by (a) time average and (b) by ensemble average. Unlike in Fig.1 these two are not same, which implies that 3 MRad sample is non-ergodic.

VI.9 Carbon Profiling using Resonant Nuclear Reaction Analysis Technique for Studying Radiation Enhanced Diffusion

Rutherford Backscattering Spectrometry (RBS) is a very popular, fast, and non-destructive technique that has been used extensively for Ion Beam Analysis (IBA). However, RBS with $^4He^+$ ion beams, in many cases, is ineffective for light element analysis due to overlapping signals and small scattering cross section. Both nuclear reaction analysis and non-Rutherford elastic scattering have been widely used for analysis of light elements in solids; these two ion-beam methods complement more traditional analysis by Rutherford backscattering spectrometry. There are several resonant elastic reactions available with narrow resonance width and enhanced cross sections. A typical nuclear resonant scattering reaction ($^{12}C(\alpha,\alpha)^{12}C$) suitable for depth profiling of carbon is shown in Fig.1. As the enhancement in cross section over Rutherford cross section is about 120, resonant scattering can be effectively utilised for the profiling of carbon.

The Resonant Nuclear Reaction Analysis (RNRA) was made use of for the study of carbon diffusion and surface segregation in silicon during carbon ion implantation at elevated temperatures. The generation of defects and their interaction under irradiation conditions can significantly affect atomic mobility and the resultant solid state phenomena. In the present study carbon ions were implanted in single crystalline silicon targets at high temperature and the defect mediated transport of carbon atoms to the surface and consequent build up of carbon at the surface was analysed by RNRA.

The n-type single crystalline silicon wafers of (100) orientation were implanted with 300 keV C^+ ions to a fluence of 2×10^{17} ions/cm^2. The implantations were carried out at three different target temperatures namely 550°C. 600°C and 650°C. The carbon prolifing in the implanted samples were carried out using $^{12}C(\alpha,\alpha)^{12}C$ reaction. The backscattered alpha particles were detected by a surface barrier detector at an angle of 165° for different incident energies varying from 4340 to 4400 keV to profile the carbon concentration.

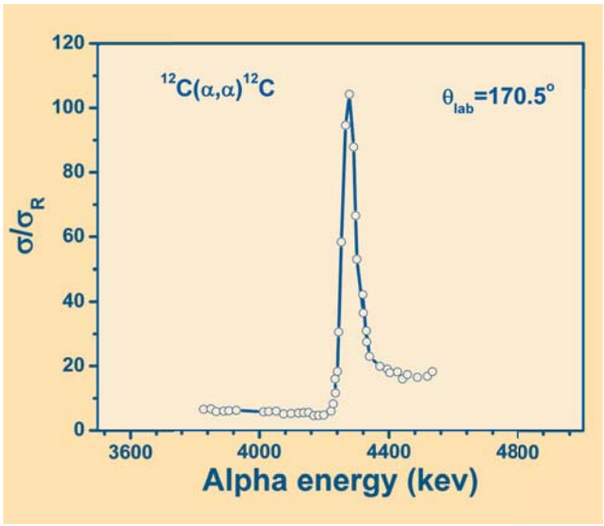

Fig.1
The Enhancement of $^{12}C(\alpha,\alpha)^{12}C$ Resonant Elastic Scattering Cross Section over the Rutherford Cross Section as a Function of Energy

Figure 2 shows the RNRA spectra for two incident alpha particle energies (4340 and 4385 keV) from a sample implanted with 300 keV C^+ ions to a fluence of 2×10^{17} ions/cm^2 at 650°C. As the resonance scattering has a width of about 36 keV the resonant scattering occurs from the carbon atoms at the surface when the incident beam energy is 4340 keV. With incident ion energy of 4385 keV the resonant scattering occurs from the carbon atoms in the bulk at a depth of around 7000 A as at this depth the ion energy becomes equal to the resonance energy due to energy loss in silicon matrix. The carbon composition at the bulk and the surface were extracted from the spectra in Fig.2 using 'SIMNRA' numerical simulation code. The simulated RNRA spectra are also shown in Fig.2.

It was seen that though most of the implanted carbon was at the depth around range of carbon ions (7000 Å), there is significant segregation of carbon atoms to the surface. The surface concentration of carbon increases with implantation temperature and is attributed to the enhancement of the atomic mobility of carbon with temperature. The number ***m*** of segregated carbon atoms / unit area at the

surface is expected to be proportional to square root of (Dt) where ***D*** is the diffusion constant and ***t*** time. For the samples implanted at different temperatures, accumulated mass of carbon per unit area at the surface (***m***) has been estimated from RNRA measurements. A plot of ln(***m***) versus 1/kT shows an Arhenius behaviour with an activation energy of 0.436 eV, as estimated from the slope of the fitted line in Fig.3. This activation energy (0.436 eV) for carbon diffusion in silicon under irradiation conditions is significantly smaller than the activation energy (0.88 eV) reported for the C diffusion in Si in equilibrium conditions. This suggests that non-equilibrium phenomena which occur during irradiation have a strong influence on the carbon diffusion. As Si interstitials are trapped by implanted carbon atoms there is an excess vacancy concentration in the implanted region and this can give rise to a net vacancy flux from the region near the range of the ions to the surface. Since carbon is known to form complexes with vacancies it is likely that the carbon atoms move along with the vacancy flux to the surface. The activation energy for carbon diffusion estimated from segregation data is close to the activation energy for vacancy migration suggesting that the transport of the carbon atoms to the surface from the implanted region occurs by the above mechanism.

VI.10 X-ray Analysis of Rutile and Anatase Thin Films of TiO_2 Prepared by Pulsed Laser Ablation

Titanium dioxide (TiO_2) has attracted considerable interest in recent years, because of its applications in sensors, solar energy, photovoltaic devices, integrated wave guides, catalysis, and in medicine. The catalytic approach of TiO_2 appear to be a very attractive for the purification of air and water from contaminants. TiO_2 is able to photocatalyze many organic substances under UV irradiation. Nanosized TiO_2 particles are useful for fine ceramics, UV light absorber and photocatalysts. Among several polymorphs of TiO_2, rutile is the most stable phase, anatase is metastable and is only synthesized at relatively low temperatures, whereas, brookite is formed only in extreme conditions. The anatase to rutile transformation is irreversible and generally occurs at temperatures greater than 973 K. The photocatlytic performance of anatase is generally considered to be superior to that of rutile. TiO_2 films are used as the active layer on the recently commercialized self-cleaning windows and are known for their photocatalytic oxidation of contaminants in air and in volatile organic compounds which are toxic to human life.

Pulsed laser deposition (PLD) technique was used for fabricating homogeneous thin films of rutile and anatse at a relatively low substrate temperature of 673 K. Two kinds of experiments were performed: (i) deposition in varing oxygen partial pressure from $3.5x10^{-5}$ to 0.1 mbar at 200 mJ/pulse and (ii) deposition at 3.5×10^{-5} mbar in the energy range 200-600 mJ/pulse.

Glancing incidence X-ray diffraction (GIXRD) patterns of the TiO_2 films prepared at 673 K at the base pressure of $3.7x10^{-5}$ mbar and 0.1 mbar oxygen partial pressure in the energy range 200-600 mJ/pulse are shown in Fig.1. Data from TiO_2 standards (PDF cards #21-1272 for anatase, #21-1276 for rutile) were used to identify the diffraction peaks of the thin films. Fig.1(a) reveals that thin films prepared in the base pressure environment were rutile, while Fig.1(b) shows that the films deposited in the oxygen partial pressure environment were anatase. These phases were more easily identified by the low index planes like (110) of the rutile phase and (101) of anatase phase. Both kinds of the films are polycrystalline and the intensity of the diffraction lines were found to increase with increasing laser energy because of the increased deposition rate.

The Riveted method was used to determine the unit cell parameters of the thin films of TiO_2 phase. The cell parameters of thin films were refined using Rietveld full profile-fitting mode in the JANA2000 program. Fig.2(a) and Fig.2(b) show the Rietveld refinement plots of the rutile and anatase thin films. The lattice constants obtained for both rutile and anatase thin films do not show any systematic variation as function of laser energy. The lattice parameters of the films are found to vary non-linearly when the size of the crystallites are in the nanometre range, where quantum

size effects are expected to be more pronounced. From the Rietveld refinement, the FWHM of the (110) and (101) peaks of rutile and anatase were calculated. The particle size of the films were calculated from the FWHM values using the Scherer equation. In the rutile film, the particle size remains at ~ 10 nm up to the laser energy of 500 mJ/pulse and it is reduced to 5 nm at 600 mJ/pulse, whereas in the anatase films, the particle size increases to 24 nm in the energy range 200-400 mJ/pulse and then reduced to 10 nm at higher energy levels.

In summary, it is demonstrated that among the two process variables studied, the influence of oxygen partial pressure is very significant compared to that of laser energy. Depending upon the oxygen partial pressure, the starting rutile target material could be used to deposit either rutile or anatase thin films at temperatures as low as 673 K. Except for minor changes in the values of lattice parameters and particle sizes, there seems to be no influence of laser energy on the phase formation of these films.

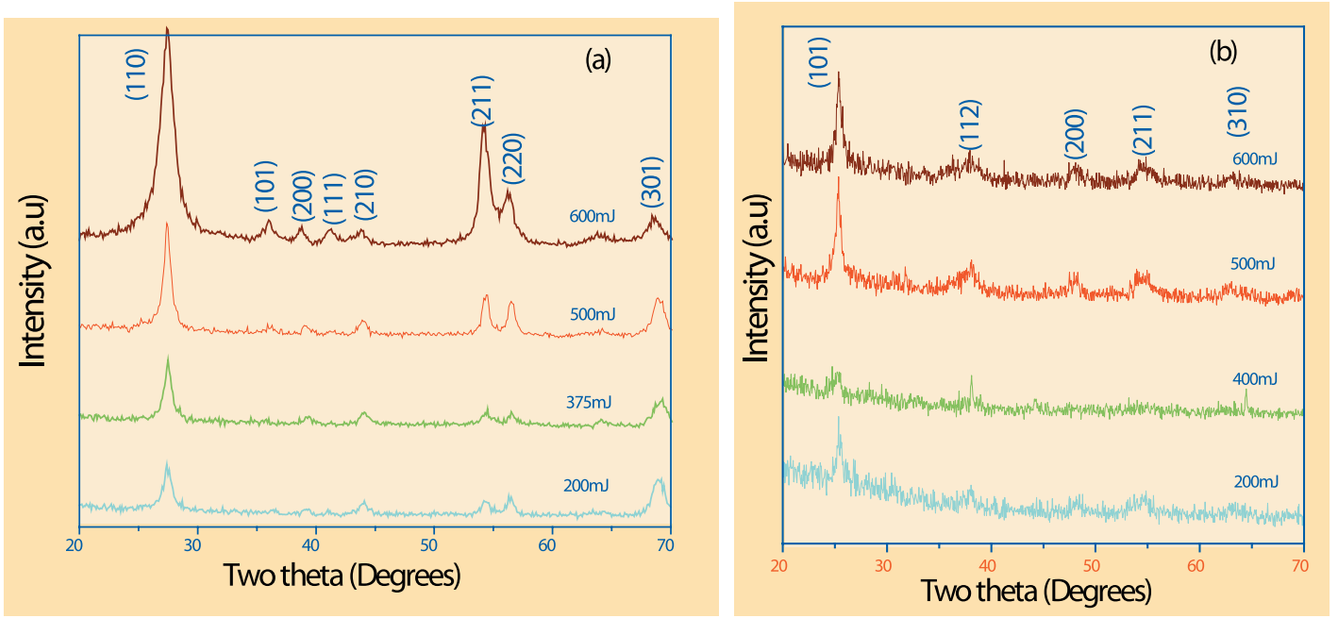

Fig.1
GIXRD Patterns of Thin Films Prepared at 673 K in the Laser Energy Range 200 - 600 mJ/pulse at (a) base pressure of $3.7x10^{-5}$mbar, and (b) 0.1 mbar O_2 partial pressure.

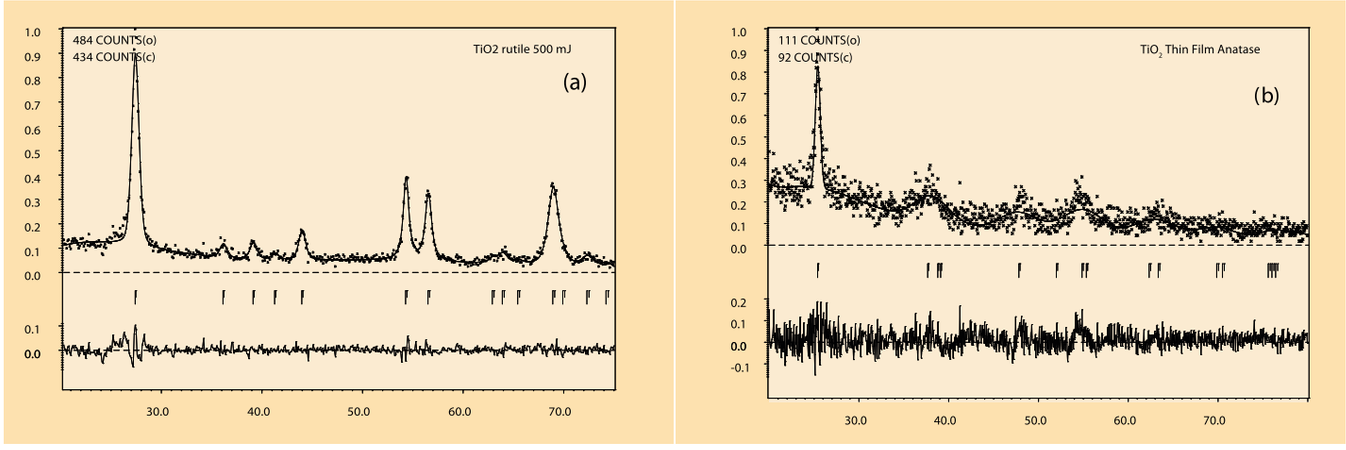

Fig.2
A Typical XRD Pattern of Results of Rietveld Analysis of (a) Rutile thin film, and (b) Anatase thin film data. The position of Bragg Reflections are indicated by vertical bars. The solid line and the dotted line represent calculated and observed intensity, respectively. The lower part of the diagram (horizontal line) shows the deviation between the experimental and the calculated intensities from the refined model.

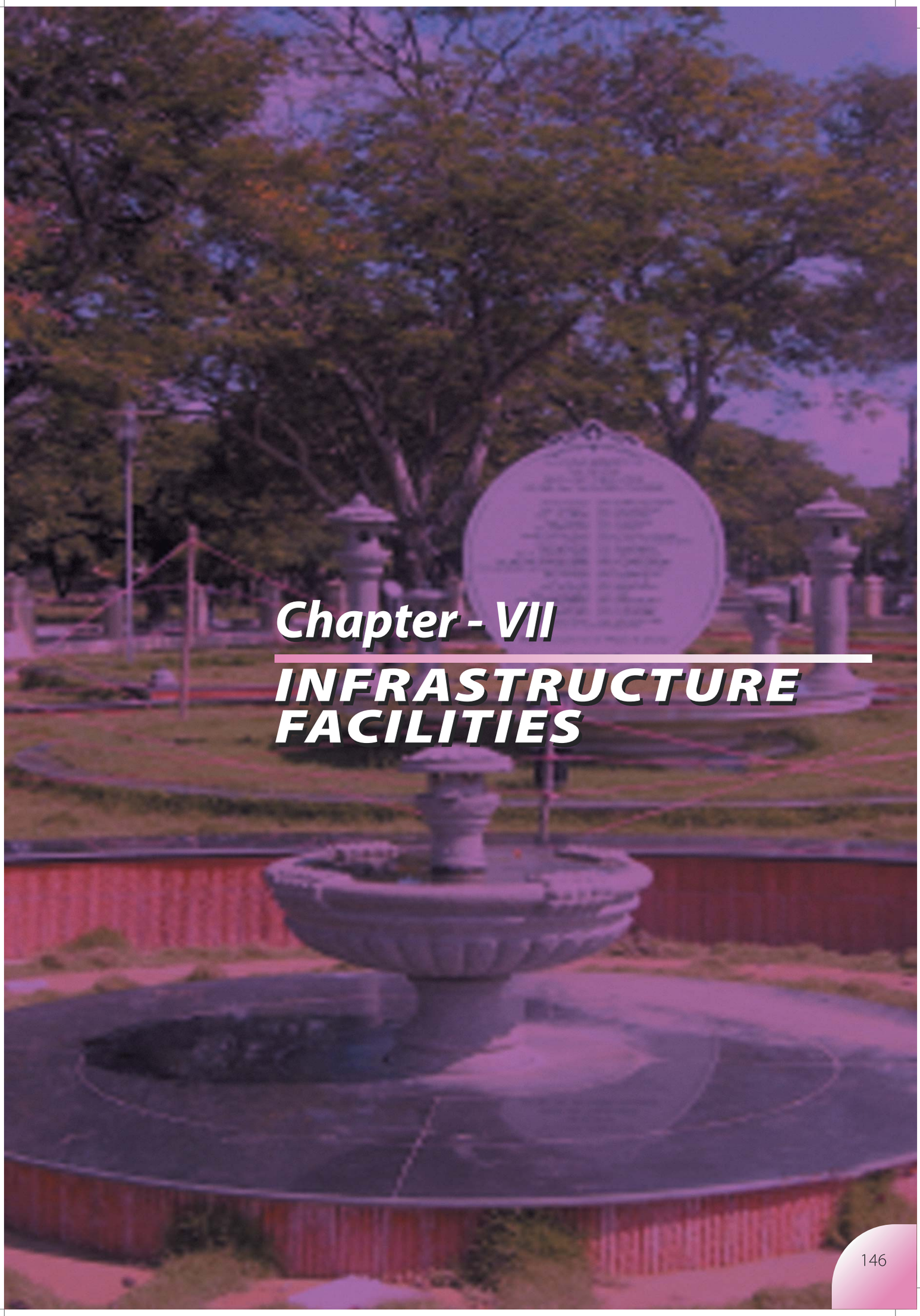

Chapter - VII

INFRASTRUCTURE FACILITIES

VII.1 Energy Conservation Strategy for the Centre

DAE units at Kalpakkam namely IGCAR, BARC Facilities, BHAVINI, AERB and two townships at Kalpakkam and Anupuram get electrical energy from MAPS. The electrical energy is distributed to all these units by means of two 25 MVA feeders located at MAPS switch yard. The monthly energy consumption at 33kV level is about 80 lakh units for all the units put together. The maximum energy demand is about 18 MVA at 11 kV level and 21 MVA at 33 kV level.

The energy consumption of IGCAR is about 1,25,000 to 1,50,000 units per day and the scope for energy conservation potential is high. Scope of energy conservation at IGCAR and the strategy adopted to implement the same are discussed below.

Preliminary Audit

As a first step Heavy Water board was requested to carry out a preliminary audit and submit a detailed report. The preliminary audit steps such as walk through audit were carried out for the entire centre and all the energy intensive areas were identified. Power measurement was carried out for major equipments to identify the scope of energy saving potential. Light intensity measurement was carried out in most of the areas. Energy meters were installed in the energy intensive areas to monitor the energy consumption pattern. The major thrust areas identified during the audit were the air-conditioning and ventilation systems, rotary equipments such as pumps and compressors and other loads at FBTR. The air-conditioning and ventilation loads including chiller units were found to contribute to 55 to 65% of the total energy consumption. The scope of energy saving expected from this area is about 15 to 20%. It is possible to save energy in lighting systems even though the contribution is expected to be less.

Subsequent to the preliminary audit, detailed auditing was carried out for Air conditioning and ventilation system. As a result of the audit, it is now proposed to replace one chiller unit for which the specific energy consumption is high compared to other units. It is found that the specific energy consumption is minimum when the unit is operated at it full capacity or near full capacity. Also it is observed that the specific energy consumption is increasing gradually due to the chocking of condenser tubes. This was attributed to be due to poor quality of water for condenser cooling water system. So it was decided to install non-chemical treatment system for the condenser cooling water system. It is also planned to optimize the operational parameters of the equipments so that all these equipments will operate at their maximum efficiency point. To improve the efficiency of the large number of ventilation blowers operating at the centre, it is proposed to replace the units with energy efficient ones and also to change the V belts to flat belts.

The energy saving potential in the lighting was identified by power and light intensity measurement. It was decided to use CFL lamps instead of fluorescent lamps in all the corridors. Wherever possible, the copper ballasts will be replaced by electronic ballast and T-5 lamps will be used in place of fluorescent lamps and this will be implemented in a phase manner. For street lighting sodium vapour lamp will be utilized along with the energy saving devices to minimize the energy consumption. Automatic switching ON/OFF for streetlights will be implemented by photoelectric sensors.

Since all the equipment at FBTR are more than 25 years old, there is enough scope for energy saving. Many of the equipments are designed for full power of 40 MW (t) and these equipments are operating at their full load irrespective of the reactor power level. It was therefore suggested to provide VFD drive for such equipments, which will contribute to energy saving. To reduce the heat loss from the hot sodium system, it was also recommended to increase the insulation material over thickness of sodium pipelines and tanks. It is also proposed to introduce 100 TR Vapour Absorption Chiller (VAB) at FRTR. The system utilizes a small portion of the bypass steam system, and will be operational whenever FBTR is in operation at a power level of more than 10.5 MW(t) power. This will lead to a power saving of 65 kW. Detailed study is being carried out to find the optimum solution.

The scope of energy saving potential has been identified for IGCAR and strategy to implement the measures has been finalized. The implementation of the scheme will be done in a phased manner and it is expected that most of the measures will be implemented during 11th plan. By implementing all the measures we expect to conserve about 15 to 20% energy.

VII.2 Clean Room Facility for Precision Assembly and Welding Work

A clean room facility of Class-7 as per ISO 14644 has been established at the Micro-machining and Assembly Facility (MAF). Installation, testing and commissioning of the clean room with complete air moving & control system and accessories have been completed.

The clean room is designed for use in assembly of precision mechanical components, probes, experiment capsules etc. required for irradiation experiments and fabrication of other precision devices. It is located in the ground floor of MAF building and shown in Fig.1. An airlock with air shower facility is provided at the entry to the clean room. The air-conditioning and filtration plant room is located in the first floor directly above the clean room. The operating parameters of the clean room are Cleanliness: ISO Class -7; Temperature: 23 ± 2 ° C; Relative humidity: 55±5%; Room pressure with respect to atmosphere: (+) 2 mm water gauge; Sound level: below 55 db; Light level: 400 Lux. Two air-cooled package air conditioner units of 5 TR capacity each are provided in the plant room. The clean room is fully commissioned and is operational. A high precision three axis non-contact measuring machine and a laminar flow assembly cabinet have been installed in the clean room. Fig.1 shows a view of the clean room.

Fig.1
Clean Room Facility at MAF Building

VII.3 IGC Knowledge Resource

Increased realization of Knowledge as the core competence, coupled with recent advances in Information Technology such as Intranets and the World Wide Web, has increased organizational interest in the topic of Knowledge Management. Knowledge Management System is mainly to improve the performance and productivity of an organization. Such a system would empower employees to access a repository of "best-of-breed" documents, information resources and external knowledge sources. R&D organizations need to build the information repository of explicit knowledge such as internal technical reports, publications, images, etc. Such an organizational information repository becomes Knowledge repository when it is analyzed, adapted and used effectively to cater the organizational requirements.

The Library has been the centre of the preservation, utilization and distribution of information items like book, journals, reports, standards etc. Digital Library has a much greater capacity to collect, catalogue, preserve and disseminate information across a wider area with greater reach. It provides access to the knowledge resources in a centralized way. Digital Libraries can build the information repository by selecting, acquiring, digitizing, organizing and finally archiving the valuable information resource obtained from several resources. The Scientific Information and Resource Division (SIRD) has initiated IGC knowledge resource management project named as "Bodhi". This is a centralized repository of knowledge documents of ICGAR, which will provide access to the following resources. A picture of home page is shown in Fig.1.

Image Archive: A comprehensive database is built to store the metadata of photographs belonging to various categories like milestones, VIP visits, important events, various facilities, historical events and experimental setups. All the photo negatives/photos of both color and black and white

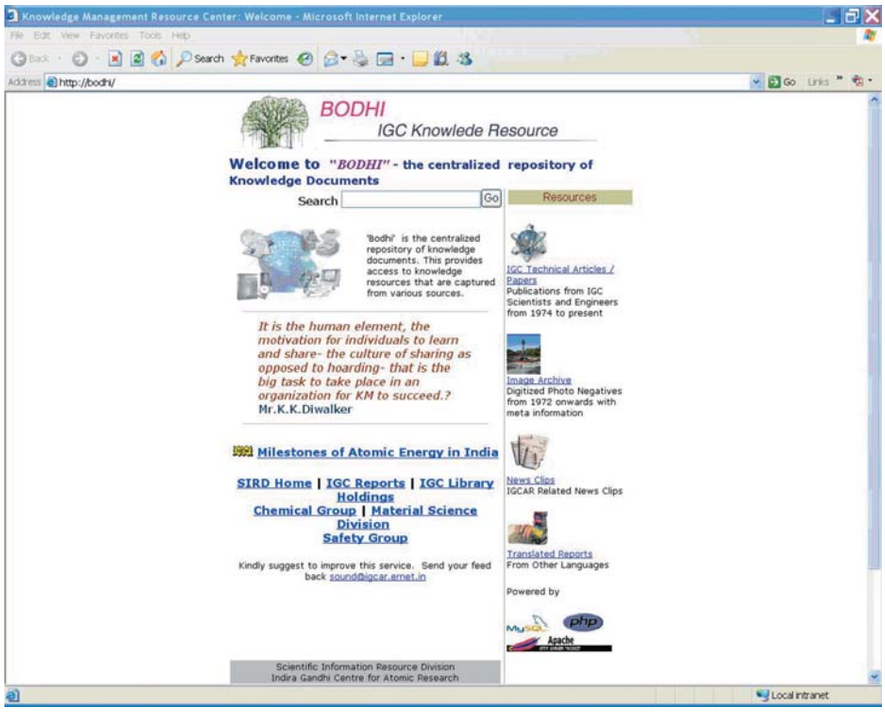

Fig.1
Home Page of IGC Knowledge Resource (Bodhi)

from the year 1973 onwards are being scanned and archived in Server system.

IGCAR News Clips Archive: It is a repository of News clips pertaining to DAE and in particular to IGCAR activities from 1973 onwards. A bibliographic database is built with required fields such as date, title, keywords etc. Individual news clips are being digitized and uploaded to servers and finally linked to their respective bibliographic entry. A search engine has been developed which can search news clips based on various fields such as date, year, tiles and source.

IGC Research Contribution: This is the database of articles published by IGC scientists and engineers in various conferences and journals from year 1973 onwards. Full text access is provided to all available articles. A suitable search interface is available to search publications based on various fields like author, title, keyword, abstract etc,

Enhanced Server Systems: To meet the additional resource required for storage of data and images and to facilitate faster access of information by the user, the server systems have been upgraded and are shown in Fig.2. The enhanced systems are commissioned with data integrity/protection like NAS (Network Attached Storage) server and backup fully automated tape library. Already Existing Pentium 3 class servers have been upgraded with P4 Xeon Bull servers with necessary resources. Two numbers of NAS have been procured with iSCSI interface to provide storage capacity in term of terra bytes.

Fig.2
SIRD Servers

VII.4 Tsunami Protection Wall for Kalpakkam Township

Kalpakkam Township is located parallel to coastline of Bay-of-Bengal. During the occurrence of Tsunami on 26th Dec.'04, the township experienced heavy inflow of seawater due to surge associated with tsunami. The masonry wall constructed earlier for physical protection failed, resulting in inundation of low-lying areas of the township on the west side of the wall. In order to protect the colony from the possible threat of storm of 100 year return period and tsunami, it is proposed to have a suitable protective system, which can withstand the impact due to storm surge and tsunami.

The protection system, designed by Ocean Engineering Centre, IIT, Chennai, involves construction of 4.5m high (3.0m above ground) RCC retaining wall in place of existing (1.8m high above ground) masonry wall with its top elevation maintained at minimum Relative Level (RL)+11.5m (i.e.

5.404m above Mean Sea Level). The wall is designed for an impact pressure of 6 t/m^2, corresponding to a wave period of 450 seconds. Structural design is based on the impact of standing wave pressure involving dynamic wave pressure and sustained wave pressure. The wall is located at a distance of about 42m from the high water line and strengthened on seaside with boulders of 800mm size with a slope of 1 in 1.5. At the base of the rubble fill, geo-textile is provided to prevent scour. A sand dune is made on the sea side of the wall to reduce dynamic forces, even though no advantage is taken from the sand dune from engineering considerations. In Sadras Backwaters mouth near bridge, the embankment is strengthened by use of 1000mm size boulders, in addition to retaining wall. This embankment has a slope of 1 in 2. Suitable geo-textiles are also used between beach sand and stone embankment to prevent scour.

A typical cross section of the wall is shown in the Fig.1. Fig.2 shows the conceived picture of the Tsunami protection wall, after growth of planned vegetation. Fig.3 shows the wall under construction. This protection wall is anticipated to mitigate the physical damage to the township from any possible future events.

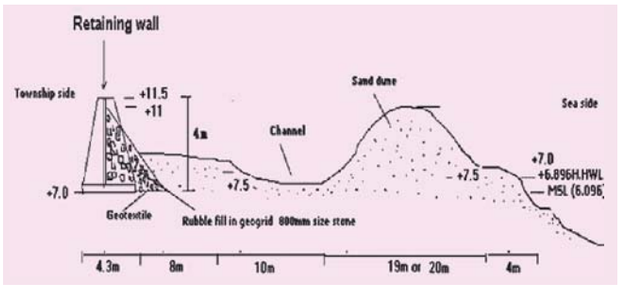

Fig.1
Cross Section of Tsunami Protection Wall

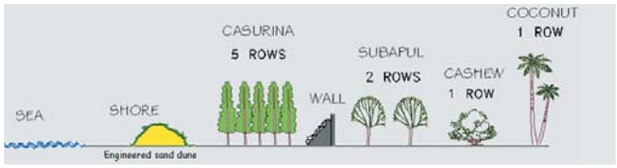

Fig.2
Tsunami Protection Wall, with Plantation

Fig.3
Tsunami Protection Wall under Construction

VII.5 Where Time Stands Still…

On the day of 26th December 2004, Kalpakkam Township had to face a heartbreaking event, which had disturbed the peaceful ambience of this wonderful seashore settlement. The residents of this township had lost some of their precious relatives and friends.

Tsunami memorial (Fig.1) had been constructed at Kalpakkam Township. This memorial park is located in the heart of the township as a mark of respect and remembrance, near the DAE hospital junction.

The monument with the names engraved is placed in the center of the park made out of elliptical white granite stone plaques, which is enhanced by stone lanterns on either side. A specially designed stone lantern stands on a raised platform at the gathering area as an ever-glowing lamp depicting the souls departed.

Fig.1
Photograph of the Tsunami Memorial Erected in the Kalpakkam Township.

AWARDS & HONOURS

- **Dr. Baldev Raj** has been elected to the Board of Directors of the International Institute of Welding. He has also been elected as a Fellow of Third World Academy of Sciences (TWAS). He has been conferred with the honorary Doctor of Science (D.Sc.) by Sathyabama Institute of Science & Technology (Deemed University), Chennai. He has been elected as Honorary Member of Indian Institute of Metals and Honorary Fellow of Indian Welding Society.
  Dr. Baldev Raj had delivered Stanley Ehrlich Distinguished Lecture and was awarded Gold Medal by Acoustical Foundation for Education and Charitable Trust, India (2006). He was also awarded International Recognition Award by Indian Society for Non-Destructive Testing (2006).
- **Dr. P. Chellapandi,** Reactor Engineering Group (REG) has been awarded Indian Nuclear Society (INS) Medal for the year 2005.
- **Dr. B. Venkataraman,** Engineering Services Group (ESG) and **Dr. Shaju K. Albert,** Metallurgy & Materials Group (MMG) have been awarded INS Medals for the year 2005.
- **Dr. C. S. Sundar,** MMG has been awarded the Materials Research Society of India MRSI-ICSC Superconductivity & Materials Science Annual Prize for the year 2007.
- **Smt. C. Sudha,** MMG has been awarded Shri Ram Arora Award for the year 2007.
- Indian Chemical Institute (ICI), India IIChE Award for Excellence in Process or Product Development for the year 2005 has been awarded to **Dr. C.Anand Babu, Dr. B.K.Sharma** and **Shri. G.Mohanakrishnan** of Fast Reactor Technology Group (FRTG) for their work on "Ion exchange chromotographic separation of isotopes of boron".
- **DAE Exhibition pavilion,** put up during 6th International Trade Fair and Conference on "Minerals, Metals, Metallurgy & Materials" commemorating the IIM Diamond Jubilee celebrations during September 11-14, 2006 has won the Commendation Award for showcasing the products, technologies and services. IGCAR along with other DAE units has participated in the above exhibition.
- **Dr. P. V. Sivaprasad,** Materials Technology Division has been awarded the "Metallurgist of the Year" for the year 2006 by the Ministry of Steel, GOI.
- **Dr A. K. Bhaduri,** Materials Technology Division has been elected as the Fellow of Indian National Academy of Engineering from January 2007.
- **Shri P Sukumar,** Non-Destructive Evaluation Division and **Shri N. Vinayagam,** Central Workshop Division, have been awarded the "DAE Meritorious Service Award" for the year 2005.
- **Shri R.Subbaratnam,** QA&NDTS won the prestigious "NDE man of the year Award" for the year 2006.
- **STAR Quality Circle of CWD** has got the "Distinguished Award" during 20th National Convention of Quality Circle (NCQC-2006) presentations at IIT, Kanpur, during December 2006.

Publications 2006

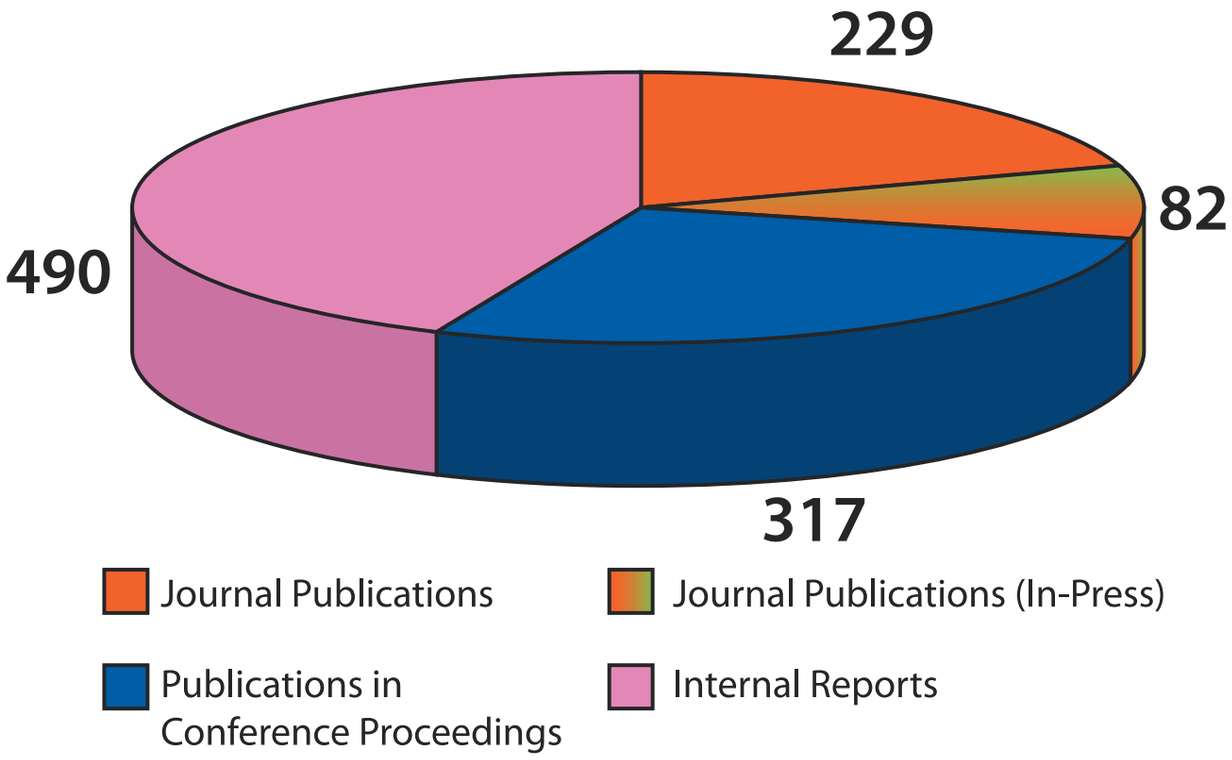

Colloquia, Seminars and Conferences - 2006

IGC Colloquia

1. Measuring Science by Dr. S. Venkatesan, Indian Institute of Science, Bangalore, on April 4, 2006.
2. An outside look of Indian Nuclear Energy Programme by Dr. Georges Vendryes, Executive Vice President, French Atomic Energy Commission on July 19, 2006
3. Sensor Networking and Emerging Trends by Prof S.S. Iyengar, Lousiana State University, USA on August 2, 2006
4. Changing Paradigm in Higher Education by Prof M.S. Ananth, Director, IIT Madras, Chennai on September 9, 2006
5. Performance of R&D and Innovation & Micro planning of R&D Projects by Prof.S.Banerjee, IIT,Mumbai on December 1, 2006
6. Gateway to New Opportunities by Dr. R.R. Puri, Head, HRDD, BARC and Dean, Homi Bhabha National Institute on December 8, 2006
7. My Road in Science by Prof. Yehuda Haas, The Hebrew University, Israel on December 12, 2006
8. Nuclear Fusion as future Energy Resource by Dr.D.D.Sood, Former Director, RC&I Group, BARC on December 15, 2006
9. Mankind, Civilisation and Nuclear Energy by Prof. Yoichi Fuji-ie, Tokyo Institute of Technology, Japan on December 15, 2006

Special Lectures

1. Waste into Wealth - A Reality at Pammal by Smt. Mangalam Balasubramanian, Vice President, Exnora, Chennai on May 18, 2006
2. Condensed Matter Physics of Actinides -- Seaborg Memorial Lecture by Dr. S.K. Sikka , Scientific Secretary, Office of the Principal Scientific Advisor to Government of India and Ex. Director, Solid State & Spectroscopy Group, BARC on July21, 2006
3. Indian Missile Programme by Dr.M.Natarajan, Scientific.Advisor to Defence Minister on September 29, 2006
4. Prof. Brahm Prakash Memorial Lecture by Dr. V.S. Arunachalam on September 30, 2006.
5. The Evolution of Medical Imaging: From X-Rays to PET -- Madamme Curie Memorial Lecture by Dr.Narendra Nair, Head, Radiation Medicine Centre,BARC on December 11, 2006.

Seminars, Workshops and Meetings

1. Radiation Awareness Programme by Indian Working Scientists Association and IGCAR on February 21, 2006
2. Indo French Technical Seminar on Fast Reactor Fuel Safety, February 27-28, 2006
3. IAEA Technical Meeting on 'Fuel Failure and Failed Fuel Detection Systems for Fast Reactors', March 1-3, 2006
4. Third Technical Meeting of Scientific and Technical Committee of the joint study on 'An innovative Nuclear Energy System based on a Closed Nuclear Fuel Cycle with Fast Reactors', March 1-3, 2006
5. 20 Years of FBTR Celebrations on March 2, 2006
6. Peer Review of Engineering Sciences Activities April 3-4, 2006
7. Award of ISO 9001 Certificate to IGCAR on April 5, 2006
8. Introduction and Demonstration of SCOPUS by Pradeep Kumar on June 8, 2006
9. Golden Jubilee Celebrations of BARCF inaugurated by Prof. M.S. Swaminathan on June 12, 2006
10. QCI Awareness Programme on July 24 and 25, 2006
11. Seminar on Disposal of Special Wastes and Clean Environment by Assn of Waste Management and Remediation of Environment (AWARE) on June 26, 2006
12. Celebrations of 20 years of Successful Operations of FBTR on July 18, 2006
13. Contributory Health Service Scheme- special talk by Medical Superintendent Dr. A. Vijaya organized by Association of Atomic Research Centre Officers (AARCO)
14. Workshop on Chemical Thermodynamics, August 22-26, 2006
15. Engineers' Day Celebrations on September 26, 2006
16. One day Workshop on Total Quality Management November 18, 2006

Nurturing Activities

1. Summer Training in Physics and Chemistry (STIPAC 06), a six weeks summer training programme in Physics and Chemistryfor final year M.Sc (Physics/Chemistry) students from May 29, 2006 to July 7, 2006
2. Professor Brahm Prakash Memorial Materials Quiz-2006, an annual event of Materials Quiz organized for students of Class XI and XII participating across the country as well as from neighbouring countries, on September 30, 2006

NEWS & EVENTS

Indo-French technical seminar on "Fast Reactor Fuel Safety", February 27-28, 2006 – Seen in the photo are the delegates of the Indian delegation, led by Dr Baldev Raj, Director, IGCAR and the French delegation led by Dr Patrick Ledermann, Deputy Director, Nuclear Energy Division, CEA, France

Joint session of the two IAEA meetings in progress - IGCAR hosted two IAEA meetings at Kalpakkam during March 1-3, 2006. These are - IAEA Technical Meeting on "Fuel Failure and Failed Fuel Detection Systems for Fast Reactors" and Third Technical Meeting of Scientific and Technical Committee of the Joint Study on "An Innovative Nuclear Energy System based on a Closed Nuclear Fuel Cycle with Fast Reactors" (CNFC-FR).

Peer Review of Engineering Sciences Activities

The R & D activities in engineering sciences being carried out at IGCAR have over the years been growing consistent with the challenges and have matured to enable design of 500 MWe Fast Breeder Reactor Project (PFBR) giving due consideration to economy so that it will be the forerunner of many FBRs to be constructed in future. With the objective of having a critical and independent evaluation of R & D activities of the Centre in engineering sciences, particularly in the context of embarking upon a multi-fold increase in power generation planned through FBRs and taking reprocessing technologies to high level of robustness, a peer review of engineering sciences activities was conducted during May 3rd and 4th 2006. The review panel consisted of eminent experts Dr. K. Kasturirangan, former Chairman, ISRO and Director, NIAS, Prof. S.P. Sukhatme, Former Chairman, AERB, Prof. M.S. Ananth, Director, IIT-Madras, Prof. M.L. Munjal, IISc, Prof. S. Ranganathan, IISc, Prof. R.K. Shyamasundar, TIFR and Shri. M.S. Konnur, Former Director, FCRI. The activities reviewed included fast reactor engineering & technology, materials technology, safety engineering, electronics & instrumentation engineering and reprocessing technology. The review was aimed to provide important inputs concerning the level of excellence in the programmes, effective utilization of facilities and human resources and suggestions for (a) mid-course corrections in on-going activities to add value, (b) collaborations, both within DAE units and with national research centres and academic institutes, (c) new programmes towards meeting the objectives of the centre, (d) increased synergism and (e) road map to meet the planned growth of FBRs.

Members of Peer Review Committee listening to a presentation (R to L) -
Shri.M.S. Konnur, Dr. M.S.Ananth, Prof.S.Ranganthan, Dr. Kasturirangan,
Dr.Baldev Raj, Prof. M.L.Munjal, Prof.S.P. Sukhatme and Prof. R.K.Shyamasundar

The review process included 31 oral presentations by various engineering groups and visits of the peers to the engineering laboratories, FBTR and BHAVINI. Detailed discussions were held during the presentations. The committee also had an in-depth discussion with Director, IGCAR and Shri S.C. Chetal, Director, REG at the end of the meeting. The committee complimented the participants for the excellent and passionate presentations and the quality of R&D that is being pursued to meet the challenges in mastering FBR technology. The committee observed that IGCAR has comprehensive facilities and expertise and is on the right path to achieve leadership in FBR technology. The interaction of IGCAR with other R&D and academic institutions within the country was well appreciated and the need for enhancing international collaborations was emphasised. Taking into consideration the enhanced role of FBRs in energy production, need for increasing the manpower commensurate with the challenges was emphasised. The committee suggested IGCAR to work towards enhancing public awareness addressing all the issues related to nuclear power specifically related to fast reactor and associated fuel cycles, as this would be a major component of nuclear energy beyond 2025. It was suggested to have joint working groups involving experts from DAE, ISRO and DRDO. It was felt that this approach would enhance expertise of all the participating strategic departments and accelerate development establishing enhanced synergy.

Dr. Baldev Raj thanked the Chairman and the members of the committee for their excellent suggestions based on their deep involvement in the Centre's programme and their rich experience. He assured the committee that their suggestions would be considered with full earnestness for implementation and he would keep the Chairman and the members posted with the developments so that the Centre can continue to have the full benefit of the peers. The Chairman and the members assured full support and deep commitment to the excellence with relevance being pursued by the Centre and wished the Centre all the success in achieving the national expectations and aspirations to achieve world leadership in FBR science and technology before 2020.

ISO 9001:2000 Certification for IGCAR Laboratories

Indira Gandhi Centre for Atomic Research (IGCAR) at Kalpakkam has received ISO 9001:2000 certification from BVQI, for twelve R&D laboratories along with the DAE Hospital laboratories. The IGCAR laboratories are in the fields of Mechanical Metallurgy, Materials Technology, Non-Destructive Evaluation, Corrosion Science & Technology, Physical Metallurgy, Design & Development of Electronic Instrumentation & Control Systems, Management of Computing & Data Communication Facilities, Quality Assurance, Structural Mechanics, Chemical Characterisation, Radiological Safety and Reactor Safety Engineering.

IGCAR is the first research Centre under the Department of Atomic Energy to receive ISO certification for its laboratories. The Certificate was handed over to Dr. Baldev Raj, Director, IGCAR by Dr.C. Venktaraman, BVQI, in a function held on April 5th, 2006. Speaking on the occasion, Dr. Baldev Raj, Director of the Centre said that IGCAR will consistently endeavour to achieve world leadership in multidisciplinary scientific and engineering research & development activities related to fast reactor and associated fuel cycle technologies to satisfy the energy needs of the country, thus providing long-term energy security to the nation. Dr. S.L. Mannan, Director, Metallurgy & Materials Group, and Chairman, Management Review Committee added that the entire certification process of all the laboratories was completed in a short period of about 12 months. Two years ago, the Reactor Engineering Group was awarded ISO certification for design and engineering of fast breeder reactor for power generation applications.

Dr. Baldev Raj, *Director, IGCAR receiving ISO 9001:2000 certificate from Dr. C Venkatraman, Head of Certifications, BVQI (India), Chennai on April 5, 2006.*

Commemoration of 20 years of Successful Operation of FBTR

A function commemorating 20 years of successful operation of FBTR was conducted on July 18th 2006 at Vikram Sarabhai Auditorium. Hon'ble Raksha Mantri Shri Pranab Mukherjee, Hon'ble Minister of State Shri Prithviraj Chavan, Dr. Georges Vendryes, Hon'ble Executive Vice President, French Atomic Energy Commission and Dr. Anil Kakodkar, Chairman, AEC graced the function. Ex. Chairmen of DAE , Ex-Directors of IGCAR, Heads of various DAE units and about 40 senior retired officers from IGCAR who worked for FBTR attended the function, in addition to senior officers from IGCAR.

Dr. Anil Kakodkar, *Chairman, AEC addressing the gathering.*
Seen on the dais (from left to right), ***Dr. Baldev Raj,*** *Director, IGCAR,*
Dr. Georges Vendryes, *Hon'ble Executive Vice President, French Atomic Energy Commission,*
Honorable Defence Minister, ***Shri Pranab Mukherjee,***
Honorable Minister of State, ***Shri Shri Prithivraj Chavan***

In his welcome address Dr Baldev Raj recalled the services of ex-Chairmen of the department and ex-Directors of IGCAR in promoting the FBR technology. Dr Anil Kakodkar highlighted the challenges ahead of the department which include the development of FBR's with high breeding ratios, building Thorium based reactors by irradiating Thorium in fast reactors and building Accelerator-Driven systems. The Hon'ble Defence Minister complemented IGCAR for successful operation of FBTR for 20 years and was confident that India's collaboration with France will enhance the coming years. Shri Prithivraj Chavan said India was among the few countries who mastered the complex technology of FBRs, facing the twin challenges of liquid sodium and Pu. He praised IGCAR for mastering the technology of reprocessing highly irradiated mixed carbide fuel for the first time in the world. Dr. Georges Vendryes complemented India for the remarkable feat in fabricating the carbide fuel without outside help and was confident that India will soon find a new place in the mainstream of international nuclear community in the sustainable development of energy. Shri P.V. Ramalingam, Director, ROMG gave the vote of thanks.

A ten minute video film titled "A Journey through FBR" was presented before the start of the function.The function was provided live coverage by DD Pothigai Channel. The retired officers who attended the function in response to our special invitation included Octogenarians and Septuagenarians. For all of them it was a day of pleasant nostalgia and pride, seeing the fulfillment of their career in the successful operation of FBTR.

The Commencement of Training School at IGCAR

So as to meet the urgent and growing need of scientific human resources with the right training and emphasis on Science & Technology of Fast Reactors and associated fuel cycle facilities, the need for Training School for fresh engineers at IGCAR has been felt for a long time. Due to immense interest and proactive steps taken by Dr. Baldev Raj, Director, IGCAR and the encouragement and support from Dr. Anil Kakodkar, Chairman, AEC and Secretary, DAE, this has become a reality. The inaugural function of IGCAR Training School was held on September 8th 2006 at the Ramanna Auditorium, IGCAR. Initially, the training programme will be conducted in three disciplines (viz.) Mechanical, Electronics & Instrumentation and Chemical engineering. The training school at IGCAR is affiliated to BARC training school. The school has started functioning at the Safety Research Institute building of AERB at Kalpakkam with 22 engineers. The faculty for teaching has been drawn from the eminent Scientists and Engineers working at IGCAR and a few others from outside.

Dr. Baldev Raj, *Director, along with the first batch of engineering trainees of IGCAR Training School on September 8, 2006*

International Trade Fair & Conference on "Minerals, Metals, Metallurgy & Materials", New Delhi, September 11-14, 2006

DAE pavilion, depicting the technical achievements of DAE, was set up during 6th International Trade Fair & Conference on "Minerals, Metals, Metallurgy & Materials", IIM Diamond Jubilee Celebrations, Pragati Maidan, New Delhi, September 11-14, 2006. IGCAR had showcased its breakthroughs and achievements in the indigenous research and development of the fast breeder technology, especially in the domains like materials and metallurgy. The panels displayed included the benchmarks and national & international records set by BHAVINI too. This DAE pavilion had won a commendation Award.

Visit of delegation from Japan Council on Energy and Security (JCES) during November 22-23, 2006

A delegation led by Prof. Kumao Kaneko from Japan Council on Energy and Security (JCES) visited IGCAR on 22nd and 23rd November, 2006. The members of the delegations were: Prof. Kumao Kaneko,President,JCES, Dr. Osamu Saito, Senior Fellow of JCES, Mr. Makio Tsuji, Senior Fellow of JCES, Mr. Kazuya Ochiai, Fellow of JCES and Dr. Naoyuki Takaki, Fellow of JCES.

Japanese delegation from Japan Council on Energy and Security led by ***Prof. Kumao Kaneko*** *during a discussion meeting with* ***Dr. Baldev Raj,*** *Director, IGCAR and other senior coll agues of the Centre*

The delegation had deliberations with senior scientists of the centre. Dr. Baldev Raj, Distinguished Scientist & Director of IGCAR in his address highlighted the activities of the centre. He also emphasised on R&D approach to FBR with improved economy and safety features. Prof. Kaneko, the leader of the Japanese delegation, talked about the current status of Japanese fast reactor program. The Japanese delegation expressed the hope that the cooperation between India and Japan would be enhanced considerably in the coming years. The delegation visited the Fast Breeder Test Reactor, facilities of the Fast Reactor Technology Group, Safety Group, Structural Mechanics Laboratory, Materials Science Laboratory and PFBR site.

Indira Gandhi Centre for Atomic Research
Organization Chart as on 10-01-2007

DIRECTOR, IGCAR
Dr. BALDEV RAJ

DIRECTOR'S ADVISORY COMMITTEE [DAC]

IGC SCIENTIFIC COMMITTEE [IGCSC]

IGC COUNCIL

DIVISIONS & HEADS

- LIQUID METALS & STRUCTURAL CHEMISTRY — Dr. T. GNANASEKARAN
- MATERIALS CHEMISTRY — Dr. V. GANESAN
- CHEMICAL FACILITIES — Shri K.C. SRINIVAS
- FUEL CHEMISTRY — Dr. T.G. SRINIVASAN

CHEMISTRY GROUP
DIRECTOR
Dr. P.R. VASUDEVA RAO

- PIE, IN-SERVICE INSPECTION, REMOTE HANDLING & ROBOTICS — Shri K.V. KASIVISWANATHAN
- NON-DESTRUCTIVE EVALUATION — Dr. T. JAYAKUMAR

INSPECTION TECHNOLOGY GROUP
ASSOCIATE DIRECTOR
Shri P. KALYANASUNDARAM

- MATERIALS TECHNOLOGY — Dr. S.K. RAY
- MECHANICAL METALLURGY — Dr. K. BHANUSANKARA RAO
- MATERIALS SCIENCE — Dr. C.S. SUNDAR
- CORROSION SCIENCE & TECHNOLOGY — Dr. H.S. KHATAK

METALLURGY & MATERIALS GROUP
DIRECTOR
Dr. P.R. VASUDEVA RAO

- PHYSICAL METALLURGY SECTION — Dr. M. VIJAYALAKSHMI
- IDEAS SECTION — Shri P.V. KUMAR

FAST REACTOR FUEL CYCLE FACILITY
PROJECT DIRECTOR
Shri P.V. KUMAR

- ELECTRONICS & INSTRUMENT, — Shri S.ILANGO SAMBASIVAM
- COMPUTER — Shri S. ATHINARAYANAN
- MEDICAL — Dr. A. VIJAYA

ELECTRONICS & INSTRUMENT, GROUP
DIRECTOR
Shri P. SWAMINATHAN

- INNOVATIVE INSTRUMENTATION SECTION — Shri. B. SAHA

- ELECTRICAL SERVICES — Shri A. JYOTHIS KUMAR
- A/C & VENTILATION SYSTEM — Shri S. KESHAVAMURTHY RAO
- CENTRAL WORKSHOP — Shri A.S.L.K. RAO
- QUALITY ASSURANCE — Shri B. VENKATARAMAN
- CIVIL ENGINEERING — Shri C. SIVATHANU PILLAI, ACE (CIVIL)

ENGINEERING SERVICES GROUP
DIRECTOR
Shri Y.C. MANJUNATHA
CHIEF ENGINEER

- TECH. COORDINATION AND QUALITY CONTROL SECTION — Shri N. VIJAYAN VARIER*

PLANNING DIVISION
Smt UMA SESHADRI

- ADMINISTRATIVE OFFICER — Shri R.G. RAGHAVAN
- ADMINISTRATIVE OFFICER (P) — Shri V.M. THOMAS

CHIEF ADMINISTRATIVE OFFICER
Shri V. DAYALAN

REACTOR OPERATION & MAINTENANCE GROUP
DIRECTOR
Shri P.V. RAMALINGAM

DIVISIONS & HEADS

- TECHNICAL SERVICES — Shri G. SRINIVASAN
- TRAINING & HRD — Shri K. RAVISHANKAR

OPERATION & MAINTENANCE
ASSOCIATE DIRECTOR
Shri B. RAJENDRAN

- REACTOR OPERATIONS — Shri B. RAJENDRAN, REACTOR SUPERINTENDENT
- REACTOR MAINTENANCE — Dr. V. RAMANATHAN

FAST REACTOR TECHNOLOGY GROUP
DIRECTOR
Shri G. VAIDYANATHAN

FAST REACTOR TECHNOLOGY GROUP
ASSOCIATE DIRECTOR
Shri P. KALYANASUNDARAM

- COMPONENTS & INSTRUMENT DEVELOPMENT — Shri B. KRISHNAKUMAR
- SEPARATION TECHNOLOGY & HYDRAULICS — Dr. C. ANAND BABU
- SODIUM FACILITIES — Shri K.K. RAJAN

REACTOR ENGINEERING GROUP
DIRECTOR
Shri S.C. CHETAL

- REACTOR PHYSICS — Dr. P. MOHANA KRISHNAN
- SODIUM CIRCUITS & COMPONENT HANDLING — Shri S.C. CHETAL
- CIVIL ENGINEERING — Shri C. SIVATHANU PILLAI (FBR Related Works)
- INSTRUMENTATION & CONTROL — Shri K. MADHUSOODANAN
- POWER PLANT ENGINEERING — Shri T.K. SHANMUGAM

NUCLEAR ENGINEERING GROUP
ASSOCIATE DIRECTOR
Dr. P. CHELLAPANDI

- REACTOR COMPONENTS — Shri P. PUTHIYAVINAYAGAM
- MECHANICS & HYDRAULICS — Dr. P. SELVARAJ

REPROCESSING GROUP
DIRECTOR
Shri R. NATARAJAN

- FUEL REPROCESSING PROCESS — Shri V. SUNDARA RAMAN
- REPROCESSING PLANT OPERATIONS — Shri M. VENKATARAMAN
- REPROCESSING R&D — Dr. S.B. KOGANTI
- REPROCESSING PROJECTS & SERVICES — Shri P. RAMKUMAR
- REPROCESSING PLANT DESIGN — Shri A. RAVISANKAR

SAFETY GROUP
DIRECTOR
Shri M. RAJAN

- SAFETY ENGINEERING — Shri N. KASINATHAN
- RADIOLOGICAL SAFETY — Dr. R. INDIRA
- SCIENTIFIC INFORMATION RESOURCE — Shri M. SOMASEKHARAN

- STRATEGIC & HUMAN RESOURCES PLANNING SECTION — Dr. M. SAIBABA

JOINT CONTROLLER (FINANCE & ACCOUNTS)
Shri S. MANI

- DEPUTY CONTROLLER OF ACCOUNTS — Shri R. SATHYAMURTHY
- SENIOR ACCTS., OFFICER (PAO) — Shri J. VINCENT SUNDARAKUMAR

AS ON 10-01-2007

* STATIONED AT MUMBAI

Indira Gandhi Centre for Atomic Research
Organization Chart as on 10-01-2007

IGC COUNCIL

CHAIRMAN

Dr. Baldev Raj, Fellow, Third Word Academy of Sciences, Indian National Science Academy, Indian National Academy of Engineering, Indian Academy of Sciences, Bangalore, The National Academy of Sciences, Allahabad, Tamil Nadu Academy of Sciences, BE from Ravishankar University and Ph.D. from IISc, Bangalore, D.Sc. (h.c.) from Sathyabama Deemed University, Chennai, is a Distinguished Scientist & Director, Indira Gandhi Centre for Atomic Research, Kalpakkam 603102, Department of Atomic Energy, Tamil Nadu. He steers science and technology programmes of an internationally renowned large research Centre namely Indira Gandhi Centre for Atomic Research with a mission to develop world class technology in Fast Breeder Reactors and Fuel Cycle through the mechanism of scientific breakthroughs and transferring science to robust technology. His specializations include materials characterization linked to performance, testing and evaluation using non-destructive evaluation methodologies, materials development and performance assessment and technology management. . He has more than 650 publications, 38 books and special volumes of journals (co-author of 11 books/monographs and co-editor of 27 books & special journal volumes). He has 5 Indian Standards and 17 patents to his credit. He has contributed 9 articles in Encyclopaedia and a large number of reviews. He is on the editorial boards of national and international journals. He has won many awards and honours, notable among these being the National Metallurgist Award (1986), Acoustic Emission Working Group of India Gold Medal (1994), G.D. Birla Gold Medal (1996), SAIL Gold Medal 1999, MRSI-ICSC Superconductivity & Materials Science Annual Prize (2004), Life Time Achievement Award of Indian Society for Nondestructive Testing (2004), Indian Welding Society (2004), Jaeger Lecture Award of International Institute of Welding (2004), International Researcher Award of International Committee on NDT (2000-2004), Indian Nuclear Society Award (2004), Stanley Ehrlich Distinguished Lecture, 15th Nayudamma Memorial Lecture. He is member of Board of Directors of International Institute of Welding, Standing Advisory Group on Nuclear Energy of IAEA and Past-President of International Committee on NDT and Chairman of Policy Committee of NDT. His interests include heritage, philosophy, religion and education.

MEMBERS

Dr. C.V. Ananda Bose, IAS, is presently Joint Secretary (Research and Development), Department of Atomic Energy. Coming from the Kerala Cadre, he has held several positions in Kerala including the Principal Secretary to Chief Minister of Kerala. He is a visiting Professor of Birla Insititute of Technology and Science, Pilani and has authored eight books and about a hundred papers and articles in the fields of Habitat, Architecture, Environment and Land Reforms. He is a recipient of several National and International Awards that include Jawaharlal Nehru Fellowship, Bremen Partnership Award and Rajiv Gandhi National Award for Excellence in Management. He has received more than a hundred prizes and medals and is a member of several International and National Expert Groups. In 2006 , Shri Ananda Bose has been appointed as Chairman of Atomic Energy Education Society,Mumbai.

Shri S.C. Chetal, B.E.(Mech), is a Distinguished Scientist & Director, Reactor Engineering Group at IGCAR. Since 1971, he has been engaged in the field of fast reactor engineering. He has made significant contributions towards design of FBTR sodium systems and components. He has also contributed to the material selection, manufacturing technology, R&D and design of 500 MWe Prototype Fast Breeder Reactor. He is a member of many professional institutions and a Fellow of the Indian National Academy of Engineering. He has received National Technology Award 2000 from DRDO for significant contributions in the field of high purity titanium sponge production & Indian Nuclear Society Award 2003 for contributions towards nuclear related high technology. His interests include pressure vessel and materials technology. He has to his credit 290 publications in Journals/Symposia/Conferences.

Shri S.C. Hiremath, a Distinguished Scientist, is the Chairman and Chief Executive of Heavy Water Board (HWB). He has been working as a key member of DAE's Heavy Water Programme right from its inception i.e. conceptualisation, application oriented R&D, including development of process equipment/machinery, technology development and setting up of the first totally indigenous H2S based plant besides being a member of "Think Tank" of maturing NH3 based plants. He is well known for achieving highest production of heavy water and making the processes energy efficient, thus realizing considerable savings in the operating costs. He is actively pursuing diversification into production of other stable isotopes including enrichment of Boron-10 through alternative routes, production of H2O18 required for medical diagnostic purposes and high end solvents required for self sufficiency in 2nd stage of India's nuclear power programme besides many other high technology issues like development of industrial scale cryo-cycle operating at around 20 K and extraction of valuable Rare Material from secondary sources. In recognition of his outstanding contributions, Shri Hiremath has been awarded the INS Award-2001 by the Indian Nuclear Society. He has also been awarded Management Excellence Award-2002 and Maharana Mewar Award-2003 for his devotion/commitment beyond the call of duty.

Shri R.N. Jayaraj is presently the Chief Executive of Nuclear Fuel Complex (NFC), Hyderabad. He is a Mechanical Engineer, graduated from Osmania University. After successful completion of one-year orientation course in Nuclear Engineering from the 17th batch of BARC Training School, he joined Atomic Fuels Division of BARC and contributed in the production of metallic uranium fuel assemblies for CIRUS reactor and development of fuel assemblies for DHRUVA reactor. After his transfer to NFC, he played a key role in establishing the assembly plant and successfully fabricated all the core sub-assemblies, for the first time in India, required for FBTR. He was instrumental in scaling up of production of fuel bundles required for all the PHWRs, thus consistently meeting the requirements of Nuclear Power Corporation of India Limited (NPCIL). He has to his credit the indigenous development of various equipment for critical processes involving welding, machining centers and assembly stations, thus creating a strong base for establishing self-reliance in PHWR fuel manufacturing. He played pioneering role in standardizing the manufacturing processes for the fuel bundles required for 540 Mwe PHWRs. He served the Department for the last 32 years in various capacities in different Units and gained rich experience in developmental and production of fuel for Thermal Research Reactors, PHWRs and BWRs. Shri Jayaraj, besides being a Member of IGC Council, is also on the Boards of UCIL and IREL.

Shri H.S. Kamath, B.E (Metallurgy), is a Distinguished Scientist and Director of the Nuclear Fuels Group in BARC. He has been associated with the development of plutonium bearing nuclear fuels for the last 35 years, which started with the fabrication of fuel for 'PURNIMA' in 1970-1972. His main area of work is in the development of uranium-plutonium mixed oxide (MOX) fuels for nuclear power programme. He has made important contributions in this field both in laboratory scale as well as industrial scale activities. His most important contribution has been the setting up of the industrial scale MOX fuel fabrication plant at Tarapur. Shri Kamath is the recipient of Indian Nuclear Society Award for the year 2003 in recognition of his outstanding contributions in the field of nuclear fuel fabrication.

Dr. M. B Kurup, MSc, Ph.D, is a Professor and Dean in the Faculty of Natural Sciences of Tata Institute of Fundamental Research (TIFR), Mumbai. His areas of specialisation are application of Ion beams for study of atomic physics, materials science and biological systems and the science and technology of accelerators. He has guided a lot of Doctoral Scholars and has a large number of publications besides prestigious honours in his field.

Shri H.S. Kushwaha, B.Sc., M.Tech.(IIT, Kanpur), is presently the Director of Health, Safety and Environment Group at BARC. He has made significant and important contributions in the design and analysis of nuclear structures, components and piping of Indian Pressurised Heavy Water Reactors (PHWR). He has done pioneering work in the area of seismic design and analysis of 500 MWe PHWR being built at Tarapur, Maharashtra. He has developed several finite element computer programmes in the field of structural mechanics, heat transfer and fluid mechanics. He has developed an improved finite element method using upwinding schemes to solve three dimensional advection-diffusion equation. He is an active member of Project Design Safety Committee of PHWRs/FBR, Civil Engineering Safety Committee and Safety Review Committee for Operating Plants (SARCOP) constituted by AERB, Mumbai. He has published around 400 papers/reports in national and international journals.

Shri Y.C. Manjunatha, Director, Engineering Services Group of Indira Gandhi Centre for Atomic Research, Kalpakkam, is a M. Tech. in Electrical Engineering from IIT, Madras and belongs to the 16th batch of BARC Training School, Department of Atomic Energy. He steers one of the largest multidisciplinary groups in the Centre which focuses on providing reliable and robust services through cutting edge technologies and methodologies. Some of his major contributions are development and sustenance of infrastructural works of IGCAR & GSO involving civil, electrical, air conditioning and ventilation, communication, workshop and QA activities. He has published more than 10 papers.

Shri S.D. Misra, B.E. (Electrical and Mechanical Engineering), is presently the Director of Nuclear Recycle Group at BARC. Right from joining BARC through the 13th Batch of Training School, he has been involved with the radioactive waste management assignments. He was a member of a team that pioneered setting up of the first vitrification plant in the country at Tarapur and also was responsible for design and construction of Waste Immobilisation Plants at Trombay and Kalpakkam. He also served as Director of the Directorate of Purchase and Stores of DAE. In this capacity he has successfully used his vast experience of managing large projects that involved procurement of various types of materials, in overcoming several challenging situations the department was facing under embargos. As Director of NRG he is holding the responsibility of setting up operation of reprocessing and waste management plants at various sites in the country.

Shri R. Natarajan is a Chemical Engineer from the Annamalai University, joined the Department of Atomic Energy in 1975. He is presently the Director, Reprocessing Group in IGCAR. Under his leadership, the CORAL facility, for establishing the process technology for the reprocessing of fast reactor fuels, was designed, erected and commissioned. His specialization is in the design process flowsheets. His other field of specialization is the design and operation of Thorium-Uranium cycles. He has participated in the irradiated thorium fuel reprocessing campaigns at the Reprocessing Development Laboratory and the Uranium - 233 recovered is used as fuel for the reactor KAMINI. He has interests in equipment and system designs of radioactive offgas circuits, ventilation design of radiochemical plants, design of clarification systems of dissolver solution, solvent extraction modeling and in acid recovery systems. As director of reprocessing group, he is responsible for the R&D activities of fast reactor fuel reprocessing and setting up of Demonstration and PFBR fuel reprocessing plants. He is also the president of Kalpakkam chapter of Indian Institute of Chemical Engineers. He has over ninety technical presentations and publications to his credit. He has won prestigious NOCIL Award for Excellence in Design and Development of Process Plant and Equipment for the year 2005 for his contribution in the development of fast reactor fuel reprocessing.

Shri. M. Rajan is currently the Director of Safety Group at Indira GandhiCentre for Atomic Research, Kalpakkam. He obtained his B.E. (Hons) in Chemical Engineering at Annamalai University in 1972. He underwent one year advanced course in Nuclear Technology at Bhabha Atomic Research Centre, Mumbai during 1972-73. His main contributions in the past 30 years are on development works related to the use of sodium as a coolant in Fast Breeder Nuclear Reactors and Engineering Safety. He has designed and constructed many high temperature sodium systems and developed many components & methods for the Fast Breeder Reactors. He is a fellow of Indian National Academy of Engineering, Indian Institute of Chemical Engineers and Institution of Engineers.

Shri P.V. Ramalingam is an Outstanding Scientist and presently Director of Reactor Operation and Maintenance Group in IGCAR. He graduated in Electrical Engineering with Honours from Madras University in 1969. He worked in CIRUS reactor, BARC from 1969 to 1975. He was transferred to IGCAR in 1975. He was actively involved in preparing the FBTR station documents and training the operation staff. He was responsible for commissioning the primary sodium system and its auxiliary circuits of FBTR and he had the privilege of making the first criticality of FBTR on October 18, 1984. He was closely associated in taking the reactor power in stages to the power level of 17.4 MWt. He was responsible for implementing many improvements in FBTR for increasing the availability factor of the reactor and in the recently concluded 13th irradiation campaign the availability factor was 94 %. He has to his credit 51 publications in journals/symposia/conferences.

Shri R.K. Sinha, B.E (Mechanical Engineering), is presently a Distinguished Scientist, Director of Reactor Design and Development Group, and Director of Design Manufacturing and Automation Group at BARC. He is a nationally and internationally recognised expert in the area of nuclear reactor technology. He has handled several major assignments relating to the Indian research and power reactors. In particular, he has specialised in design, development and safety related activities relating to coolant channels of heavy water reactors. He is currently guiding the design and development of the innovative Advanced Heavy Water Reactor and Compact High Temperature Reactor. Shri Sinha has received several awards and honours including the Homi Bhabha Science and Technology Award, VASVIK Award and Indian Nuclear Society Award. He is a Fellow of the Indian National Academy of Engineering.

Shri P Swaminathan graduated with honours degree in Electronics & Communication Engineering from Regional Engineering College, Trichirapalli in 1971. He is the Gold medalist of University of Madras. After undergoing one year course in Nuclear Science & Engineering from BARC Training School. Shri P Swaminathan joined Indira Gandhi Centre for Atomic Research in 1972. He further underwent one year course in Main frame system from International Honeywell Bull Training Institute, Paris. Shri P Swaminathan is the main architect for the design, development, installation and commissioning of Fault Tolerant Safety Critical Real Time Computer System for Fast Breeder Test Reactor. As Director of Electronics & Instrumentation Group, Shri Swaminathan is actively engaged in the development of Safety Instrumentation, Innovative Digital Instrumentation, Full scope Training Simulator and Knowledge Management System for Fast Breeder Reactor Programe. Shri P Swaminathan is fellow of Institution of Engineers and also holds Master Degree in Management Science. He has over 40 publications in International journals/seminars. Also as Chairman, Hospital Management Committee, Shri P Swaminathan ensures the smooth functioning of Health Care System.

Shri Umesh Chandra, B.Tech (IIT, Kanpur), is a graduate from IIT, Kanpur. Currently he is the Senior Executive Director (CA and R&D) in NPCIL. He has been responsible for establishment of R&D facilities for nuclear and electronic systems in NPCIL. These facilities are located at R&D Centre, Tarapur and R&D Lab., NUB, Mumbai. He is also directing development and deployment of Computer Based Systems in nuclear power plants for Control and Instrumentation Systems, Main Control Rooms and Training Simulators for PHWR and LWRs. He is also guiding establishment of IT infrastructure and applications in the organisation. He has guided design of control mechanisms for reactor shutdown, various types of remote inspection tools, manipulators and equipment and instruments for monitoring radiation. He is also directing the Knowledge Management activities in NPCIL. He was responsible for Control and Instrumentation of 540MWe TAPP-4 nuclear power plant, which achieved criticality within 5 years of start of construction.

Earlier at Reactor Control Division, BARC, he has been engaged in the development of computer based control and operator information systems for nuclear power plants. He was responsible for computerized control system for on-power refuelling machines of PHWRs from NAPS onwards and Dual Processor Hot Standby (DPHS) based – Processs Control System and Reactor Regulating System for Kaiga-1,2 and RAPP-3,4 reactors. He participated in activities of AERB as a member of several safety committees and Advisory Committee for Code, Guides and manuals for safety in design for nuclear power plants.

Shri. G. Vaidyanathan, is an Outstanding Scientist and Director, Fast Reactor Technology Group at IGCAR. Since 1972, he has been actively involved in the field of Fast reactor design, analysis and experiments. He has made significant contributions to numerical simulation of heat transfer and fluid flow processes in sodium cooled fast reactors. He has meticulously planned and carried out R&D for the thermal hydraulics of Fast Reactors. He has also contributed significantly as member of the IGCAR safety committee. He was instrumental in setting up the Steam Generator Test Facility at IGCAR. He has to his credit about 175 publications in journal/conferences and has co-authored one book.

Dr. P.R. Vasudeva Rao, is an Outstanding Scientist and presently Director of Chemistry Group as well as Metallurgy and Materials Group in IGCAR. He obtained his Doctorate degree in Inorganic Chemistry from Bombay University in 1979. He has played an active role in shaping the Chemistry Programme of IGCAR to its current status. His research interests span over a wide range of areas such as development of alternate extractants and resins for actinide recovery solvent extraction, third phase formation, thermodynamics, diluent effects, development of pyrochemical and other non-aqueous processes for recovery of actinides and rare earths, thermochemical studies on nuclear materials, application of microwaves in synthesis of nuclear fuels and other ceramic materials, nuclear fuel cycle, fuel behaviour in reactors, burn-up measurements and non-destructive assay. He has published more than 130 papers in reputed international journals apart from guiding several research scholars for their doctorate degrees. He is a life member of Indian Nuclear Society, Materials Research Society of India, Society for Advancement of Electrochemical Science and Technology, Indian Association of Nuclear Chemists and Allied Scientists (IANCAS), and President of the Southern Regional Chapter – IANCAS. He has been awarded the MRSI Medal in 1998 and is a Fellow of Tamil Nadu Academy of Sciences.

Dr. V. Venugopal, M.Sc.,Ph.D, is presently an Outstanding Scientist and the Director of Radio Chemistry and Isotope Group at BARC, Mumbai, and Head, Nuclear Material Accounting and Control (NUMAC) cell of DAE. He is a specialist in the field of thermal/ thermodynamics of plutonium based fuels at high temperature, chemical quality control of fuel, X-ray and solid state chemistry. He has to his credit more than 300 publications out of which 165 are published in reputed international journals. Widely acclaimed as an expert in the area of thermodynamics, he is currently the regional editor of Journal of Thermal analysis and Calorimetry. Dr. Venugopal is the President of Indian Thermal Analysis Society (ITAS) and vice president and editor, INS news of Indian Nuclear Society (INS). He is also a member of several professional bodies IANCAS, NAARRI, ISAS, ISEAS, ISMAS, MRSI and Hindi Vigyan Parishad. He has received many awards including the Netzsch-ITAS award in 2001, ISCAS silver medal in 2002 and MRSI medal for 2003-04 and INS award for 2005.

Indira Gandhi Centre Scientific Committee (IGCSC) and Activities of Various Groups

CHAIRMAN

Dr. Baldev Raj
Director, IGCAR

REACTOR ENGINEERING GROUP

Shri S. C. Chetal
Director - Head, SCHD

Dr. P. Chellapandi
Associate Director, NEG

Dr. P. Mohanakrishnan
Head, RPD

Shri T.K. Shanmugam
Head, PPED

Shri P. Puthiyavinayagam
Head, RCD

Shri K. Madhusoodanan
Head, ICD

Shri C. Sivathanu Pillai
Head, CED

Dr. P. Selvaraj
Head, MHD

Reactor Engineering Group (REG) is responsible for the design of 500 MWe Prototype Fast Breeder Reactor. Design of Nuclear Steam Supply System is carried out in-house. For Balance of Plant, design coordination is carried out by REG while the consultants are assigned the design work. REG is responsible for getting the design clearance of 500 MWe FBR from AERB. R&D coordination towards FBR and execution of R&D for structural mechanics is the responsibility of the Group. As FBR is primarily based on indigenous technology, the manufacturing technology development of important nuclear components was undertaken by REG with the active participation of Indian Industries and has been successfully completed. The components include main vessel, inner vessel, grid plate, roof slab, shutdown mechanisms, steam generator and largest size sodium service valve. REG provides the design support to FBTR. REG has acquired expertise in design of fast reactor. As a spin-off, structural mechanics expertise is being provided for non-reactor activities.

METALLURGY AND MATERIALS GROUP

Dr. P.R. Vasudeva Rao
Director

Shri P. Kalyana Sundaram
Associate Director, ITG

Dr. H. S.Khatak
Head, CSTD

Dr. S. K. Ray
Head, MTD

Dr. K. Bhanu Sanakara Rao
Head, MMD

Shri P. V. Kumar
Head, IDEAS

Dr. C. S. Sundar
Head, MSD

Shri K. V. Kasiviswanathan
Head, PIRD

Dr. T. Jayakumar
Head NDED

Dr. M. Vijayalakshmi
Head, PMS

The Metallurgy and Materials Group has the mandate for comprehensive materials R & D programme focussed towards FBR technology. This requires multifaceted and multidisciplinary approaches that include development of special alloys, welding consumables, optimisation of fabrication schedules, characterisation of mechanical properties under sustained as well as varying loads at elevated temperatures over a wide ranges of strain rates, comprehensive characterisation of corrosion and bio-fouling, development and application of specialised NDE techniques, innovative designs, and robotics for remote handling. This has been backed by fundamental studies in basic science that includes studies on microstructure dependence of the various properties, radiation damage, positron annihilation, thermo-physical properties and mathematical modelling. Some significant contributions of the group include PIE of FBTR fuel pins that has led to enhancement of target burn up, and development of indigenous structural steels and welding consumables for PFBR applications. At the same time, the outstanding research contributions have brought international recognition in fields as diverse as life prediction under creep and creep-fatigue conditions, characterisation of microstructures by NDE techniques, welding science and technology, and materials science.

FAST REACTOR TECHNOLOGY GROUP

Shri G. Vaidyanathan
Director

Shri. P. Kalyana Sundaram
Associate Director, FRTG

Dr. C. Ananda Babu
Head, ST & HD

Shri B. Krishna Kumar
Head, CIDD

Shri K. K. Rajan
Head, SFD

The Fast Reactor Technology Group is involved in heat and mass transfer studies in cover gas above sodium free levels, development of sodium components like cold trap, plugging indicator, filters, heaters, valves etc., development and testing of sodium sensors for level and flow and leak detection sensors for sodium leak, sodium pump development, testing of control rod mechanisms, testing of inflatable seals, testing of fuel and other subassemblies for pressure drop and cavitation, reactor assembly flow patterns, vibration testing of steam generator and intermediate heat exchanger etc., instability measurement in steam generators, testing of full scale fuel handling machines in air and sodium. To achieve the above, the group has many water and sodium rigs. The biggest rig is the Steam Generator Test Facility (5.5 MWt). The R&D and testing activities for the 500 MWe Fast Breeder Reactor (FBR) are presently in progress.

REACTOR OPERATION AND MAINTENANCE GROUP

Shri P. V. Ramalingam
Director

Shri B. Rajendran
Associate Director

Shri G. Srinivasan
Head, TSD

Shri K. Ravishankar
Head, THRDD

Dr. V. Ramanathan
Head, RMD

ROMG is responsible for safe operation of Fast Breeder Test Reactor (FBTR) and KAMINI reactor with in the limits given in technical specification documents. The group takes part in the operational safety review of 500 MWe Fast Breeder Reactor (FBR) Project documents. The Training and Human Resources Development Division of the group besides training O&M staff of FBTR and KAMINI is also responsible for training the O&M staff of FBR. Introducing innovations and new features in FBTR to increase its availability, enhancing safety, and gaining newer experience for incorporation of inferred ideas in FBR construction and operation, govern a part of ROMG's activities.

REPROCESSING GROUP

Shri R. Natarajan
Director

Dr. S. B. Koganti
Head, RRDD

Shri P. Ramkumar
Head, RPSD

Shri A. Ravisankar
Head,RPDD

Shri M. Venkataraman
Head, RPOD

Shri V. Sundararaman
Head, FRPD

The Reprocessing Group (Rp G)of IGCAR is responsible for the development of Fast reactor fuel reprocessing technology and construction of the reprocessing plants.

RDL has two hot cell facilities: In one of them, U-233 was recovered from irradiated thorium rods on campaign basis and used as fuel in KAMINI reactor and in FBTR (as PFBR test fuel). The other hot cell facility, called, Lead Mini Cell (LMC) commissioned in 2003, is a test bed for validating the process flow sheet and scaling up of equipment designs for fast reactor fuel reprocessing, by processing the FBTR fuel itself. LMC has already processed mixed carbide fuels irradiated in FBTR with 25 and 50 GWd/t burnups. This has provided valuable experience to the Demonstration Fast reactor fuel Reprocessing Plant, DFRP, in which the FBTR fuels will be regularly reprocessed. DFRP, which will also demonstrate the reprocessing of PFBR fuel subassemblies, is slated for commissioning by 2007.

Various R&D activities are being carried in the Reprocessing Development Laboratory. Engineering scale testing of equipment and systems are done here before installing in for hot cell. Chopper, dissolver, feed clarification equipment, centrifugal extractors are few of the important equipment developed at RDL. Apart from equipment development, research is undertaken for understanding and solving various process and chemistry problems of fast reactor fuel reprocessing such as, mathematical modeling of solvent extraction of the complex U-Pu system, efficient solvent management, development of online monitoring of Pu for process control, liquid flow metering in high radio active fields etc.,

CHEMISTRY GROUP

Dr. P. R. Vasudeva Rao,
Director

Dr. V. Ganesan
Head, MCD

Dr. T. G. Srinivasan,
Head, FChD

Dr. T. Gnanasekaran,
Head, LMSCD

Shri K.C. Srinivas,
Head, CFD

The Chemistry Group is responsible for carrying out R & D to provide inputs with respect to all the chemistry aspects of the fast reactor and its fuel cycle. In addition, it also takes up R&D programmes which would have a long term impact on the reactor programmes. Besides the R&D activities, the Chemistry Group also provides extensive analytical support using a wide range of analytical techniques to all the programmes in the Centre. The Chemistry Group has also specialized in setting up of facilities for experiments with radioactive or air-sensitive materials, and in indigenous development of chemical instrumentation.

The areas of R & D in Chemistry Group include sodium chemistry, chemistry of un-irradiated as well as irradiated fuel materials, development of fuel cycle, analytical chemistry, spectroscopy and more recently, boron chemistry. Development of sensors for PFBR and sensors for environmental applications, cover gas purification system for PFBR, development of Laser Induced Breakdown Spectroscopy and X-ray absorption based techniques for on-line monitoring of Pu streams in reprocessing plants, development of technology for production of Pu rich fuels and minor actinide containing fuels through sol-gel route and development of sodium bonding for metallic fuels are some of the R & D programmes on the anvil.

SAFETY GROUP

Shri M. Rajan
Director

Shri N. Kasinathan
Head, SED

Dr R. Indira
Head, RSD

Shri M. Somasekaran
Head, SIRD

Safety Group consists of Safety Engineering Division, Radiological Safety Division and Scientific Information Resource Division.

Safety Engineering Division is engaged in the simulated experimental studies and development of mathematical models for FBR accident scenarios such as core subassembly flow blockage, molten fuel relocation, core debris cooling in core catcher, mitigation of consequences of sodium fires and radioactivity transport and deposition in sodium circuits.

Radiological Safety Division is mainly responsible for the research and development activities in radiation safety. The division provides health physics services for all the radioactive facilities in IGCAR. Studies on criticality safety, radiological safety analysis of BDBA in PFBR, radiation detector development, biodosimetry with reference to low level radiation exposure effects, development of a neutron generator for actinide assay in wastes, studies on thermo-luminescence and radioactivity transport in media are some of the major research work being carried out presently.

The group organizes public awareness programmes on radiation safety and nuclear energy. It also carries out industrial training programme to increase safety awareness.

The Scientific Information Resource Division is taking care of the Library and Information Services at the Centre. Work is in progress towards creation of a digital library for the FBR literature and making it available for campus wide access using the IGC Network. All the IGC publications are made available in full text electronic form.

ELECTRONICS AND INSTRUMENTATION GROUP

Shri P. Swaminathan
Director

Shri S. Athinarayanan
Head, CD

Shri S. Ilango Sambasivan
Head, EID

Shri B. Saha
Head, IIS

Dr. A. Vijaya
Medical Superindent,
DAE Hospital

Shri S.A.V. Satyamurty
Head, NS, CD

The Electronics and Instrumentation Group is actively engaged in the development of Strategic Safety Systems for Fast Breeder Reactor Programme such as VME based Real Time Computer systems and Safety Logic Systems. Electro magnetic Time domain survey system is also being developed to detect deeply buried uranium ore. Highly reliable Instrumentation systems are being developed using VLSI design tools, thermal design tools and EMI/EMC design tools. Application software packages are being developed using modern CASE TOOL.A Full scope Replica Type Training Simulator is being developed for training the operators of the Plant. Both normal operation of the plant such as start-up, power raising as well as incidents such as station black-out, tripping of pumps etc are simulated. Walk through of different areas of the reactor are being developed using PDMS packages. Intranet based Knowledge Management System is being grown. Simplicity in instrumentation is being realised through the innovative programme on creation of pulsating sensors for diverse parameters, enabling development of completely indigenous plant monitoring and surveillance systems, rapid analytical and diagnostic tools. The group is also responsible to ensure satisfactory health services to the residents of Kalpakkam and Anupuram Townships.

ENGINEERING SERVICES GROUP

Shri Y. C. Manjunatha
Director

Shri A.Jyotish Kumar
Head, ESD

Shri A.S.L.K. Rao
Head, CWD

Shri B. Venkatraman
Head, QAD

Shri S. Keshvamurthy Rao
Head, AC&VSD

Shri N. Vijayan Varier
Head, QC & CS

Engineering Services Group is responsible for providing quality services pertaining to Civil Engineering, Electrical Engineering, Voice Communication Systems, Air-conditioning & Ventilation Systems, Material Handling Equipments, Central Workshop activities, Quality Control & Quality Assurance and Testing. The Group also coordinates the telecommunication requirements of the centre. The Group has a mandate to establish additional infrastructure requirements so as to meet Design, R&D and operational objectives of IGCAR. The Group has expert teams with capability to design, engineer and execute systems under their jurisdiction. Electricity, water, quality-air and other services are being extended to other units of DAE located at Kalpakkam. The nature of work involves interaction with several State-Government and Central Government - organizations.

FAST REACTOR FUEL CYCLE FACILITY (FRFCF)

Shri P.V. Kumar
Project Director,
FRFCF

Fast Reactor Fuel Cycle Facility (FRFCF) Project Group is engaged in planning and designing a fuel cycle facility to close the fuel cycle of the 500 MWe Prototype Fast Breeder Reactor (PFBR) that is being constructed at present. FRFCF would be first of a kind facility in the country and would have all the plants required to reprocess the spent fuel, fabricate fuel pins and assemblies, and manage the wastes generated. The technology for the plants would be provided by BARC, NFC and IGCAR. IGCAR would coordinate all the work related to the facility. The Group is presently engaged in designing the plants, preparation of documents for safety review, and obtaining statutory clearances.

PLANNING DIVISION

Smt. Uma Seshadrl
Head, PD

Planning Division (PD) shoulders the responsibilities of planning, budgeting and continuous monitoring of expenditure of capital projects. It also generates various reports, which are vital in decision making processes. The activities briefly are: Capital project planning (under all sectors viz., R&D, Industries and Power); Preparation of budget for all the projects; Monitoring and controlling expenditure under capital project heads. Conducting Budget Review Meetings (BRM) every month to expedite and sort out pending issues; Automation and integration of activities as well as coordination between indentors at IGCAR, MRPU, Accounts and Stores regarding procurement and expenditure bookings; Preparing various reports and forwarding to DAE.

STRATEGIC AND HUMAN RESOURCES PLANNING SECTION

Dr. M. Sai Baba
Head, SHRPS

The section has the mandate of planning for the Strategic and Human Resource needs of the Centre which involve: Planning and running the training school programs at IGCAR-Training School; Collaborative projects with various R&D organizations and Academic institutes; Compilation of technical reports on important activities of the Centre; Interacting and coordinating with National and International delegations; Assessing and projecting the human resource needs of the center for effective deployment and utilization; Interacting with the research scholars at the Centre; Planning and organizing meetings related to human resource and personality development.

ADMINISTRATION & ACCOUNTS

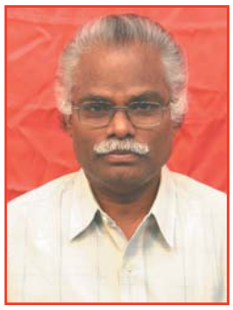

Shri V. Dayalan
Chief Administrative Officer

Shri S. Mani
Joint Controller (Finance & Accounts)

Shri T.Y. Prahalad Rao
CAO, GSO

Shri R.G. Raghavan
AO, Secretary, IGCSC

MADRAS REGIONAL PURCHASE UNIT

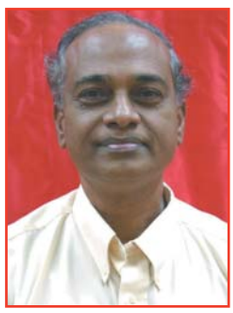

Shri K. Balachander
Regional Director, MRPU

Material Management services are taken care by Directorate of Purchase & Stores for IGCAR. MRPU's procurement and accounting activity is located at Chennai and Stores activity is located at Kalpakkam. There has been a consistent improvement in the quality and the pace of the services rendered. The procurement activity per annum including high value and state of the art equipment has reached a value of around Rs.75 crores in the current year. To name a few, Magneto Encephalograph facility and XPS system were procured and are being installed at IGCAR complex.

LIST OF IMPORTANT ABBREVIATIONS

AERB	Atomic Energy Regulatory Board
BARC	Bhabha Atomic Research Centre
BARCF	BARC Facilities
BHAVINI	Bharatiya Nabhikiya Vidyut Nigam Limited
BHEL	Bharat Heavy Electricals Limited
CD	Computer Division
CDO	Central Design office
CDPS	Central Data Processing System
CERMON	Continuous Environmental Radiation Monitoring Network
CG	Chemical Group
CORAL	Compact facility for Reprocessing Advanced fuels in Lead cell
CSTD	Corrosion Science and Technology Division
CWD	Central Workshop Division
ED	Electronics Division
EIG	Electronics and Instrumentation Group
ESG	Engineering Services Group
FBR	Fast Breeder Reactor
FBTR	Fast Breeder Test Reactor
FChD	Fuel Chemistry Division
FRFCF	Fast Reactor Fuel Cycle Facility
FRTG	Fast Reactor Technology Group
IDEAS	Innovative Design, Engineering and Synthesis
IIS	Innovative Instrumentation Section
IIT	Indian Institute of Technology
IMSc	Institute of mathematical Sciences
ITG	Inspection Technology Group
LMFBR	Liquid Metal Cooled Fast Breeder Reactor
MAPS	Madras Atomic Power Station
MCD	Materials Chemistry Division
MMD	Mechanical and Metallurgy Division
MMG	Metallurgy and Materials Group
MSD	Materials Science Division
MTD	Materials Science Division
NFC	Nuclear Fuel Complex
NICB	Nuclear Island Connected Buildings
NPC	Nuclear Power Corporation
NSSS	Nuclear Steam Supply System
PFBR	Prototype Fast Breeder Reactor
PHWR	pressurized Heavy Water Reactor
REG	Reactor Engineering Group
RHS	Remote Handling Section
ROMG	Reactor Operation and Maintenance Group
RPD	Reactor Physics Division
RpG	Reprocessing Group
RRDD	Reprocessing Research and Development Division
RSD	Radiological Safety Division
SED	Safety Engineering Division
SG	Safety Group
SGTF	Steam Generator Test Facility
SIRD	Scientific Information and Resources Division
SOWART	Sodium Water Reaction Test facility